

# Novel formation regimes and mechanisms for macropores and porous anodic oxides in silicon

Dissertation  
zur Erlangung des akademischen Grades  
Doktor der Naturwissenschaften  
(Dr. rer. nat.)  
der Technischen Fakultät  
der Christian-Albrechts-Universität zu Kiel

Stefan Frey

Kiel  
2005

1. Gutachter:

Prof. Dr. H. Föll

2. Gutachter:

Prof. Dr. F. Faupel

Datum der mündlichen Prüfung: 16.12.2005



# Contents

<b>1</b>	<b>Introduction</b>	<b>1</b>
<b>2</b>	<b>Semiconductors and electrolytes</b>	<b>5</b>
2.1	Semiconductors . . . . .	5
2.1.1	Intrinsic semiconductors . . . . .	5
2.1.2	Doping . . . . .	8
2.1.3	Generation and recombination of carriers . . . . .	8
2.1.4	Current transport mechanisms . . . . .	8
2.2	Semiconductor metal junctions . . . . .	10
2.2.1	Contact formation and transport characteristics . . . . .	10
2.2.2	Junction breakdown . . . . .	13
2.3	Semiconductor-electrolyte junctions (SEJ) . . . . .	14
2.3.1	Structure of the SEJ . . . . .	14
2.3.2	Kinetics at the SEJ . . . . .	15
2.3.3	Current limiting factors for the SEJ . . . . .	19
2.4	Modification of Electrolytes . . . . .	20
2.4.1	Buffered Electrolytes . . . . .	20
2.4.2	Surfactants . . . . .	21
<b>3</b>	<b>The silicon/HF contact</b>	<b>25</b>
3.1	Aqueous electrolytes . . . . .	25
3.1.1	Chemical reactions . . . . .	25
3.1.2	<i>IV</i> characteristic of p-type silicon . . . . .	26
3.1.3	<i>IV</i> characteristic of n-type silicon . . . . .	28
3.2	Organic electrolytes . . . . .	28
<b>4</b>	<b>Anodic oxides</b>	<b>33</b>
4.1	Oxide types and properties . . . . .	33
4.2	Growth of anodic oxides . . . . .	35
4.3	Porous oxides . . . . .	36
4.3.1	Other porous oxides . . . . .	36
4.3.2	Anodically formed porous silica . . . . .	37
4.4	Etching of oxides . . . . .	38
4.5	Electrochemical oscillations . . . . .	42
4.6	Modelling . . . . .	43
4.6.1	Overview of models . . . . .	43
4.6.2	Current Burst Model (CBM) . . . . .	44

<b>5</b>	<b>Pores in Silicon and InP</b>	<b>49</b>
5.1	Classification . . . . .	49
5.2	Pores in silicon . . . . .	50
5.2.1	Macropores . . . . .	50
	n(bsi,aq) . . . . .	51
	n(bsi,org) . . . . .	53
	p(org) . . . . .	53
	p(aq) . . . . .	54
	Applications . . . . .	54
5.2.2	Meso- and breakthrough pores . . . . .	54
5.2.3	Influence of surfactants . . . . .	56
5.3	Pores in InP . . . . .	58
5.4	Pore growth in the current burst model (CBM) . . . . .	59
5.5	Impedance analysis of pore growth . . . . .	60
<b>6</b>	<b>Experimental set-up and sample analysis</b>	<b>63</b>
6.1	Anodization set-ups and sample preparation . . . . .	63
6.1.1	General notes on electrochemical anodization procedures . . . . .	63
6.1.2	Peristaltic pump set-up . . . . .	65
6.1.3	Rotating disk electrode (RDE) . . . . .	68
	Theoretical notes on RDE systems . . . . .	69
6.2	Sample analysis . . . . .	71
6.2.1	Scanning electron microscope (SEM) . . . . .	71
6.2.2	UV-VIS spectrometry . . . . .	74
<b>7</b>	<b>Experimental results on porous silicon</b>	<b>77</b>
7.1	n <sup>+</sup> mesopore growth . . . . .	77
7.1.1	Introduction and experimental set-up . . . . .	77
7.1.2	Experimental results . . . . .	78
7.1.3	Discussion . . . . .	86
	Ethanol content . . . . .	86
	HF concentration . . . . .	88
	UV-VIS data . . . . .	88
7.2	Octahedral growth . . . . .	91
7.2.1	Introduction and experimental set-up . . . . .	91
7.2.2	Experimental results . . . . .	91
7.2.3	Discussion . . . . .	93
	Comparison of meso- and macropore growth . . . . .	93
	Model for the octahedral pore growth . . . . .	96
7.3	Fast macropore growth . . . . .	99
7.3.1	Introduction and experimental set-up . . . . .	99
7.3.2	Experimental results . . . . .	100
	Aqueous electrolytes . . . . .	100
	DMF based electrolytes . . . . .	104
	MeCN based electrolytes - general observations . . . . .	107
	MeCN based electrolytes - parameter optimization . . . . .	115
7.3.3	Discussion . . . . .	131

Oxide influence . . . . .	131
Passivation influence . . . . .	132
Growth model . . . . .	133
Voltage transients versus morphology . . . . .	136
Solvent versus morphology . . . . .	136
Nucleation behavior . . . . .	140
Close packaging patterns . . . . .	141
Role of surfactants . . . . .	143
7.3.4 Conclusions . . . . .	146
<b>8 Porous oxides - Experimental results</b>	<b>149</b>
8.1 Introduction and experimental set-up . . . . .	149
8.2 Experimental results . . . . .	150
8.3 Discussion . . . . .	172
8.3.1 Granular morphology . . . . .	172
8.3.2 Reactions, etch rates and the influence of the buffer . . . . .	174
8.3.3 Impedance analysis . . . . .	177
8.3.4 Flat and corrugated morphology . . . . .	181
8.4 Conclusions . . . . .	184
<b>9 Summary and outlook</b>	<b>187</b>
9.1 Results and outlook on porous silicon . . . . .	187
9.2 Results and outlook on porous anodic oxides . . . . .	189
<b>Bibliography</b>	<b>191</b>



# Chapter 1

## Introduction

Although the first transistors were based on Germanium [1], in the middle of the 1950s silicon (Si) has started its triumphant success in microelectronics. Especially the extremely stable oxide ( $\text{SiO}_2$ ) which can be formed on Si without inducing strong mechanical stress, helped silicon a lot, because this provided the basic masking technique for the planar process for integrated circuits (ICs). The uses of this oxide in nowadays microelectronics are numerous and go from device isolation over the use as a gate oxide in MOS<sup>1</sup> structures to masking purposes for other processes [2].

Many times, silicon has been pronounced dead, but it has proven always that “there is life in the old dog yet”. E.g. the carrier mobility has always been seen as a limiting factor when the transistor speeds reach the GHz range. However, recently AMD has proven with its “dual stress liner” concept [3], that it is even possible (in a VLSI<sup>2</sup> compatible process) to strain the one transistor of a CMOS<sup>3</sup> element while compressing the other one, which leads again to a 24 % speed increase of the transistors. Therefore - at least for the moment - the saying in microelectronics industry that “Gallium arsenide is the material of the future and always will be...” [4] remains true.

Chemistry steps have always been important in silicon manufacturing; nowadays over 150 out of 400 process steps in DRAM fabrication involve wet chemistry [2]. Especially hydrofluoric acid (HF) is elementary for most steps, because it is the only acid which can dissolve  $\text{SiO}_2$  effectively. Silicon itself on the other hand is nearly inert in pure HF without applying an external voltage. However in the presence of oxidizing agents, e.g. hydrogen peroxide  $\text{H}_2\text{O}_2$  or nitric acid  $\text{HNO}_3$ , the silicon surface is transformed into  $\text{SiO}_2$  and then quickly dissolved if HF is present. The chemistry behind these processes is always also electrochemistry with the sole difference that “pure chemistry” supplies the necessary voltages by internal sources rather than by external batteries or power supply units. When an external voltage is applied to silicon in HF (without further oxidizers) the variety of features of the Si/HF contact becomes visible: At negative voltages (i.e. polarized “cathodically”<sup>4</sup>) the silicon is inert and only hydrogen is generated at the electrode. When switching to positive potentials (i.e. polarizing “anodically”) the silicon electrode corrodes. At low voltages it becomes porous, while at high voltages surface

---

<sup>1</sup>MOS = Metal Oxide Semiconductor

<sup>2</sup>VLSI = Very Large Scale Integration

<sup>3</sup>CMOS = Complementary Metal Oxide Semiconductor technique; there two different field effect transistors (FETs) are coupled. This is the base element of most modern microelectronic circuits.

<sup>4</sup>Strictly speaking the cathodic regime is defined as the voltage region where a negative current flows, i.e. positive charges flow from the solution into the silicon. Due to offsets in the voltage, this does not necessarily have to coincide with the sign of the voltage.

oxide grows, the so-called anodic oxide. The pores can have extremely different morphologies, starting from sponge-like micropores with dimensions in the nm range up to tubular macropores with diameters of more than 100 micron [5]. Occasionally, also fractal surface structures are found instead of deep structures.

Steven Weinberg, one of the architects of the standard model in particle physics, wrote in an essay about his “Four golden lessons” for a scientist [6] that “my advice is to go for the messes - that’s where the action is”. What he tried to express in his article is that especially as a young scientist, one should always aim at the unclear fields of science, even if this causes unease at first sight. From that point of view, silicon electrochemistry is an ideal starting point for a PhD thesis: Although silicon is - as sketched above - THE material for microelectronics, still the chemistry steps in this industry are often handled as “black art” [2]. When a solution works for a certain task, it is kept with the motto “never change a winning team”.

This thesis addresses mainly new parameter regions for the growth of macro- and mesopores as well as anodically grown oxide. Although this sounds like classical ivory tower work, almost no month passed during this thesis without requests from an industry company or another lab for “custom-made” pore layers. Albeit many receipts for the production of porous silicon are known, the exact tailoring of a pore morphology for a distinct application is hard if not impossible without a deeper understanding of the formation mechanisms of porous silicon, or, in other words, a deeper understanding of the Si/HF contact itself.

Mesopores can be characterized roughly as small (10 - 100 nm diameter), fast (growth rates of several ten micron per minute), and “ugly”. The morphology is hardly controllable, the pores often branch and have a serrated look. However they are fairly simple to make, even on large areas, therefore applications which simply need a certain porosity, e.g. for the modulation of the refractive index in Bragg mirrors [7], often use to mesopores. The first part of the experimental results (section 7.1) depicts the development of a recipe for “custom” made mesopores along given specifications of an industrial project for the wafer industry. This also comprised the development of a non-destructive monitoring process to allow for a quick evaluation of the pore film quality and lateral homogeneity.

Macropores are complementary to mesopores: they are large (diameters 1 - 100  $\mu\text{m}$ ), slow (growth rates typically 0.5 - 1  $\mu\text{m}/\text{min}$ ), and of high structural quality. Under optimized conditions they can be grown as unbranched tubes with smooth walls and tremendous aspect ratios of 500:1 (length to diameter of the pore). The extreme geometries and the structural quality combined with a low-cost technology have triggered various ideas for applications, e.g. as an electrode material for micro fuel cells [8]. However, the extremely long etching times, which can easily rise to 20 h for the etching of a single wafer, are a big economical obstacle for the introduction of this process into any production line. Any previous attempts to reduce the etching time (e.g. by a simple increase of the current density or the HF concentration) always led to a quick deterioration of the pore quality. Section 7.3 describes a newly discovered macropore growth regime which allows for the growth of “nice” macropores with a multiple of the old velocity.

On the other hand, especially bio-tech applications call for smaller macropores, i.e. the structural quality of macropores is requested but at shrunken dimensions. This addresses e.g. templating and filtering issues [9] as well as the use of porous membranes for DNA sensing [10] or unfolding [11], where pore diameters of 250 nm or smaller are demanded. With mesopores, it has shown to be hard to grow stable and homogeneous pore layers with pore diameters larger than 50 nm. Macropores have only shown in p-type silicon such small dimensions as 200 nm and this yet only at a low structural quality. Without very sophisticated wafer material,

macropores range however always above 1 micron. The new pore type discussed in section 7.3 has also shown to be able to cover this former gap in pore sizes.

Silicon dioxide substrates have been always the workhorse for a lot of (bio)chemical applications, e.g. chromatography, which is used to determine the constituents of a protein mixture. One variant of this process relies for over 40 years on so-called “controlled pore glasses” CPG [12,13], i.e. porous oxide substrates. Also in microelectronics, low-k dielectrics are calling or will soon call for porous oxides [14], of course happily at first for a porosified silicon dioxide. While it is possible to grow porous oxides by anodization, they always operate in the shadow of the sol-gel manufactured porous oxides which is also a fairly cheap and well-controllable process. The nanopores in the sol-gel oxides can be processed with a variety of perfectly self-organized pore lattices [15,16]. Several electrochemically produced porous oxides, namely porous alumina [17,18], have shown nice ordering by self-organization. Porous (anodic) silica is however only rarely encountered in literature [19,20]. In the last experimental chapter 8 investigations on the formation mechanism and ordering phenomena in this material are discussed for the special case of weakly buffered neutral electrolyte, where oxide dissolution is strongly reduced.

In chapter 2 the basic background of semiconductors and electrochemistry is discussed. This includes special electrolyte modifications like buffers and surfactants. In chapter 3 the general characteristic of the the Si-HF contact is discussed. As already exemplified above the anodic part of the characteristic can comprise the formation of pores as well as of anodic oxide. The properties of the latter will be described first in chapter 4, because the understanding of anodic oxidation is a key to understand pore growth, which is covered by chapter 5. While the majority of experiments was executed at the CAU Kiel, Germany, a part of this thesis was accomplished at the Ecole Polytechnique/CNRS, Palaiseau, France. The experimental set-ups used at both sites as well as the characterization tools are described in chapter 6. Chapter 7 bundles the results on porous silicon. This comprises the already mentioned projects on thin mesoporous films and fast macropore growth as well as fundamental investigations on the formation of octahedral cavity chains during mesopore growth. The experimental results on porous anodic oxides fill the last experimental chapter 8. The thesis closes with a summary and an outlook in chapter 9.





# Chapter 2

## Semiconductors and electrolytes

### 2.1 Semiconductors

#### 2.1.1 Intrinsic semiconductors

The resistivity  $\rho$  is one of the prime parameters to classify materials:

- Metals:  $\rho \approx 1 - 100\mu\Omega cm$
- Semiconductors:  $\rho \approx 1m\Omega cm - 10k\Omega cm$
- Insulators:  $\rho \approx 100k\Omega cm - 10^{18}\Omega cm$

Semiconductors offer the unique possibility to change the conductivity of one specific material over several orders of magnitude by the addition of so-called dopants (cf. p. 7). Intrinsic semiconductors have per se no free carriers at  $T = 0$  K, at higher temperatures the conductivity begins to rise (in contrast to metals whose conductivity shrinks with  $T$ ). This can be understood when the transition from a single atom (e.g. Si) to a crystal lattice is looked at (cf. Fig. 2.1a). A single atom has discrete energy levels. When two atoms form a molecule, the orbitals of the individual atoms overlap, which leads to new energetic positions for electronic levels. Each electronic level splits up into a level a little bit lower ("binding state") than the original level and one, which is a little bit higher ("antibinding state"). This can be continued for larger agglomerations of atoms (e.g. in a crystal lattice) where the number of levels gets so high that quasi-continuous bands of energy levels form. The last occupied band is then called "valence band" while the "conduction band" is the first unoccupied band.

Like for free electrons (with a parabolic dispersion) also the dispersion relation between momentum and energy of electrons in a crystal lattice can be calculated (Fig. 2.1(b) shows the band structure for silicon). As can be seen from Fig. 2.1(b) the valence band (maximum at 0 eV) is separated from the next band (= conduction band) by the band gap energy  $E_G = E_C - E_V$  ( $E_C$ : absolute minimum of the conduction band,  $E_V$ : absolute maximum of the valence band). Electrons in a fully filled band (like it is the case for semiconductors<sup>1</sup>) cannot conduct current, a phenomena which can only be understood in the picture of quantum mechanics [21]: In a completely filled band the individual motions of the electrons cancel out each other, i.e. there is no net current going into a specific direction<sup>2</sup>. Only if it is possible to accelerate some electrons

---

<sup>1</sup>Strictly speaking, this is only true at  $T = 0$  K, otherwise there is a thermal excitation of carriers.

<sup>2</sup>The image of electrons as cars in a fully occupied parking lot [21], where they cannot move, is nice but nevertheless wrong...

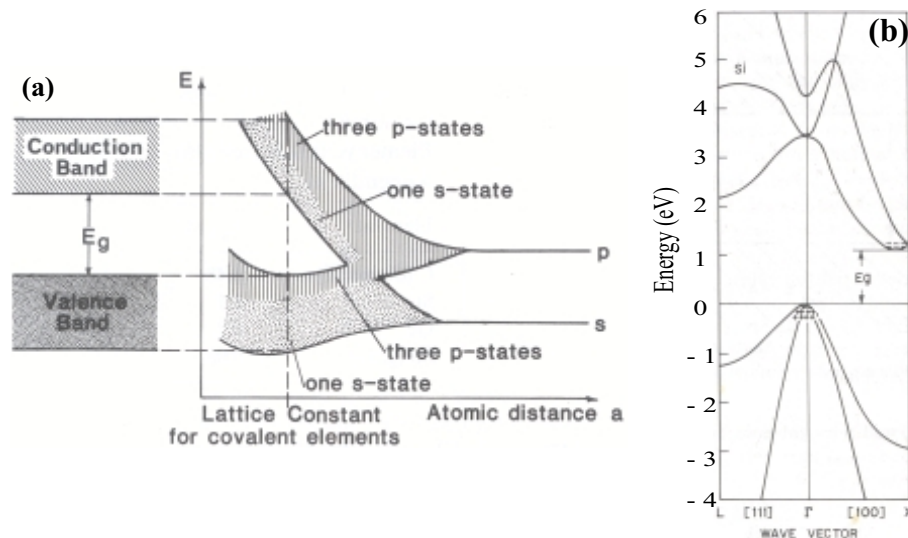


Figure 2.1: **(a)** Electron energy levels as a function of interatomic distance: Isolated atoms have discrete electron energy levels, which widen into energy bands for atoms in close contact. For covalently bound elements the last occupied levels ("valence band") are separated from the non-occupied levels ("conduction band") by an energetical band gap  $E_g$  (from [21]). **(b)** Energy band diagram for Si (from [22]).

by an external field, i.e. put them into a higher energetic state, a net current will flow, which is carried by the excited carriers. Clearly, this is not possible if a band is fully filled and separated from the next band by an energetic barrier  $E_G$ . Electrons are fermions, therefore each state can be occupied by only one electron according to Pauli's principle, i.e. when all states in a band are filled up, an electron cannot gain extra energy during an intra-band excitation because there is simply no empty state to which it could be elevated. Metals have only partially filled bands which allow for their high conductivity. Semiconductors are by definition materials with band gaps up to 3 eV (Si:  $E_G = 1.1$  eV), materials with higher  $E_G$  are called insulators.

As previously mentioned, only at  $T = 0$  K, the conduction band is completely empty. In general, the distribution of fermions over the energy levels is described by the Fermi-Dirac statistic  $f(E)$  (where the Fermi energy is defined by  $f(E_F) = 1/2$ ):

$$f(E, T) = \frac{1}{1 + e^{\left(\frac{E-E_F}{kT}\right)}} \quad (2.1)$$

( $k$ : Boltzmann constant)

At  $T = 0$  K, the Fermi energy  $E_F$  designates the last occupied energy level, i.e. it separates the empty and the filled states. For semiconductors the Fermi energy is always<sup>3</sup> located within the band gap. To obtain the number  $n$  of electrons which are populating the conduction band due to thermal activation, the Fermi-Dirac distribution  $f(E, T)$  has to be folded with the density of states (DOS)  $D(E)$  [22]:

<sup>3</sup>Except for so-called degenerately doped semiconductors.

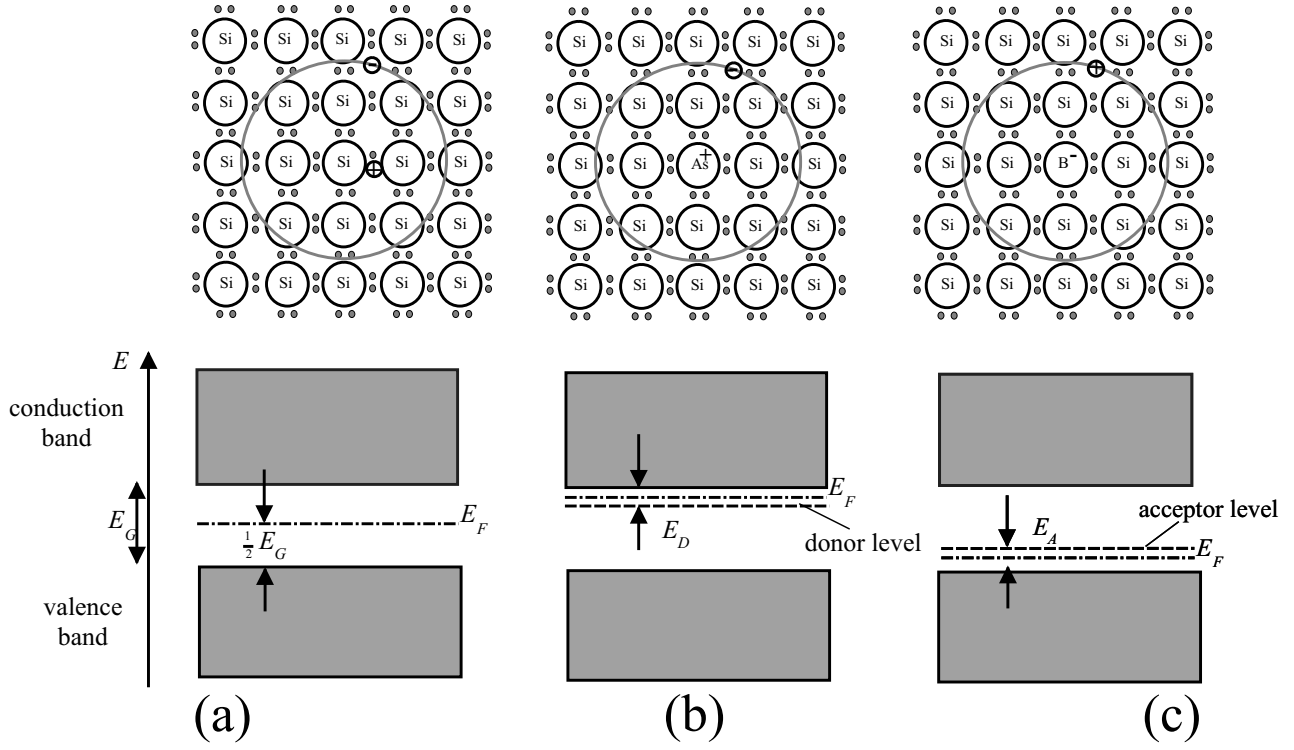


Figure 2.2: Doping of a semiconductor (crystal lattice and resulting energy band diagrams): (a) intrinsic case. (b) n-doped. (c) p-doped.

$$n = \int_{E_C}^{E_{top}} D(E) f(E, T) dE \approx N_C e^{-\frac{E_C - E_F}{kT}} \quad (2.2)$$

( $E_{top}$ : energy at the top of the conduction band,  $N_C$ : effective density of states in the conduction band (cf. [22])).

In standard semiconductors the DOS can be calculated as follows:

$$D(E) = M_c \frac{\sqrt{2(E - E_C)}}{\pi^2 \hbar^3} m_{de}^{3/2} \quad (2.3)$$

( $M_c$ : number of equivalent minima in the conduction band,  $m_{de}$ : density-of-state effective mass for electrons (cf. [22]),  $\hbar$ : Planck's constant divided by  $2\pi$ )

The right part of Eq. (2.2) is correct for non-degenerate semiconductors, where  $E_F$  is several  $kT$  below  $E_C$ . For every electron which leaves the valence band an empty "space" remains in the valence band, a "hole"  $h^+$ . When holes move through the crystal they carry effectively a positive charge and they can also be attributed a mass, a velocity etc. In intrinsic semiconductors, of course, the number of holes is equal to the number of electrons in the equilibrium case.

### 2.1.2 Doping

The equality of carrier concentrations disappears when the semiconductor is doped with impurities (Fig. 2.2). For so-called n-type doping, tiny fractions of the silicon atoms are replaced by an electron "donator", an element with five valence electrons in the outermost shell (e.g. arsenic). When the As atom replaces a Si atom (cf. Fig. 2.2b), it again has to bind four surrounding silicon atoms, i.e. finally the fifth electron remains surplus. It is only weakly bound to its original atom, therefore it can move quite freely and conduct current. Energetically the "fifth" electrons of the phosphor are (before thermal excitation) just a few meV below the conduction band edge. Hence at room temperature ( $kT \approx 25\text{meV}$ ) almost all donor atoms are ionized because their "fifth" electron is easily excited to the conduction band. In the case of p-type doping (Fig. 2.2c), an element with only three valence electron in the outermost shell is taken (e.g. boron) whose energetic level is just shortly above the valence band maximum. In this case the dopant atoms "accept" electrons from the valence band, i.e. holes are created as free carriers.

### 2.1.3 Generation and recombination of carriers

If the semiconductor is illuminated (Fig. 2.3a) additional carriers can be induced. The absorbed photon has to have an energy  $E_{phot} > E_g$  above the bandgap energy of the semiconductor in order to excite an electron from the valence to the conduction band. The minority carriers (e.g. the holes in n-type Si) have a certain lifetime before they recombine with one of the majority carriers to reestablish thermal equilibrium conditions. During that lifetime  $\tau$  they move by diffusion on average a distance  $L$ , the diffusion length :

$$L = \sqrt{D\tau} \quad (2.4)$$

( $D$  : diffusion constant)

Recombination can happen via several paths (Fig. 2.3c-d):

- direct recombination under emission of a photon (Fig. 2.3b)
- Shockley-Read-Hall recombination via defect states in the band gap (Fig. 2.3b)
- direct recombination under emission of an Auger electron (Fig. 2.3c)
- recombination via surface states (Fig. 2.3d)

### 2.1.4 Current transport mechanisms

The movement of carriers in a semiconductor can be due to two effects:

- drift in an electric field (= gradient in the electrostatic potential)
- diffusion due to concentration gradients

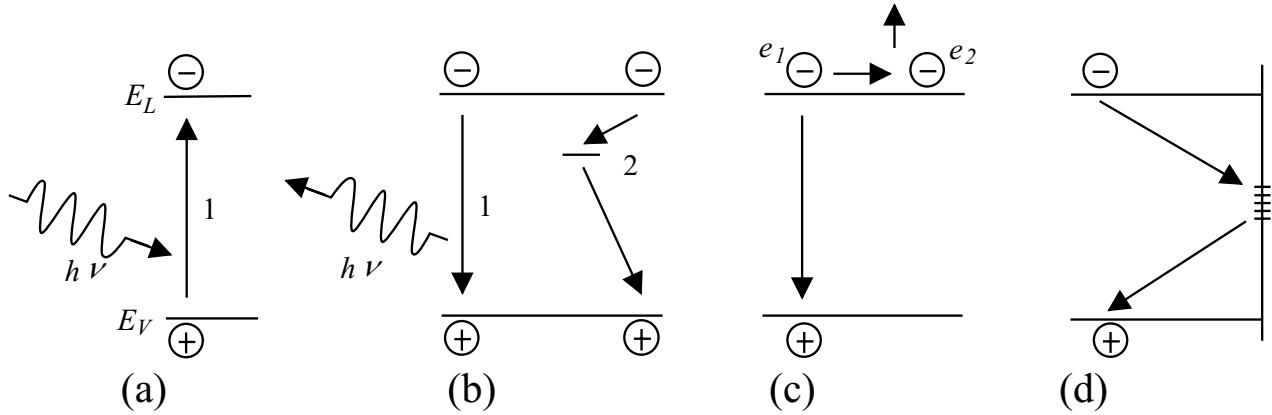


Figure 2.3: Generation and recombination in semiconductors: **(a)** a photon with  $E_{phot} > E_g = 1.1\text{eV}$  is absorbed and an electron-hole pair is created. **(b-d)** Recombination: direct with emission of a photon or via a defect level in the band gap (Shockley-Read-Hall mechanism)**(b)**, direct with emission of an auger electron **(c)**, or via surface states **(d)**.

If an electrical field  $\vec{E}$  is present within a semiconductor (e.g. in the junction region of a pn-contact), electrically charged particles like electrons and holes will move and cause a current density  $j$  according to

$$\vec{j} = \sigma \vec{E} = -\sigma \vec{\nabla} \phi = -e(n_0 \mu_n + p_0 \mu_p) \vec{\nabla} \phi \quad (2.5)$$

( $\sigma$ : conductivity,  $\phi$ : electrostatic potential,  $\mu_{p/n}$ : mobility of holes/electrons,  $p_0/n_0$ : carrier densities).

Diffusion can be described by random walk, which is shown in Fig. 2.4 for the 1D case, i.e. a particle can move in a time step  $t_0$  the distance  $+a$  or  $-a$ . Fig. 2.4(b) shows in a histogram the probabilities for the position of the particle after 4 iterations. The same histogram applies to evaluate the relative distribution of a batch of particles starting at  $x = 0$  at  $t = 0$ . With a finer stepping one finally ends up with a gaussian distribution. If this model is expanded to 3 dimensions the movement of minority carriers can be described before they are recombining. When looking at spatially inhomogeneous distributions of particles, one finally can derive the two Fick's laws to link changes in the concentration  $c$  in time  $t$  and space  $x$  with (particle) current densities<sup>4</sup>  $j$  :

$$-j(x, t) = D \frac{\partial c(x, t)}{\partial x} \quad (2.6)$$

$$\frac{\partial c(x, t)}{\partial t} = D \left( \frac{\partial^2 c(x, t)}{\partial x^2} \right) \quad (2.7)$$

<sup>4</sup>For the diffusion process, it is not of importance whether charged or neutral particles are regarded. To get electrical the equations have to be simply multiplied by the charge that of each particle.

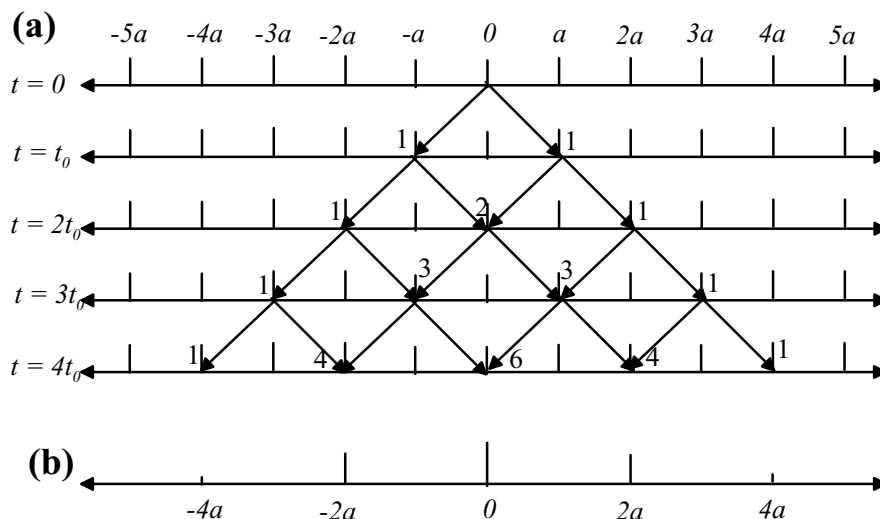


Figure 2.4: 1D random walk model: **(a)** A certain number of particles starts at  $x = 0$ . During each time step  $t_0$  a particle can move a distance  $a$  in either positive or negative direction. After each time step the relative number of particles arriving at a certain  $x$ -position is noted. **(b)** Histogram of the particle distribution after  $t = 4t_0$ . (redrawn from [23])

## 2.2 Semiconductor metal junctions

### 2.2.1 Contact formation and transport characteristics

When ionizing a crystal atom this is equivalent to bringing an electron to infinite distance from the crystal potential, where it is free from any binding forces. The energy level at infinite distance is called the vacuum level  $E_\infty$ . The energy difference between the Fermi energy  $E_F$  and  $E_\infty$  is the "workfunction"  $\phi$  (cf. Fig. 2.5). The electron affinity  $\chi$  designates the difference between the conduction band edge and  $E_\infty$ . When a metal and a semiconductor are brought into contact, excess currents will flow, until the Fermi levels are equal, i.e. when  $\phi_M > \phi_S$ <sup>5</sup> electrons flow from the semiconductor into the metal, depleting the semiconductor close to the contact (Fig. 2.5a). Therefore the bands of the semiconductor are bent upwards by  $\phi_M - \phi_S$ . From the metal side the contact barrier height is  $\phi_B = \phi_M - \chi$ . From the semiconductor side the barrier is lower and equals  $\phi_M - \phi_S$ .

The transport characteristics (cf. Fig. 2.6c) show a rectifying behavior: When the metal is on negative potential compared to the semiconductor, the contact blocks. In forward direction (i.e. the metal is on positive potential with regard to the semiconductor) the current rises exponentially. Schottky [24] calculated the current across the junction by looking at the potentials and the carrier densities in the semiconductor in the bulk material (i.e. far away from the junction) and directly at the junction. Bethe [25], on the other hand, developed the theory of thermionic emission to describe how many electrons overcome the contact barrier without taking into account the specific form of the barrier. For the current from the metal to the semiconductor the barrier height is not affected by an applied potential, hence this current

<sup>5</sup>In the following, always the case of an n-type semiconductor/metal contact is discussed. The discussion works similarly for p-type semiconductors (cf. e.g. [21]).

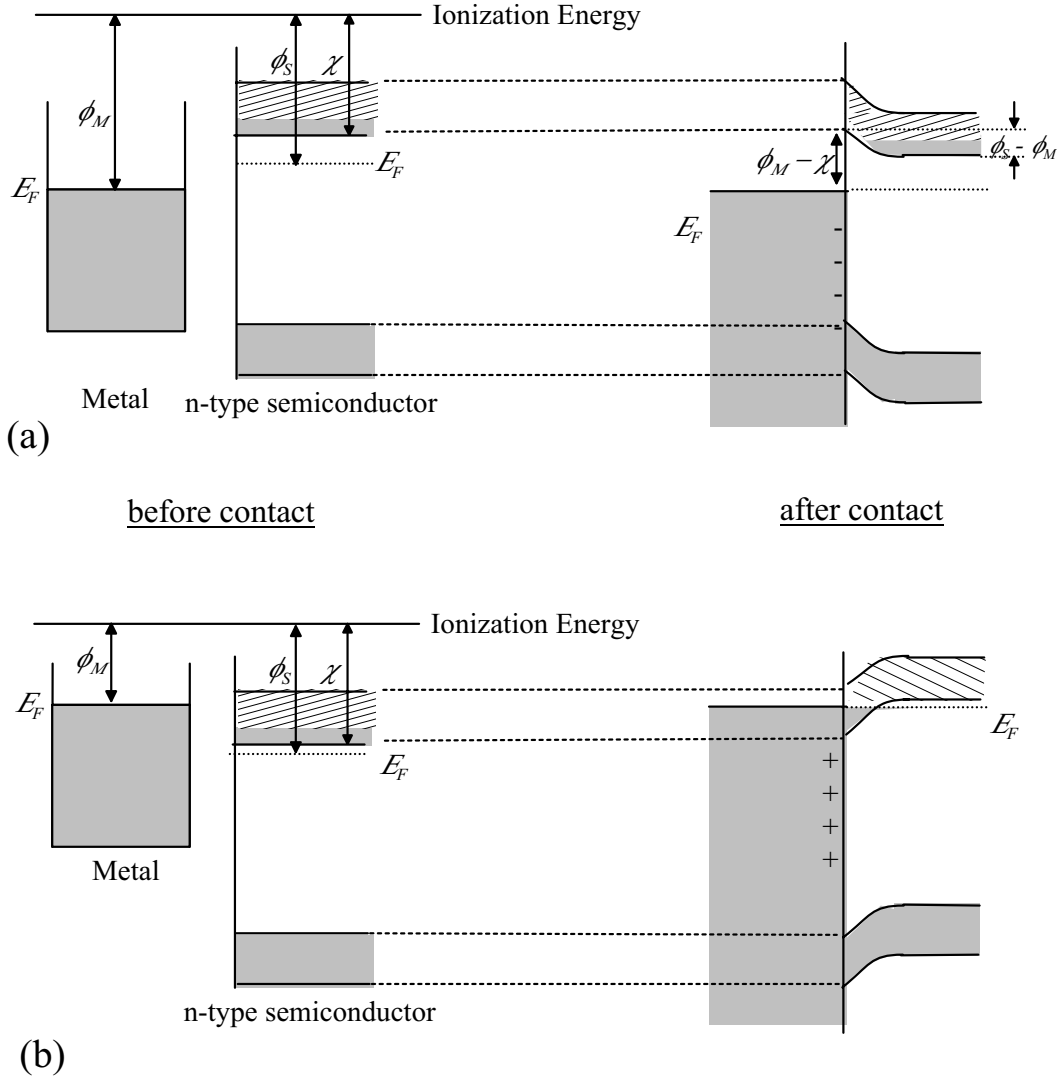


Figure 2.5: Energy bands of the metal-semiconductor contact: (a) Schottky contact. (b) Ohmic contact. (redrawn from [21])

stays always the same:

$$J_{M \rightarrow S} = -A^* T^2 \exp\left(-\frac{q\phi_B}{kT}\right) \quad (2.8)$$

( $A^*$ : effective Richardson constant for thermionic emission (cf. [22])).

The barrier height from the semiconductor towards the metal is strongly influenced by the applied potential  $V$  and so is the current from the semiconductor to the metal:

$$J_{S \rightarrow M} = -A * T^2 \exp\left(-\frac{q\phi_B}{kT}\right) \exp\left(-\frac{qV}{kT}\right) \quad (2.9)$$

The overall current across the junction is the sum of Eq. (2.8) and (2.9):

$$J = -A * T^2 \exp\left(-\frac{q\phi_B}{kT}\right) \left[\exp\left(-\frac{qV}{kT}\right) - 1\right] = J_0 \left[\exp\left(-\frac{qV}{kT}\right) - 1\right] \quad (2.10)$$

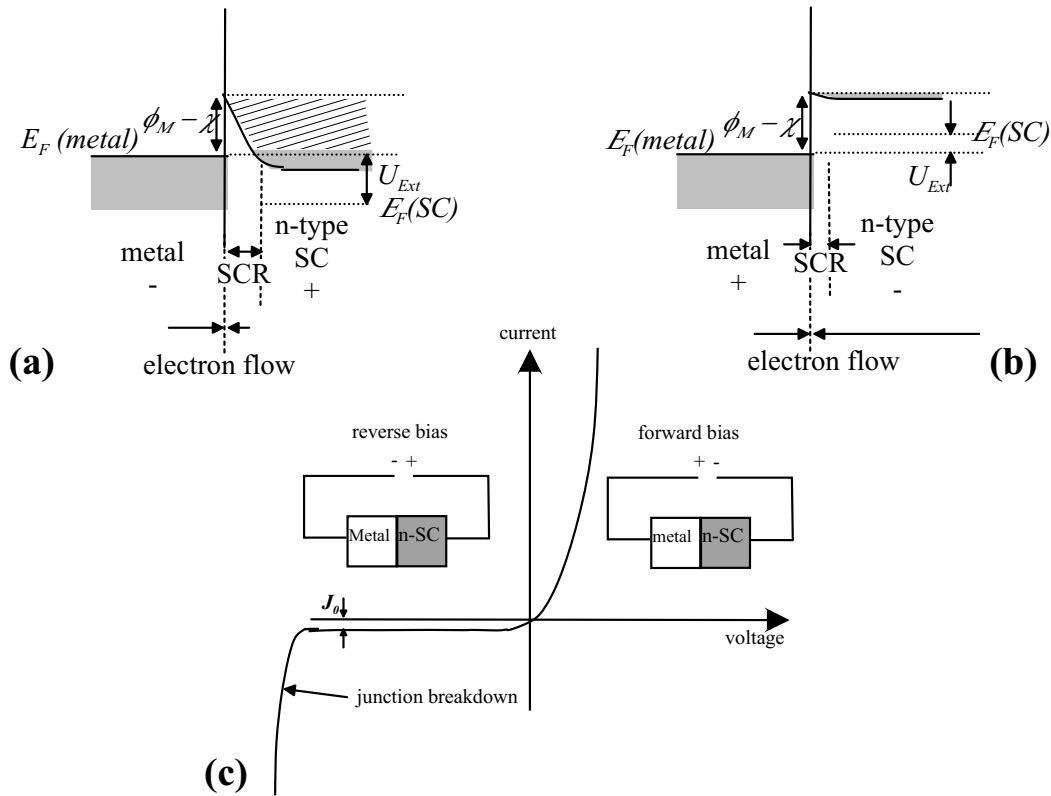


Figure 2.6: Schottky contact: band diagram under reverse bias (a) and forward bias (b). (c) Resulting current-voltage characteristic (redrawn from [21])

$J_0$  classifies the reverse current when the contact is blocking. The Schottky approach reaches qualitatively the same result, only the expression for  $J_0$  is different. Sze et al. have developed a joint theory where thermoionic elements are combined with the diffusion theory [26].

Of course, it is also possible that the metal workfunction is smaller than that of the semiconductor (Fig. 2.5b). In this case no barrier exists, but the semiconductor bands are bent downwards leading to accumulation. This contact shows ohmic behavior, i.e. the current is directly proportional to the applied voltage and not rectifying (i.e. the contact acts like an ohmic resistor).

Essentially there exist three modes into which a semiconductor can be driven when in contact with other materials<sup>6</sup>:

- Accumulation: The bands are bent downwards, i.e. electrons accumulate at the interface (cf. Fig. 2.5b).
- Depletion: With upward bent bands carriers leave the interface region and a space charge region (SCR) builds up<sup>7</sup>, i.e. the interface region becomes depleted of carriers (cf. Fig. 2.5a).

<sup>6</sup>Band bendings and carrier types are noted for n-type semiconductors.

<sup>7</sup>The name SCR originates from the fact that the remaining charges are the fixed donor ions when the mobile charges are driven out of that region.



- Inversion: When the bands are bent down so far that  $E_F$  is below the middle of the band gap, holes become the majority carriers in the interface-near region, i.e. the semiconductor becomes inverted.

### 2.2.2 Junction breakdown

As shown in Fig. 2.6c) the junction breaks down at a sufficiently high reverse potential. There are 3 major breakdown mechanisms [22]:

- thermal instability.
- tunneling effect (Fig. 2.7a).
- avalanche multiplication (Fig. 2.7b).

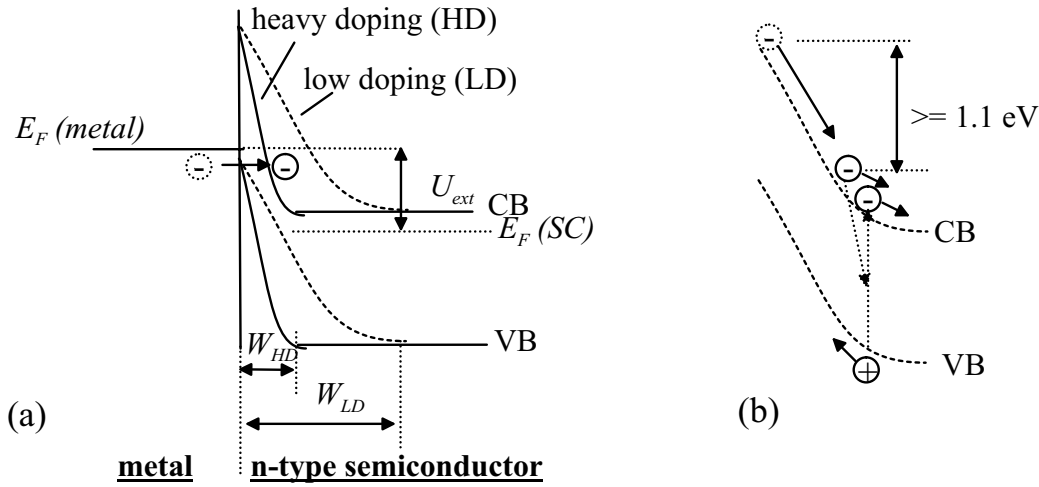


Figure 2.7: Junction breakdown mechanisms: (a) Tunneling and (b) avalanche breakdown.

The reverse current of a junction (cf. Eq. (2.8),(2.10)) rises with the junction temperature according to  $j \propto T^{3+\gamma/2} \exp(-E_g/kT)$  (with  $\gamma = \text{constant}$  [22]). The heating of the junction is proportional to the product of  $I$  and  $V$ , i.e. at a certain degree of heating this is a self-enhancing process that finally destroys the device. Of course, this rarely applies to the later-on discussed electrolytic junctions as the electrolyte permanently cools the contact.

Tunneling through a potential barrier occurs when the barrier width turns out to be small enough. Fig. 2.7a) sketches the principle mechanism: An electron<sup>8</sup> can tunnel from the metal into the conduction band of the semiconductor if the applied potential and/or the doping of the semiconductor is high enough. The quantum mechanical tunneling probability is exponentially dependent on the width  $x$  of the energetical barrier<sup>9</sup> [22]:

$$T_t \approx \frac{16E(E_0 - E)}{E_0^2} \exp(-2\kappa x) \quad (2.11)$$

<sup>8</sup>Again, an analog discussion can be made for holes.

<sup>9</sup>The tunneling barrier width  $x$  ( $\sim nm$ ) is NOT identical with the space charge region width  $W$  ( $\sim \mu m$ ).

( $E$ : energy of the carrier,  $E_0$ : barrier height,  $\kappa \equiv \sqrt{\frac{2m(E_0-E)}{\hbar^2}}$ ,  $m$ : (effective) mass of the tunneling particle).

The approximation in Eq. (2.11) holds for  $\kappa x \gg 1$ , i.e. not too low or too narrow barriers, an assumption which is correct for the case of semiconductor junctions [22]. As sketched in Fig. 2.7(a), the tunneling barrier which an electron in the metal "sees" depends on the steepness of the band bending in the semiconductor. Directly related to the bending is the space charge region width  $W$  given by:

$$W = \sqrt{\frac{2\epsilon_S}{qN}(\phi_M - \phi_S - U_{ext} - 2kT/e)} \quad (2.12)$$

( $\epsilon_S$ : dielectric constant of the semiconductor,  $N$ : doping of the semiconductor,  $U_{ext}$ : externally applied voltage).

Hence the SCR width is smaller for higher doping (cf. Fig. 2.7a) which allows for tunneling at lower voltage.

Avalanche generation of electron-hole pairs (Fig. 2.7b) becomes possible when the kinetic energy of a conduction band electron supersedes  $E_g$ : In this case, a part of the energy from the primary electron can be used to excite a valence band electron to the conduction band, i.e. an electron-hole pair is generated. This current multiplication process can happen several times until the kinetic energies of the primary as well as the generated carriers drops below  $E_g$ .

Generally, breakdown voltages below  $4E_g/e$  point towards an onset of tunneling effect as the primary breakdown mechanism, while avalanche is responsible for voltages above  $6E_g/e$ . For junctions with  $4 - 6E_g/e$  a mixing of both mechanisms is assumed [22]. Both mechanisms can be distinguished by their temperature dependance: Avalanche multiplication has a positive temperature coefficient, i.e. higher  $T$  leads to higher  $U_{break}$ , while tunneling becomes more probable with higher temperatures.

## 2.3 Semiconductor-electrolyte junctions (SEJ)

### 2.3.1 Structure of the SEJ

When a semiconductor electrode is immersed in an electrolyte, this junction will behave similarly to a metal-semiconductor junction (cf. chap. 2.2): The electrolyte with its high charge densities resembles the metal in this case. When the electrode and the electrolyte come into contact, the Fermi energy  $E_F$  in the semiconductor is being equalized with the redox potential  $E_{redox}$  (see below) of the appropriate electrolyte redox couple. The difference  $E_F$  and  $E_{redox}$  is called the Helmholtz potential  $U_H$  [27], which leads again to net currents in a particular direction which subsequently invoke a band bending and a SCR in the semiconductor. Within the electrolyte, several densely packed layers of ions and solvation molecules align at the contact (Fig. 2.8): The inner Helmholtz layer (IHP) consists of solvent molecules ( $H_2O$ ) which are attracted with their negative tails to the positively charged semiconductor interface. The rest of this rigid layer is formed by specifically adsorbed and partially desolvated cations. Next, the outer Helmholtz plane (OHP) marks the closest distance which fully solvated ions can reach<sup>10</sup>. If the electrolyte concentration is below 0.1 M a noteworthy diffuse layer of attracted

<sup>10</sup>The solvation shell hinders them to come any closer.

ions, the Gouy-Chapman layer, builds up behind the OHP. In higher concentrated solutions already the two Helmholtz planes contain a large enough charge density to fully shield the electrical field.

As also noted in Fig. 2.8 the semiconductor can show diverse surface states from surface defect sites which are located energetically in the band gap. Already a perfect semiconductor without “extrinsic” defects has so-called “intrinsic” defects [27] at the surface: There the semiconductor lattice ends and the outermost lattice atoms are missing at least one binding partner. The unpaired electron is a “dangling bond” or “Shockley surface state”, which can act both as an acceptor (= trapping of an electron from the bulk) or a donor (= the unpaired electron gets excited to the conduction band). Therefore these sites can get positively charged as well as also positive. The defect becomes “healed” (here discussed for the case of silicon) when a hydrogen atom binds to the defect site. Then all the bonds of the surface silicon atom are saturated, i.e. the electronic mid-gap state disappears.

The defect density without passivation is usually quite high, so that only some defects are occupied. Hence the Fermi level gets pinned to the last occupied surface state and the bending of the semiconductor bands doesn’t depend on the difference between the workfunctions  $E_{redox}$  and  $\phi_S$  anymore, but only on the energetic position of the defects within the band gap. If those states become passivated this can dramatically change the potential drop at the interface (cf. also section 7.3.3 on p. 143ff.).

The simple galvanic reaction



shall serve as an example to explain the energetic levels within an electrolyte (Fig. 2.8a (right side)):  $Cu^{2+}/Cu$  are the redox couple;  $Cu^{2+}$  is the OXidized state, which accepts electrons, i.e. it is an empty state from the point of view of electrons coming from the semiconductor. On the other hand  $Cu$  means a REDuced state, which tries to get rid of electrons, i.e. it is occupied from the point of view of an electron. For holes arriving at the interface, it is just vice versa: The RED state accepts holes while the OX state can donate holes. These states are not sharp energy levels but are smeared out because of thermal fluctuations of the solvate shell around the reduced/oxidized ions. The redox potential which is assumed under given conditions is governed by the Nernst equation:

$$E_{redox} = E_{redox}^0 + kT/e \ln(c_{ox}/c_{red}) \quad (2.14)$$

( $E_{redox}^0$ : standard potential of the electrode,  $c_{ox}$ : concentration of the oxidized species,  $c_{red}$ : concentration of the reduced species).

In a strict quotation of Eq.(2.14) the concentrations have to be replaced by the activities of the individual ions, which becomes necessary in heavy concentrated solutions. The redox potential is via  $E_{redox} = 1/2(E_{Ox} + E_{Red})$  related to the most probable energy level for the oxidized (reduced) ion  $E_{Ox}$  ( $E_{Red}$ ) [28].

### 2.3.2 Kinetics at the SEJ

The reaction rate of a semiconductor - electrolyte interface depends on a variety of parameters (Fig. 2.9) in the semiconductor as well as in the electrolyte. For the semiconductor

- the type and density of carriers in the bulk,

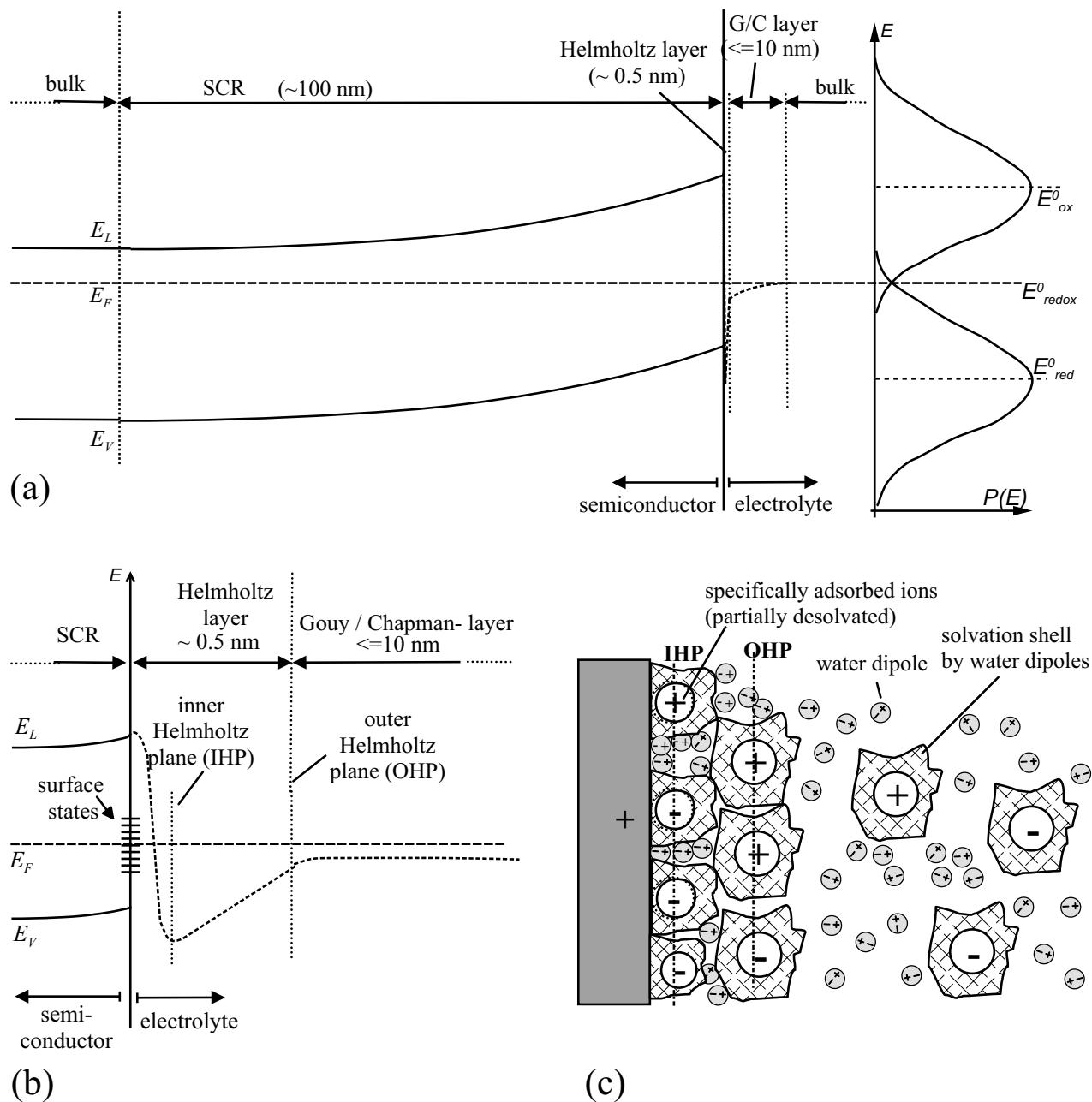


Figure 2.8: (a) Energy band structure for a n-type semiconductor in contact and at equilibrium with an electrolyte. The dashed continuation of the conduction band on the electrolyte side of the junction shows the potential energy for a (fictitious) negative probe charge. The Fermi energy  $E_F$  (in the semiconductor) is equilibrated with the redox energy  $E_{redox}$  of the dominant redox couple (in the electrolyte) which is defined as  $E_{redox} = 0.5(E_{ox} + E_{red})$ . The most probable energy  $E_{ox}$  and  $E_{red}$  for the oxidized and the reduced ionic states differ due to different solvation energies. Thermal fluctuations in the solvation shell cause a gaussian distribution of the ionic energies around  $E_{ox}$  and  $E_{red}$ . (b) Magnification of the interface region of the electrolyte with a heavy influence of specifically adsorbed ions and surface states. (c) Schematic distribution of ions and solvent molecules at the contact.

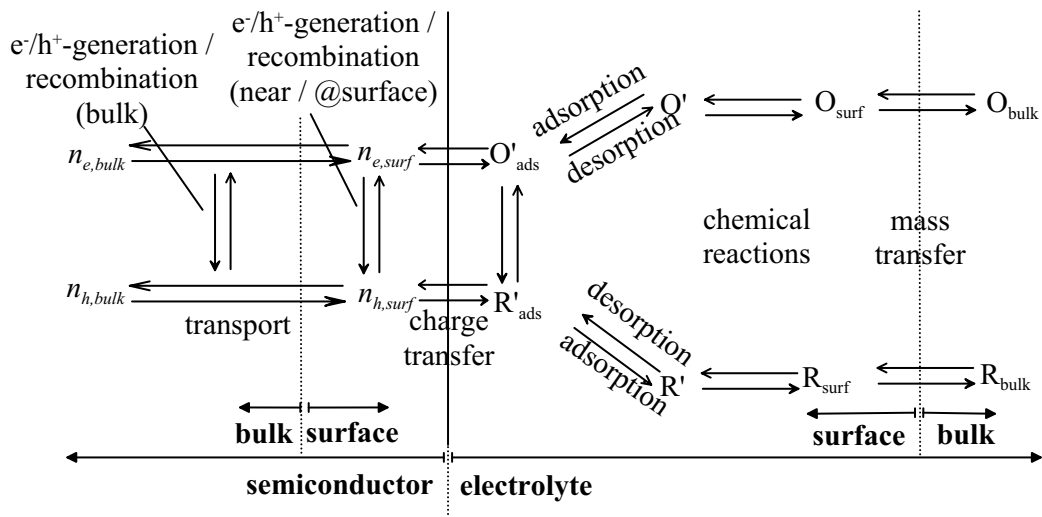


Figure 2.9: Rate-determining steps in electrochemical reactions at semiconductor electrodes (modified from [23]).

- the generation and recombination of carriers in the bulk and near the reaction site,
- the transport mechanisms from the bulk to the reaction site

are of prime importance. The

- concentration of species in the bulk electrolyte as well as close to the reaction site,
- mass transfer mechanisms from the bulk to the reaction site,
- pure chemical reactions prior to/after the electrochemical reaction,
- and the adsorption/desorption rates of species

can be rate limiting steps from the electrolyte side of the reaction. The charge transfer reaction



( $k_f$ : reaction rate of forward reaction,  $k_b$ : reaction rate of backward reaction))

can be described by the so-called Butler-Volmer kinetics [23] in case that none of the points listed above limits the current (Fig. 2.10): The reaction coordinate designates the spacial position of a certain species, e.g. a solvated  $Cu^{2+}$  in front of a copper electrode. Up to a certain distance from the electrode the energy is nearly constant ( $\Delta G_{0,c}$  below the energy of the so-called "activated complex". When the ion is reduced, it (partially) has to dismantle from its solvation shell, hence its free energy becomes higher and it goes into the "activated complex" state. When the ion is reduced finally to copper and is integrated in the atomic lattice of the electrode, it reaches again a lower free energy which is  $\Delta G_{0,a}$  below the activated complex. First, let's regard the basic case without any applied external voltages: The reaction

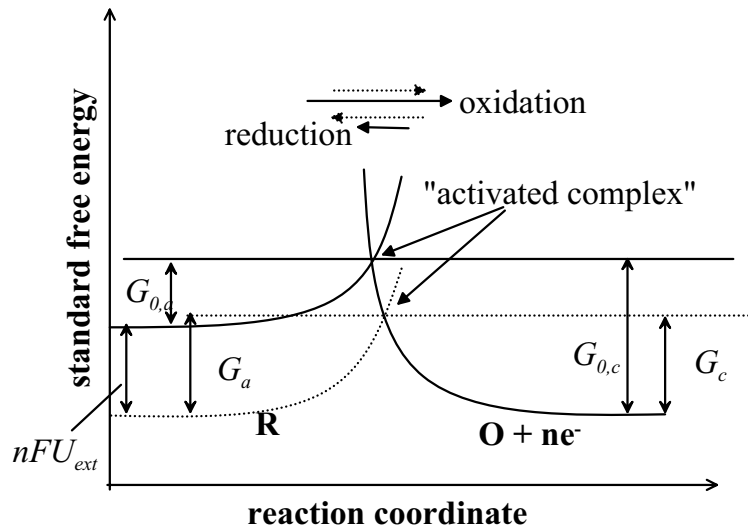


Figure 2.10: Butler-Volmer kinetics: The dotted lines indicate the energy levels where the net current becomes zero because of an externally applied potential, while the solid lines (no applied potential) show an enhanced oxidation.

rates in the cathodic as well as in the anodic direction are determined purely by the energy differences  $\Delta G_{0,c}$  and  $\Delta G_{0,a}$  and the electrolyte temperature:

$$k_{f,0} = A_f e^{-\Delta G_{0,c}/RT} \quad (2.16)$$

and

$$k_{b,0} = A_b e^{-\Delta G_{0,a}/RT} \quad (2.17)$$

( $A_b$  and  $A_f$ : constants,  $R$ : gas constant).

When an external voltage is applied the potential of the electrode shifts by  $nFU_{ext}$  ( $F$ : Faraday's constant) which enters into the exponent of Eq. (2.16) and (2.17). Together with the transfer coefficient  $\alpha$  which classifies the symmetry of the potential curves in Fig. 2.10 the final to be expected current is given by the Butler-Volmer equation:

$$i = i_0 [e^{-\alpha n f \eta} - e^{(1-\alpha) n f \eta}] \quad (2.18)$$

( $i_0$ : exchange current,  $f = F/RT$ ,  $\eta$ : overpotential).

The overpotential  $\eta$  is the deviation of the potential of an electrode from its equilibrium value required to cause a given current to flow through the electrode [23]. For high overpotentials, one of the currents in Eq. (2.18) can be neglected, i.e. an exponential relationship between current and potential results from the "Tafel equation":

$$\eta = a + b \log i \quad (2.19)$$

( $a$ ,  $b$ : constants).

Thus typical "Tafel behavior" appears as a straight line in a  $\log i(\eta)$  plot.

### 2.3.3 Current limiting factors for the SEJ

For semiconductors, only at low potentials, the current follows a Tafel behavior; at higher potential other steps become rate limiting. Generally the externally measurable current always depends on the slowest process - the "bottleneck" - within the chain depicted in Fig. 2.9. At high current densities the current at an electrode becomes often limited by the mass transfer to and away from the electrode. The (particle) current density  $J_j$  of a species  $j$  in an electrolyte is then<sup>11</sup> governed by the Nernst-Planck equation [23]:

$$\vec{J}_j = -D_j \vec{\nabla} C_j - \frac{z_j F}{RT} D_j C_j \vec{\nabla} \phi + C_j \vec{v} \quad (2.20)$$

( $D_j, C_j, z_j$ : diffusion coefficient, concentration, and charge of one ion of species  $j$ ,  $\phi$ : electrostatic potential,  $\vec{v}$ : convection velocity).

The first term of Eq.(2.20) refers to diffusive species' movement induced by concentration gradients. The second term addresses the movement of charged species due to an electrical field within the solution. For both contributions the same laws and remarks hold as given in section 2.1, where only values for electrons/holes have to be replaced by the respective values for ions (charge, mobility, etc.). The last term deals with movements induced by convective forces. When a solution is externally brought into motion (e.g. by stirring) this displacement of charge is just like any other driving force leading to a current flow. In most electrochemical experiments, conditions are chosen so that at least one of the above contributions becomes negligible.

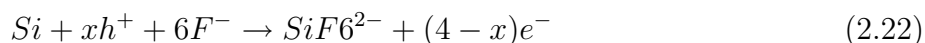
When diffusion is the dominant process for the mass transfer, concentration gradients are the driving forces. An increase in current and therewith also in the demand for educts, leads to a stronger concentration gradient between bulk electrolyte (concentration  $C_0^*$ ) and interface ( $C_0(x=0)$ ). When the interface concentration reaches zero the limiting current  $I_l$

$$I_l = nFAm_0C_0^* \quad (2.21)$$

( $n$ : charges per electrolyzed atom or molecule,  $F$ : Faraday's constant,  $A$ : electrode area,  $m_0$ : mass transfer coefficient [23])

is reached after which a further increase of applied potential does not effect the current. The diffusion layer thickness  $\delta$  designates the depth in front of the electrode with a concentration  $C < C_0^*$ . If only diffusion drives the mass transfer the layer thickness increases with  $\delta(t) = \sqrt{D_0 t}$  and the current drops according to  $I \propto t^{-1/2}$ .

At semiconductor electrodes a current limitation may occur due to missing carriers. In the case of e.g. tetravalent silicon dissolution (cf. chap. 3)



( $1 \leq x \leq 4$ : number of holes),

it is mandatory to have at least one electronic hole participating in the reaction<sup>12</sup> [29]. In the case of n-type silicon holes are the minority carriers, i.e. the dissolution rate becomes very

<sup>11</sup>I.e. the interface chemistry is fast compared to the mass transfer of reactants to the electrode.

<sup>12</sup>The rest of the necessary carriers can then be electrons.

small. If the semiconductor becomes illuminated, electron-hole pairs are generated which is immediately seen in the current potential curves (cf. Fig. 3.3 on p. 28), i.e. in this case the number of available holes and their transport mechanisms determine the maximum possible current.

## 2.4 Modification of Electrolytes

### 2.4.1 Buffered Electrolytes

The pH of a solution is defined as the negative logarithm of the proton concentration ( $pH = -\log_{10}[H_3O^+]$ ). A weak<sup>13</sup> acid and its conjugated base  $A^-$  are related to each other by the reaction



with the equilibrium constant

$$K_S = \frac{[H_3O^+][A^-]}{[HA]} \quad (2.24)$$

linking the individual concentrations. From Eq. (2.24) it follows that the pH of the solution is given by  $[A^-]$  and  $[HA]$  leading to the Henderson-Hasselbach equation

$$pH = pK_S + \lg \frac{[A^-]}{[HA]} \quad (2.25)$$

( $pK_S = -\log K_S$ ).

Fig. 2.11 shows the pH characteristic for several common acid/base couples (with  $x_B = \frac{[A^-]}{[A^-] + [HA]}$  as the relative amount of the base  $A^-$ ). If now an amount  $[HB]$  of a strong acid  $HB$  (e.g.  $HCl$ ), immediately splitting into  $H^+ + B^-$ , is added to the buffered solution Eq. (2.23) becomes imbalanced due to the large concentration of protons on the right side and  $A^-$  will react to  $HA$  until all new protons are consumed, i.e.

$$[HA] = [HA]_0 + [HB], [A^-] = [A^-]_0 - [HB] \quad (2.26)$$

The new pH is again given by Eq. (2.25). The inverse of the slope of the curves in Fig. 2.11a) indicates the buffer capacity  $\beta = \frac{dC}{dpH}$  (Fig. 2.11b) which quantifies the change in pH when a certain amount of strong acid is added.

In the silicon etching, often  $NH_4F$  salt is used instead of hydrofluoric acid HF.  $NH_4F$  splits in solution immediately in  $NH_4^+$  and  $F^-$ . If additionally  $NH_3$  is added, the pH value of the solution can be set by the ammonia buffer couple  $NH_3/NH_4^+$  (cf. Fig. 2.11a). Thus by combining HF,  $NH_4F$  and  $NH_3$  the amount of fluoride ions and the pH of the solution can be set in wide ranges individually. Because the pH of the solution has a drastic influence on the etch rate of silicon oxides in fluoride media, this technique is often used.

<sup>13</sup> "Weak" acid means that it only weakly splits off its proton(s) in form of the reaction (2.23). In most cases  $[HA]_0 \approx [HA]$  is therefore valid, i.e. the amount of undissociated acid  $HA$  equals the initially added amount  $[HA]_0$ . "Strong" acid means that all molecules split, i.e.  $[HA] \approx 0, [A^-] \approx [H_3O^+] \approx [HA]_0$ .



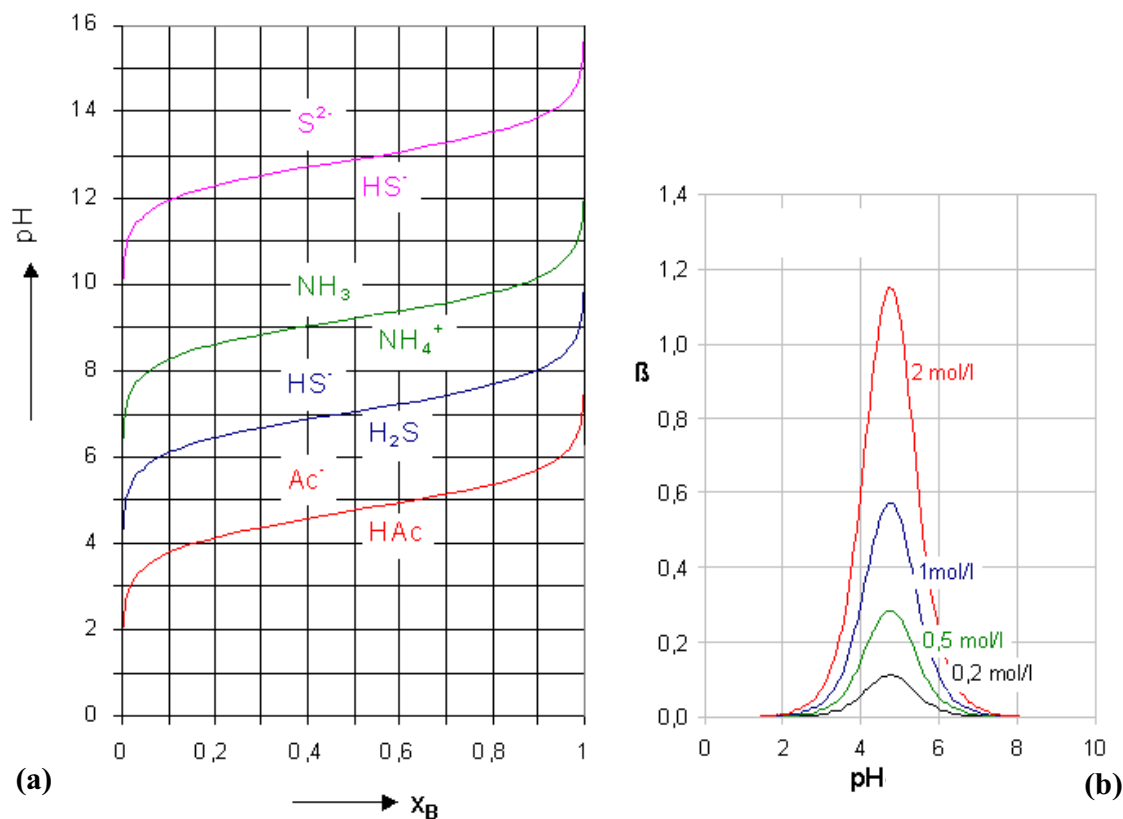


Figure 2.11: (a) pH of a buffered solution versus its buffer ratio for several common buffer couples. (b) Buffer capacity  $\beta$  versus pH.

## 2.4.2 Surfactants

A surfactant is generally a molecule which has a hydrophilic as well as a hydrophobic part [30]. This predestinates these molecules to accumulate at interfaces between different substances, e.g. at solid-liquid interfaces. The wettability of the solid is thereby increased and the surface tension of the liquid decreases. The concentration of the surfactant and the electrolyte temperature determine to which extent the surfactant will form larger molecule ensembles, so-called “micelles”, which can again drastically change the effect of the surfactant. The surfactant concentration, at which micelles start forming is called the critical micelle concentration (CMC).

The hydrophobic part of the molecule is in most cases an aliphatic hydrocarbon which can be split by double bonds, hetero atoms or hetero groups. The common classification of surfactants (Fig. 2.12) is given by the type of the hydrophilic molecule part. In most cases the hydrophilic part is a salt which dissociates when immersed in an electrolyte. The surfactant is classified (anionic or cationic) by the charge type of the part, which remains with the surfactant molecule. Some organic chains are already hydrophilic without splitting off a counter ion, such compounds are called non-ionic surfactants. Besides these three basic types also more complex forms are known, e.g. amphoteric molecules with both anionic and cationic hydrophilic groups, where it depends on the pH of the electrolyte which group will be active.

In addition, the potential distribution across a semiconductor-electrolyte interface will change, because the surfactant adsorbs at the semiconductor surface (cf. Fig. 2.8). In the

<u>type</u>	<u>interface active group</u>	<u>counterion</u>
anionic	$R-COO^-$	$Na^+$
cationic	$\left[ \begin{array}{c} CH_3 \\   \\ R-N-CH_3 \\   \\ CH_3 \end{array} \right]^+$	$Cl^-$
non-ionic	$R-O-(CH_2CH_2O)_x-H$	-

Figure 2.12: Types of surfactant with common examples for the interface active groups and the counter ions.

case of ionic surfactants, the surfactant will bring additional charges to the surface, which will be added (correctly signed!) to the charges of the semiconductor. If the charge is positive (cationic surfactant) and the charges in the space charge region are negative (p-type semiconductor), this will lead to an increase of the space charge region width in order to re-balance the charge equality with the electrolyte side. Similarly an anionic surfactant decreases the space charge region width of a p-type electrode. For n-type electrode the situation is just vice versa. Besides that, the surfactant can change the surface reaction kinetics either directly or by stimulating or hindering the transport of certain species from and to the interface. Especially at the semiconductor-electrolyte interface surface passivation plays a distinctive role whether Fermi level pinning occurs (cf. Fig. 2.8) or not and thus how strong the band bending in the semiconductor will be (cf. also section 7.3).

Fig. 2.13 shows all used surfactants from the present work. In most cases NCW 601-A from WAKO Chemicals, Inc. was used. This surfactant is frequently used in semiconductor industry, however the exact structure formula is not disclosed. The other surfactants are standard detergent surfactants from Clariant Inc.

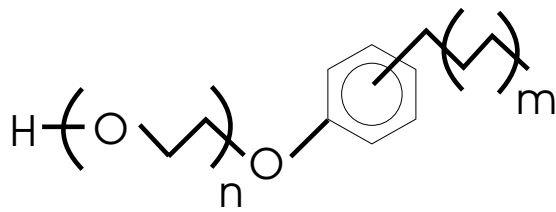
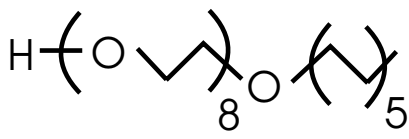
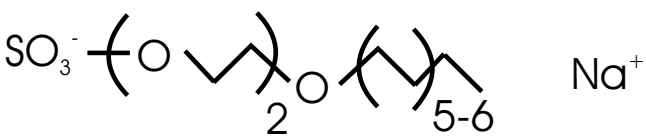
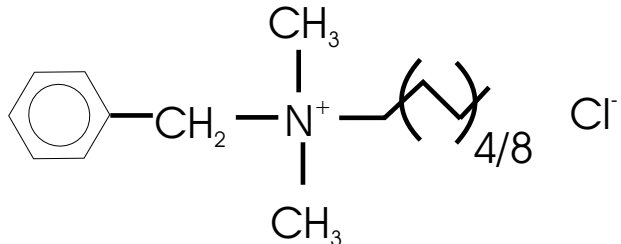
<u>type</u>	<u>name</u>	<u>structure formula</u>
N	NCW 601-A	
N	Genapol UD 88	
A	Genapol LRO liq.	
C	Dodigen 226	

Figure 2.13: List of all used surfactants (N = non-ionic, C = cationic, A = anionic)



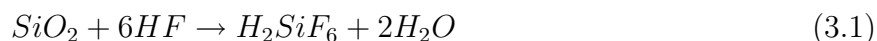
# Chapter 3

## The silicon/HF contact

### 3.1 Aqueous electrolytes

#### 3.1.1 Chemical reactions

The surface of any single crystal poses a symmetry breaking: While bulk atoms have all four outer valence electrons bound in covalent bonds in the tetragonal lattice, the surface atoms have unsaturated electrons ("dangling bonds"). These electrons show a high reactivity, resulting in a quick coverage of the surface by  $H$ ,  $OH$ , metal traces, and/or last, but not least, oxide [28]. In oxygen containing atmosphere or in water containing electrolytes always "native"<sup>1</sup> oxide with a thickness  $d \approx 0.5 - 2nm$  forms on the surface of silicon. As soon a solution contains about 10 ppm of  $HF$  [28], this film will be dissolved [33]:



After the dissolution of the oxide, the silicon atoms at the surface become terminated by hydrogen (see below). The resulting H-passivated surface is very stable and remains H-passivated even in ambient atmosphere; e.g. the regrowth of native oxide after a 15s dip in 1%  $HF$  takes several hours [32]. For a long time, it was assumed that the dangling bonds are terminated with  $F$  [34], [35], because thermodynamics favors a  $SiF$  ( $E_{SiF} = 6.0eV$ ) instead of a  $SiH$

<sup>1</sup>Sometimes there also called chemical oxides [32].

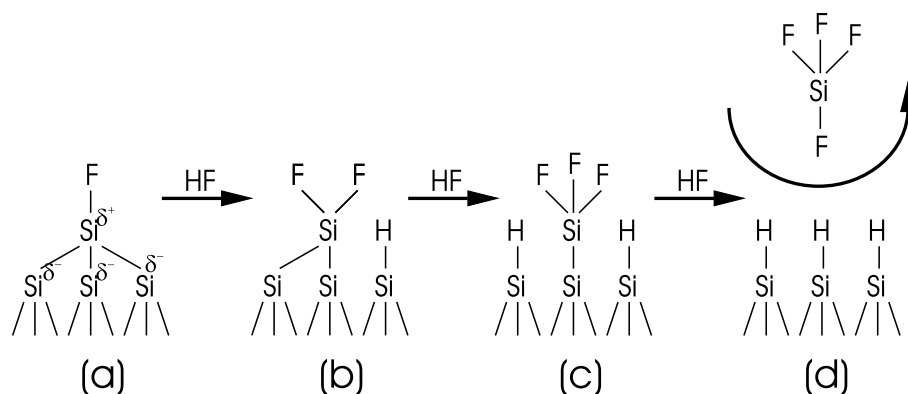


Figure 3.1: Hydrogen termination of Si in HF [31].

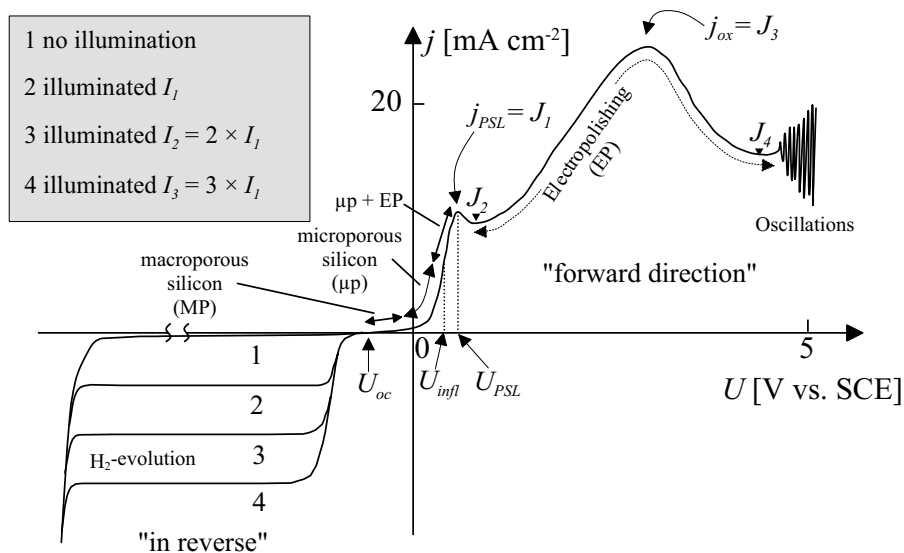


Figure 3.2:  $IV$ -characteristic of p-Si in HF. ( $J_{1-4}$  refer the measurement points in Fig. 4.7.)

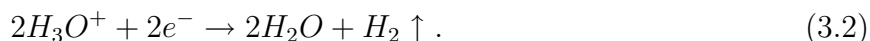
bond ( $E_{SiH} = 3.5eV$ ). But  $IR$  measurements have shown an exclusive  $H$  termination [36]. The generally accepted scheme is that kinetic effects dominate the interface termination [31]: When the surface offers a dangling bond, of course at first instance it will be saturated with a  $F$ -atom. The  $Si - F$  bond is strongly polarized, which also polarizes the  $Si - Si$  back bonds (Fig. 3.1a). This enables the reaction with a  $HF$  molecule (Fig. 3.1b), breaking the  $Si^{\delta-} - Si^{\delta+}$  bond. Further reactions with  $HF$  (Fig. 3.1c) lead to a fully hydrogenated surface (Fig. 3.1d) which is then inert to further  $HF$  attacks [37]. The  $SiF_4$  molecule further reacts with 2  $HF$  to  $H_2SiF_6$ , which is by far the dominant fluoride complex to be found in solutions after such reactions [28].

### 3.1.2 $IV$ characteristic of p-type silicon

Fig. 3.2 shows the  $IV$  characteristic for p-type silicon in aqueous  $HF$  where several regimes can be distinguished:

- Hydrogen reduction at cathodic potentials.
- Macropore formation at very low (a few 100 meV) anodic potentials.
- Formation of nanoporous silicon at anodic potentials below the point of inflection ( $U_{infl}$ ) between  $U_{OC}$  and  $U_{PSL}$ .
- Transition from micropore formation to electropolishing between  $U_{infl}$  and  $U_{PSL}$ .
- Electropolishing for  $U > U_{PSL}$ .

For cathodic potentials (of the Si electrode versus the counter electrode) the contact is operated in reverse (cf. section 2.2). The main reaction occurring at the electrode is hydrogen evolution

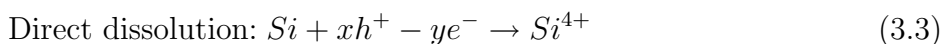


If the semiconductor is not illuminated, there flow extremely low leakage currents which are proportional to the number of minority carriers. In case of illumination additional electrons are generated (cf. section 2.1.3), and the current that can flow across the junction is directly proportional to the number of generated carriers [29].

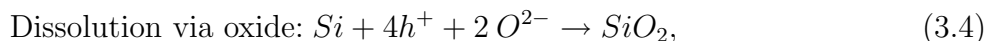
The open circuit potential  $U_{OC}$  varies between -0.7 and -0.2 V vs. SCE<sup>2</sup> strongly depending on illumination, surface conditions, HF concentrations, etc. Especially after the first minutes of immersing a Si electrode into HF containing electrolyte the native oxide is dissolved and the hydrogen passivation builds up which causes a shift in  $U_{OC}$  of several 100 meV.

At very low anodic voltages<sup>3</sup> macropores<sup>4</sup> (cf. section 7.3) grow [38]. Micropore<sup>5</sup> formation occurs at further anodic potentials up to  $U_{infl}$  [39]. Recent investigations [40] have shown, however, that it seems not possible to obtain macropores as well as micropores with the same electrolyte and doping. Between the point of inflection in the  $IV$  curve and the PSL maximum in the current density the surface reaction is in a transition state from micropores to electropolishing [39], an observation which goes hand in hand with the detection of first traces of anodic oxide after  $U_{infl}$  [41, 42]. Beyond the PSL<sup>6</sup> peak the silicon removal becomes homogeneous, i.e. the surface becomes polished. This is done via tetravalent oxidation of the silicon (cf. Eq. (3.4)) and subsequent oxide dissolution according to reaction (3.1). The oxide dissolution and therefore the supply with  $HF$  molecules becomes the rate limiting step. After a peak  $j_{ox}$  the current as well as the oxide thickness starts to oscillate. [43].

It has been measured that always at least one hole is necessary to trigger the dissolution of a Si atom [29]. The valence<sup>7</sup>  $v$  changes drastically in the vicinity of  $j_{PSL}$  from 2 to 4. This is due to the fact that there are two major mechanisms to dissolve silicon [5]:



and



whereupon the oxide is dissolved by the reaction 3.1. Reaction (3.3) is often accompanied by hydrogen reduction (cf. Eq. (3.2)), effectively reducing the valence of the reaction. The externally measurable valence  $v$  is a mixture of reaction (3.3) ( $v = 1 - 4$ ) and reaction (3.3) ( $v = 4$ ) which then leads to a valence of the process from 1 to 4 depending on how much hydrogen is produced and how the reactions (3.3) and (3.4) are weighted.

The direct dissolution (3.3) works via a complexation of the silicon atoms by e.g.  $OH^-$  or  $F^-$  ligands. This process is best known from the anisotropic chemical etching solutions, e.g. KOH [44]. However, in HF containing electrolytes, the only stable end product which is found is  $H_2SiF_6$ , either because  $F^-$  is indeed the attacking species or it replaces e.g.  $OH^-$  in the complexed  $Si(OH)_4$  later on.

<sup>2</sup>The SCE (= Saturated Calomel Electrode) is one of the most used reference electrodes against which potential differences are measured. It has a potential of  $U_{NHE} = 0.24$  V versus the normal hydrogen electrode (NHE) [23].

<sup>3</sup>Anodic voltage refers to positive currents (i.e. net flow of positive charges from the Si to the counter electrode). Because the voltage scale is defined only relative to a reference electrode, the regimes "cathodic"/"anodic" are defined as lower/higher than the open circuit potential  $U_{OC}$ .

<sup>4</sup>Classification according to the IUPAC (International Union of Pure and Applied Chemistry) scheme: micro: pore diameters  $d$  up to  $2nm$ ; meso:  $d = 2 - 50nm$ ; macro:  $d > 50nm$ .

<sup>5</sup>Sometimes also referred to as "nanoporous" Si.

<sup>6</sup>PSL = Porous Silicon Layer. The  $j_{PSL}$  peak has this name due to historical reasons, because in a very coarse view it separates PS formation from electropolishing.

<sup>7</sup>The valence is the number of charges which is necessary to bring one Si atom into solution.

### 3.1.3 $IV$ characteristic of n-type silicon

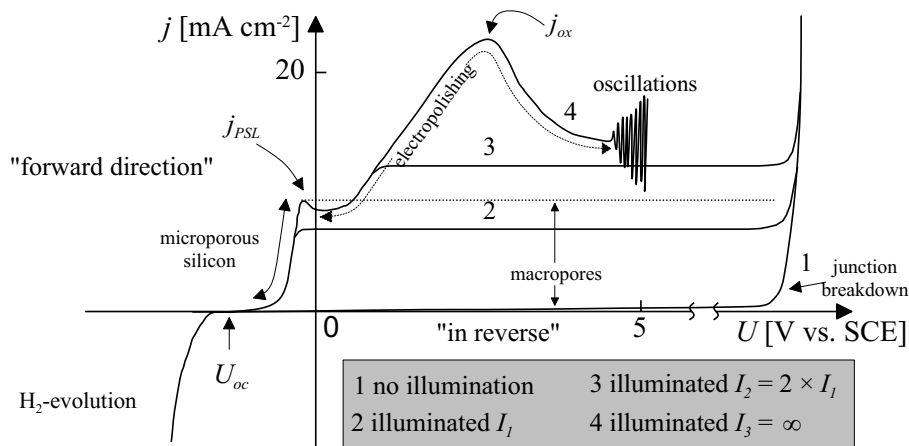


Figure 3.3:  $IV$ -characteristic of n-Si in HF.

Only under strong illumination p- (Fig. 3.2) and n-type silicon (Fig. 3.3) have nearly identical  $IV$  characteristics. The open circuit potential should differ due to the different position of the Fermi Energy  $E_F$ , but as previously stated other effects (cf. Sec. 3.1.2) can compensate this effect and  $U_{OC}$  is therefore also in the range of -0.6 to -0.2 V vs. SCE [28].

The cathodic regime of the n-Si/HF contact reacts like a Schottky diode biased in forward direction. The reaction at the electrode is again hydrogen reduction. The difference to p-Si is that the reaction is not limited by the number of available electrons (which are the majority carriers in p-Si). On the anodic side, when there is no illumination (curve 1 in Fig. 3.3), the contact operates in reverse bias, i.e. it blocks, because at least one hole is necessary to invoke a dissolution reaction. Just like in the Schottky case, at a sufficiently positive potential the junction will break down (cf. Sec. 2.2.2) and fir tree shaped pores (so-called breakthrough pores) grow. It depends on the doping of the semiconductor whether tunnelling (for high doping) or avalanche multiplication (for lower dopings) is the prevalent mechanism, which is assumed to strongly influence the pore morphology [45].

With limited illumination (curves 2 and 3 in Fig. 3.3) the n-Si characteristic follows the p-Si curve up to the point where the supply with holes becomes the rate limiting step. After that point the bias can be varied over several volts (up to the point where breakdown of the junction occurs) without significant change in the current density. For  $j < j_{PSL}$  this is the regime for macropore formation [46], where the current density can be varied (relatively) independently of the junction bias. The current is not proportional to the illumination intensity (i.e. the number of generated carriers) unlike in the cathodic case in p-Si. This is due to reaction (3.3), where the number of consumed holes per dissolved Si atom can be varied from 1 to 4, while the rest of the charges can be supplied by electrons and/or  $H^+$ . This results in a up to 4 times higher photocurrent than expected from the number of generated holes [29].

## 3.2 Organic electrolytes

Besides water a whole zoo of other solvents exists in which HF can be dissolved and which can be used for electrochemical experiments. Fig. 3.4 shows two typical solvents which are



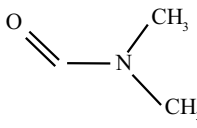
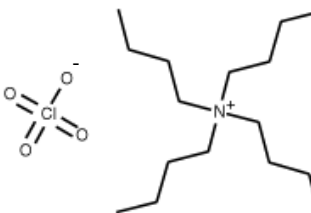
name	abbr.	formula	structure
Acetonitril	MeCN	$C_2H_3N$	$H_3C \text{ --- } \equiv N$
Dimethylformamid	DMF	$C_3H_7NO$	
Tetrabutylammonium-perchlorat	TBAP	$C_{16}H_{36}ClNO_4$	

Figure 3.4: Structure and formula of DMF, MeCN, and TBAP.

commonly used in electrochemistry and also in the present work:

- Dimethylformamide (DMF)
- Acetonitrile (MeCN)

In most cases the conductivity of these sometimes called "organic" solvents is much worse than that of water, therefore supporting salts have to be added to overcome limitations due to the lack of electrolyte conductivity. The non-polar nature of organic electrolytes severely limits the solubility of most salts which necessitates complex salts like tetra-butyl-ammonium-perchlorate (TBAP, cf. Fig. 3.4). The conducting salt should consist generally of non-electroactive species, e.g. it does not participate in the processes at the electrode to hinder a distortion of the experiment.

The interest in organic/HF mixtures comes from the inherent problems with water containing electrolytes: Already water quantities in the sub-vol% region strongly promote surface oxide growth on the silicon electrode. Also dissolved oxygen and water from ambient atmosphere will do so [47]. Therefore several groups have investigated e.g. MeCN/anhydrous HF mixtures under inert atmospheres [47, 48].

Without the addition of HF, classical anodic oxidation in organic electrolytes was investigated by several groups [28]: It is possible to grow anodic oxides up to 100 nm thickness and more with only minimal water contents (e.g. 0.35 vol%  $H_2O$  in ethylene glycol + 0.04 M  $KNO_3$  [49]). The density, (electrical) quality and thickness of the oxide show an extremely strong dependance on the water content of the solution. On the other hand, Song et al. [50] were able to show an oxidation upon immersing porous silicon in waterfree DMSO (Dimethylsulfoxide), i.e. also oxygen containing molecules in the solution can be responsible for the oxidation of silicon.

Under the absence of water and oxygen, Si in an HF/MeCN/TBAP electrolyte behaves like an idealized semiconductor-electrolyte junction [47](cf. section 2.3)<sup>8</sup>. For fresh electrodes during anodization, the current becomes essentially limited only by the serial resistance of the

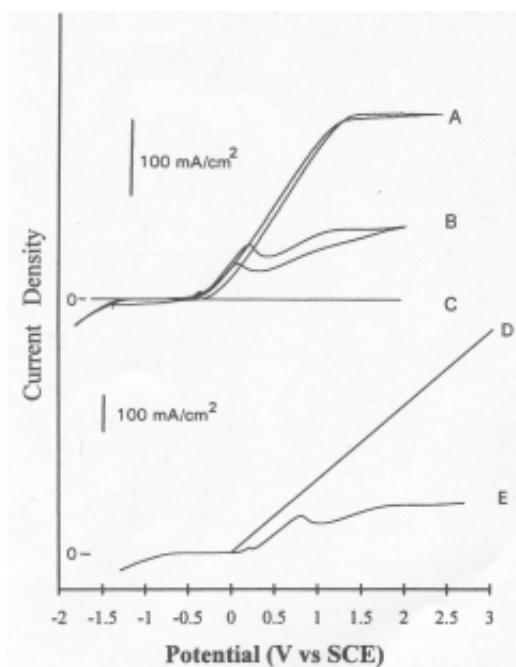


Figure 3.5: *IV*-characteristic of Si in HF/MeCN versus HF/H<sub>2</sub>O: A-C) n-Si (A: HF(2M)/TBAP(0.25M)/MeCN, illuminated (300 mW/cm<sup>2</sup> quartz halogen lamp); B: HF(2M)/NH<sub>4</sub>F(1M)/H<sub>2</sub>O, illum.; C: like B but dark). D-E) p-Si (D: HF/MeCN; E: HF/H<sub>2</sub>O) [48].

electrolyte and the silicon [48] (Fig. 3.5), which leads to current densities of up to 1400 mA/cm<sup>2</sup>, which is a factor of 25 higher than in aqueous electrolyte with the same HF concentration. The surface in the anodic regime is purely hydrogen terminated as in aqueous electrolyte (cf. section 3.1) with no surface oxide present. Unlike water-based HF no hydrogen evolution occurs at low anodic potentials and no microporous Si is formed. On the other hand, at higher potentials macropores were found in a variety of electrolytes (DMA [51], MeCN [48], DMF [52]), while in aqueous solution always electropolishing is found under such conditions. Propst et al. [48] proposed a mechanism (Fig. 3.6 similar to the hydrogen termination process (Fig. 3.1) to explain the tetravalent dissolution of Si without the formation of an oxide.

To classify electrolytes, Christophersen [51] developed the concept of "oxidation power" (Fig. 3.7): The voltage transients during galvanostatic anodization of silicon in a yet HF-free solvent is measured. The slope during the first minutes of anodization are compared, which should give a measure of the electrolyte's ability to oxidize the silicon. An oxidation of the surface should lead to an increasing resistance and therefore to a higher necessary anodization voltage to drive the same current; i.e. solvents which oxidize the silicon quickly show in first approximation a steeper transient than slowly oxidizing electrolytes. In this approach not the absolute voltage but only the change in voltage is regarded. The oxidation power can be used to optimize an electrolyte to obtain a desired pore morphology [5].

<sup>8</sup>Prolonged exposure of the electrode to the solution over several hours causes oxidation due to residual water and then the Schottky barrier height becomes independent of the added redox couples and stays always at 0.7 eV [47]. Due to the large number of surface states the Fermi energy becomes pinned which causes the irrelevance of the redox couples.

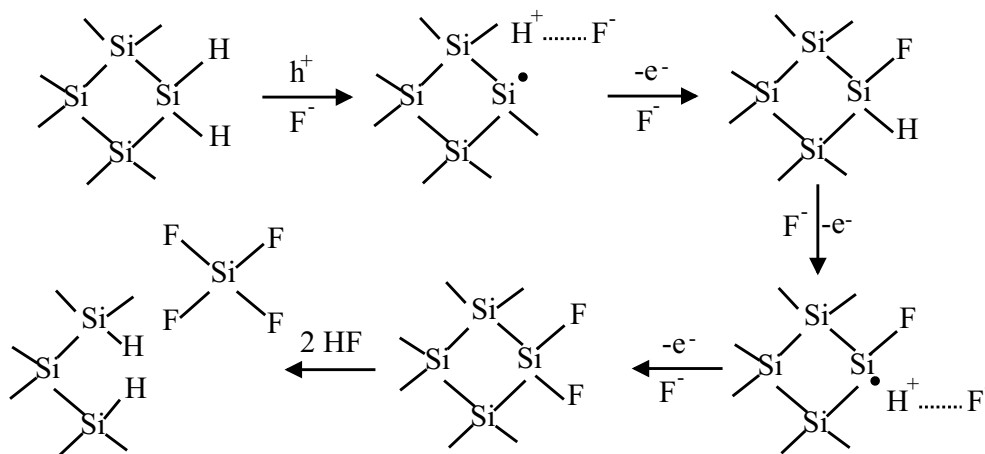


Figure 3.6: Proposed tetravalent silicon dissolution mechanism in MeCN [48].

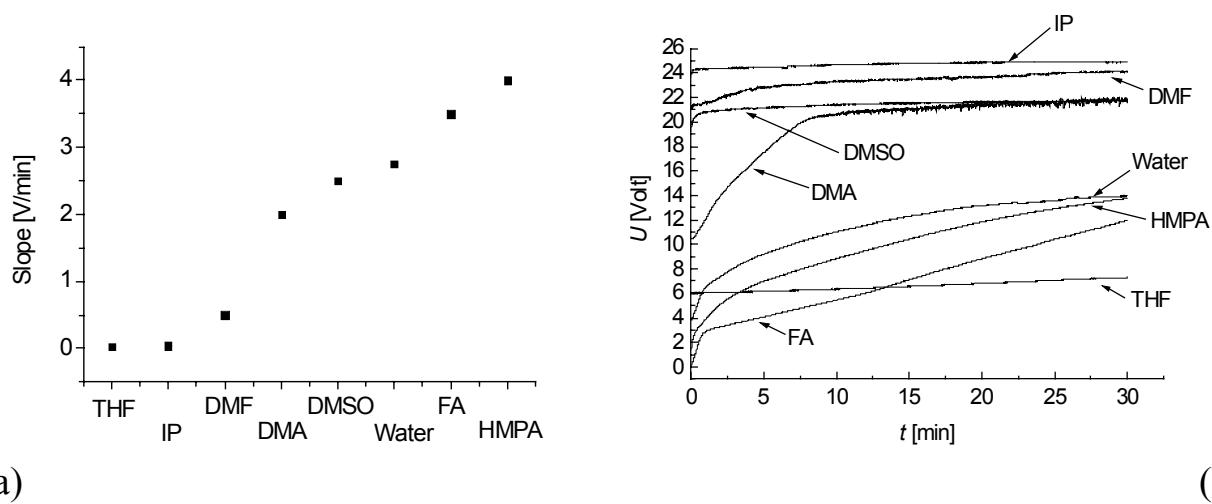


Figure 3.7: (a) Voltage transients for galvanostatic ( $j = 4\text{mA}/\text{cm}^2$ ) oxidation of p-Si ( $\rho = 10 - 20\Omega\text{cm}$ ) in HF-free solvents. (b) Slope of the transients from (a) during the first 2.5 min is defined by Christophersen as the "oxidation power" of the electrolyte (from [51]).



# Chapter 4

## Anodic oxides

### 4.1 Oxide types and properties

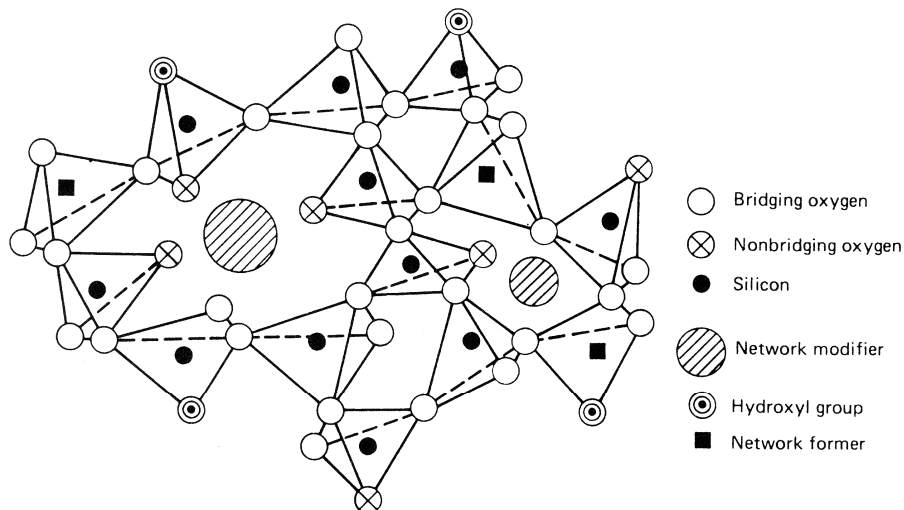


Figure 4.1: Structure of amorphous silica glass. The oxygen ions form a randomly arranged polyhedral network, which often incorporates large alkali ions as network modifiers to prevent crystallization (after [53]).

When silicon is oxidized in most cases the stoichiometric oxide  $\text{SiO}_2$  forms<sup>1</sup>. In natural form, mostly as sand, this compound composes around 28 % of the earth's crust [21], besides that it is the basis of glassware of all kinds. Additionally, the possibility to easily form a well insulating and chemically stable oxide, is one of the major reasons for silicon's success in microelectronics. Many subtypes of silicon dioxide can be distinguished:

Thermal oxide is grown in dry or wet oxygen atmosphere between 900 and 1200 °C [28]:



<sup>1</sup>Under special conditions so-called suboxides  $\text{SiO}_x$ ,  $x < 2$  form, cf. [54] and section 4.2

Table 4.1: Types of silicon dioxide and their densities

oxide type	density $\rho$ [g/cm <sup>3</sup> ] [28, 32]
native (cf. p. 25)	2.07 - 2.25
thermal	2.20 - 2.45
CVD	no ref.
spin-on-glass	no ref.
anodic (cf. p. 35 ff.)	1.80 - 2.25 <sup>a</sup>
quartz	2.66

<sup>a</sup>Under anodization in pure DI water, densities down to  $\rho = 1.5\text{g/cm}^3$  have been measured.

The growth proceeds at the Si/SiO<sub>2</sub> interface, so oxygen has to diffuse through the already formed oxide layer to the reaction site. Within the Deal-Grove model [55] which holds for oxide thicknesses of more than a few nm, the oxide thickness  $d$  depends linearly on the oxidation time up to approx. 30 nm:

$$d = \text{const.} \times t, \quad (4.3)$$

for thicker oxides a parabolic relationship is found:

$$d = \text{const.} \times \sqrt{D \times t}. \quad (4.4)$$

( $D$ : diffusion constant for O<sub>2</sub> through SiO<sub>2</sub>)

The oxide thickness is approx. 2.3 times the thickness of consumed silicon. If a consumption of substrate material is not possible, oxide can be grown by chemical vapor deposition (CVD). In this process, the silicon substrate is heated in a furnace to 700 - 1000 °C. Reaction educts are supplied in gaseous form and react on the hot substrate surface to form SiO<sub>2</sub>:



In more sophisticated processing, silane (SiH<sub>4</sub>) is replaced by e.g. tetraethyl-ortho-silicate (TEOS) which allows lower processing temperatures [2]. The oxide growth rates are between 8 and 17 Å/s.

If the oxide needs to be fabricated at low temperatures, spin-on-glasses in a sol-gel process are used: Silicon-tetra-acetate (Si(CH<sub>2</sub>COOH)<sub>4</sub>) is dissolved in a solvent and dripped in the center of a rapidly spinning substrate where it forms a homogeneous film of some hundred nm. Afterwards the solvent is heated out at ca. 200 °C [2].

Most of the discussed silicon dioxide fabrication techniques lead to an amorphous structure. In many cases, alkali atoms ("network modifiers") are added to the melt to prevent ordered crystallization (Fig. 4.1). In nature, as well as under special production conditions, SiO<sub>2</sub> grows in the crystalline form, i.e. as quartz. A comparison of the properties of anodic and thermal oxides is shown in Fig. 4.2 (for the dissolution of oxides cf. section 4.4). Especially the technically most relevant breakdown field is much lower in anodic oxides due to numerous defects in the oxide, although it is possible to attain the level of thermal oxides ( $BF \approx 10^7$  V/cm) with ultra-pure water [56] or in special electrolyte mixtures [49]. Generally, slow growth at low current densities  $j$  yields electronically more perfect oxides [32].

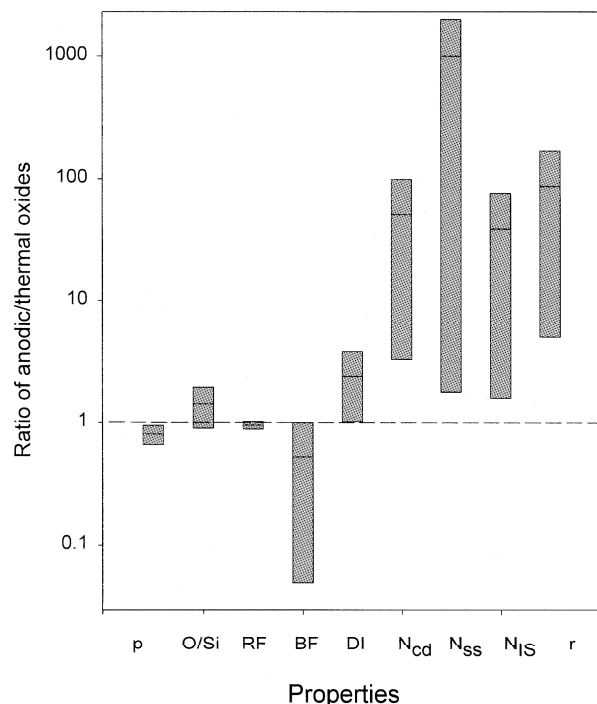


Figure 4.2: Comparison of anodic and thermal oxides ( $\rho$ : density, O/Si: atomic ratio, RF: refractive index, BF: breakdown fields, DI: dielectric constant,  $N_{cd}$ : effective interface charge density at flatband potential,  $N_{ss}$ : interface surface state density,  $N_{IS}$ : mobile ionic charge density,  $r$ : etch rates [28]).

## 4.2 Growth of anodic oxides

A fresh "optimal" silicon surface (e.g. after HF-Dip) is H-terminated (cf. section 3.1). When the silicon is anodically oxidized, first the Si-H bonds are weakened by an electronic hole. Afterwards the bond can be broken by  $H_2O$  (Fig. 4.3)<sup>2</sup>. OH groups replace the hydrogen bonds (end of first oxidation step in Fig. 4.3). In a second oxidation step the backbonds of the silicon atom are broken, which finally leads to a Si-O lattice where one oxygen atom is introduced between two neighboring silicon atoms. This two-step process breaks the initial H-termination and oxidizes the first layer of silicon. Afterwards only the second oxidation step from Fig. 4.3 successively occurs.

Most experimental observations suggest [60] that  $O^{2-}$  and/or  $OH^{-3}$  is the migrating species and that the oxide growth continues at the silicon-silica interface (although discussions are still controversial [28]). Like shown in Fig. 4.4 [59], the transition from silicon to stoichiometric silica is not abrupt but by a sub-stoichiometric oxide  $SiO_x$  ( $x < 2$ ) layer, which causes an electron injection back into the substrate when the oxide is dissolved. The stoichiometric oxide incorporates a lot of  $OH^-$  and the outer surface of the oxide is hydroxyl terminated (Fig. 4.4). Detailed analysis of the transient flatband potentials during dissolution of the oxide [60] showed that positive as well as negative fixed charges exist in the oxide.

To study the formation of anodic oxides, it is much easier to investigate a fluoride-free system, e.g.  $H_2SO_4$  [61], where no dissolution of the oxide film occurs. In solutions with low water content at current densities above  $1 \text{ mA/cm}^2$  [32] the thickness  $D$  varies linearly with

<sup>2</sup>Similar reaction schemes can be made up with HF and  $OH^-$ . The exact intermediates are hard to determine and still under debate [57], therefore Fig. 4.3 is only one possible variant.

<sup>3</sup>In detail regarded, if the oxide growth is beyond the initial state displayed in Fig. 4.3, only atomic lattice diffusion is possible in the innermost part of the silica, and  $OH^-$  diffusion becomes improbable because this would require a  $H^+$  outward diffusion after the reaction.

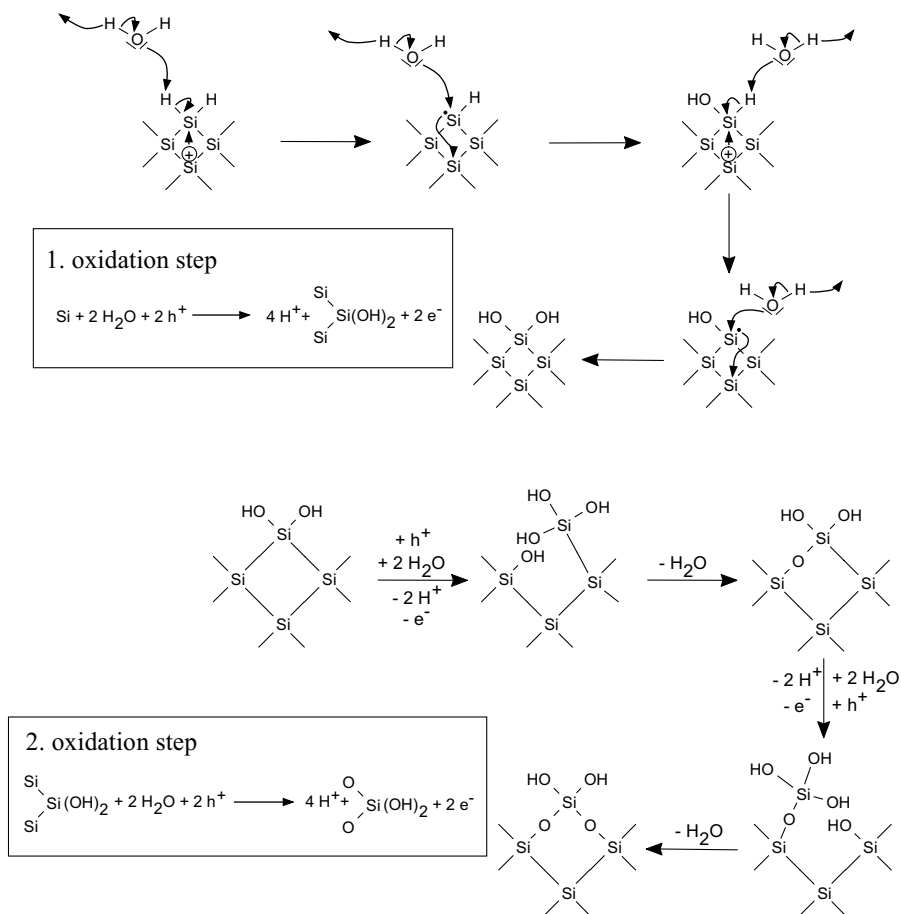


Figure 4.3: Beginning tetraivalent oxide formation mechanism on a hydrogenated silicon surface (after [57, 58]).

the applied potential  $U$ :

$$D = 1.7 \text{ nm} + 0.5 (\text{nm}/\text{V}) U \quad (4.6)$$

In electrolytes with high water content, the thickness increases monotonically with applied bias. Galvanostatic conditions (10 % acetic acid) lead to a log-log dependence with the anodization time  $t$ :

$$\log D = a + b \log t \quad (4.7)$$

( $a, b$ : constants depending on applied current density)

## 4.3 Porous oxides

### 4.3.1 Other porous oxides

Porous oxides are known for over 50 years in electrochemistry. Porous alumina [62] attracted by far the most attention when it became possible to produce ordered structures [17, 18]. Titania



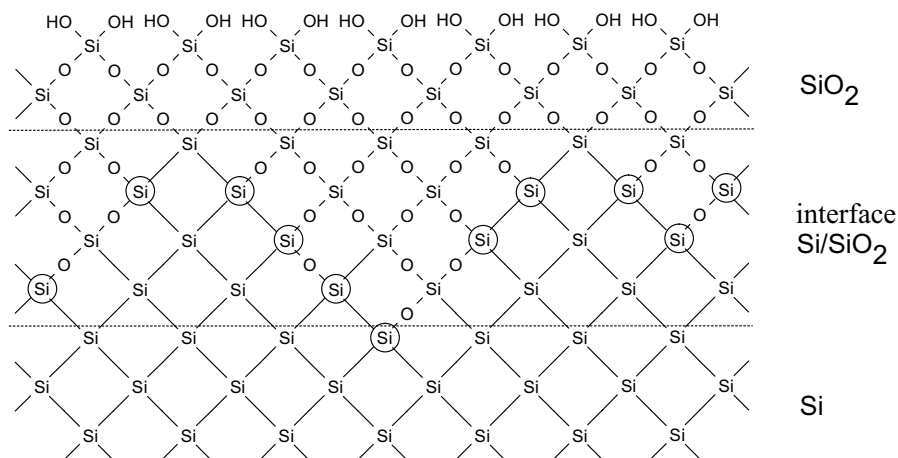


Figure 4.4: Structure of the silicon to silica transition region, which is deficient of oxygen. The circled Si atoms have still at least one bond with another silicon atom and can therefore inject electrons into the conduction band of silicon during dissolution (after [59]).

$\text{TiO}_2$  has also been shown to exhibit ordered domains [63], though not yet in the beauty of  $\text{Al}_2\text{O}_3$ , a difference plausibly due to the semiconducting properties of titania [64].

Also, (meso)porous oxides can be synthesized by other techniques, e.g. the sol-gel process mentioned in section 4.1. By the optimal choice of surfactant as well as other parameters, mesoporous silica with several different pore lattice types [15] as well as with a single-crystalline pore lattice structures [16] has been fabricated. Rouffignac et al. have recently demonstrated an effective electrical sealing for low-k dielectrics based on porous silica [65].

### 4.3.2 Anodically formed porous silica

Already in 1988, Madou et al. [66] suggested the existence of “flaws or channels” in silica to allow for the fast hydroxyl diffusion they found in the presence of certain impurities. Parkhutik [61] performed anodic oxidation of silicon in fluoride-free media where he found significant amounts of impurity anions from the respective acids (e.g.  $\text{SO}_4^{2-}$ ) at Si/SiO<sub>2</sub> - interface. This is again explained by an enhanced diffusion through pores in the oxide.

Several papers on the modelling of the electrochemical oscillations of Si (cf. section 4.5) also invoke pores in the oxide to explain the oscillations. Lewerenz et al. [19] measured in detail the dependence of the oscillations on pH and total fluoride concentration  $c_F$ . Due to the heavy volume expansion of the silicon, it should come to point defects in the oxide which then lead to pores. These opening and closing pores are suggested to be responsible for the strong oscillations in current with only weak thickness changes. Nevertheless no direct evidence of oxide pores is presented. In 1995, Aggour et al. [67] performed ellipsometry, XPS, and TEM measurements on oxides which showed pores with diameters  $d \approx 60 - 130 \text{ \AA}$  and a density on the TEM images of  $\rho = 9 - 18 \times 10^{11} \text{ cm}^{-2}$ , which verifies the assumption of pores in their earlier paper [19]. Lehmann [68] performed ellipsometry, x-ray reflectometry, and AFM measurements after the anodization which show a distinct change in morphology after approx. 11 nm oxide growth. The oxide splits into a dense ( $\rho = 2.1 \text{ g/cm}^3$ ,  $d = 2.9 \text{ nm}$ ) and a porous oxide ( $\rho = 1.75 \text{ g/cm}^3$ ,  $d = 10.2 \text{ nm}$ ) according to fits of the ellipsometry data. For a thickness below 11 nm the whole oxide was measured to be dense ( $\rho = 2.1 \text{ g/cm}^3$ ). Also the roughness

and the residual stress changed at 11 nm (and subsequent loops after again 11 nm nominal oxide growth). The author develops from that a model of periodically released stress within the oxide film, a behavior which is comparable to the growth of thin SiGe films on Si substrates. This leads to the externally visible oscillation phenomena in fluoride as well as in non-fluoride media.

Also Parkhutik et al. address oscillation phenomena in non-fluoride as well as slightly fluoridized media (0.1 M  $\text{H}_3\text{PO}_4$  / 0.005 M HF) which lead to a layered structure of porous oxide as measured by SEM [69] and x-ray reflectometry [70]. The pores in the oxide films show characteristic sizes between 4 and 7 nm. Up to  $j = 0.7 \text{ mA/cm}^2$  no oscillations are observed, while for  $j = 0.7 - 1.0 \text{ mA/cm}^2$  oscillations with frequencies comparable to Lehmann [68] are visible. For higher  $j$  a second, faster oscillation frequency arises which above  $2.6 \text{ mA/cm}^2$  fully dominates the system's electric response. These fast oscillations are accompanied by the formation of surface corrugations (with diameters around 1 micron) which are covered by the (porous) anodic oxide.

Because the present work on porous anodic oxides continues to a large degree the work of Lharch et al. [20], their results shall be described in more detail. They anodized p-type silicon ( $\rho \approx 0.4 \Omega\text{cm}$ ) in acidic fluoride media (mixtures of  $\text{NH}_4\text{F}$ ,  $\text{NH}_4\text{Cl}$  and HF with  $c_F = 0.05 - 0.33 \text{ M}$ ,  $\text{pH} = 2 - 3$ ) at potentials up to  $U = 90 \text{ V}$ , previously scarcely explored [69]. Simultaneously with voltammetry (Fig. 4.5 (a)), the electroluminescence (EL) (Fig. 4.5 (a) + (b)) as well as *in-situ* IR measurements was measured and the samples were afterwards imaged by SEM. The anodic polarization can (following the authors measurements and conclusions) thereafter be divided in three parts:

- (i)  $U = 3 - 12 \text{ V}$ : The oxide thickness increases monotonously with applied potential. The oxide is compact (i.e. not porous) and no EL is detectable. The current which flows through the oxide is purely ionic.
- (ii)  $U = 12 - 25 \text{ V}$ : The oxide splits into a dense inner and a porous outer part. The ionic part of the current remains constant, i.e. the oxide thickness doesn't change much. An electronic current contribution and therewith electroluminescence (EL) (with a red (dominating) and a blue band) arises with increasing voltage.
- (iii)  $U > 25 \text{ V}$ : Oxide thickness as well as the EL rises with current density. Strong gas evolution due to oxygen formation occurs. The blue band dominates the EL.

The surface often showed an increased roughness and micron-sized macro structures on the surface [20] (comparable to those of [69]). Detailed SEM analysis of the surface [71] yielded a porosity of 15 % with pores with diameters around  $d = 20 \text{ nm}$  with an interpore distance (pitch) of approx.  $p = 100 \text{ nm}$ . The appearance of pores is also visible in the comparison of IR measurements and electrical impedance spectroscopy (EIS) data (Fig. 4.5 (c)); IR detects the full thickness of the oxide while EIS only detects the isolating dense oxide.

## 4.4 Etching of oxides

Fig. 4.6 shows a possible sequence<sup>4</sup> for the dissolution of silica in HF containing electrolytes: As shown in Fig. 4.4 the silica surface is hydroxyl-terminated. A Si-O backbond of this front line is

---

<sup>4</sup>Like in the case of the anodic formation of silica, also the dissolution intermediates are under controversial discussion [28, 57].

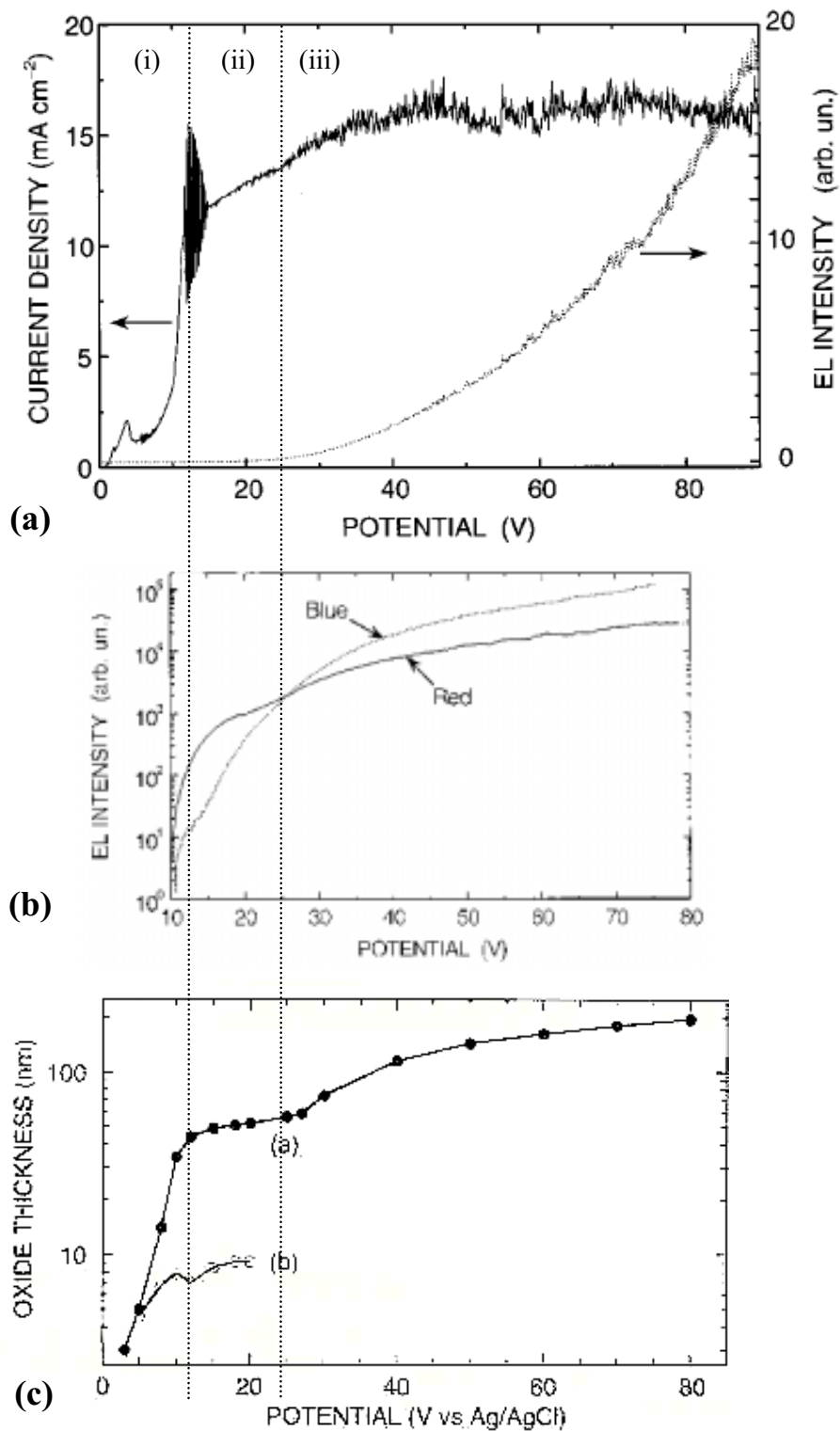


Figure 4.5: (a) *IV* characteristic and electroluminescence (EL) of p-Si for  $U = 0 - 90$  V [20]. (b) Spectral analysis of EL on a logarithmic scale [20]. (c) Comparison of apparent oxide thickness measured by (a) IR spectroscopy and (b) by electrical impedance spectroscopy (EIS) [71].

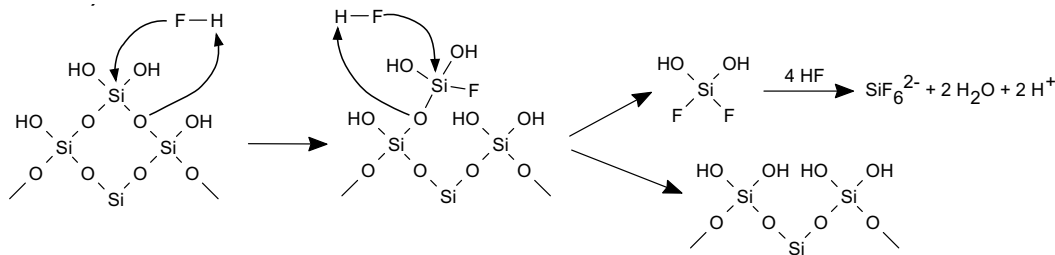
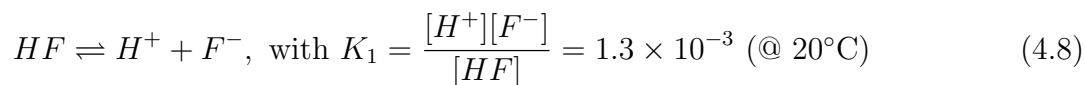


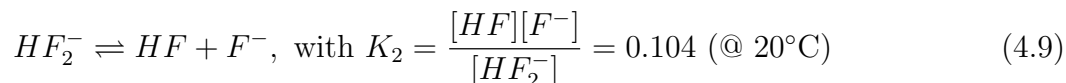
Figure 4.6: Dissolution mechanism for a stoichiometric silica layer [58] .

cut by a splitting HF. The Si-O bond becomes a Si-F bond and the hydrogen forms a hydroxyl group with the left-over oxygen bond. This process repeats so that  $\text{SiF}_2(\text{OH})_2$  goes into the solution leaving an again hydroxyl-terminated surface behind. With four more HF molecules the  $\text{SiF}_2(\text{OH})_2$  transforms into the only thermodynamically stable end product  $\text{H}_2\text{SiF}_6$ .

The etch rate of silica in fluoride media shows a distinct dependance on the pH value [73] which also indicates that not  $[\text{F}^-]$  but  $[\text{HF}]$  (cf. Fig. 4.6),  $[\text{HF}_2^-]$ , and probably even higher polymerized forms  $\text{H}_x\text{F}_{x+1}$  are responsible for the dissolution. The concentrations of these species are linked to the pH value and the absolute number of added fluor ions by the reactions



and



Figs. 4.7 e,f show the concentrations of these species at various fluoride concentrations and pH values. Judge [73] showed a correlation between temperature  $T$ , species concentrations and etching rate  $R$ :

$$R(\text{\AA}/\text{s}) = 5.0 \times 10^7 [\text{HF}_2^-] e^{(-\Delta E_1/RT)} + 2.2 \times 10^6 [\text{HF}] e^{(-\Delta E_2/RT)} + C(T) \quad (4.10)$$

( $\Delta E_1 = 9.1 \text{ kcal/mol}$ ,  $\Delta E_2 = 8.1 \text{ kcal/mol}$ ,  $C = 0.025 (T - 292)$ ).

According to Yahyaoui et al. [74] (Fig. 4.8) also the dissolution of anodic oxides follows a dissolution rate equation type  $R = a[\text{HF}] + b[\text{HF}_2^-] + c$ . The coefficients  $a$ ,  $b$ , and  $c$  are dependant on the total fluoride concentration  $c_F$  (inset of Fig. 4.8), a behavior which still lacks a full explanation.

Ethanol is often added in microelectronics oxide removal etches [75], because the etch rate slows down and the etching becomes more homogeneous. Also an otherwise common micro roughness after oxide etches on (100) surfaces is avoided. Garrido et al. [75] measured the etch rate of thermally grown oxides for various ethanol and HF concentrations, whereby the etch rate dropped over two orders of magnitude when switching from a pure aqueous to a pure ethanoic<sup>5</sup> 2.6 M HF solution. The best modelling is reached here if the model of Kikuyama et

<sup>5</sup>The residual water of approximately 3 wt% from the 50 wt% HF base solution was taken into account for all their modelings.

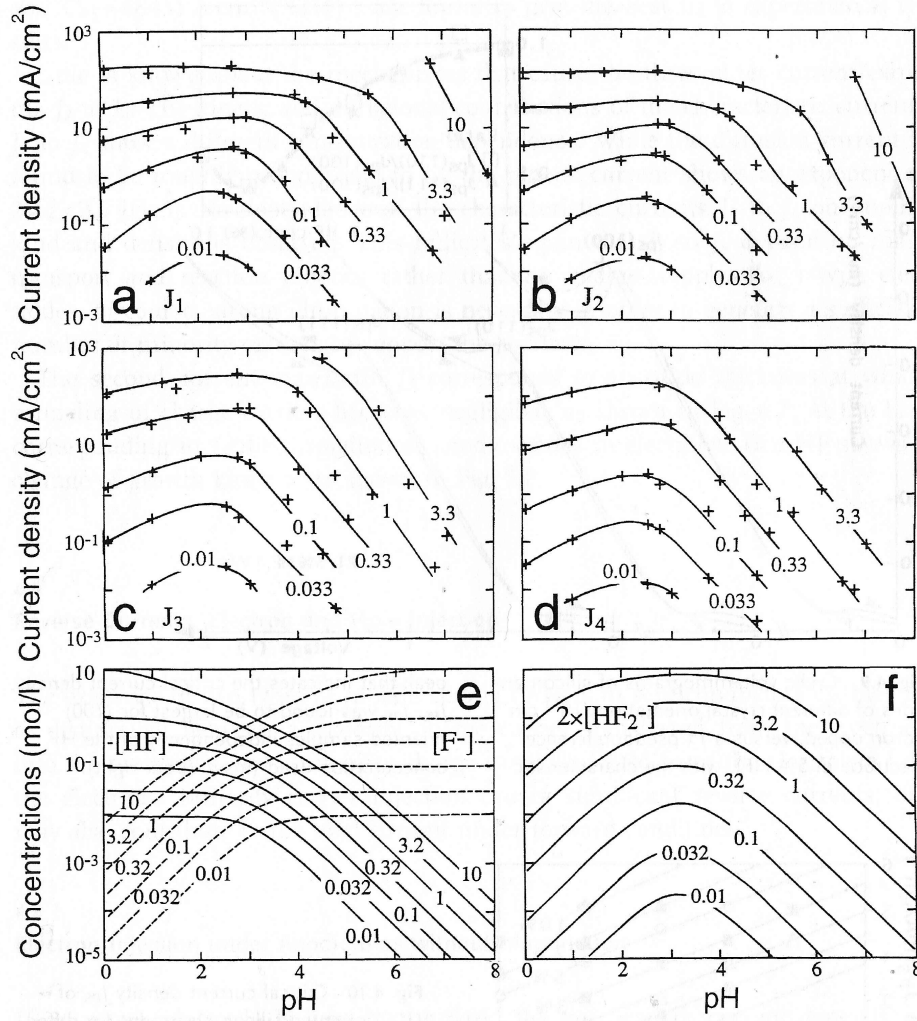


Figure 4.7: **(a-d)** Characteristic currents (as denoted in Fig. 3.2) for the Si/HF system versus pH and electrolyte concentrations (in mol/l at the curves). **(e-f)** Concentration of fluor containing species versus pH [72] .

al. [76] is used with an ethanol-content dependant activation energy for the oxide etching by  $H_2F_2$ :

$$R(\text{\AA}/\text{min}) = 257e^{-bc_{Eth}}[H_2F_2] + 55.3e^{-bc_{Eth}}[H_2F_2]^2 + 1282.8[HF_2^-] + 388.8[HF_2^-] \log\left(\frac{[H^+]}{[HF_2^-]}\right) \quad (4.11)$$

( $b$ : linear coefficient (free parameter)).

As can be seen from Eq.4.11, contrary to Judge (Eq.4.10), these authors neglect the influence of HF and take the dimer  $H_2F_2$  as one of the dominating species into account.

The dissolution rates strongly depend on the type of oxide ( $R_{anodic\ oxide} > R_{thermal\ oxide} > R_{Quartz}$ , e.g. in 1 % HF:  $R_{anodic\ oxide} \approx 1\text{nm}/s$ ,  $R_{thermal\ oxide} \approx 0.1\text{nm}/s$ ,  $R_{Quartz} \approx 0.001\text{nm}/s$  [28]). Anodic oxides contain the largest amount of defects and dissolve therefore most quickly, while quartz, as the crystalline form of  $SiO_2$  dissolves most slowly. The etch rate of anodic oxides can be decreased by an order of magnitude by a thermal annealing step after the anodization

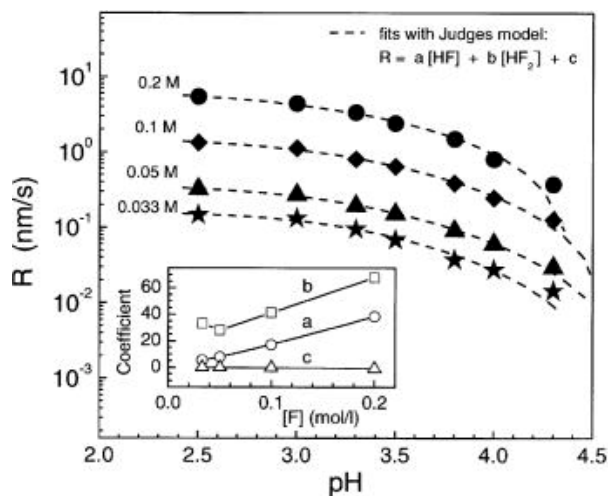


Figure 4.8: Experimentally measured etch rates  $R$  of anodic oxides versus pH for several  $NH_4F$  concentrations [74] and fits to Judge's model. Inset: Dependence of coefficients  $a$ ,  $b$ , and  $c$  versus fluoride concentration  $c_F$ .

[32].

The characteristic currents at the Si/HF contact also strongly change with pH (Fig.4.7a-d) in close correlation to the dissolution active species HF and  $HF_2^-$ , which immediately suggests that the dissolution of oxide is one of the key features to understanding the behavior of this contact.

## 4.5 Electrochemical oscillations

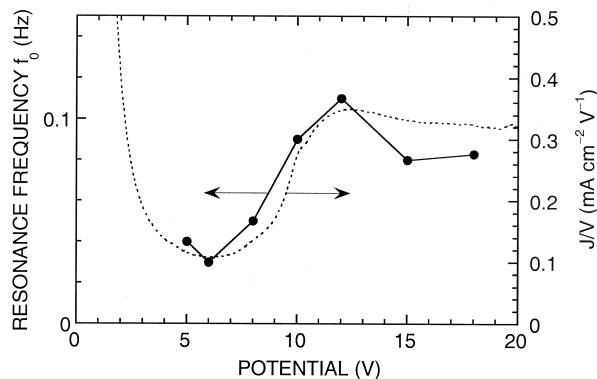


Figure 4.9: Oscillation frequency versus current density and voltage at higher potentials [77].

Many chemical systems never reach thermodynamical equilibrium, but exhibit pronounced oscillations [78]. Oscillations in electrochemical systems were first observed by Fechner [79] and Faraday [80]. Turner [33] was the first to report oscillations during the electropolishing of silicon in aqueous HF. These are the oscillations already mentioned in section 3.1.2 (cf. Fig. 3.2) which start to occur at potentials around 3-8 V [81]. They occur not only under

potentiodynamic conditions (i.e. during  $IV$  scans), but also under potentiostatic [19] as well as under galvanostatic conditions [68]. The shape of the oscillations is only in special cases sinusoidal, in many cases it contains higher harmonics or anharmonic contributions [81, 82]. Chazalviel et al. [43] demonstrated that the oscillations in the electrical signal are accompanied by periodic changes in the oxide thickness. Essentially the oscillations strongly depend on:

- applied potential [81]
- HF concentration [81]
- pH [19]
- external serial resistance [83]

The substrate doping and orientation as well as the electrolyte temperature only plays a minor role for the behavior of the oscillations [82]. Ozanam et al. [81] measured a linear dependence between applied potential  $U$  and the oscillation period  $\tau$ , i.e.  $U \propto \tau = \frac{1}{f_0}$  ( $f_0$ : oscillation frequency). In a similar manner, the HF concentration  $c_F$  and therewith the current density  $j$  is directly proportional to the frequency, i.e.  $j \propto f_0$ . Overall, the ratio of  $j/U$  is directly proportional to the frequency  $f_0$ . Fig. 4.9 shows that this relationship even holds for higher potentials as measured during the work of Lharch et al. [20, 77] which is discussed in section 4.3.2.

## 4.6 Modelling

### 4.6.1 Overview of models

The peculiar behavior of the Si-HF contact including formation of pores, electropolishing and oscillations has been addressed by several models:

- Gerischer et al. [84] link the oscillations to a non-linear correlation between formation and dissolution of the anodic oxide due to a change in stoichiometry of the oxide. With increasing thickness the oxide becomes more and more perfectly stoichiometric (cf. also the interface structure proposed by Morrison et al. [59](Fig. 4.4)), which in turn decreases the ionic conductivity.
- Föll [29] proposed a periodic shift from a tunnelling (at low oxide thicknesses) to an avalanche driven current (at high oxide thicknesses) as a driving mechanism for the oscillations.
- Smith et al. [85] assume a “soft” and a “hard” oxide (based on a proposal by Eddowes [86]) which dissolve with different rates. Depending on the actual thickness and therewith the field strength the oxide morphology changes, which is assumed to lead to the oscillatory behavior.
- The “fluctuating pore model” of Lewerenz et al. [19] assumes that due to the different volumes of silica and silicon, the growing silica layer has to contain point defects, which can develop into pores. Dissolution occurs primarily at defects (point defects, pores, ...) in the oxide. These pores are also preferential oxide growth spots which are blocked as soon

as the oxide thickness exceeds a certain limit. Because of the preferential attack of the fluoride ions at the point defects and pores, always new pores develop (out of point defects) as well as existing pores are expanded. Depending on the degree of synchronization between the pores, sustained, damped, or an absence of oscillations are explainable. This, at first only qualitative model, has been mathematically modelled by Grzanna et al. in 2000 [87,88]

- Chazalviel and Ozanam [89] are lead by their experimental results to the conclusion of small, independent oscillating oxide domains on the surface with a size of approx. 100 nm [90]. When these oscillators become synchronized (e.g. by an external perturbation) externally visible oscillations occur.
- Also the model of Lehmann [68] links a porous oxide (cf. section 4.3.2) with oscillations: Due to thermodynamical reasons, above a certain critical thickness (around 10 nm) the residual stress in the oxide layer is released by the formation of pores in the oxide. Ions can enter the porous region and lead to a quicker oxide dissolution, leaving finally only a dense bottom part of the oxide behind. A repetition of this cycle is seen as the cause of the oscillations.
- In the current burst model (CBM) by Carstensen et al. [91] the (microscopic) current flows discontinuously in nm-sized current bursts which can be synchronized to from externally visible oscillations. It is discussed in detail in section 4.6.2.

### 4.6.2 Current Burst Model (CBM)

The current burst model (CBM) by Carstensen et al. [91] integrates several of the approaches from section 4.6.1. The general assumption is that the current across the interface is not homogeneous but discretized on a nm scale, which is under non-oscillating conditions not visible on a macroscopic scale. Each of these tiny spots is a micro-oscillator that runs individually through current burst cycles (CBC) (Fig. 4.10). The behavior of larger ensembles can then be adequately simulated with a Monte-Carlo-approach like e.g. in [82,94].

A CBC consists of the following phases<sup>6</sup> (Fig. 4.10):

1. direct divalent dissolution of Si
2. tetravalent oxidation of Si to SiO<sub>2</sub>
3. dissolution of SiO<sub>2</sub>
4. H-passivation of the surface

The direct dissolution as well as the passivation (Fig. 4.11) are highly anisotropic, while oxide formation and dissolution are isotropic. The oxide dissolution is by far the slowest process, so in first approximation the duration of a CBC is given by the dissolution time. After each cycle the probability for the nucleation (i.e. start) of a new CB is strongly related to the passivation of the surface (Fig. 4.11).

---

<sup>6</sup>The Si/HF CBC is shown here, albeit the CBM is not bound to this specific system (cf. e.g. [95]).



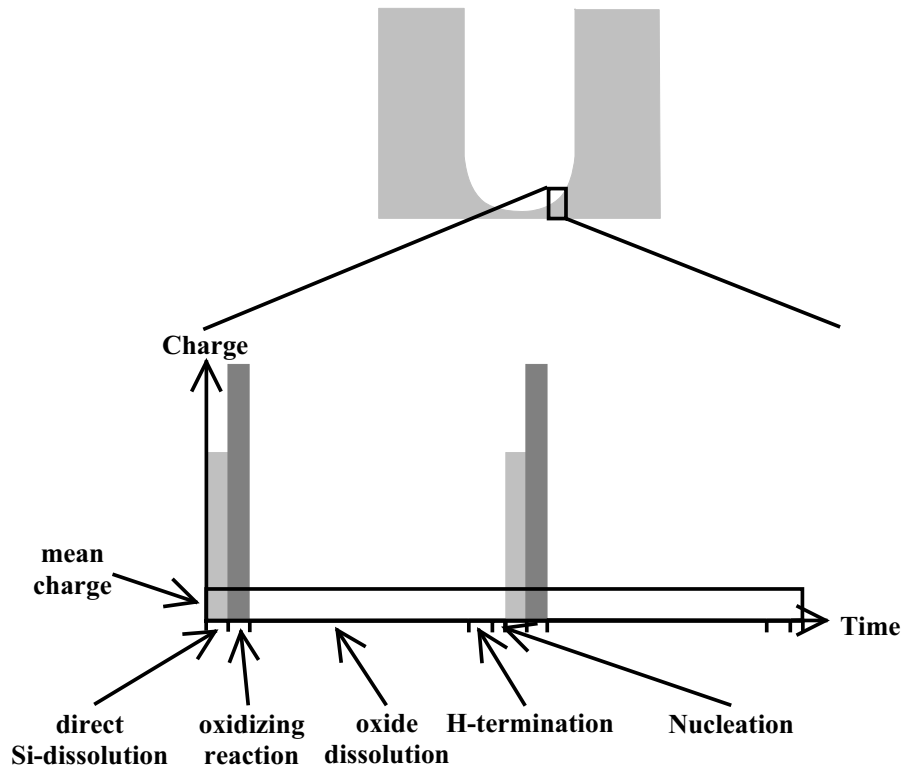


Figure 4.10: Current burst cycle (CBC): The current across a semiconductor-electrolyte interface, e.g. at a pore tip, can be divided into nm-sized areas which run individually through the displayed stages of a “current burst” [92].

The change in oxide thickness  $s$  at a given spot  $(x, y)$  on the surface at a time  $t$  is described by the continuity equation [82]

$$\frac{ds}{dt}(x, y, t) = \beta J_{ox}(x, y, t) - \alpha(x, y, t) \quad (4.12)$$

( $\beta = 0,74 \frac{\text{nm}}{\text{s}} (\frac{\text{mA}}{\text{cm}^2})^{-1}$ : proportionality factor;  $J_{ox}$ : current density leading to oxidation;  $\alpha$ : oxide dissolution rate).

This can be converted into a spatially averaged continuity equation

$$\frac{d\bar{s}}{dt} = \beta \overline{J_{ox}} - \bar{\alpha}, \quad (4.13)$$

which combines the averaged current density  $\overline{J_{ox}}$  and the averaged oxide dissolution  $\bar{\alpha}$ . The total current density  $J = J_{ox} + J_{nox}$  comprises an oxidizing  $J_{ox}$  as well as a non-oxidizing component  $J_{nox}$ . As long as other reduction/oxidation processes can be excluded at the Si electrode (i.e. no  $\text{O}_2$  formation due to extreme voltages),  $J_{nox}$  is equal to the current density caused by direct dissolution, which is in the electropolishing regime nearly zero, i.e.  $J \approx J_{ox}$ . If the system is in a steady state the average oxide thickness doesn't change and  $\frac{ds}{dt} = 0$ .

Up to now, only conditions in the electropolishing regime, where there is always an oxide coverage, were modelled, although in principle, also modelling including oxide-free surfaces

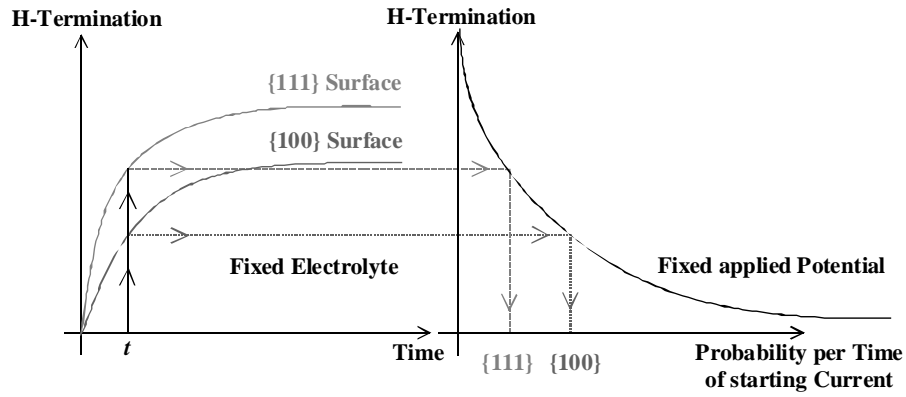


Figure 4.11: Passivation versus nucleation probabilities for current bursts: The orientation sensitive H-passivation prefers (111) surfaces to (100) surfaces which in turn makes new current bursts on (100) surfaces more probable than on (111) surfaces [92].

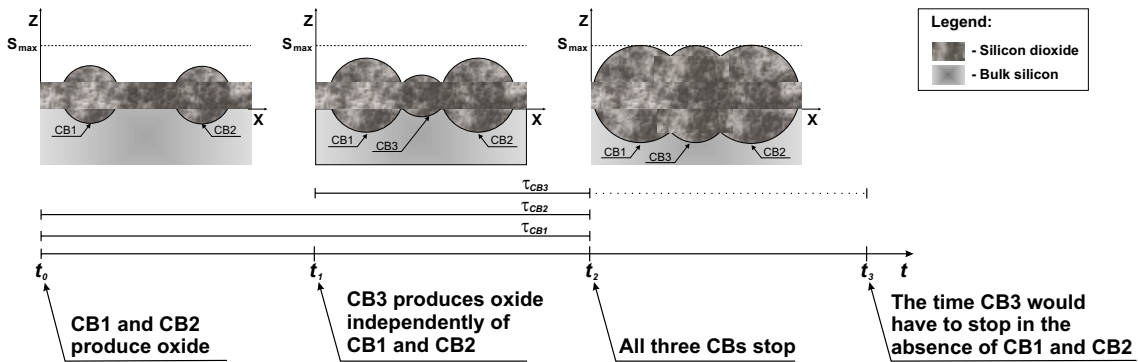


Figure 4.12: Synchronization mechanism within the CBM: When a current burst (CB) nucleates between two already active CBs, it stops tendentially earlier and gets in phase with the surrounding CBs [93].

with passivation is possible. In the Monte-Carlo modelling [82] in the electropolishing regime, the probability  $W(E)$  that a CB starts is linked to the field strength  $E$  in the oxide layer. For  $E > E_{max}$  the probability is unity, below it falls off with a characteristic to be chosen appropriately for the respective modelling case. That means that above a certain limit  $E_{max}$  the CB is “ON”. While the CB is “ON”, oxide is produced, and the field strength in the oxide therefore decreases until the  $E$  reaches the vicinity of a lower limit  $E_{min}$ : The probability  $R(E)$  that the conducting (ionic) channel through the oxide closes is unity for  $E < E_{min}$ , for higher field strengths it shows a modelling dependant falling edge. When the CB is “OFF”, the oxide is dissolved, which increases the field strength in the oxide again until  $E \approx E_{max}$  and a new CBC starts. Only with an offset between  $E_{min}$  and  $E_{max}$  it is possible to generate an oscillating behavior. The exact form of the oscillations is strongly related to the shape of  $W(E)$  and  $R(E)$  and the absolute values for  $E_{min}$  and  $E_{max}$ . With experimentally proven parameters (e.g. oxide etching rate  $\alpha$ ) and properly chosen  $W(E)$  and  $R(E)$  it was possible for the first time to model quantitatively the experimentally observed dependencies (cf. section 4.5)  $f_0 \propto \frac{1}{V}$  as well as  $f_0 \propto c_{HF}$  for electrochemical oscillations at the Si/HF contact.

Generally, any model which tries to explain the macroscopic oscillations by ensembles of micro-oscillators has to provide three general ingredients:

1. a mechanism leading to local oscillators
2. a synchronization mechanism
3. a desynchronization mechanism

The first point is provided by the CBC construct: Every spot runs through on/off cycles of current flow. The inherent synchronization mechanism becomes clear when two neighboring CBs are regarded (Fig. 4.12). When another CB nucleates between them, it will produce oxide up to a certain thickness according to the voltage applied. Because of the surrounding CBs this oxide thickness is reached earlier than without neighbors. This mechanism tendentially brings neighboring CBs in phase. A desynchronization happens when CBs are too close together: Near a CB the local current density is higher, which in turn leads to higher diffusion and ohmic losses. So the voltage available and therefore the probability for the nucleation of an additional CB in the proximate vicinity of an active CB is lower.

A strong advantage is, that the CBM is a far-reaching model: It explains the events at a semiconductor electrode in a bottom-up approach. The starting point of small independent oscillators is not bound to a specific part of the  $IV$  characteristic of the contact. Also it allows to model the transient development of the electrode morphology, e.g. the formation of pores (cf. section 5.4).



# Chapter 5

## Pores in Silicon and InP

### 5.1 Classification

The most common classification for porous materials is the IUPAC (International Union of Pure and Applied Chemistry) notation which distinguishes the pores according to their diameter  $d$ :

- Macropores:  $d > 50$  nm
- Mesopores:  $2 \text{ nm} < d < 50$  nm
- Micropores:  $d < 2$  nm

It is not addressing pore spacing (pitch) or morphological features, like degree of interconnection, branching, pore shape, etc. Fig. 5.1 shows examples of meso- and macropores in silicon which were etched in two industry projects in the course of this work. A second possibility is to distinguish between the mechanisms for hole generation (in n-type semiconductors):

- tunnelling breakdown
- avalanche breakdown
- illumination

The first two points are sometimes joint under the keyword “breakthrough” pores. Concerning the last point, front-side (fsi) and backside (bsi) illumination are commonly distinguished. In InP another classification according to the pore direction has been set (cf. section 5.3):

- crystallographically-oriented (“crysto”) pores
- current-line (“curro”) pores

Finally, it has been frequently shown [5, 97], that pores from an organic electrolyte strongly deviate from those etched in aqueous electrolytes. In light of all of this, the simple IUPAC definition is questionably coarse and a notation like “n-macro(org, bsi)” (cf. [5]) is more appropriate. In the present work, pores are grouped according to the underlying mechanisms, i.e. the crysto/curro as well as the breakdown/illumination distinction are mainly used.

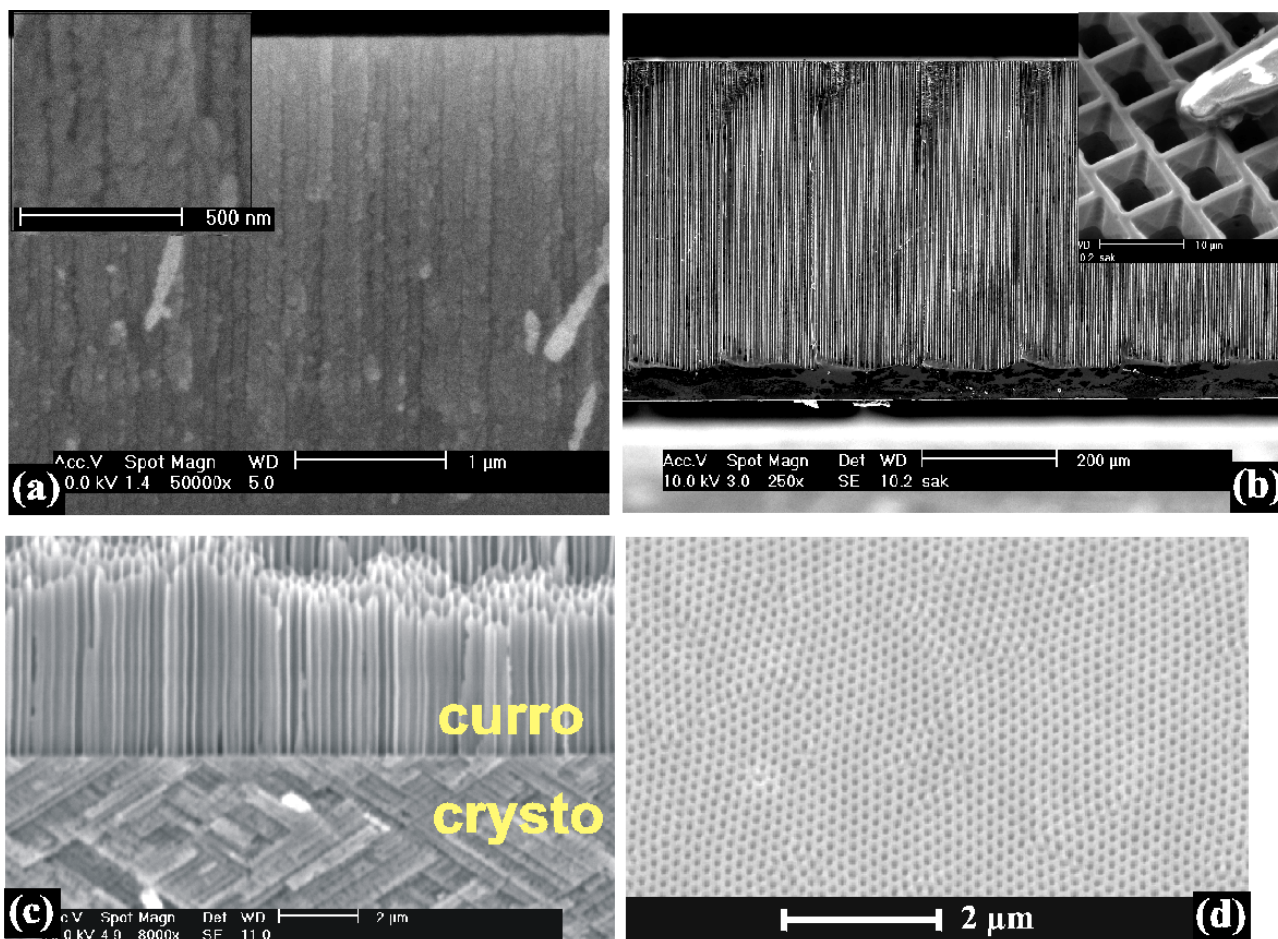


Figure 5.1: Examples of meso (a) - and macroporous (b) silicon which were etched in the framework of two industrial projects in the course of the present work (Main pictures: SEM cross sections. Inset (a): Magnification. Inset (b) Top view with the tip of a bee sting for comparison). (c) Crysto and curro pores in InP [96]. (d) Monocrystalline curro pore crystal in InP [95].

## 5.2 Pores in silicon

Silicon exhibits all three IUPAC pore types. However, in the present work, micropores are not concerned (for further informations on micro-PS and its luminescence cf. e.g. [28, 32, 85]). Only macro- and mesoporous Si shall be discussed in the following sections. A more detailed overview can be found in [5].

### 5.2.1 Macropores

To adequately give an overview over the types of macropores in silicon the notation of Föll et al. (cf. section 5.1 and [5]) is used. Only the basic characteristics are addressed in this classification with additional references in the ‘application’ section.

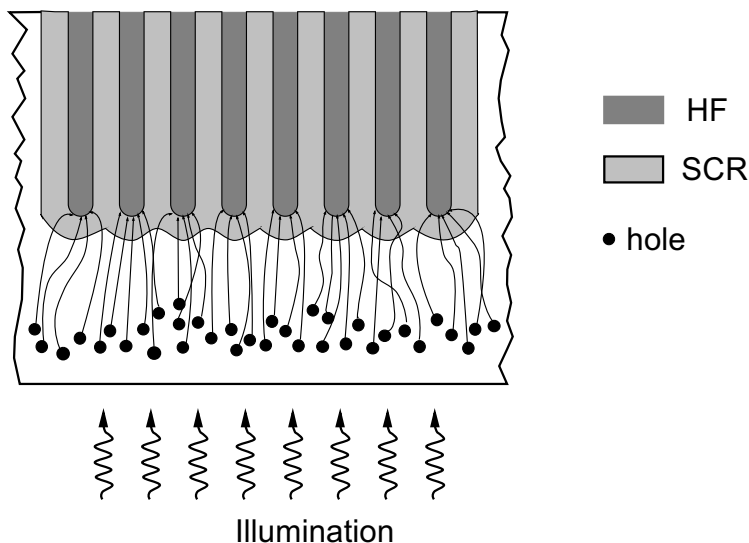


Figure 5.2: Schematic sketch of the macropore growth mechanism using backside illumination.

### **n(bsi,aq)**

Lehmann and Föll [46] were the first to present micron-sized pores by electrochemical etching in silicon: n-type silicon with low doping is illuminated from the backside through a short-pass filter so that most of the light is absorbed in the first microns of the wafer backside. The generated holes (necessary for electrochemical dissolution (cf. section 3.1.2)) diffuse to the frontside where they are focussed by the space charge region (SCR) (Fig. 5.2) onto the pore tips. Due to recombination the number of holes decays exponentially with the distance between backside and pore tips. To always allow the same number of holes to arrive at the pore tips which approach the backside, it is necessary to level down the illumination accordingly. On the other hand, this means that the efficiency ratio  $\ln I_{etch}/I_{illum}$  rises linearly with time.

The walls of the pores stay well protected due to two reasons: Overlapping of adjacent SCRs (cf. Fig. 5.2) and/or passivation of the walls. If the SCRs are overlapping the remaining silicon wall is depleted of carriers and all arriving holes from the backside are forced to the pore tips. However, pores remain stable with wide lithographical prestructuring without significant branches [58]. Then only the passivation of the pore walls due a different crystallographic orientation can be invoked as an explanation [5].

Lehmann assumes that the pore tip carries  $j_{PSL}$  (cf. section 3.1.2), while the rest of the surface is inert, i.e.  $j_{rest} = 0$ . This can then be translated in a simple formula for the area occupied by pores  $A_{pores}$  versus the total electrode area  $A_{total}$ :

$$\frac{A_{pores}}{A_{total}} = \frac{j}{j_{PSL}} \quad (5.1)$$

( $j$ : externally applied current density)

Taking into account the specific shape of the pores, this can be easily translated into pore diameters  $d$ . Also this offers the possibility to change the pore diameter easily during growth by modulating the illumination intensity, resulting in modulated [98] or saw-shaped pores [99]. Lehmann [98] gives the following limits for the bsi technique:

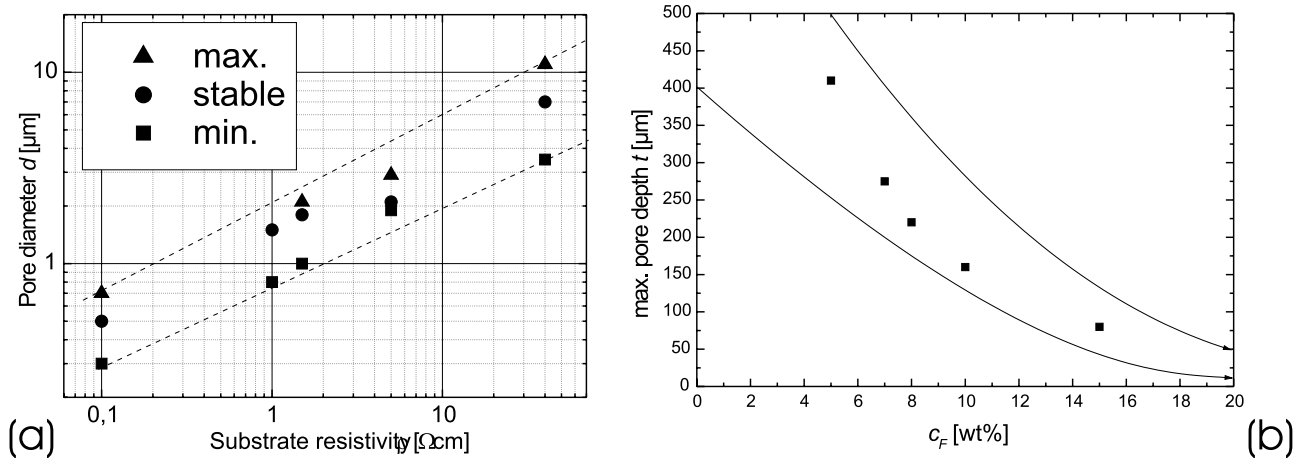


Figure 5.3: Limits of bsi macropore growth: (a) pore diameter vs. doping level, (b) pore depth vs. HF concentration (redrawn from [98]).

- the diameter  $d = 0.3 - 20 \mu\text{m}$  is limited on the lower edge by the formation of breakthrough side pores (cf. section 5.2.2) and on the upper limit by formation of hydrogen bubbles within the pores. Kleimann et al. [100] have however shown pores with diameters up to  $d = 100 \mu\text{m}$ . The doping level of the substrate has to be chosen adequately (cf. Fig. 5.3a).
- maximum pore depth  $t_{max}$  is drastically reducing with HF concentration (Fig. 5.3b). By choosing a low temperature and/or a low HF concentration, it is possible to etch macropores through the whole wafer thickness<sup>1</sup> (approx.  $525 \mu\text{m}$  for most 4 and 6" wafers) [101].
- the pitch-to-diameter ratio  $p : d = 1 - 10$ .
- the porosity can vary between 1 to nearly 100 % for sample-wide homogeneous porosities [32]. In case of varying porosities, the illumination intensity has to be also varied. The lateral resolution for variation is limited by the diffusive smear-out of the generated holes during their path from the back- to the frontside.

The cross sectional shape of the pores can be varied from circular over squared to star-shaped by changing the applied bias [102]. The primary direction is either the  $\langle 100 \rangle$ - [102] or the  $\langle 113 \rangle$ -direction [103].

A tremendous disadvantage of bsi-macropores is their slow growth speed of  $1 \mu\text{m}/\text{min}$  or less. For applications where pores have to be etched through the whole wafer, the extreme pore depth calls for low temperatures and/or low HF concentrations. This even further decreases the etch speed, so that etch times of 14 hours per wafer or more become the standard. Due to the high price for a full professional etching setup (50,000 - 100,000 €/ per wafer etching station) such a processing time is only tolerable for extremely expensive end products.

<sup>1</sup>In most cases, it has not been possible to grow macropores through the last few microns of the backside, which has to be opened by different processes (e.g. plasma etching).



### n(bsi,org)

Propst et al. [48] reported pores in the MeCN/HF system for n-Si, bsi (without pictures for n-Si or any further morphological information). Pores in DMF [104] are smaller than in the aqueous electrolyte and show a stronger tendency towards branching. The formation of sidepores can be suppressed by a 20% modulation of the illumination in the mHz range. How strong the modulation is represented in the pore diameter variations strongly depends on conditions [51]. In DMSO, e.g., a heavily non-linear response of the diameter results, which leads to spherical bulges of the pores.

Probably because of the beautiful results in aqueous electrolytes, organic electrolytes combined with backside illumination are to a large degree unexplored. Nevertheless, this system could offer further insight into the pore formation mechanisms of the Si/HF system.

### p(org)

Kohl et al. [48, 105] were the first to use acetonitrile to get macropores on p-type silicon. Meanwhile, also pores in conjunction with DMF [52], poly-carbonate [106], DMSO [107], and DMA [51] have been shown. Because the organic electrolytes offer only a mediocre conductivity often conducting salts like TBAP are added (cf. section 3.2) to decrease the serial resistance of the electrolyte. The pore morphology (and whether pores are achievable at all) strongly depends on the following parameters:

- Si doping level [108]
- oxidizing power of electrolyte [5]
- passivation abilities of electrolyte [5]
- water content of the electrolyte [52]
- conductivity of the electrolyte [52]

The water content of the electrolyte decides upon pore depth (less for higher water content) and diameter (wider for higher water content) [52]. Similar to n-type silicon, the macropores follow either  $\langle 100 \rangle$  or  $\langle 113 \rangle$  directions [109], in contrast to the results of Ponomarev et al. [52], where the pores obviously not follow a precise crystallographic orientation, nor a directly perpendicular direction (i.e. current-line oriented growth). The wall thickness of macropores is much smaller than in the n-type case, which is due to a much smaller SCR because the p-Si/HF contact is switched in forward direction in contrast to n-Si. To still explain the stability of pore walls in the p-type case (where the etching-initiating holes are majority carriers), several explanations have been invoked [48, 51, 110, 111]. Other than the n-Si case, where the large SCR dominates most effects, in p-Si the pore walls are likely to be protected by a mixture of surface passivation and SCR effects [51]. The rather thin walls in p-type make deep macropores harder to achieve than in n-bsi, but Chao et al. [112] have demonstrated pores with depths up to 400  $\mu\text{m}$ . Likewise, prestructuring works only in a narrow range compared to n-bsi, but helps tremendously to stabilize the pore growth [112].

## p(aq)

Wehrspohn et al. [108] found macropores in p<sup>-</sup>-Si using high HF concentrations and (in connection with the high HF concentration) low current densities. They explain their results with a superior conductivity of the electrolyte compared to the silicon. Lehmann et Rönnebeck [38] link their results on p-type pores in aqueous solutions to a similar model like for n-type (cf. p. 51).

## Applications

Macropores are currently used in several (industrial) applications (though most of these products are still under development). This includes the following areas:

- optical applications, e.g. as photonic crystals [113, 114], optical short-pass filters [115, 116], antireflection coating for solar cells [107]
- x-ray imaging [101, 117]
- (bio)chemical applications, e.g. as micro reactors [118], DNA-chips [32], electrodes for micro fuel cells [8]
- MEMS [119]
- brownian ratchets [99]

### 5.2.2 Meso- and breakthrough pores

Classically, mesopores in silicon are grown on highly doped n<sup>+</sup>- or p<sup>+</sup>-doped substrates. On these substrates a supply of holes is given via tunnelling (cf. section 2.2.2). To simplify the discussion, mesopores in the present work also include so-called “breakthrough” pores. The pore size limitation given by IUPAC (50 nm) is a purely artificial one and the formation mechanisms of these pores can be better understood if pores which have similar underlying formation mechanisms are grouped together. “Breakthrough” pores are obtained if low to medium doped n-Si is anodized in the dark. The only hole generation mechanism is avalanche or tunnelling breakdown. First star-shaped breakdown pores with several 100 nm pore diameter have been reported by Theunissen [120]. Herino et al. [121], Halimou [122], as well as Lehmann et al. [45] investigated mesopores in detail:

- Pore diameter  $d$ : p-type silicon resulted for various conditions always in  $d < 20$  nm (cf. also [123]), while n-type yielded  $d < 10$  nm up to  $d = 200$  nm. Increasing doping density decreased  $d$ , while  $j$  enlarges  $d$ . A higher HF concentration shrinks the pores for all doping levels and types.
- Growth rate  $r$ : Strong increase with  $j$  (From  $r = 0.2\mu\text{m}/\text{min}$  up to  $r = 20\mu\text{m}/\text{min}$ ); p-type doping density showed no major influence on  $r$ , while  $r$  dropped with increasing n-type doping.
- Porosity  $P$ : Increases strongly with doping density for n-type, while it drops weakly in the case of p-type. In n-type it first decreases strongly with increasing  $j$  for low current densities, but then increases monotonically with  $j$  (cf. [122] for experimental conditions), while it increases with  $j$  (cf. also [7]) for all  $j$  when using p-type. Increasing the HF concentration lowers the porosity.

For large structures like multilayer systems of several microns thickness, all etching parameters have to be depth adjusted to keep the pore morphology [7] constant, because the HF concentration decreases with depth.

Based on electrical field simulations, Lehmann et al. [45] draw the conclusion that exclusively tunnelling is responsible for mesopore growth, while avalanche breakdown leads to large pits surrounded by a homogeneously etched area.

Often ethanol ( $C_2H_5OH$ ) partly or fully replaces water as diluent for the HF (popular mixtures include 1:1 = HF(48%): Eth, 1:1:1 = HF(48%): Eth:  $H_2O$ ) without further mentioning of the reasons for the use of ethanol. Systematic studies on the influence of ethanol on pore etching behavior are rare and only attribute to the ethanol the ability to decrease the surface tension and to reduce therewith bubble-related problems:

- Bomchil et al. [124] used p-type ( $0.01 \Omega\text{cm}$ ,  $j = 10\text{-}240 \text{ mA/cm}^2$ ) in 1:1:2 =  $H_2O$ :HF:Eth (equivalent to 42.6 wt%  $H_2O$ , 14.8 wt% HF, and 42.6 wt% Eth) which resulted in a smoother surface of the porous layer than with a similar pure aqueous mixture. The hydrogen bubbles forming during the PS formation were smaller and detached easier from the surface due to the drastically reduced surface tension in alcohol based solutions. No microstructural images were given.
- Searson et al. [125] show cross sectional images of meso-PS (n-Si  $0.1 \Omega\text{cm}$ ,  $j = 50 \text{ mA/cm}^2$ ) etched in 20 wt% pure ethanoic<sup>2</sup> HF as well as in 20 wt% pure aqueous HF. The pore diameter in ethanoic HF was  $d = 70 \text{ nm}$  (no values for the aqueous electrolyte). In a direct comparison of the images the pores from ethanoic HF are smoother and show less side pores. It is proposed that this is due to less sticking probability of hydrogen bubbles at the pore walls when using ethanol.
- Halimou [122] states that a minimum of 15 vol% of ethanol is necessary for effective bubble removal. Also the wettability of a porous layer increases drastically upon the use of ethanol. In case the PS shall be removed chemically after anodization addition of ethanol helps drastically to infiltrate the pores and increases by that the dissolution rate (without direct participation in the dissolution reaction).

Generally, the morphology of mesopores (Fig. 5.1(a) and Fig. 5.4) is often dendritic. The pores branch quite often which can lead to fir tree images like in Fig. 5.4a). The main pores as well as the side pores always grow along  $\langle 100 \rangle$ -directions [127] (cf. Fig. 5.4). Under special conditions, the mesopores are built from a succession of octahedral cavities (Fig. 5.4b) which have tips pointing in the  $\langle 100 \rangle$  directions [51]. When an octahedron's tip breaks through (Fig. 5.5a) first an isotropic cavity forms. Due to the differing passivation for different crystallographic directions, this cavity becomes a (111) walled octahedron (Fig. 5.5b-d). With increasing oxidation power of the electrolyte passivation becomes less important and the octahedrons are "rounded out" and only smeared-out contours remain visible.

If the doping level and/or the applied voltage during bsi macropore growth are too high, the macropore walls are perforated by mesopores. Also if a macropore "dies", a mesopore can continue at its tip (Fig. 5.4a).

Mesopores have several applications:

- gas and biochemical sensors [128]

---

<sup>2</sup>When taking into account the residual water from the 48 wt% HF base solution, the composition is equivalent to 22 wt%  $H_2O$ , 20 wt% HF, and 58 wt% Eth

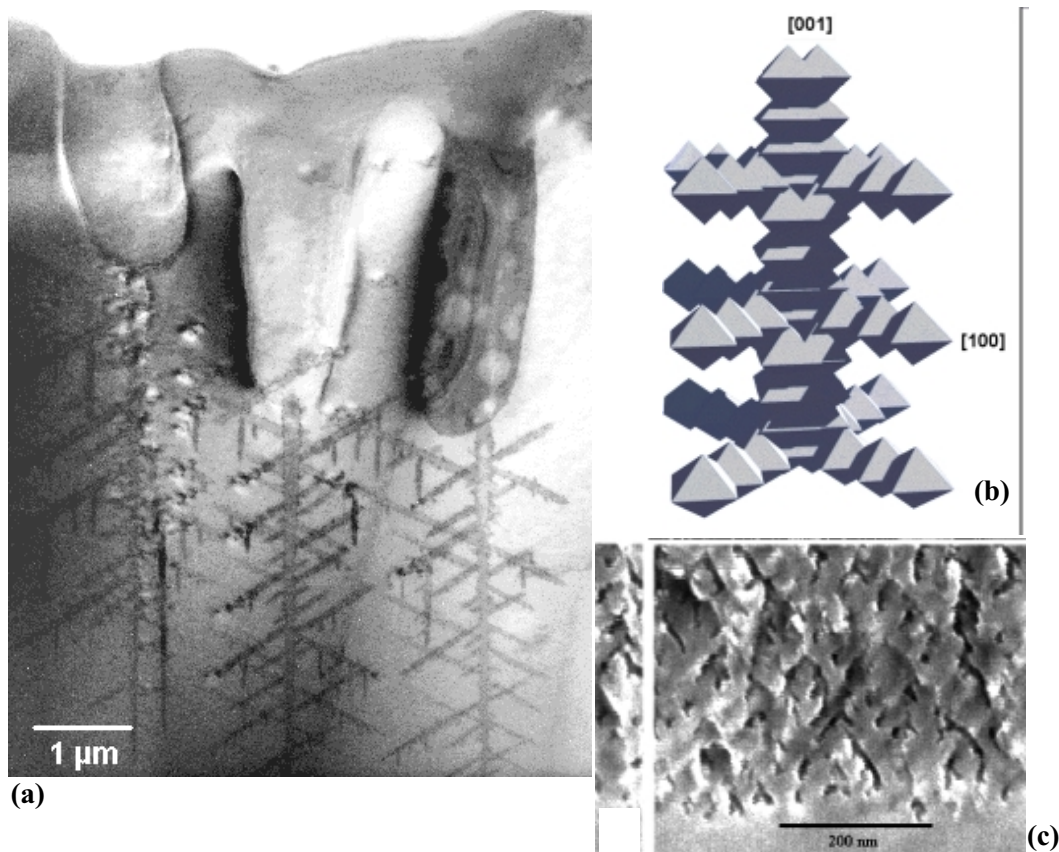


Figure 5.4: Mesopore growth: (a) Breakthrough pores grow at the end of macropores [126]. (b) Schematic sketch of octahedral growth of mesopores [5]. (c) Mesopore growth on (111) substrates [45].

- bragg and rugate mirrors by multilayers [129, 130]
- As a “zipper” layer during SOI production (ELTRAN process) [131]

Overall, mesopores show a “worse” morphology (serrated, branched) than macropores. On the other hand, growth speeds of up  $r = 20\mu\text{m}/\text{min}$  are possible. Also the production is much easier to accomplish, as it doesn’t involve illumination and the pores are not very sensitive to parameter fluctuations.

### 5.2.3 Influence of surfactants

Already early experiments showed that the high surface tension of water and the hydrophobicity of hydrogen-passivated silicon lead to inhomogeneous etching results for all kinds of pores in silicon. To circumvent problems with e.g. sticking hydrogen bubbles, besides ethanol (cf. section 5.2.2) small amounts of surfactants are added to the etching solution.

Ogata et al. [132] have investigated in detail the effect of several surfactants and the growth of meso- and micropores in  $p^+$ - respectively  $p$ -type silicon. They used polyoxyethylene octylphenyl ether (non-ionic surfactant, same molecule class like WAKO NCW601-A (cf. 2.13)), sodium dodecyl sulfate (SDS) (anionic, similar to Genapol LRO (cf. 2.13), but without

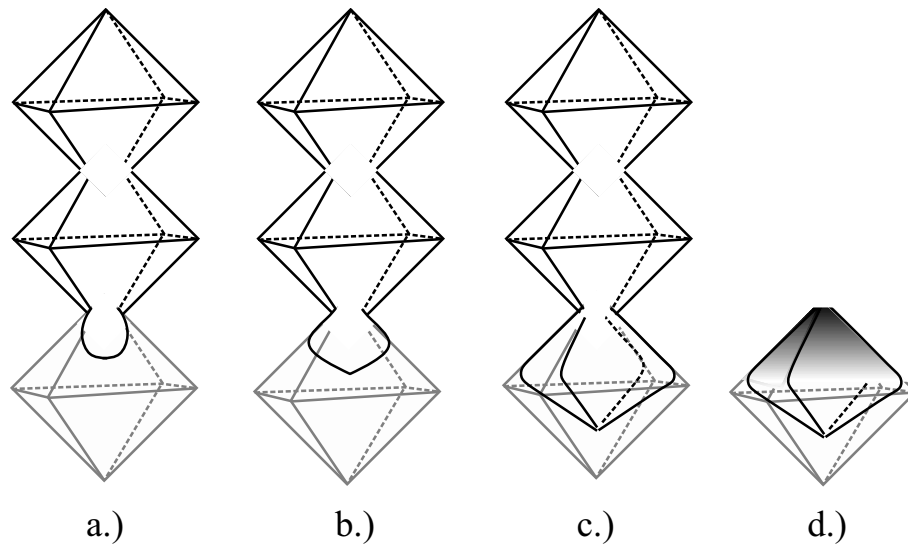


Figure 5.5: Octahedral growth of mesopores: The tip of the last octahedra breaks through (a) and grows (b-c). The walls which form out are determined by the degree of passivation (shown in (d) by grey scale) [51].

ethoxylate groups), and dodecyltrimethylammonium bromide (cationic, similar to Dodigen 226 (cf. Fig. 2.13), but without the phenyl ring chain). The highly doped samples showed only a weak reaction to the surfactants. For the low doped samples the capacity measurements and the IR absorbance measurements indicated that the anionic surfactant increased the band bending and led to an even better protection of the surface than without surfactant. The non-ionic and the cationic surfactant led to a smaller space charge region and a faster chemical dissolution of the pore walls. Surface oxidation was not detected in any IR measurements.

Chao et al. [112] grew macropores in p-type silicon with Triton X-100 (non-ionic surfactant, same molecule class like WAKO NCW601-A (cf. 2.13)), SDS (anionic, see above), and cetyltrimethylammonium chloride (CTAC) (cationic, similar to Dodigen 226 (cf. Fig. 2.13), but without the phenyl ring chain). Only the cationic surfactant resulted in straight macropores of high quality, where the growth rate was also slightly increased compared to a etching without surfactant. Other surfactants or no surfactant at all lead to thin pore walls and bent pores. Chao et al. suggest in a short discussion that probably the additional charges introduced by the ionic surfactant with the interface and/or the arriving and departing ions cause the opposing behavior of the surfactants.

Schweizer et al. [133] added SDS (anionic, see above), CTAB (cationic, similar to CTAC (see above), but the counter ion is bromide instead of chloride) and 8-methyl-1-nonanol propoxylate-block-ethoxylate (non-ionic,  $(\text{CH}_3)_2\text{CH}_2(\text{CH}_2)_5\text{CH}_2(\text{OC}_3\text{H}_6)_x(\text{OCH}_2\text{CH}_2)_y\text{OH}$ ) during macropore etching in n-type silicon with backside illumination. The cationic surfactant resulted in the worst pores showing heavy branching, followed by the non-ionic surfactant which exhibited unbranched but carrot-shaped pores. The anionic surfactant gave the best results with straight pores over a length of 200  $\mu\text{m}$ . The dark current which is partially a measure of the leakage current in the pore walls (also the pore tip will draw a significant portion of the dark current due to its curvature) replicated this behavior, i.e. with the anionic surfactant it was by far lowest followed by the non-ionic and the cationic surfactant. The authors correlate this with

the changes in band bending due to the additional charges brought into the interface region by the ionic surfactant. Several experiments to reproduce this behavior in p-type silicon similar to Chao et al. [112] however failed [134].

Several other authors (e.g. [135]) use the non-ionic surfactant NCW 601-A (cf. section 2.4.2, Wako chemicals Inc.) for macropore etching which is known from semiconductor manufacturing and MEMS etching [136]. Sarro et al. [136] measured that the etching rate and the anisotropy ratio of tetramethyl ammonium hydroxide (TMAH) as well as the surface roughness are decreased by slight additions of NCW-601 A. TMAH is an organic hydroxide containing etchant which essentially has similar properties like KOH, i.e. it etches silicon anisotropically ( $r_{100} \gg r_{111}$ ) without an oxidizing component, i.e. it directly dissolves silicon. Jeon et al. [137] have investigated the wetting behavior of various polyethylene oxide based nonionic surfactants in combination with alkaline etchants. Their investigations comprised surfactants containing an alkyl phenoxy group as well as those with only an alkyl group without aromatic ring. They have measured the critical micelle concentration (cf. section 2.4.2) to be between  $c = 50$  ppm and  $c = 400$  ppm. It showed that the wetting behavior depends on whether the alkyl chain is linear or branched and how long the hydrophobic alkyl chain as well as how long the hydrophilic ethylene-oxide arm is. The best wetting abilities showed the group of phenolated surfactants with branched alkyl chains.

### 5.3 Pores in InP

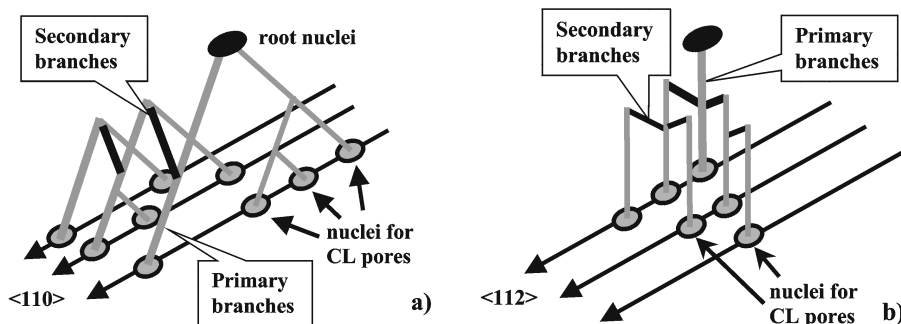


Figure 5.6: Schematic representation of the nucleation layer in (111) (a) and (100) (b) InP [95].

Several authors have reported pores in n-type InP after anodization in various acids [138–140], e.g. HCl, H<sub>2</sub>SO<sub>4</sub>, or HF. Unlike silicon the oxides formed from InP can be dissolved in nearly all acids, which relaxes the choice of acid. Due to the bad diffusion length in commercially available InP, bsi techniques like in Si (cf. section 5.2.1) hardly work, therefore in most experiments holes are supplied via electrical breakdown, i.e. in the context of the present work they are regarded as mesopores. Also different to in silicon, InP is a compound semiconductor, which results in different etch rates for the <111A> and <111B> directions<sup>3</sup> in most etching solutions ( $r_{100} > r_{111B} > r_{111A}$ ) [141]. Two types of pores are encountered in InP [95]:

- Crysto pores: growth along <111B> directions, triangular cross section

<sup>3</sup>For details on the A/B-notation, cf. e.g. [95].

- Curro pores: growth along electrical field lines, i.e. along the direction of current, round cross section, tendency to order in a close-packed hexagonal lattice

Both types grow with high growth speeds of up to several 10  $\mu\text{m}/\text{min}$ . On a fresh surface or after a pause in the etching, always at first, cristo pores grow. When the current density exceeds a critical value (above 10  $\text{mA}/\text{cm}^2$ ), the pore walls cannot be fully passivated anymore and the system tries to reduce the current density at each pore tip by branching in all available  $\langle 111\text{B} \rangle$  - directions (Fig. 5.6), also upwards. This increases the pore density with etching time until branching becomes unfavorable because the pore density is too high. Then the pores switch into current-line oriented growth where the major passivating force for the walls is the overlap of the SCR.

The thickness of the cristo layer decides upon the ordering of the curro layer [142]. During potentiostatic anodization, the thickness of the cristo layer decreasing monotonically with applied potential. Using an optimal voltage, a monocrystalline self-ordered pore lattice can be obtained.

During the pore growth in InP heavy electrical as well as diameter oscillations can be found [95], which can be accurately modelled by the CBM (cf. section 4.6.2).

## 5.4 Pore growth in the current burst model (CBM)

In section 4.6.2 the basic principle underlying the current burst model (CBM) were sketched: The current flow is not homogeneous in time and space, but consists of individual current bursts (CBs) on a nm scale. Generally an agglomeration of synchronized CBs is called a “domain” in reference to the term introduced by Chazalviel and Ozanam [81]. Such a domain will lead to a depression of the surface, because spots, where CBs have been active have a worse passivation and are therefore more prone to new CBs. After some time the depression will elongate and become a pore. Under ideal conditions, the system becomes separated in active surfaces (the pore tips) and inert areas (the pore walls and the surface areas between pores). Inertness of a Si surface is mainly achieved via two ways:

- depletion of carriers to promote a reaction, e.g. overlapping space charge regions between pores
- hydrogen passivation

The morphology of the pores depends heavily on the weighting of the individual parts of a current burst cycle (CBC) [51, 95]:

- Dominance of oxidative reactions leads to smoother and bigger pores. Crystallographical preferences can be suppressed to a certain degree.
- Strong passivation and direct dissolution yields highly directional pores with sharp contours (in extreme cases dendritic pores result). The pore growth is much faster if oxidation is less pronounced.

Unlike the electropolishing regime (where always an oxide coverage is present and the dissolution happens almost exclusively via oxide formation and dissolution), the averaged valence during pore growth lies between 1 and 4, i.e. direct dissolution has to be taken into account. The question which process is more dominant is ruled by the following properties of electrolyte and substrate:

- ratio between supply and consumption capability of holes (“relative lack of holes”), which is a complex function of the used chemistry, doping, and applied voltage/current density
- oxidizing power of the electrolyte (oxide forming capabilities)
- oxide dissolving capabilities of electrolyte
- surface passivation capabilities of the electrolyte

Continuous and stable growth of pores necessitates that all parts of the system are on average in a steady state (otherwise the morphology would change all the time). The oxidative parts of the current follow the continuity equation (Eq. 4.13) for the average oxide thickness. For steady state conditions,  $ds/dt = 0$ , i.e.  $\beta \overline{J_{ox}} = \overline{\alpha}$ .

## 5.5 Impedance analysis of pore growth

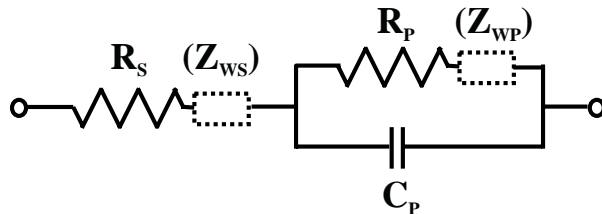


Figure 5.7: Typical equivalent circuit for the impedance analysis of pores:  $R_P$ : Parallel resistance,  $R_S$ : Serial resistance,  $Z_{WS,P}$ : Warburg impedance (element for diffusion processes),  $C_P$ : Parallel capacitance.

An *in-situ* control of pore growth is for most set-ups limited to watching the evolution of voltage in a galvanostatic experiment (or alternatively the current during a potentiostatic experiment). Similar to standard electrochemistry on non-porous electrodes, this only offers limited insight into the interface behavior. A powerful tool in standard electrochemistry to learn more about the system is FFT impedance spectroscopy: a small, multifrequent AC signal is superimposed to e.g. the current of a galvanostatic experiment and the resulting response in the voltage is recorded. For a stationary system and applying small perturbation signals the response can be analyzed by linear response theory. The semiconductor-electrolyte interface can often be described by (fairly simple) equivalent electric circuits [143]. Changes in the values of the individual constituents of this equivalent circuit can then be attributed to changes in e.g. a specific electrochemical interface reaction. Fig. 5.7 (see below for further information on the individual components of the circuit) shows one of the standard equivalent circuits used for modelling.

The same technique can be used during pore growth [144]. The components of the equivalent circuit in Fig. 5.7 can then be attributed as follows:

- $R_S$  (serial resistance): Quantifies the ohmic resistance through the electrolyte inside and the outside pores as well as the resistances of the substrate and the backside contact. Under normal condition (substrate and contact resistivity low) this parameter can show nicely the constantly growing length of the pores.



- $C_P$  (parallel capacitance): Denotes the capacity of the interfacial oxide layer, the Helmholtz layer, and the space charge region. As soon as an insulating oxide layer is present, it will dominate the capacitance.
- $R_P$  (parallel resistance): Summarizes the resistance for chemical processes (transfer resistance) at the interface.
- $Z_W$  (Warburg impedances): Addresses diffusion related processes during the transport of reactants to and away from the reaction site.



# Chapter 6

## Experimental set-up and sample analysis

### 6.1 Anodization set-ups and sample preparation

#### 6.1.1 General notes on electrochemical anodization procedures

In the simplest fashion, an electrochemical experiment only needs a few ingredients :

- a sample = the working electrode (WE)
- a counter electrode (CE) made best out of a non-corroding material like Pt
- a battery or power source
- a voltmeter and amperemeter

As mentioned in section 2.3 each electrode has its own electrochemical standard potential  $E_{redox}^0$ . Therefore each couple of a specific working and counter electrode has its own built-in potential difference. To decouple the electrodes into two independent half-cells, a third, currentless electrode - the reference electrode (RE) - is used. It is designed in a way that its potential neither shifts during the measurements, e.g. due to uncontrolled gas evolution, changes in the surface area etc., nor between measurements (as long as it is stored correctly). All potentials in a specific electrochemical experiment are then measured “versus” the chosen reference electrode (e.g.  $U_{vsNHE} = 1.7$  V), which allows for setting e.g. the WE onto a defined potential versus the electrolyte. In sufficiently conducting electrolytes the exact position of the RE in the electrolyte is only of minor importance.

A prominent reference electrodes is the NHE (Normal Hydrogen Electrode), which is a blackened Pt wire in a solution with an 1 M  $H^+$  activity where the wire is constantly rinsed with hydrogen gas with a pressure of 101.3 kPa [145]. In practice, however, easier-to-handle reference electrodes like the  $Ag^+/AgCl$  ( $U_{NHE} \approx 200$  mV) are employed, which have a constant offset to NHE. When knowing this offset, the values for different reference electrodes can be converted into each other. In the  $Ag/AgCl$  electrode a silver wire is immersed in a saturated KCl solution (Fig. 6.1). In commercially available RE, the connection to the electrolyte to be probed is often through a glass membrane at the tip of the electrode and the electrode itself is made out of glass. Because glass is not inert in HF, it was necessary to build a HF resistant reference electrode out of poly-ethylene (PE)(Fig. 6.1 shows a schematic sketch of the silver

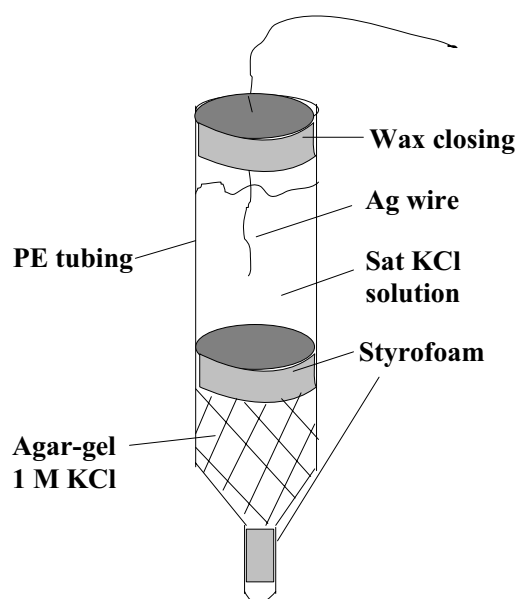


Figure 6.1: HF resistant Ag/AgCl reference electrode. Unlike commercially available RE, the electrode is in a PE tubing and the membranes are made of styrofoam.

reference electrode used in the experiments on porous silica (chapter 8)). The ionic connection between the saturated KCl solution and the electrolyte was done by an agar-agar gel 1M KCl salt bridge.

Problems with the position of the RE arise if badly conducting electrolytes are used. Then the ohmic losses in the electrolyte call for a short distance between the RE and the sample. In this case (cf. experiments in MeCN (section 7.3)), a Pt wire was put at 1-3 mm distance of the sample surface. With this it is possible to get closer to the surface with same or less shadowing of the sample by the RE than with a conventional RE. In any case the RE should only be put as close to the sample as it doesn't adulterate current and electrolyte flow. The trade-off of a simple Pt wire is that its potential is not exactly fixed, which makes very precise measurements of the potential impossible. But in electrolytes where the potential drop within a few mm is already in the order of volts, a 10-100 mV shift due to a not exactly defined reference potential represents only a pretended disadvantage.

When a reference electrode is introduced into the simple set-up of p. 63, a potentiostat instead of a battery or power source becomes necessary if the applied voltage between counter and working electrode shall be controlled by the potential at the RE. The potentiostat monitors the voltage difference between RE and WE and regulates the voltage between the CE and WE accordingly. Internally this is done by operational amplifiers (OP) which translate a difference between desired and actual RE voltage into the necessary change in CE versus WE voltage. In case of metal electrodes three electrodes at the potentiostat (Fig. 6.2a) are enough. If a semiconductor has to be contacted, a four electrode set-up (Fig. 6.2b) with a sense electrode for the semiconductor potential can avoid problems due to imperfect ohmic contacts. The reference voltage which controls the applied voltage is then taken between sense and reference electrode.

In the present work, mainly three different measurement modes were used:

- galvanostatic, i.e. the current density  $j$  through the sample is kept constant, the potential

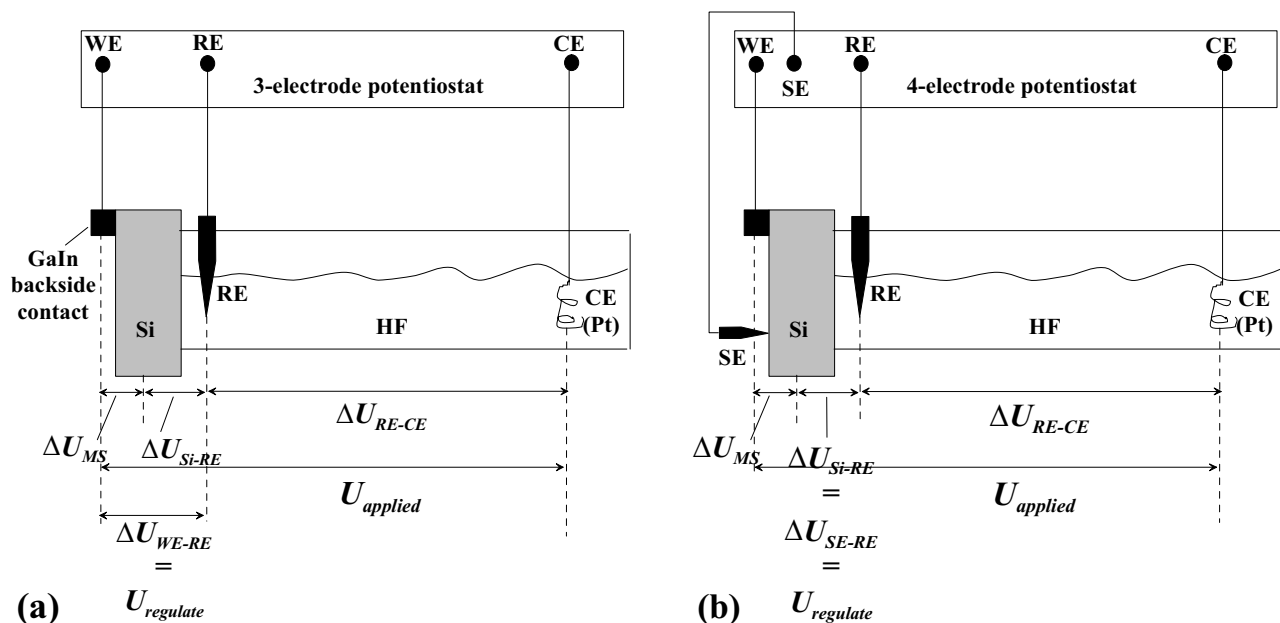


Figure 6.2: In the case of a three electrode potentiostat (a) the potential difference between working (WE) and reference electrode (RE) controls the applied voltage between counter electrode (CE) and WE. The voltage  $\Delta U_{Si-RE}$  available for electrochemical reactions at the interface may be significantly lower than  $U_{WE-RE}$ , if the metal-semiconductor backside contact causes substantial losses  $U_{MS}$ . This is compensated with a (currentless) sense electrode (SE) using a four-electrode potentiostat (b).

$U$  between SE and RE (4 electrodes) respectively WE and RE (3 electrodes) is regulated accordingly and monitored.

- potentiostatic, i.e.  $U$  is kept constant and  $j$  is measured.
- potentiodynamic, i.e.  $U$  is ramped at a constant speed (e.g. 50 mV/s) and  $j$  is measured.

In a simple view, one can say that the only aspect which is changed is the applied voltage between CE and WE, the question is the choice of control variable.

### 6.1.2 Peristaltic pump set-up

Fig. 6.3 shows the experimental setup from ET&TE GmbH, Kiel [146] used in the experiments on porous silicon. All components are controlled by a Windows98 personal computer (Pentium PIII, 800 MHz) running the Delphi based SiPor-Software developed by Dr. Carstensen [147].

The electrochemical cell (Fig. 6.4) is connected to a 250 ml electrolyte reservoir via a circulation which is driven by a peristaltic pump (Ismatec Inc., model ‘MCP’). The reservoir as well as the etching cell are machined out of Teflon which has been the only material to withstand all used combinations of organic electrolytes and acids. The tubings (Norton Inc./Saint-Gobain Verneret, model ‘Ismaprene’/‘PharMed’) have shown to offer the best compromise between mechanical and chemical stability. The heating/cooling water circuit which runs through the walls of the container is completely isolated from the electrolyte circulation. The heater/cooler (Julabo, model ‘F25’) is controlled by the central personal computer which evaluates the electrolyte

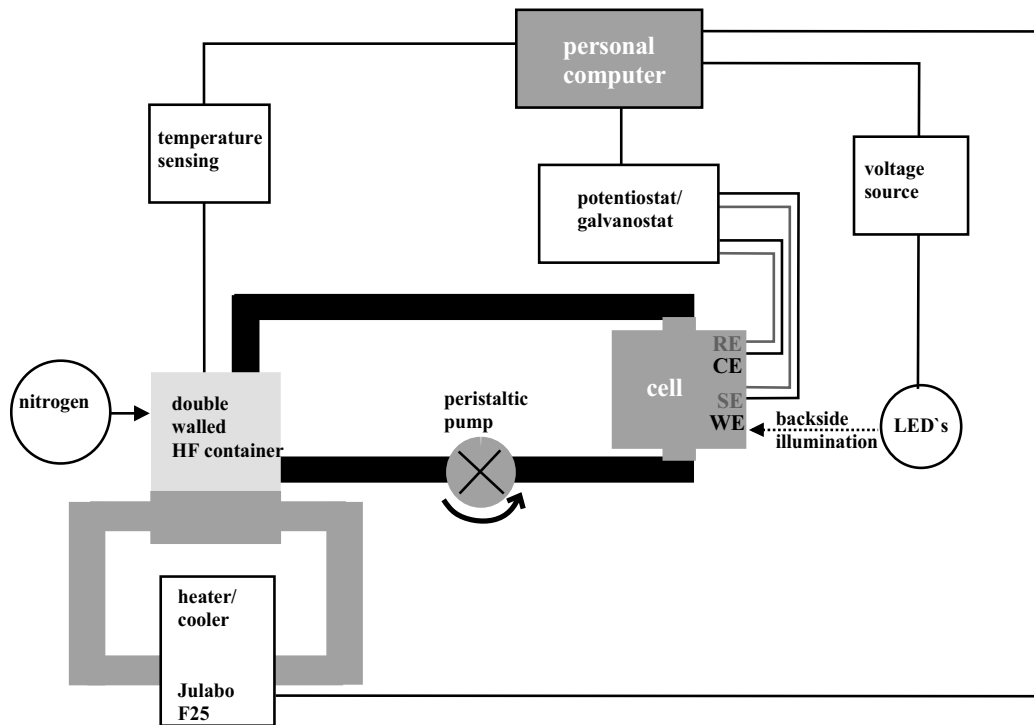


Figure 6.3: Electrochemical etching set-up with peristaltic pump.

temperature from a teflon-coated Pt100-probe in the electrolyte container with a precision of  $0.1^\circ\text{C}$ . To avoid oxygenation or hydration, organic electrolytes are constantly bubbled with nitrogen (The pressure was regulated by a pressure reducer to approx. 1 bar so that a decent bubbling was visible).

For backside illumination experiments a  $5 \times 5$  array of high-intensity NIR LEDs (Osram, model ‘SFH487P’,  $\lambda = 880\text{nm}$ ) is stacked onto the cell. The illumination intensity of LEDs is generally linearly correlated to the current applied to the LEDs [148] over a wide range. The illumination controller is designed so that the input voltage  $U_{illum}$  is linearly related to the output current, i.e.  $U_{illum}$  is directly proportional to the light intensity and therefore to the number of generated carriers in the semiconductor. The control is either possible via a direct hardware feedback within the potentiostat/galvanostat or via the SiPor software.

Most experiments were carried out with the four-electrode (cf. section 6.1.1) potentiostat/galvanostat (ET&TE, model ‘Elypor3-SL’) built by Prof. Dr. Popkirov [146]. It can supply currents up to  $I = 1\text{ A}$  and voltages up to  $U = 120\text{ V}$ , whereby a variable measurement range allows also to accurately measure much lower currents and voltages.

The electrochemical cell (Fig. 6.4) uses the optical micro bank system of Spindler & Hoyer, i.e. all components are mounted on 4 stainless steel rods. The whole ensemble is stuck into a base plate to mount the sample, which is pressed by a PMMA window (to allow for backside illumination) against a viton o-ring (etching area  $A = 1\text{ cm}^2$ ). For the experiment the cell is turned upside down (compared to Fig. 6.4) so that the sample is at the bottom. The electrolyte is then pumped into the low-lying connection stub. Inside, the electrolyte is conducted in a way that allows for a homogeneous flushing of the inner cylindrical volume where the electrodes are. The electrolyte is flowing out of the cell through the high-lying connection stub so that a

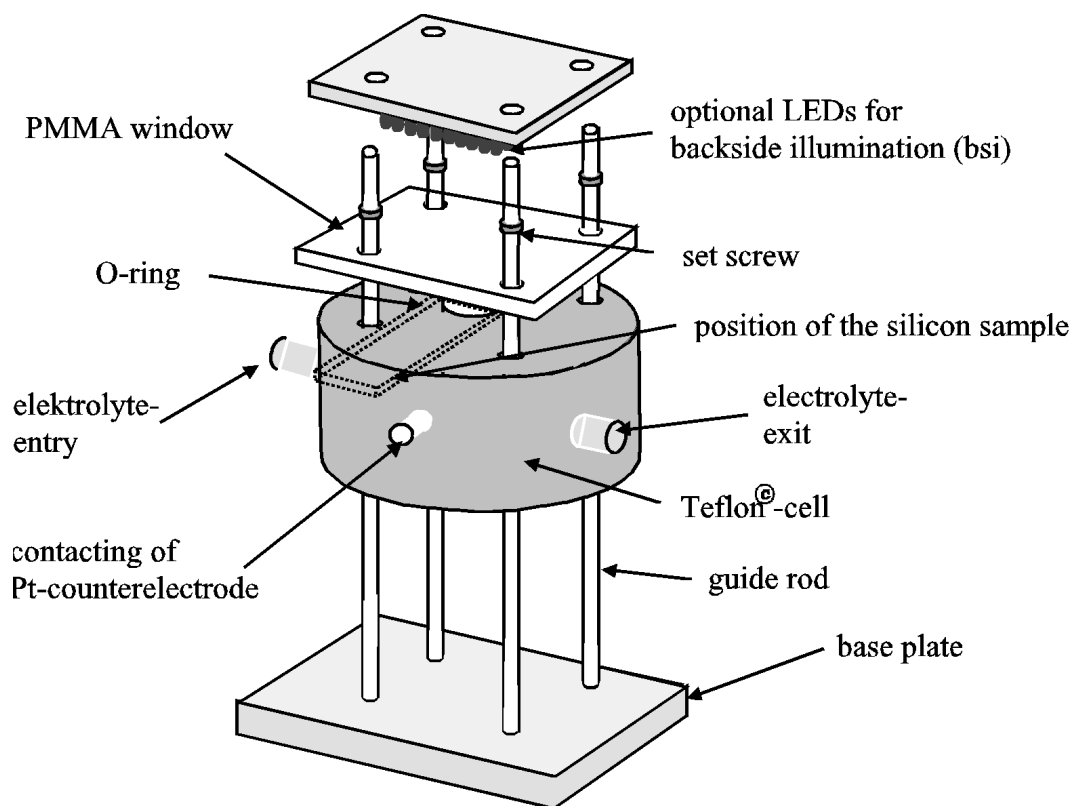


Figure 6.4: Schematic drawing of the etching cell used in the peristaltic pump setup (LEDs optional). After the sample is built in, the cell is rotated 180° for the experiment.

filling of the cell is always guaranteed. The counter and reference electrodes are both Pt wires which end on banana bushings which are screwed on the outside of the cell. The sense and working contact are clamped with crocodile clamps to the sticking out end of the sample.

The samples were cut from commercially available n-type silicon wafers (mostly 4 and 6" from MEMC and Wacker Siltronic; the doping level and orientation is given in the experimental results section) into 5 cm x 2 cm rectangles. The wafers were dipped for 1 minute in 10 % aq. HF to dissolve any native oxide. One corner of the backside was scratched with a diamond cutter and a drop of GaIn eutecticum (Aesar Inc.) was rubbed in with the tip of tweezers to form an ohmic backside contact. This corner was then used as working contact while the other one was clamped with the sense electrode. If the contact showed a Schottky-like behavior during the experiments<sup>1</sup>, a new sample was prepared.

For the experiments on fast pores (chapter 7.3) the electrolytes were prepared from 71-75 wt% HF (p.a., Fluka Inc., Nr. 47610) to minimize the water content from the HF solution, while the rest of the experiments were based on 48 %wt HF (p.a., Merck Inc., Nr. 1.00334.5000). The organic electrolytes (DMF, MeCN) were all p.a. grade from Merck Inc. The water used, was deionized to a conductivity of  $\sigma = 0.1 \mu S/cm$ . TBAP (purum, Fluka Inc., Nr. 86885) was added in some experiments. In case of organic electrolytes, the solution was filled as quickly as possible into the nitrogen bubbled container and the nitrogen bubbling was running until the disposal of the electrolyte. These electrolytes were furthermore replaced every day or every

<sup>1</sup>On n-type the metal-semiconductor junction is switched in reverse when an anodic bias is applied, and in the case of a Schottky-like contact only a much lower current than with an ohmic contact will flow.

two days (then  $N_2$  bubbling was left running overnight). It is clear that such a procedure is not comparable to the care taken using an inert gas glove box like e.g. in [48], but it avoids already most of the oxidation of the electrolyte in ambient atmosphere while it allows for production-friendly handling times.

### 6.1.3 Rotating disk electrode (RDE)

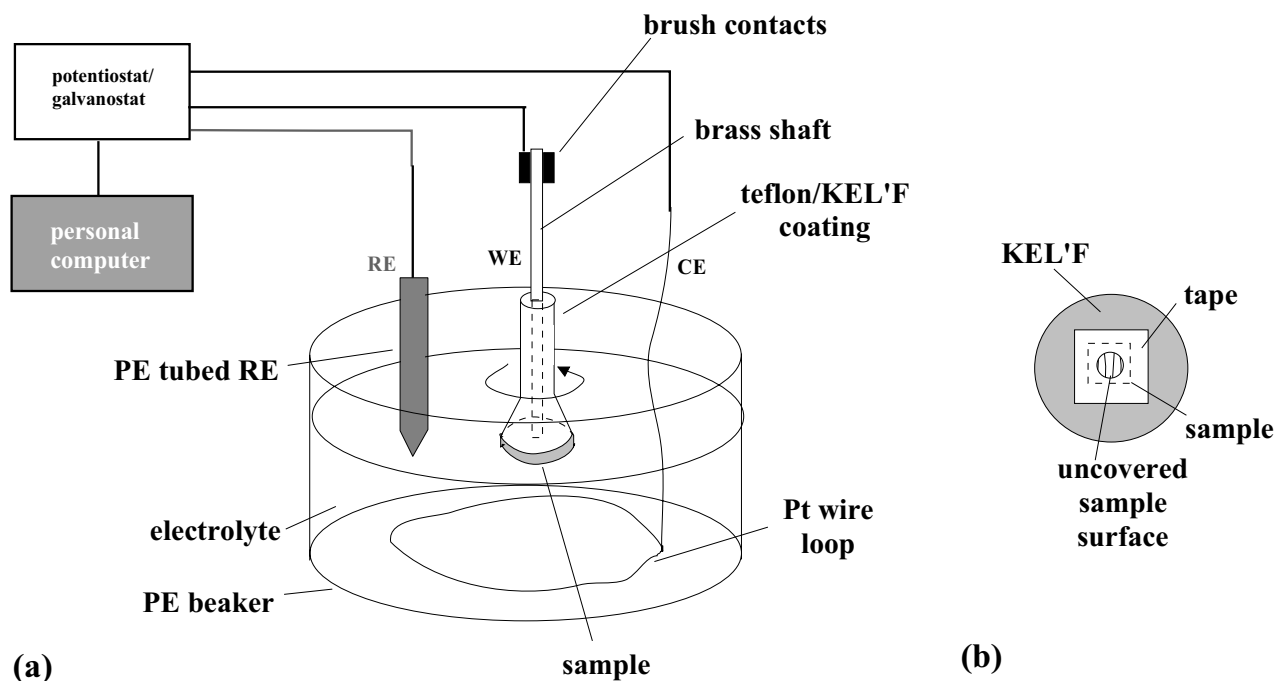


Figure 6.5: (a) Rotating disk electrode (RDE) set-up. (b) Bottom view of RDE with sample.

For the experiments on porous silica a 3-electrode rotating disk electrode (RDE) system (Fig. 6.5) from EG&G (model 636) was used. The electrical contact to the rotating electrode is realized with brush contacts which are attached to the brass core of the RDE. In the lower third the electrode is covered with Teflon respectively KEL'F (a mechanically more stable variant of Teflon which shows similar chemical inertness) to isolate the electrode from the electrolyte. At the tip of the RDE a punched<sup>2</sup> KEL'F disk with the sample (Fig. 6.5b) is mounted. The sample itself is attached to the disk by a chemically resistive tape (Struers Inc., model 'TENKI') which only leaves a defined circular area on the sample surface open (etching area  $A = 0.14 \text{ cm}^2$  respectively  $A = 0.04 \text{ cm}^2$ ). After initial problems due to bubble formation and sticking at this circular opening a small, triangular cut was added after the punching of the tape to allow for the bubbles to detach easier. It has shown that this way of mounting works in minutes without substantial inhomogeneity drawbacks [77], while the traditional RDE sample preparation (grinding of sample to circular shape and countersinking in the electrode to form a perfect planar surface) takes sometimes more than an hour.

The experiments were carried out in a 100 ml plastic beaker with a Pt wire loop at the bottom as counter electrode (CE). The Ag/AgCl reference electrode (RE) had to be custom-

<sup>2</sup>It is punched so that a spring mounted bolt can contact the sample backside.



built (cf. section 6.1.1) to be able to withstand HF. The potentiostat/galvanostat is custom-built by Prof. Chazalviel and Dr. Ozanam, Palaiseau [77] and can supply up to  $U = 100$  V and  $I = 60$  mA.

The electrolytes were mixed using millipore ultra-pure water,  $\text{NH}_4\text{F}$  salt and  $\text{NH}_3$  (25 wt%, p.a. grade, Merck Inc.). The pH was tested with pH indicator sticks (0.5 scale steps, Merck Inc.) after preparation of the solution as well as after each 4 experiments. At the latest when the pH dropped more than 0.5 the solution was replaced.

All experiments were carried out using commercially available p-type silicon wafers ((111) and (100) oriented,  $\rho = 1 - 15\Omega\text{cm}$  unless otherwise indicated). To ensure a well working ohmic backside contact, an Au/Al (99:1) alloy was evaporated onto the backside. The wafers were therefore first cleaned in a sulfochromic glass ware cleaning mixture for 30 min at RT. After heavy rinsing under DI water the wafer is dipped in a 10% HF solution. When all surface showed hydrophobic behavior (i.e. no wetting) the silicon was built into the evaporation chamber. After sufficient evacuation the sample was heated on a special holder to 600 °C. Then the heater was switched off and evaporation was done in 4 steps. At each 100°C downcooling a 100 nm layer was deposited. The high temperature at the beginning allowed for the formation of a silicide, while the afterwards deposited alloy layers form a metallic contact to the silicide for outside contacting. The ohmic contact was always tested with IV-curves before other experiments. Although this is no explicit testing of the contacts by a classical 4 point probe, the IV-curves showed no ohmic limiting due to a bad contact.

For the experiments the samples were cut in 7 mm x 7 mm squares with a diamond cutter and attached to the KEL'F disk by adhesive tape (cf. p. 68). After the experiment the KEL'F disk with the sample was flipped off the RDE immediately and immersed in DI water. After stripping off the tape, the sample was again rinsed several times in DI water to ensure full removal of the electrolyte.

### Theoretical notes on RDE systems

The RDE is a forced convective system, i.e. it reaches faster steady state and offers higher rates of mass transfer [23]. In essence, the whole system is correctly described by the Nernst-Planck equation (2.20) as long as mass transfer limits the current. For the analytical treatment of rotating disk electrodes the second term of Eq. 2.20 is mostly neglected [23] as it shall also be done in the following<sup>3</sup>. Together with Fick's first law Eq. 2.20 can be transformed into the temporal derivation of the concentration  $C_j$  of the species  $j$

$$\frac{\partial C_j}{\partial t} = D_j(\vec{\nabla})^2 C_j - \vec{v} \vec{\nabla} C_j. \quad (6.1)$$

To solve Eq. 6.1, it becomes necessary to link the electrolyte convection velocity profile  $\vec{v}(x, y, z)$  to external parameters like the rotation rate of the disk. Essentially, the disk drags the electrolyte along during its rotation. Centrifugal forces drive the liquid radially outwards from the center of the disk. Consequently a stream normal to the disk sets in (Fig. 6.6a). Rigorous mathematical treatment [23] leads to the radial and normal components of the fluid

---

<sup>3</sup>Strictly speaking the migration term in 2.20 can only be neglected if the solution contains a supporting electrolyte, i.e. ions are added which do not participate in the electrode reactions but which carry most of the current in the bulk electrolyte where diffusion and convection become negligible

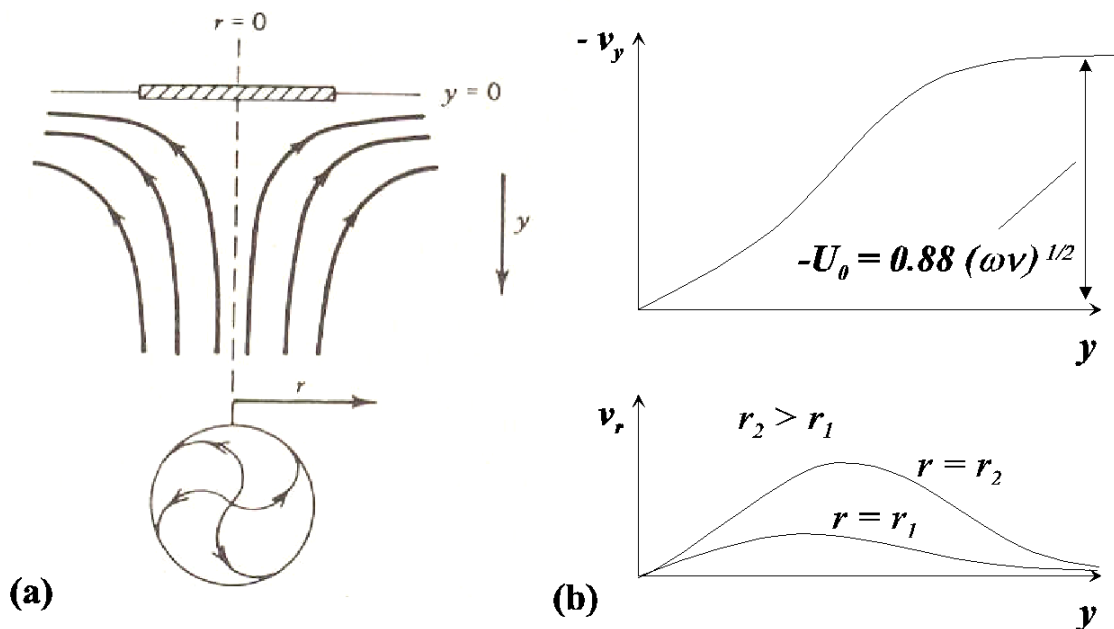


Figure 6.6: Rotating disk electrode (RDE): (a) Schematic stream lines. (b) Radial and normal fluid velocities near the disk versus distance  $y$  to the disk surface ( $U_0$  is the velocity normal to the disk far away from the surface).

velocity versus the distance  $y$  to the disk surface (Fig. 6.6b)<sup>4</sup>:

$$v_r = r\omega\left(a\gamma - \frac{\gamma^2}{2} - \frac{1}{3}b\gamma^3 + \dots\right) \quad (6.2)$$

$$v_y = (\omega\nu)^{1/2}\left(a\gamma^2 - \frac{\gamma^3}{3} - \frac{1}{6}b\gamma^4 + \dots\right) \quad (6.3)$$

$$\text{with } \gamma = \left(\frac{\omega}{\nu}\right)^{(1/2)}y, \quad a = 0.51023, \quad b = -0.6159 \quad (6.4)$$

( $\nu$ : kinematic viscosity,  $\omega$ : disk angular velocity)

The so-called hydrodynamic boundary layer thickness  $y_h = 3.6\sqrt{\nu/\omega}$  classifies to which depth the fluid is dragged along (For standard conditions ( $\nu = 0.01\text{cm}^2/\text{s}$ ,  $\omega = 100\text{ s}^{-1}$  ( $\approx$  rotation rate = 1000 r.p.m.)):  $y_h \approx 360\mu\text{m}$ ). With the velocity functions Eq.(6.1) can be solved which leads to the Levich equation for the totally mass-transfer limited current  $I_l$  (c.f. Eq.(2.21) for pure diffusion controlled systems and explanation of variables):

$$I_l = 0.62nFAD_0^{2/3}\omega^{1/2}\nu^{-1/6}C_0^* \quad (6.5)$$

While the current transient of a planar electrode in an unstirred electrolyte decays in the extreme to values near zero (when the diffusion layer thickness becomes very large), the diffusion layer thickness in convective systems is fixed to

$$\delta_0 = 1.61D_0^{1/3}\omega^{-1/2}\nu^{-1/6} \quad (6.6)$$

<sup>4</sup>The circular velocity  $v_\Phi$  can be calculated similarly but is not of prime importance for most electrochemical experiments.

For standard conditions (see above),  $\delta_0 \approx 20\mu\text{m}$ . With  $m_0 = D_0/\delta_0$  Eq.(6.5) can be translated into Eq.(2.21). The current after a potential step (or similar disturbances of the system) decays under standard RDE conditions (see above) within 200 ms to a 1 % range around its constant value  $I_l$ . I.e. the electrode is always in a steady-state on a second scale.

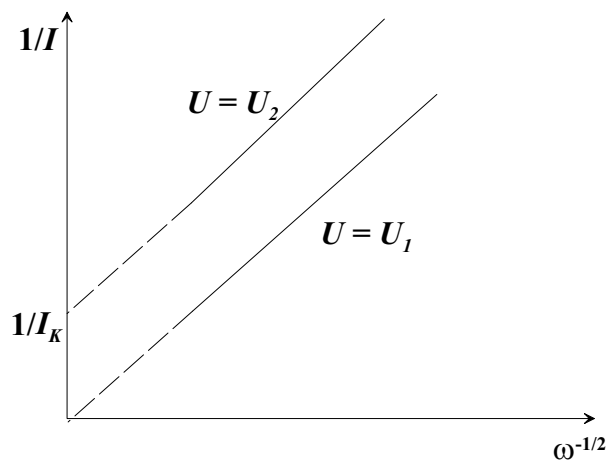


Figure 6.7: Kinetic limitation at the RDE: While at  $U = U_1$  the straight line can be extrapolated to the origin, i.e. no kinetic limitations occur, at  $U = U_2$  kinetic processes at the electrode become limiting and the  $1/I$  line is offset by  $1/I_K$  [23].

Under pure diffusional limitation the current is directly proportional to  $\sqrt{\omega}$  (voltage  $U_1$  in Fig. 6.7). When kinetical limitations also occur, the current follows the Koutecky-Levich law (voltage  $U_2$  in Fig. 6.7):

$$\frac{1}{I} = \frac{1}{I_k} + \frac{1}{I_l} \quad (6.7)$$

Only the second term is dependent on  $\omega$  and this is why a kinetic limitation only causes a shift in Fig. 6.7.

## 6.2 Sample analysis

In most cases, the samples were first investigated with an optical microscope (Leitz Inc., model ‘Ergolux 200’). The resolution of a microscope is given by Abbe’s formula [149]. In case of optical microscopes, a resolution better than  $1\mu\text{m}$  is hardly achievable. Optical microscopy could therefore only be used for first overviews, while detailed investigations called for an electron microscope.

### 6.2.1 Scanning electron microscope (SEM)

One of the most useful tools for analyzing the morphology of porous samples is the scanning electron microscope (SEM). During operation a beam of electrons is scanned across the sample. The electrons interact with the specimen and produce radiation, kick electrons out of the material or the so-called primary electrons from the incident beam are simply scattered elastically. An appropriate detector then detects the “reaction” of the sample when the incident beam impinges on a certain spot. Afterwards the beam moves on and excites an adjacent area of the

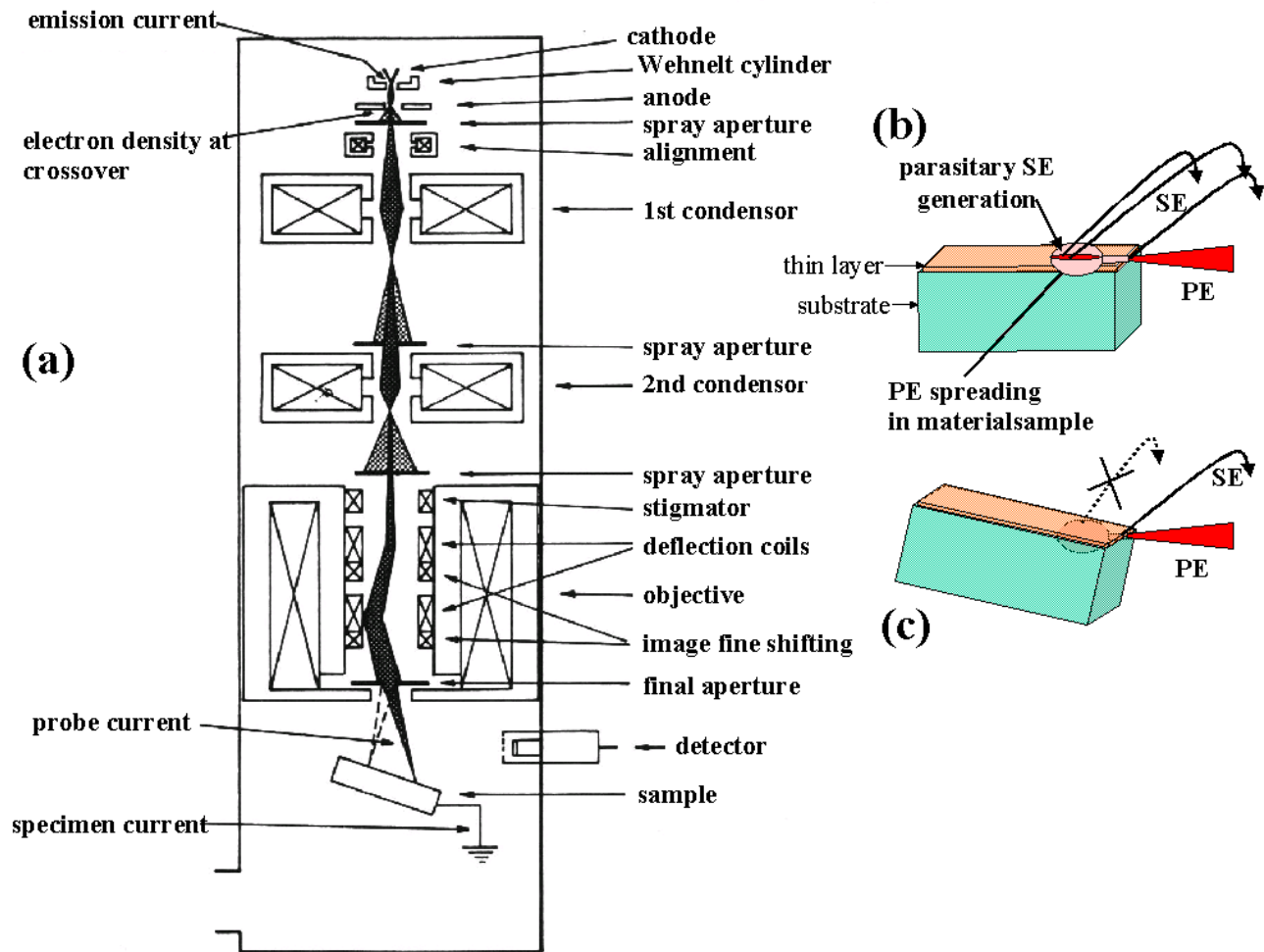


Figure 6.8: (a) Schematic cross section of a scanning electron microscope (SEM). (b)-(c) Imaging of cross section without (b) and with (c) tilting of the sample.

sample. The whole sample area of interest is "rastered" in such a manner and an "image" of the sample can be generated by linking detector signal and beam position. It has to be made clear that this "image" is not automatically a topographical or an optical image of the sample, but of course only depicts the ability of the sample to produce a certain excitation type; e.g. when the sample consists of two materials which have a largely different secondary electron yield the main information which will be seen on the later image is not the topography or morphology of the sample but the transitions from one material to the other [150].

Fig. 6.8 a) shows the principle set-up of a SEM: The electrons are generated in the electron gun. This is in most cases a heated tungsten filament, a truncated pyramidal  $\text{LaB}_6$  crystal or a sharp wolfram tip where the electrons are extracted by the application of a high field (field-emission cathode). The electrons are accelerated by 1-30 kV towards the anode where they enter the electromagnetic lens system through a hole in the anode. Around the electron gun is the so-called Wehnelt cylinder, a slightly negatively biased metal cap which helps to shape the emission pattern. The electromagnetic lenses are quadrupol lenses which deviate the beam by applying Lorentzian forces on the electrons. In the condensor lens the working distance between last aperture and sample and hence the numerical aperture of the system is regulated.

The stigmator lenses correct elliptical beam deformations which are mostly due to carbon contaminations on the aperture holes. Finally, the beam is narrowed by a metal aperture of variable diameter. This further reduces the spot diameter and excludes the outermost beam portions which are mainly responsible for aberrations. When the electron beam hits the sample, the primary electrons are either scattered elastically or inelastically multiple times within the sample (for samples thicker than some  $\mu\text{m}$ ). During inelastic scattering, new particles or quasiparticles can be generated and detected. Overall the most important secondary effects for SEM detection are:

- a) Secondary electrons (SE)
- b) Backscattered electrons (BSE)
- c) Relaxation of excited atoms

SE (**a**) are electrons which originate from the sampled material itself. The energies which are transferred to them are generally well below 50 eV. Although there are some backscattered primary electrons (PE) (**b**) with such low energies after multiple scattering, most of the electrons in this regime come from the sampled material itself. SE with their low energy originate from excitations at or just below the surface, i.e. SE generally yields good topographical images. BSE (**b**) are PE which re-escape the sample after several scattering events. Their energies are several hundred eV to keV, therefore also BSE which have been scattered in greater depth are detected. The images give more information on volume properties and composition of the sample than surface information. By detecting the energy or wavelength of x-rays (**c**) which are emitted by relaxing atoms the chemical composition of the sample can be analyzed. The detection of Auger electrons falls into the same category.

All images in the present work have been made with SE detection, hence only their detection will be discussed: Because of their low energy the SE are easily influenced by electrostatic fields. The so-called Everhart-Thornly detector uses a positively charged grid to attract the SE. Inside the detector the electrons hit a scintillator crystal whose light output is amplified by a photo multiplier.

Of course, some of the PE are absorbed within the material, i.e. the investigated material becomes charged. Good conducting samples (also medium to highly doped semiconductors) can easily lead off this charge. Isolating or badly conducting samples are sputtered beforehand with a thin Au or Au/Pd layer of around 10 nm to prevent charging. Au also has a very high SE yield, i.e. enhances the signal-to-noise ratio. On the other hand at structure sizes in the vicinity of 10 nm, it becomes unclear whether the fine structure originates from the coating or the underlying material.

For cross sectional images of layers of submicron thickness (like the thin granular  $\text{SiO}_2$  layers in chapter 8.2) it becomes necessary to tilt the sample at least  $10^\circ$  (cf. Fig. 6.8 b)-c): Normally the pear-shaped excitation doesn't contribute to the SE signal. But when imaging the very top of the cross section all further in the back lying surface is also excited, i.e. the image doesn't depict the rastered surface only but becomes blurred (Fig. 6.8 b)). With some tilting the excitation happens again within the volume and the cross section can be examined up to the top with great detail (Fig. 6.8 c)).

In the present work all images were made on a Philips XL30 (at university of Kiel) as well as an XL40 machine (at Ecole Polytechnique Palaiseau) mainly with 10 and 15 kV acceleration voltage.

## 6.2.2 UV-VIS spectrometry

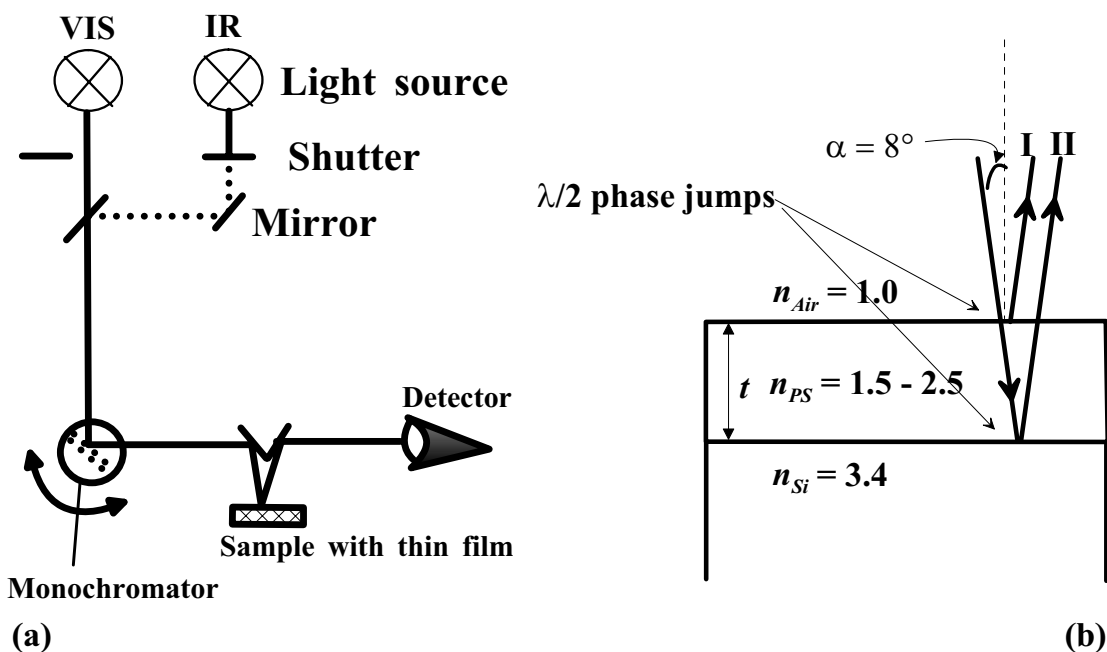


Figure 6.9: UV-VIS spectrometry: (a) Schematic reflection measurement setup. (b) Reflection at front and back side of a thin film on silicon.

Thin films of mesoporous silicon have been analyzed using an optical spectrometer (Perkin-Elmer Lambda 900). Fig. 6.9a) sketches the basic setup: A spectrally broad light beam is generated by either a UV lamp or halogen lamp depending on the desired spectral range (Overall the range from  $\lambda = 185 - 3300$  nm can be covered). A monochromator grating selects a single wavelength which is mirrored onto the sample surface under an angle  $\alpha = 8^\circ$  to the surface normal. The reflected part of the light leaves the sample again under  $8^\circ$  and is mirrored in the direction of an intensity detector. A personal computer correlates the actual monochromator wavelength with the measured intensity to create a spectra. Before the sample is measured, a baseline from a reference mirror or a silicon sample without a thin film is recorded. Afterwards, the sample spectra is recorded and divided by the baseline to get the reflectance. With this procedure the data gets independent of the spectral response of the detector. If a Si wafer is taken as a baseline, also the spectral features originating from the silicon substrate are excluded and only features due to the thin film show up.

When a beam impinges on the sample surface, a part of it is reflected with a phase jump of  $\pi$  (beam I in Fig. 6.9b). The total sum of transmittance  $T$ , absorbance  $A$ , and reflectance  $R$  must be equal to 100% = 1 =  $T + R + A$ . When  $A$  is neglected the reflectance  $R$  for normal incidence is calculated after Fresnel's formulas [151]

$$R = \left( \frac{n_1 - n_0}{n_1 + n_0} \right)^2 \quad (6.8)$$

( $n_0, n_1$ : refractive index of the two interfacing materials).

The transmitted part of the incoming light is again (partially) reflected at the next refractive index step at the thin film - silicon interface (beam II) again with a phase jump of  $\pi$ . When

the small angle of incidence is neglected and a normal incidence is assumed, a simple formula arises for the constructive interference of the reflected beams<sup>5</sup>:

$$m\lambda_m = 2nt \quad (6.9)$$

( $m$ : order of the maximum,  $\lambda_m$ : wavelength of the  $m$ -th maximum,  $n$ : refractive index of the thin film,  $t$ : thickness of the film)

The resulting spectra (cf. Fig.7.14) shows (as long as the film thickness  $t$  is not below some 10 nm or above 100 microns) a series of maxima in the long wave length regime<sup>6</sup>. The product  $nt$  - the optical thickness - can be deduced from two adjacent maxima which avoids the problem of exact identification of  $m$ :

$$nt = \frac{\lambda_m \lambda_{m+1}}{2(\lambda_m - \lambda_{m+1})} = \frac{1}{2(\nu_{m+1} - \nu_m)} \quad (6.10)$$

With a complementary measurement (e.g. measurement of the film thickness in the SEM), the second quantity can be determined.

The effective medium approach (EMA) for composite materials links the fractions of the constituents material to their dielectric functions  $\epsilon$  to obtain the effective dielectric function  $\epsilon_{eff}$  of the composite material. The effective refractive index is then given by the simple relation  $n_{eff} = \sqrt{\epsilon_{eff}}$  for non-magnetic materials [149]. To approximate a mixed material by a single material with an effective refractive index  $n_{eff}$  is only justified as long as the wavelength is (much) larger than the structural dimensions. In the case of porous silicon the material consists of air ( $\epsilon_{air} = 1$ ) and silicon ( $\epsilon_{Si}^0 = 11.9$ ). The Bruggemann [152] EMA is the most prominent one and correlates porosity  $P$  and a measured effective refractive index  $n_{eff}$  via

$$P = \frac{1}{1 + \frac{(n_{eff}^2 - 1)(\epsilon_{Si} + 2n_{eff}^2)}{(\epsilon_{Si} - n_{eff}^2)(1 + 2n_{eff})}}. \quad (6.11)$$

The Looyenga approximation [153]

$$\epsilon_{eff}^{1/3} = (1 - P)\epsilon_{Si}^{1/3} + P \quad (6.12)$$

has also proven [7] to show sufficient matching of simulation and experiment and is somewhat simpler to calculate. For a measured effective refractive index  $n_{eff}$  the porosity  $P$  is there given by:

$$P = \frac{\epsilon_{Si}^{1/3} - n_{eff}^{2/3}}{\epsilon_{Si}^{1/3} - 1} \quad (6.13)$$

Often however, approaches like the Bruggemann [152] and the Maxwell-Garnet [154] approximations are too simple and lead to incorrect results [155]. Similarly, the Looyenga approach becomes limited when the porosities are too low and a high degree of percolation in the silicon network is given. In this case more advanced theories like the Bergman approximation [156] have to be used.

<sup>5</sup>The phase jumps cancel out each other in this special case.

<sup>6</sup>All spectra are given in wavenumbers  $\nu$  [ $\text{cm}^{-1}$ ] which can be converted into wavelengths  $\lambda$  [nm] by  $\lambda[\text{nm}] = \frac{10^7}{\nu[\text{cm}^{-1}]}$ . On the energy based wavenumber scale the oscillation maxima are in first approximation equally spaced which makes comparisons between spectra easier.





# Chapter 7

## Experimental results on porous silicon

### 7.1 n<sup>+</sup> mesopore growth

#### 7.1.1 Introduction and experimental set-up

Conventional mesoporous layers are grown on highly doped p-type or n-type substrates, e.g. for Bragg filter applications [7,130]. Optical applications make use of the effective refractive index  $n_{eff}$  which a porous layer exhibits with a specific porosity. However, the approach to treat a porous material by an effective medium approximation (EMA, cf. p.74) is only valid as long as the pores are much smaller than the wavelength of light. Pores larger than some 10 nm are thus unfavorable for this application and therefore often avoided. On the other hand, applications like biochemical filtering applications would call for somewhat larger pores in the 10 - 100 nm range. As stated in section 5.2.1 this size regime is not reachable with conventional bsi macropores. In the frame of an exploratory industry project on thin porous layers on silicon with a defined thickness, pore diameter, and porosity, possible growth conditions were investigated to reach pore sizes in the 10 - 100 nm region. The parameters were optimized on the small etching cell ( $A = 1 \text{ cm}^2$ ) before the etching procedure was transferred to the large area etcher (for description of the large area etching system cf. [5,146]). Therefore it was also important to develop a nondestructive and quick technique to check whether the layers are identical on both etching cells.

As already indicated by Herino et al. [121] as well as Lehmann et al. [45] (cf. p. 77), p<sup>+</sup> mesopores have always sizes below 20 nm. n<sup>+</sup> mesopores however, shows an increase in pore size up to 200 nm when using lower doped material and/or lower HF concentrations [45]. Mainly the change in substrate resistivity is addressed in [45] while changes due to HF concentration are only discussed using two totally different HF concentrations, namely 6 wt% aqueous and 29 wt% ethanoic HF. In the present work it was chosen to vary the HF concentration and to stay with n<sup>+</sup> substrates ((100),  $\rho = 5 - 20 \text{ m}\Omega\text{cm}$ ) because in this case no further back side contact preparation is necessary, which would also be a cost advantage in an industrial production process.

For the voltammogram measurements, p-type (100) - silicon wafers ( $\rho = 10 - 20 \Omega\text{cm}$ , resp.  $\rho = 10 - 45 \Omega\text{cm}$ ) with aluminum backside metallization in 2 wt% HF were used. The voltammograms were all taken with a sweep rate of 10 mV/s. For the pore etching experiments, the wafers were commercially available n<sup>+</sup> substrates ((100),  $\rho = 5 - 20 \text{ m}\Omega\text{cm}$ ), which were cut and dipped in 10 wt% HF to remove any native oxide prior to the experiments. The solutions were mixed from ethanol (Merck KGaA, Nr. 100974, p.a. grade, denatured with 1% methyl

ethyl ketone p.a. grade), deionized water and 48 wt% hydrofluoric acid (Merck KGaA, Nr. 100334, p.a. grade). The HF concentration  $c_{HF}$  ranged from 4-15 wt%. For the experiments on the ethanol content, always the relative amount of water (including the residual water from the HF base solution) resp. ethanol in % is given. Therefore the mass of water in the solution was divided by the sum of the water and the ethanol mass. The water content ranged from 6% (residual water in the 48 wt% HF base solution in the case of ethanol/HF mixtures) up to 100% for aqueous HF solutions. All experiments in the following section were carried out using the peristaltic pump set-up (cf. section 6.1.2) with a pump speed of 100. The etching time was always 100 s except otherwise noted with galvanostatic control and an etching current density  $j = 30 \text{ mA/cm}^2$ . Therefore the depth is a measure of the etching speed. The temperature was always kept at 20 °C.

The samples were weighted before and after the etching with a Satorius MC 210P precision weighing machine to obtain gravimetric data. The reflectance spectra was recorded using the Perkin-Elmer spectrometer as described in section 6.2.2. The baseline was an unetched Si wafer of the same lot. Afterwards the samples were cleaved and analyzed with the Philips XL30 SEM in cross section. The gravimetric porosity  $P$  was then calculated from the weight loss  $m_{loss}$  and the thickness  $t$  measured in the SEM by the formula (cf. [122])

$$P = \frac{m_{loss}}{\rho_{Si}At} \quad (7.1)$$

( $\rho_{Si} = 2.33 \text{ g/cm}^3$ : density of silicon).

The porosity from the UV-VIS measurements were determined by using the depth  $t$  from the SEM data and the formulas given in section 6.2.2.

### 7.1.2 Experimental results

First, the influence of ethanol for a given HF concentration of  $c_{HF} = 2 \text{ wt}\%$  was investigated<sup>1</sup> with p-type samples. Unlike n-type samples these are independent of the illumination and the basic  $j(U)$  behavior can thus be more clearly analyzed. The voltammogram in the aqueous electrolyte shows  $j_{PSL} = 14.0 \text{ mA/cm}^2$  at  $U = 0.6 \text{ V}$ . Due to an inherent serial resistance, probably the low substrate conductivity, the rises in the voltammogram show a strongly linearized character. With a water (ethanol) content of 84% (16%) the voltammogram is similar up to  $j_{PSL}$  but shows a less steep slope beyond that point. When the water content is lowered to 56%, only a weak peak at  $U = 0.4 \text{ V}$  and  $j = 5.6 \text{ mA/cm}^2$  appears and the slope on both sides of  $j_{PSL}$  is strongly reduced.

To separate the effects of the ethanol and the HF content on the pore morphology, experiments were guided along the path sketched in Fig. 7.1(a). The experiments from [45] formed the two end points of these investigations (29 wt% eth. and 6 wt% aq. HF). The pore diameters  $d$  and layer thicknesses  $t$  measured by SEM are summarized in Fig. 7.2. The “optical” thickness  $nt$  in Fig. 7.2(b) is deduced from the UV-VIS reflection measurements (Fig. 7.3) as described above. The porosities  $P$  are displayed in Fig. 7.4. The gravimetric method always yielded unphysical values above 100 % except for the 15 wt% experiment, so in most cases only the optically determined porosities are shown.

<sup>1</sup>The HF concentration was chosen lower than in the other experiments to be able to measure also far beyond  $j_{PSL}$ . At 6 wt%, already  $j_{PSL}$  would be around 60 mA/cm<sup>2</sup>.

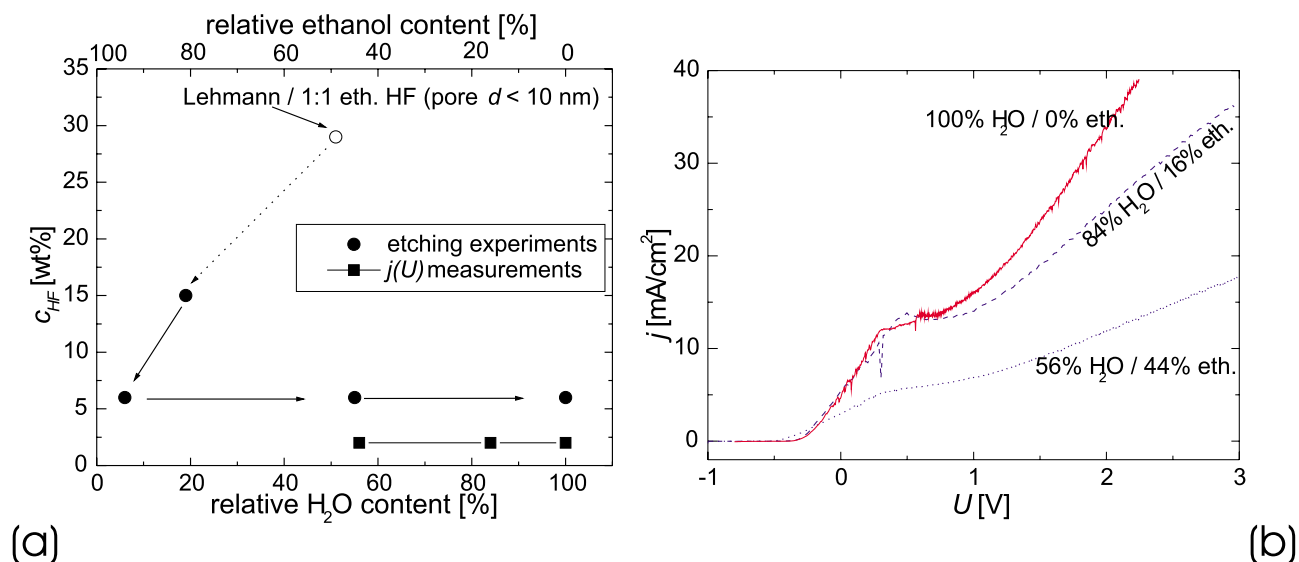


Figure 7.1: (a) Overview of experimental conditions for the investigation of the influence of ethanol on the mesopore morphology (The conditions from [45] for ethanoic HF are also displayed for comparison.). (b) Voltammograms for various ethanol contents @ 2 wt% HF.

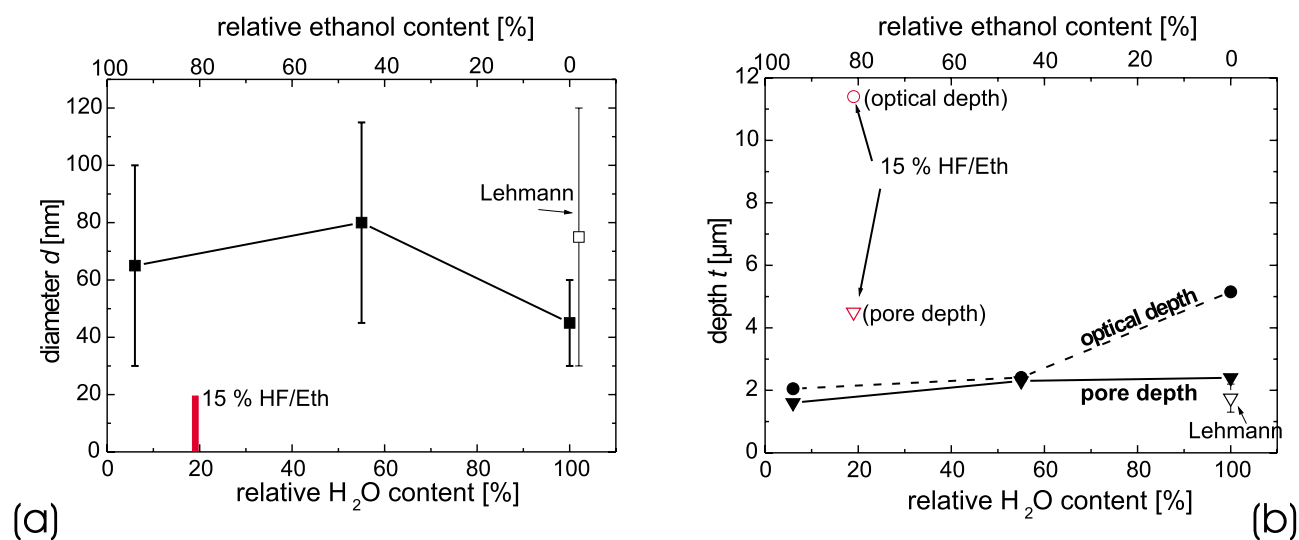


Figure 7.2: Mesopore dimensions versus water/ethanol content ( $c_{HF} = 6$  wt%,  $j = 30$  mA/cm<sup>2</sup>,  $t = 100$  s; additionally the values for 15 wt% HF in ethanol and the results from Lehmann [45] for 6 wt% aq. are listed.): (a) Diameter  $d$  of mesopores versus relative water content. (b) Depth  $t$  of mesopores from SEM and UV-VIS interference measurements versus relative water content.

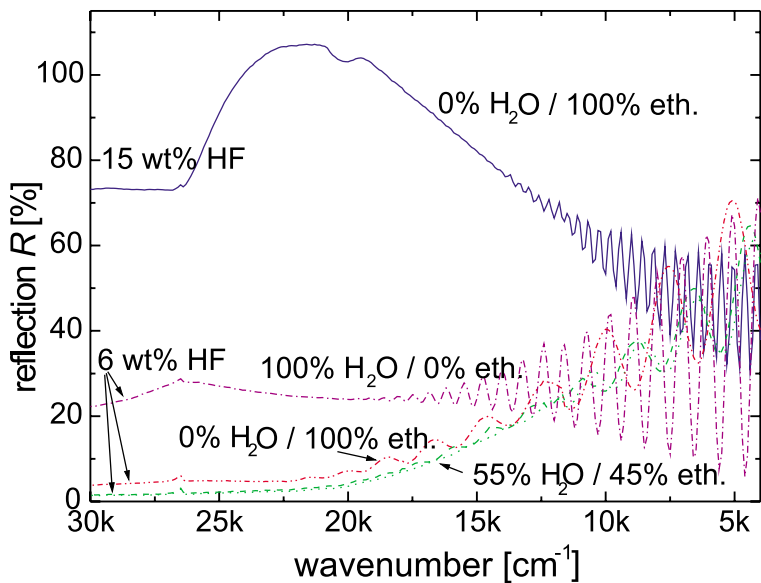


Figure 7.3: UV-VIS reflectance measurements on mesoporous layers versus water/ethanol content.

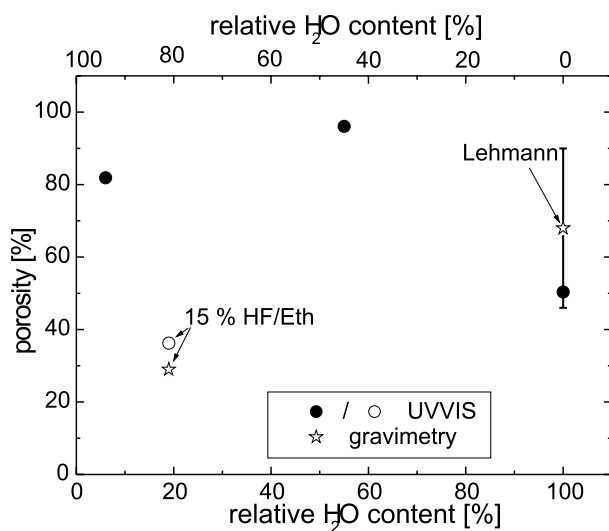


Figure 7.4: Mesopore porosity versus water/ethanol content (from the experimental data from Fig. 7.2).

Because in all experiments by Lehmann et al. the pore diameter stayed below 20 nm for 29 wt% ethanoic HF, in a first series the HF content was reduced to 15 respectively 6 wt%, with pure ethanol as solvent. At 15 wt% the porous layer showed a faint blue color, and during SEM imaging, the individual pores of the 4500 nm thick layer could not be resolved, therefore they are assumed to be smaller than 20 nm. The UV-VIS reflection measurements indicated an optical thickness  $nt = 11400$  nm, i.e. an effective refractive index of 2.54 and therefore a porosity  $P$  of 36 % using the Bruggemann approximation. The gravimetric analysis indicated a slightly lower porosity of 29 %. At 6 wt% the porous layer was black with a blue borderline and showed green and red reflexes upon tilting. The thickness decreased drastically to 1600 nm, also the optical thickness  $nt$  fell to 2050 nm. The high porosity of 82 % was in agreement with SEM observations, which showed a high density of 30 to 100 nm sized pores. Unlike the 15 wt% case, which showed an overall increase of the averaged reflectivity from 40 % at  $4000\text{ cm}^{-1}$  ( $\lambda = 2500\text{ nm}$ ) up to  $20000\text{ cm}^{-1}$  ( $\lambda = 500\text{ nm}$ ), the 6 wt% sample's averaged reflectivity decreased from 40% to 6%.

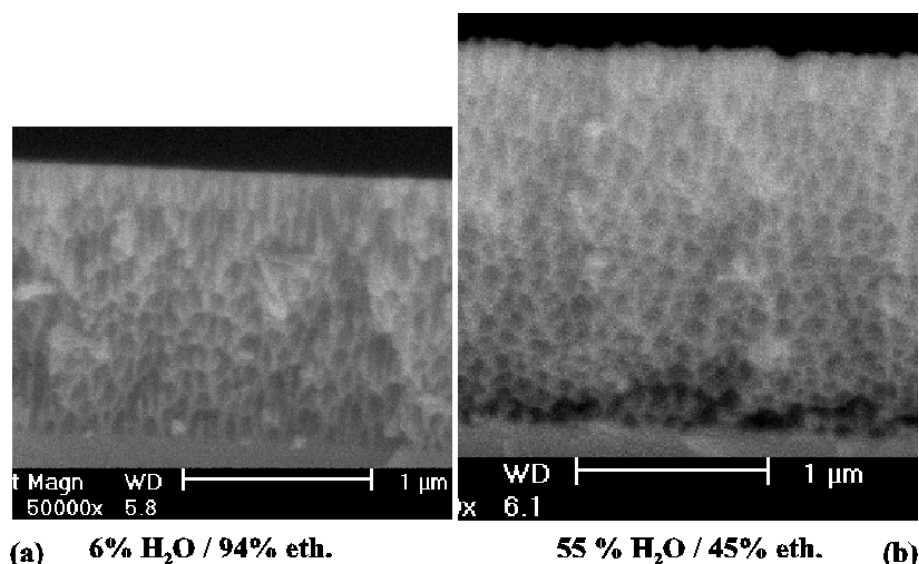


Figure 7.5: SEM cross sections of mesoporous layers for (a) 6/94 and (b) 55/45 relative %  $\text{H}_2\text{O}/\text{eth.}$  content ( $c_{\text{HF}} = 6\text{ wt}\%$ ). The cross section for aqueous 6 wt% HF is shown in Fig. 7.8(b).

In a second run the HF concentration was kept constant at 6 wt% and the solvent was changed from pure ethanol over a 55/45 mixture of water and ethanol to a purely aqueous based solution. The 55/45 sample was inhomogeneously colored in black and dark brown. To verify the results (also the optical measurements) the etching was repeated once which essentially gave the same result (cf. Fig. 7.3). The pore sizes ( $80 \pm 35\text{ nm}$ ) showed the same strong variation as for pure ethanol based solutions (Fig. 7.5). The pore depth slightly increased to 2300 nm, which is consistent with an increase of the optical thickness to 2400 nm. The optical measurements showed the same overall decrease like for the 6/94 mixture (i.e. 6 wt% eth. HF) etching, however, with far less pronounced oscillations. The porosity reached 96 %, but as it can be seen from Fig. 7.5 the interfaces between air and PS respectively between PS and substrate become very rough for the 55/45 mixture compared to the etching with pure ethanol, which makes optical measurements as well as the SEM thickness determination less

reliable. Therefore the number of 96 % porosity should be regarded with caution or at least with a substantial error range. Pure aqueous based 6 wt% HF gave a black-grey homogeneous appearance to the sample. The SEM cross section (Fig. 7.8b) exhibits a much lower porosity ( $P = 49\%$ ) than with ethanol, while the pore diameter decreased to  $45 \pm 15$  nm, i.e. also the size distribution got significantly smaller. The depth was 2400 nm, with an optical depth of 5150 nm. The oscillations in the spectra were by far the most pronounced ones compared to solutions containing ethanol.

The results from Lehmann et al. [45] show a higher porosity, larger diameters and similar depth. At some point, it gets difficult to compare the results adequately because in [45] the doping is given without margins of variation. Therefore the values for  $N_D = 1 \times 10^{18}$ ,  $2 \times 10^{18}$ , and  $1 \times 10^{19}$  (which are all in the range of the resistivity  $\rho = 5 - 20$  m $\Omega$ cm) were averaged to generate the ‘‘Lehmann’’- data points in Figs. 7.2 and 7.4 and the error bars were chosen so that all results from [45] for these doping levels are included.

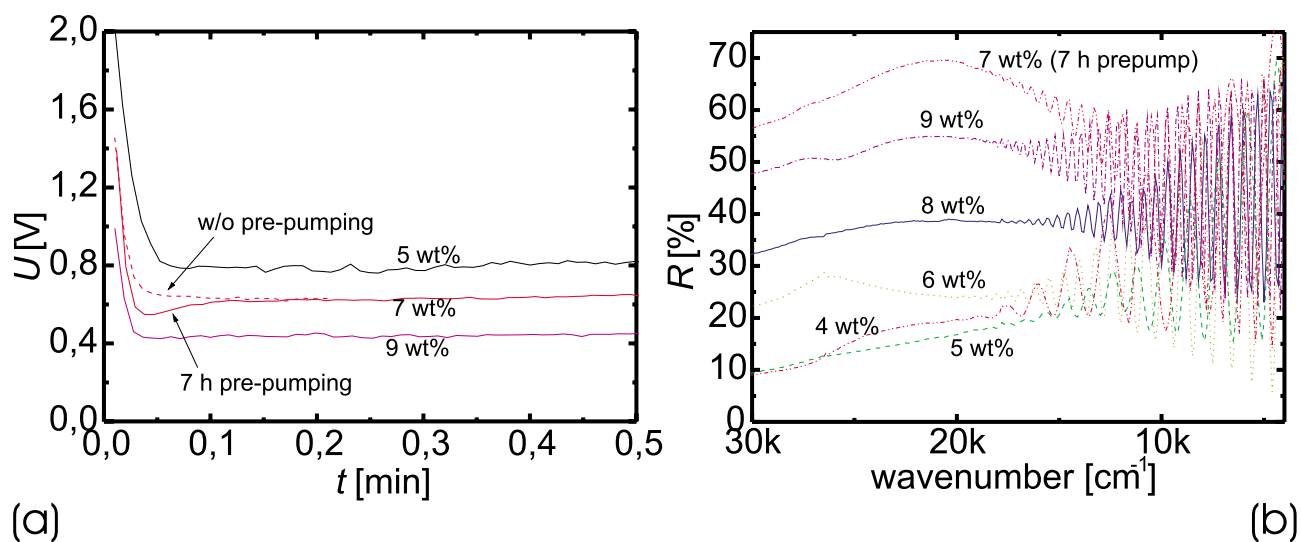


Figure 7.6: (a) First 30 s of the potential transient during the etching of mesoporous layers for various HF concentrations. A long pre-pumping leads to a dip in the potential at the beginning of the etching. (b) UV-VIS reflectance measurements on mesoporous layers versus HF concentration  $c_{HF}$ . In the case of 7 wt%, the long pre-pumping leads to a strongly increased reflection signal for  $\nu > 10\text{k cm}^{-1}$ .

In a further series, the change of pore diameter (Fig. 7.7a), depth (Fig. 7.7b), and porosity (Fig. 7.9) was investigated for a variation of HF content in aqueous solutions. The voltage transient during the galvanostatic experiments (Fig. 7.6a) started with a comparatively high voltage (from 2.3 V @ 4 wt% to 0.9 V @ 9 wt%) which dropped within 3 s to a minimum (from 0.9 V @ 4 wt% to 0.4 V @ 9 wt%). Afterwards the voltage slowly rose linearly until the end of the etching (end values: from 1.1 V @ 4 wt% to 0.5 V @ 9 wt%). As can be seen from Fig. 7.6(a) the voltages drop monotonically with increasing HF concentration.

The diameter decreased nearly exponentially with the increase of HF concentration from  $105 \pm 25$  nm @ 4 wt% HF to  $15 \pm 5$  nm @ 9 wt% HF. The variation of the values decreased in a similar way (cf. Fig. 7.7a). This change is clearly seen in the SEM cross sections, too (Fig. 7.8). The depth of the pores increased from 1550 nm @ 4 wt% HF to 3700 nm @ 9 wt% HF. The optical depth derived from the UV-VIS measurements (Fig. 7.6b) showed a monotonic

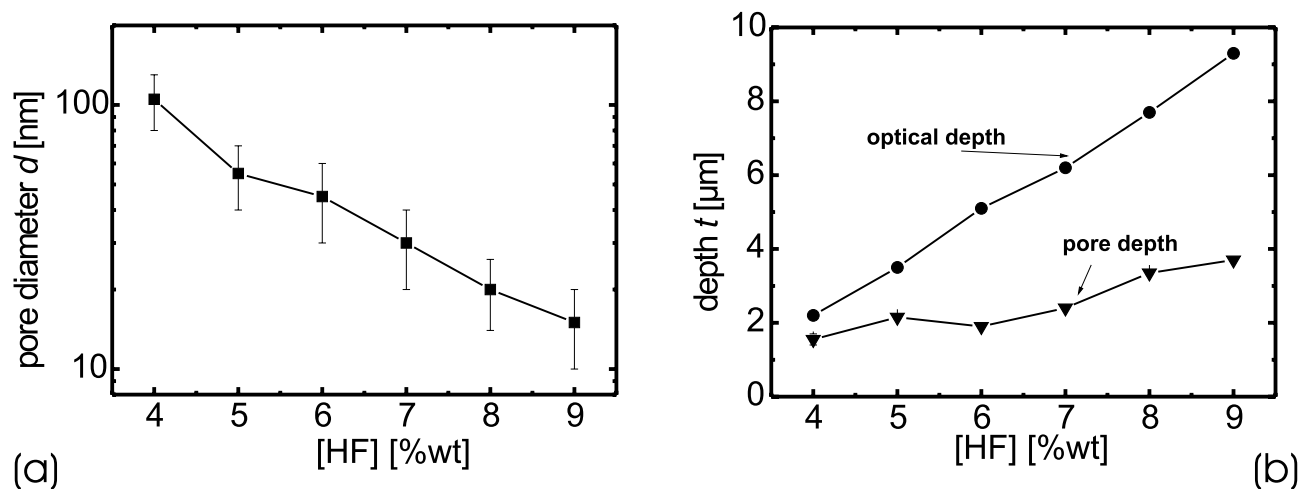


Figure 7.7: Mesopore dimensions versus HF content (aq.,  $j = 30 \text{ mA/cm}^2$ ,  $t = 100 \text{ s}$ ): (a) Diameter  $d$  of mesopores versus HF content. (b) Depth  $t$  of mesopores from SEM ('pore depth') and UV-VIS interference ('optical depth') measurements.

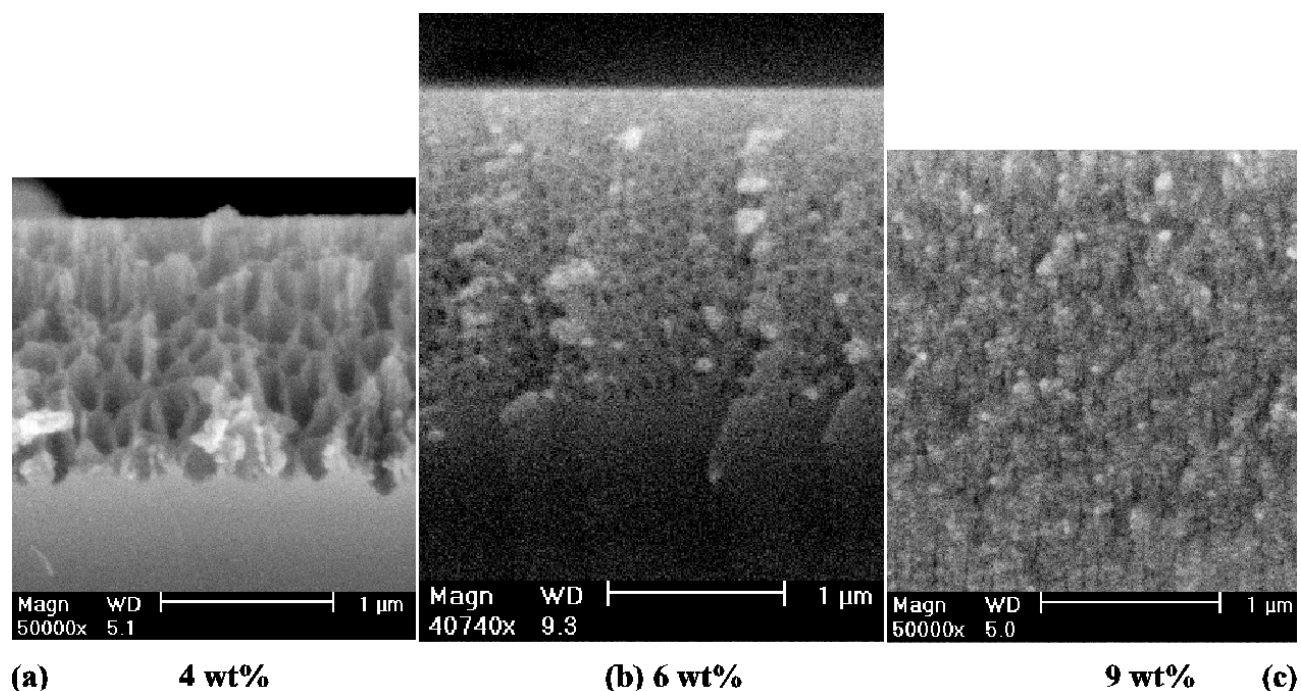


Figure 7.8: SEM cross sections of mesoporous layers for various HF concentrations (aqueous,  $j = 30 \text{ mA/cm}^2$ ,  $t = 100 \text{ s}$ , middle image resized to have same scale): (a)  $c_{HF} = 4 \text{ wt\%}$ , (b)  $c_{HF} = 6 \text{ wt\%}$ , (c)  $c_{HF} = 9 \text{ wt\%}$ .

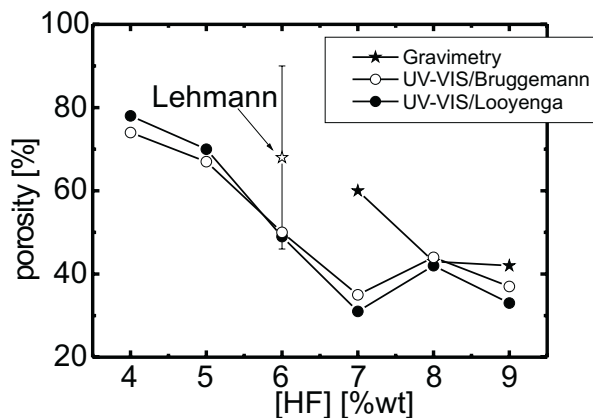


Figure 7.9: Mesopore porosity versus HF content (from the experimental data from Fig. 7.7): Calculation from UV-VIS measurements and SEM thickness measurements (circles) as well as gravimetric data (stars). For 4 - 6 wt%, gravimetry did not produce reasonable results (porosities > 100 %).

increase from 2200 nm @ 4 wt% to 9300 nm @ 9 wt%. The porosities for the samples on 4 - 6 wt% could only be determined optically while gravimetry always yielded 100%+ porosities. In Fig. 7.9 the porosities following the Bruggemann approximation (Eq. 6.11) as well as the values for the Looyenga approach (Eq. 6.12) are displayed. As can be seen the curves only deviate by about 5 % even at the extreme borders 30 and 80 % porosity. Unless very exact measurements on thickness and refractive index are available, it is therefore within the given measurement errors unimportant which of both approaches is chosen for the determination of the porosity.

The results on 7 wt%, especially the optical spectra (Fig. 7.6b) are clearly off-beat. This sample was left built-in for 7h before the etching was started. The diameter and the optical depth follows the trend expected from the other HF concentrations, however the absolute depth shows a significantly lower value than expected (Fig. 7.7). Correspondingly, the optically determined porosity is much lower (Fig. 7.9), while the gravimetric porosity of 60 % is in accordance with the expected trend (compared to 8 and 9 wt%) of higher porosities with lower HF concentration (cf. also [45, 121]). The reflectivity increases stronger than for all other samples in this series in the spectral range from  $4000\text{ cm}^{-1}$  to  $20000\text{ cm}^{-1}$ . During the etching, the voltage transient shows a distinct minimum after 2 - 3 s, while a comparable sample<sup>2</sup> which was etched without the long pre-pumping shows similar  $U(t)$  curves as the other concentrations. After this initial discrepancy both 7 wt% transients merge after approx. 0.1 min.

Fig. 7.10 shows that the UV-VIS spectra for a sample etched on the small etching cell ( $A = 1\text{ cm}^2$ ) is to a large degree reproduced by a full 4" wafer etched on the large area etcher. In both cases identical etching conditions ( $j = 30\text{ mA/cm}^2$ ,  $t = 13\text{ s}$ ,  $c_{HF} = 7\text{ wt}\%$  aq.) were used. The spectral response shows a slightly larger spacing of the oscillations which points according to Eq. 6.10 to a smaller layer thickness on the large area system. The reflectivity at high energies is approx. 7 % higher in case of the large area etcher. Also the oscillations are more pronounced, which suggests in first order slightly better defined interfaces on the big

<sup>2</sup>An optical spectra of the other 7 wt% sample is shown in Fig. 7.10. Because this sample was etched (for a different purpose) only 0.22 min, the optical response strongly differs from the 100 s samples and a direct comparison is therefore of little use.



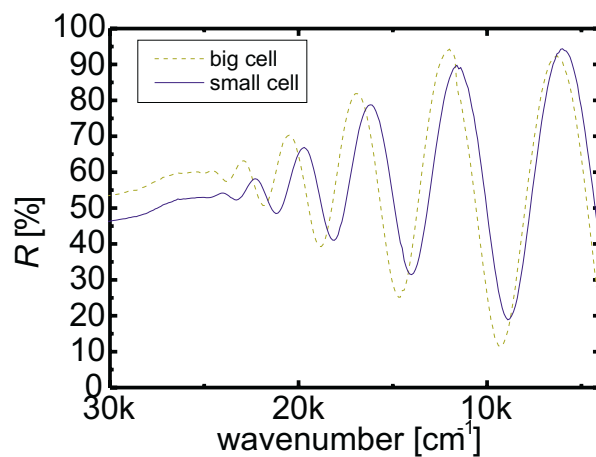
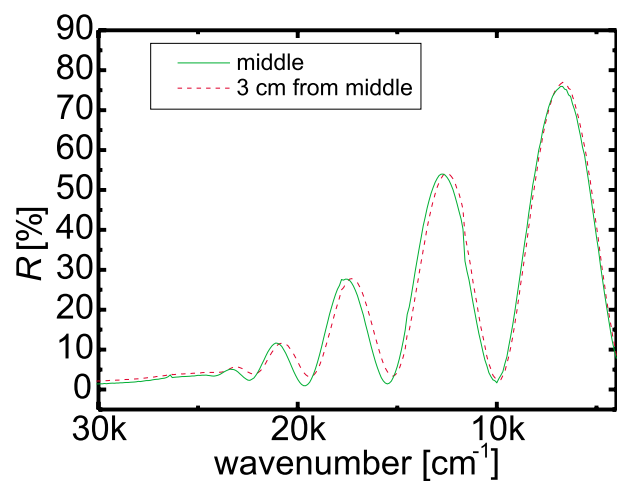
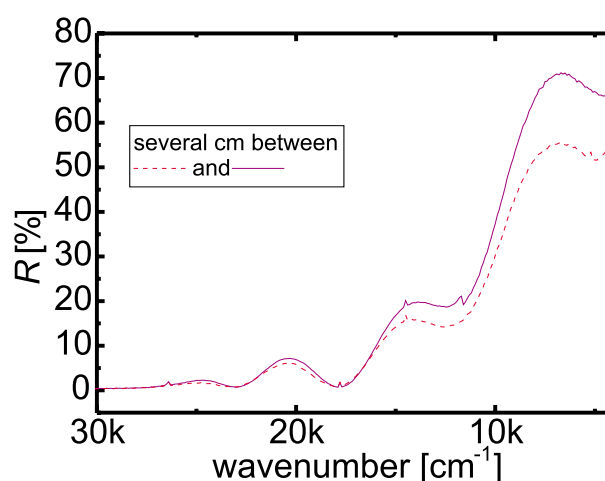


Figure 7.10: UV-VIS spectra after transfer from the small to the 4" etching cell ( $j = 30$  mA/cm<sup>2</sup>,  $t = 13$  s,  $c_{HF} = 7$  wt% aq.).



(a)



(b)

Figure 7.11: Lateral homogeneity of mesoporous layers on large area samples (4"): (a)  $j = 30$  mA/cm<sup>2</sup>,  $t = 30$  s,  $c_{HF} = 6$  wt% aq.(52 wt%)/eth., (b)  $j = 30$  mA/cm<sup>2</sup>,  $t = 50$  s,  $c_{HF} = 6$  wt% eth.

etching cell. During several other large area experiments (Fig. 7.11) the lateral homogeneity on the wafer was checked. In the case of etching in a 6 wt% aq./eth. mixture (Fig. 7.11a) the spectra from two spots (distance: 3 cm) are practically identical. For an etching in 6 wt% eth. (Fig. 7.11b) only the height of the oscillations is differing, while the position is identical (and therefore also the layer thickness) as well as the spectra itself above  $\nu = 16000 \text{ cm}^{-1}$ .

### 7.1.3 Discussion

#### Ethanol content

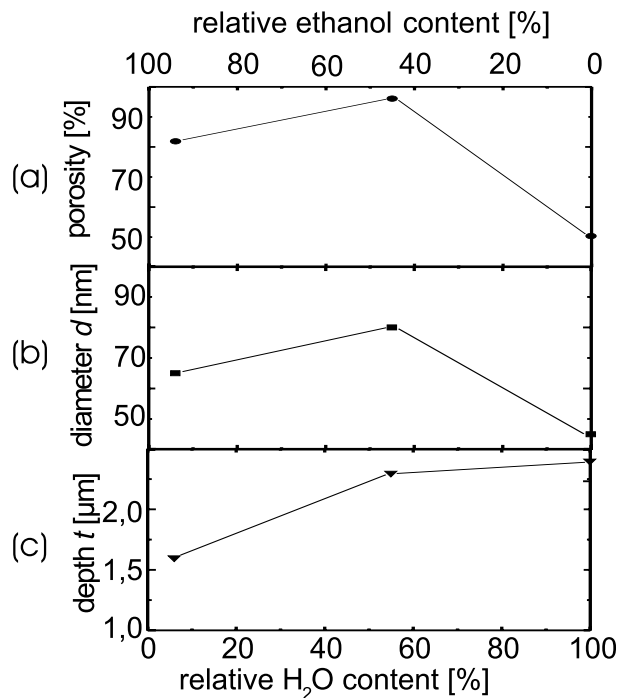


Figure 7.12: Mesopore key figures versus (ethanol:water) ratio: (a) Porosity  $p$ . (b) Diameter  $d$ . (c) Depth  $t$ .

First, the results on the change of the ethanol/H<sub>2</sub>O-ratio ( $c_{HF} = 6 \text{ \%wt}$ ) shall be discussed (Fig. 7.12). The replacement of water by ethanol obviously leads to larger pores ( $\langle d_{aq} \rangle = 45 \text{ nm} \rightarrow \langle d_{eth} \rangle = 60 \text{ nm}$ ) and smaller depth ( $\langle t_{aq} \rangle = 2400 \text{ nm} \rightarrow \langle d_{eth} \rangle = 1600 \text{ nm}$ ), which is accompanied by a drastically increased porosity ( $\langle P_{aq} \rangle = 50 \text{ \%} \rightarrow \langle P_{eth} \rangle = 82 \text{ \%}$ ). When normally analyzing organic electrolytes, the oxidation power (cf. section 3.2) is a proven parameter to predict the pore growth behavior. In a very simplified view, a low oxidation power leads to small, dendritic pores while high oxidation powers yield smooth and broad pores. However, in the case of ethanol, a very low oxidation power like for propanol can be expected, which is in strong contrast to the clearly observed enlargement of the pores. But an argumentation like this only addresses oxide formation properties of an electrolyte. To understand the influence of ethanol, one has to look at the impact of ethanol on the oxide dissolution capabilities of the HF: Garrido et al. [75] (cf. section 4.4) showed for thermal oxides that a switch from an aqueous solution to an ethanoic solution leads to reduction of the etch rate by two orders of magnitude. Taking this into account not the oxidation properties of

the ethanol are important but its function as a hinderance for oxide dissolution. As stated in section 5.4 the oxide related current parts  $j_{ox}$  of the current density at the pore tip follows the continuity equation Eq. 4.13, i.e. when the oxide dissolution rate  $\alpha$  drops also  $j_{ox}$  drops. Consequently the growth rate of the pores into the depth decreases with increasing ethanol content as observed in the experiments.

If the oxidic current density  $j_{ox}$  decreases due to ethanol addition, also the total current density in a single pore  $j_{pore} = j_{ox} + j_{direct}$  will decrease. To keep the overall current density across the sample at  $j = 30 \text{ mA/cm}^2$  the system will either enlarge the active area (i.e. the porosity) and shift parts of the current to direct dissolution. As can be seen from Fig. 7.4 the porosity increases drastically with the addition of ethanol which is in good agreement with the reasoning given above. The other point on a shift to more direct dissolution is at the present state not quantifiable. The diameter of pores is to a wide degree ruled by the size of oxide domains. A lower dissolution rate leads to larger correlated oxidic domains [82]. The enlarged diameter upon the addition of ethanol reflects these larger domains. However, it has to be stated that also other factors strongly affect the pore size, e.g. nucleation density at the starting surface or protection of remaining walls by overlapping space charge regions. Therefore the pore size and also the porosity are not directly proportional to the amount of ethanol, but change rather drastically from 94 wt% aq. to 52 %wt aq. and stay then almost constant. The pore depth behaves almost inverse.

This argumentation is supported by the observation that the anodic currents drop especially after the  $j_{PSL}$ -peak (Fig. 7.1b) upon the replacement of water by ethanol. After the  $j_{PSL}$ -peak a full oxide coverage of the electrode has been measured at all times (cf. section 3.1) and the reaction valence is four, so the current transfer at the electrode happens exclusively via anodic oxidation of silicon and subsequent removal of that oxide. Therefore it is clear that a suppression of the oxide dissolution capabilities of the HF will reduce the current density  $j = j_{ox}$  which is for steady state in equilibrium with the oxide dissolution rate  $\alpha$ . For current densities smaller than  $j_{PSL}$  an involvement of oxidic currents has been shown (cf. section 3.1.2) down to the point of inflection in the  $IU$  characteristic, but there the oxide influence is less and only heavy addition of ethanol shows an impact. This dissolution suppressing behavior and its influence on anodic currents is similar to the evolution of HF properties with increasing pH (cf. Fig. 4.6).

A simple serial resistance argumentation, i.e. that the resistivity of the ethanol or a lesser dissociation of HF in it causes a damping of the characteristic can only be fully countered by an impedance measurement which wasn't done during the present experiments because of its additional complexity. However, several signs render such an effect implausible, e.g. a serial resistance (in first order) shifts the  $j_{PSL}$ -peak only to higher voltages, but leaves the magnitude untouched [157], which is clearly not the case in the present observations. Still the possibility of a mixed behavior exists, i.e. that diffusional forces and serial resistance compete.

As already delineated in section 7.1, the only explanation for the use of ethanol based mixtures during pore etching, has been so far the reduction of surface tension and the enhanced detachment of hydrogen bubbles which often form during pore growth with valences near two. For the outer sample surface this is certainly correct, albeit inside mesopores a "nano"-bubble formation seems hardly possible. Lehmann [32] assumes even for micron-sized macropores that bubbles cannot be formed within the pores. Results like those from Searson et al. [125] show that 70 nm mesopores etched in aqueous solutions show rougher walls and more side branches than those etched in ethanoic solutions. The explanation which is given in [125] holds responsible the better detachment of bubbles within the pores. While this seems to be hardly

vindicable, the observation of smoothed pores upon the addition of ethanol is perfectly in line with the reasoning given above.

### HF concentration

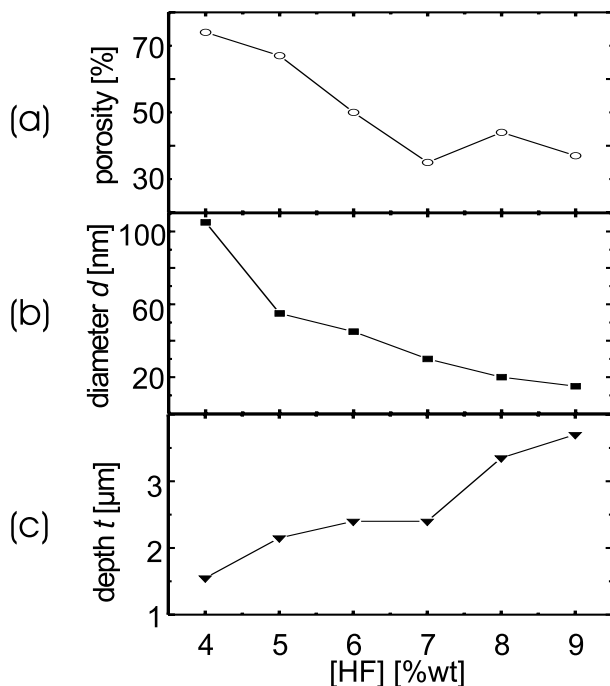


Figure 7.13: Mesopore key figures versus HF concentration: (a) Porosity  $p$ . (b) Diameter  $d$ . (c) Depth  $t$ .

Upon an increase of the HF concentration (for ethanoic as well as aqueous solutions) the morphology changes strictly monotonically: The pores become smaller and deeper (Fig. 7.13). The porosity decreases also monotonically (with the exception of 7 wt% aq., which is discussed separately in the UV-VIS data section). The increasing depth reached within 100 s etch time can again be explained with a recourse to the continuity equation (Eq. 4.13) under steady state conditions. Here an increase in  $\alpha$  leads to a faster growth into the depth because the oxide related current density is higher. Again, because the current density was kept at 30 mA/cm<sup>2</sup> during all experiments the active area and therefore the porosity  $P$  has to decrease. A decrease of porosity does not yet explain why pores are getting smaller (less pores of the old diameter would have the same effect on the total current density). Here again, the concept of (correlated) oxide domains is invoked, which has shown in simulations that a high dissolution rate leads to smaller correlated areas. This then also shrinks the average pore size which is tied to a large extent to the domain size [51].

### UV-VIS data

First, for the example of ethanol (Fig. 7.14) the features seen in the UV-VIS spectra and their use for pore growth optimization shall be discussed. The spectra gives beyond a simple thickness calculation also further - at least qualitative - information (cf. Fig. 7.14): The

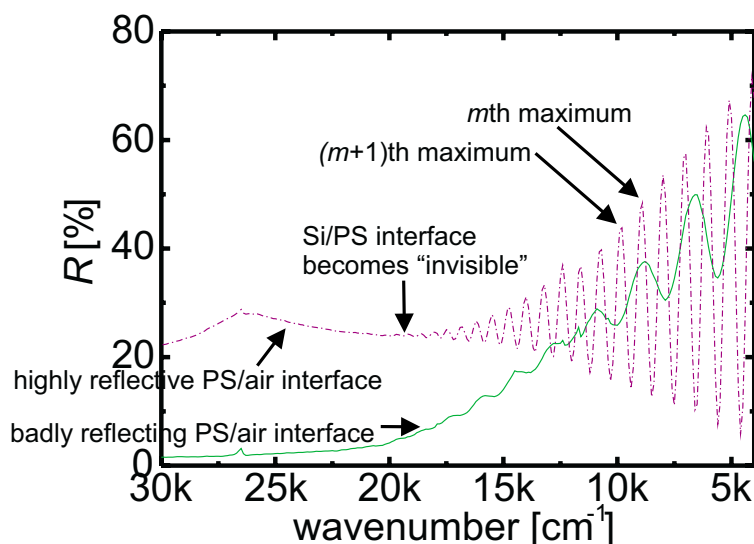


Figure 7.14: Exemplary UV-VIS reflectance spectra from the series of ethanol experiments (Fig. 7.3): 6 wt% HF aq. with a sample with good interface quality (violet, dash-dotted line) versus 6 wt% HF (55/45 = H<sub>2</sub>O/eth.) with rough interfaces (green, solid line)(based on Fig. 7.3).

relative difference between maxima and minima indicates the ratio of the intensities of beam I and II. If one of the interfaces only shows a weak reflection due to a rough interface or due to a low index contrast (cf. Eq. 6.8) then it can only weakly modulate the other, stronger beam. The point at higher energies, where the modulations cease, gives information when the absorption (at energies  $h\nu > E_{g,si}$ ) gets so high that beam II becomes absorbed on its way twice through the porous layer. Finally, the intensity at higher wavenumbers gives information about the roughness and the porosity of the sample surface; e.g. a highly porous sample has only a minimal outer surface which can contribute to beam I, so the reflection at high energies is very low. As can be seen from Figs. 7.3, 7.4, 7.6, and 7.9 the reflectivity at high energies is directly imaging the porosities of the samples, whereupon it always has to be kept in mind that here only the porosity at the sample surface can be probed.

Also this technique helps to reveal otherwise unclear phenomena like in the experiment with 7 wt% aq. HF. There the sample was left built in for 7 h prior to the etching, where the electrolyte just circulated without an applied current. This led to a different electrical as well as optical signal from which the following facts can be distilled:

- Less surface is etched than under normal conditions. This is evidenced by the strong rise in the reflectivity measurement at 20k  $\text{cm}^{-1}$ .
- At least the voltage signal only differs in the first few seconds of the etching as the comparison with the other 7 wt% experiment and the experiments at other HF concentrations show.
- The diameter of the pores deeper in the sample stays in the observed trend of exponential decrease with increasing HF concentration
- The porosity measurements are contradictory. However a lower porosity and a decrease in depth cannot be easily explained without a heavy change in the valence (which is not

seen in the other parameters), therefore the optical measurement seems to give wrong values.

- The reached depth is significantly lower, this is however not seen in the optical thickness.

A possible conclusion is that the long rinsing time led to an extremely perfect H termination of the interface. This of course has a major impact on the starting conditions for the pores (like it is also reflected in the electrical signal), but as growth proceeds the interface conditions (and the electrical signal) change into the “normal” conditions. This favors a bottleneck model: At first the passivation and direct dissolution component is strongly enhanced compared to oxidative parts, i.e. pores grow in a similar manner like for higher HF concentration, i.e. faster, smaller and with less porosity. After the nucleation, the pore tips return more and more to their standard growth conditions, i.e. the standard diameter and porosity for 7 wt%. The slower growth rate can have several possible reasons: First, if the pores have only nucleated slightly denser, the current density per pore is finally lower which leads to slower pores (cf. section 5.2.2), or secondly, a bottleneck at the beginning of the pores poses a diffusional barrier for HF which reduces the HF concentration within the pore faster than under ‘normal’ conditions. Such a high index bottleneck layer can corrupt the optical porosity determination which assumes a single layer. The refractive index (porosity) of this fictitious single layer is always overestimated (underestimated).

In general, the UV-VIS spectra already without further complementary measurement like SEM, are a good choice to compare samples because already small changes are visible immediately. The “footprint” of a porous layer is so complex that an accidental similarity between morphologically different wafers is nearly impossible. However, to give absolute number about thickness, porosity, interface quality etc. is only possible with a careful calibration of this method by other, more direct methods, e.g. SEM, TEM, or AFM. Furthermore already the measurements of the present work show that in order to evaluate the spectra really correct, it is necessary to simulate spectra with a software like SCOUT [158] which is specialized on the simulation of the spectral response of porous (multi)layers. As it was shown in the last part of the results section, the method is

- very fast (1-5 minutes per measurement)
- non-destructive
- giving easily comparable quantities

compared to other techniques (e.g. SEM). Therefore the goal was reached to establish a technique to monitor the transfer from small laboratory equipment to larger production entities. Also it has shown that the lateral homogeneity at least over a scale of several centimeters is very good on the large area etcher, although this should be verified with additional measurements along one line across the whole wafer.

## 7.2 Octahedral growth

### 7.2.1 Introduction and experimental set-up

As shortly discussed in section 5.2.2, Jäger et al. [126] have shown with TEM investigations that mesopore growth in silicon proceeds under certain conditions as a chain of octahedrons. In other semiconductors like GaAs [159] as well as recently discovered in InP [160] tetrahedron-like pores are the basis for the crystal pores (cf. p. 58). It has become clear that in III/V semiconductors pores develop with other shapes than those in silicon due to their polarity which induces other directions for preferential etching and passivation [95].

For silicon however detailed investigations on the parameter dependence of the morphology of the octahedrons were still missing. In the following the dependence of the diameter of the octahedrons as well as the overlap of adjacent octahedrons as a function of

- applied bias  $U$
- illumination intensity
- HF concentration  $c_{HF}$
- pH of the solution

Because the crystallographic features during pore growth always compete with isotropic oxidation features, an organic electrolyte was chosen for the following experiments; here oxidation and a smear-out of structures is strongly suppressed.

The experiments were carried out using the etching setup with the peristaltic pump (cf. section 6.1.2;  $T = 20^\circ\text{C}$  in all experiments) in potentiostatic mode with additional backside illumination. The illumination was controlled so that the current stayed constant. The current through the LEDs (and therewith the illumination intensity) is directly proportional to the (control) voltage at the illumination controller  $U_{illum}$ . The applied current density ranged between  $j = 0 - 8 \text{ mA/cm}^2$  and the voltage  $U$  was chosen from 1 to 20 V.

The electrolyte was HF in DMF with final HF concentrations between  $c_{HF} = 2.0$  and  $6.5 \text{ wt}\%$ . In some experiments the pH was adjusted by adding HCl (37 wt%) in small amounts. The pH was then determined with indicator sticks (Merck Inc., 0.1 scale steps). In one experiment, 44 mg of strongly oxidizing Cr(IV)-oxide was added to an electrolyte volume of 270 ml. The silicon wafers were n-type (100, CZ) with a resistivity of  $\rho = 3.5 - 6.5 \Omega\text{cm}$ .

On all samples the diameter and the overlap of adjacent octahedrons was analyzed in SEM cross section. The overlap  $o$  was determined from the pitch  $p$  of two adjacent octahedrons and their diameter  $d$  ( $o = d - p$ , cf. also Fig. 7.15a). The overlap accounts also for the size of the octahedrons and is therefore more meaningful than the pitch.

### 7.2.2 Experimental results

In an initial series of experiments the regime was checked in which octahedral pores can grow. Keeping the other etching parameters constant ( $U = 4 \text{ V}$ , 4 %wt HF in DMF) the etching current was varied between  $j = 0 - 1.2 \text{ mA/cm}^2$ . Only for low illumination intensities, octahedral pores grew (Fig. 7.15a,b:  $U_{illum} = 0.8 - 1.0 \text{ V}$ ); under strong illumination (Fig. 7.15c:  $U_{illum} = \text{max.} = 10.0 \text{ V}$ ) only macropores were found. The actual values for the current density were not strongly differing (Fig. 7.15b:  $j = 1.0 \text{ mA/cm}^2$  versus Fig. 7.15c:  $j = 1.1 - 1.2 \text{ mA/cm}^2$ ). As can

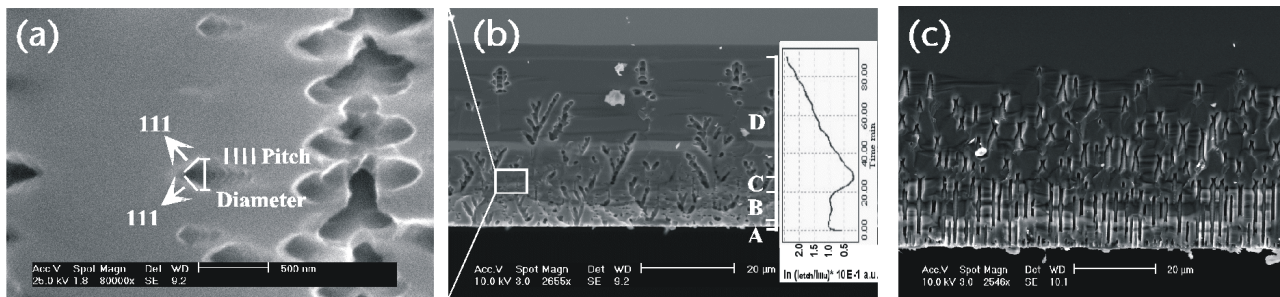


Figure 7.15: Influence of illumination on octahedral cavity growth ( $U = 4\text{V}$ ,  $c_{HF} = 4\text{ wt}\%$ ): (a) The magnification of (b) shows clearly stacked octahedral growth between the macropores. During all experiments the diameter  $d$  and the overlap  $o = d - p$  of the octahedrons was analyzed. (b) At low illumination intensities octahedrons and macropores grow simultaneously ( $U_{illu} \approx 0.8 - 1.0\text{ V}$ ,  $j = 1.0\text{ mA/cm}^2$ ) up to a depth  $t \approx 15\mu\text{m}$ . After a nucleation phase (A) macropores and octahedrons grow simultaneously (B) until the octahedrons die out (C) and stable macropore growth starts (D). These phases clearly show up in  $\ln(I_{etch}/I_{illu})$  as a function of etching time (Inset of b). (c) At high illumination intensities ( $U_{illu} = U_{illu}^{max} = 10\text{ V}$ ,  $j = 1.1 - 1.2\text{ mA/cm}^2$  no octahedrons are found between perfect macropores.)

be seen from Fig. 7.15(b) first macropores and octahedral pores grew simultaneously for about  $15\mu\text{m}$ . Then the octahedral pores vanished and only the macropores continued to grow. The etch rate on such a shallow depths as some 10 microns can be assumed to be constant [32], i.e. it is justified to directly compare transient behavior of electrical signals during the etching with SEM cross sections. In Fig. 7.15(b) the ratio between etching current and illumination current is plotted logarithmically. At the start of the pore growth (the “nucleation”) a steep increase is visible. While both pore types co-existed the function stayed nearly constant. During the dying out of the mesopores it fell to a minimum. When only macropores were left the logarithmic ratio showed the known linear behavior for bsi macropores (cf. section 5.2.1).

Increasing the applied voltage from  $4\text{ V}$  to  $8\text{ V}$  and  $12\text{ V}$  (under otherwise identical conditions) the octahedral pores grow much deeper with monotonically decreasing density, but applying  $20\text{ V}$  through the complete etched area octahedral pores are found without any significant reduction of the density (Fig. 7.15b and Fig. 7.16). Additionally the diameter and the overlap of the octahedrons change significantly with the variation of the applied voltage (Fig. 7.17 and Fig. 7.19a). As illustrated in Fig. 7.19(a) the diameter of the octahedral pores decreases from  $300 (\pm 20)$  ( $@ U = 4\text{ V}$ ) to  $180 (\pm 50)$  nm ( $@ U = 20\text{ V}$ ) and the overlap of the octahedral pores increases from  $25 (\pm 10)$  ( $@ U = 4\text{ V}$ ) to  $155 (\pm 15)$  nm ( $@ U = 20\text{ V}$ ) with increasing etching potential.

In a second series of experiments the influence of the HF-concentrations for fixed  $U = 12\text{ V}$  and  $j = 1\text{ mA/cm}^2$  was investigated (Fig. 7.18). The diameter rose slightly from  $160 (\pm 70)$  ( $@ c_{HF} = 2.0\text{ wt}\%$ ) to  $215 (\pm 65)$  nm ( $@ c_{HF} = 6.5\text{ wt}\%$ ) with HF concentration. Similarly, the overlap of the octahedrons increased from  $105 (\pm 40)$  ( $@ c_{HF} = 2.0\text{ wt}\%$ ) to  $135 (\pm 40)$  nm ( $@ c_{HF} = 6.5\text{ wt}\%$ ) (Fig. 7.19b). In contrast to this result, the variation of the pH-value by adding HCl to the electrolyte has no clear influence on the octahedra geometry (Fig. 7.20).

In a control experiment, Cr(IV)-oxide was added to analyze also a strongly oxidizing electrolyte ( $c_{HF} = 2\text{ wt}\%$ ,  $U = 12\text{ V}$ ,  $j = 1\text{ mA/cm}^2$ ). Only few small octahedrons were encountered, in exchange large amounts of chains of interconnected spherical cavities were found (diameters



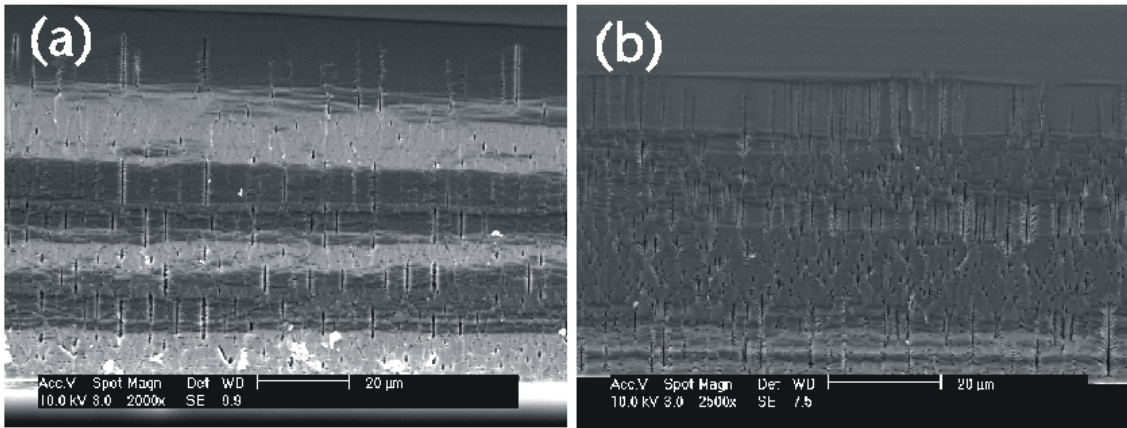


Figure 7.16: Density of octahedrons versus applied bias ( $c_{HF} = 4 \text{ wt}\%$ ,  $j = 1$  resp.  $2 \text{ mA/cm}^2$ ): At  $U = 4 \text{ V}$  (Fig. 7.15b) the octahedrons die out at a certain depth, while at  $U = 8 \text{ V}$  (a) the density of octahedrons only decreases with depth. (b) At  $U = 20 \text{ V}$ , no significant reduction of octahedron density is found with depth.

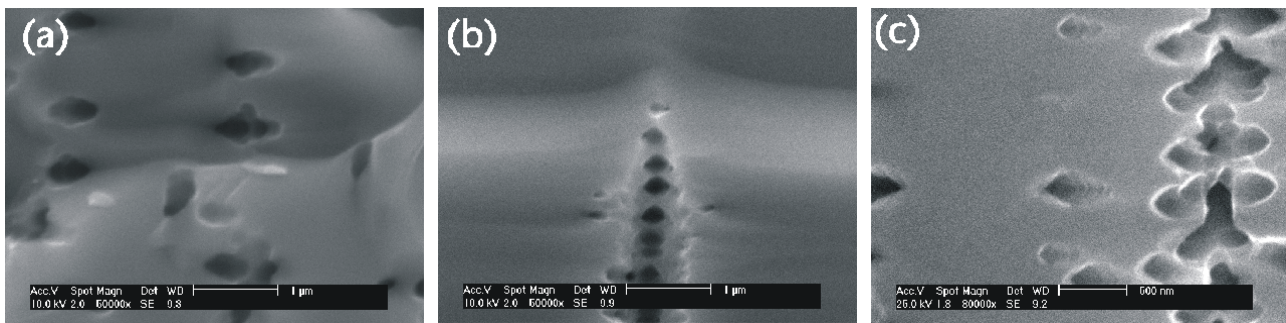


Figure 7.17: Influence of applied bias  $U$  on octahedral cavity growth ( $c_{HF} = 4 \text{ wt}\%$ ): (a)  $U = 4 \text{ V}$ ,  $j = 1 \text{ mA/cm}^2$ , (b)  $U = 8 \text{ V}$ ,  $j = 1 \text{ mA/cm}^2$ , (c)  $U = 20 \text{ V}$ ,  $j = 2 \text{ mA/cm}^2$  (At  $U = 20 \text{ V}$  it was even with switched off illumination not possible to reach a low current like  $j = 1 \text{ mA/cm}^2$ ). A quantitative evaluation is given in Fig. 7.19.

$\approx 500 - 700 \text{ nm}$ ).

### 7.2.3 Discussion

#### Comparison of meso- and macropore growth

First the growth conditions for meso- and macropore growth are compared based on an analysis of Fig. 7.15(b) and its inset: At the beginning, a comparably high voltage  $U_{Si-HF}$  is available at the Si/HF contact. Carrier generation by electrical breakdown is the main source for holes, while the distance of pore tips to the backside obviously has no influence because the ratio of etching current to illumination current stays nearly constant. When the pores grow deeper into the substrate, the voltage available for breakdown drops because an increasing portion of the total voltage drops in the electrolyte in the pores which poses an ever increasing serial resistance in the set-up. This continues until  $U_{Si-HF}$  drops below the breakdown voltage  $U_{BD}$  of

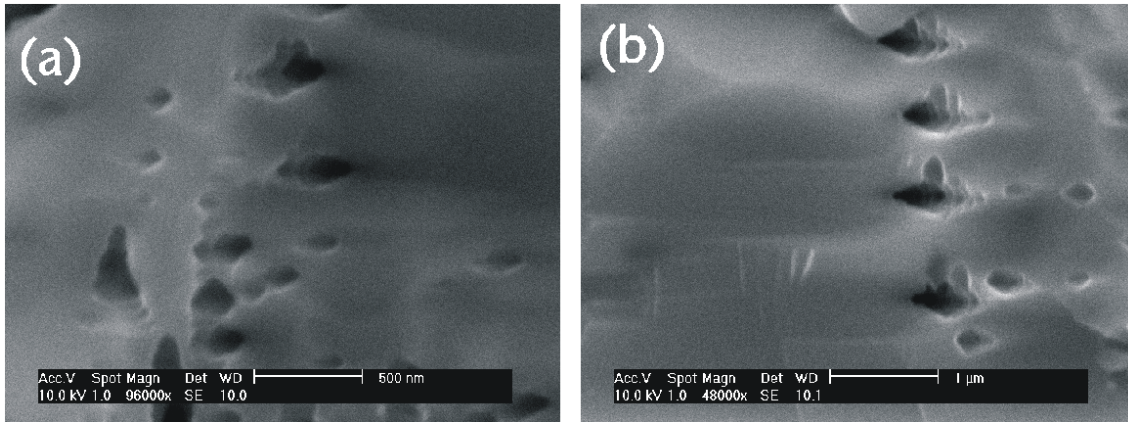


Figure 7.18: Influence of HF concentration on octahedral cavity growth ( $U = 12$  V,  $j = 1$  mA/cm<sup>2</sup>): (a)  $c_{HF} = 2$  wt%, (b)  $c_{HF} = 6.5$  wt%. A quantitative evaluation is given in Fig. 7.19.

the contact. This is the point where the mesopores die out. The rapid drop in the illumination efficiency ratio has two reasons:

1. While breakdown is possible, the etching current  $I_{etch}$  is supplied by both illumination and breakdown, i.e.  $I_{etch} = I_{BD} + I_{illu}$ . While  $U_{Si-HF} > U_{BD}$  the control algorithm regulates the illumination source to a low value to keep the overall current  $I_{etch}$  constant, i.e.  $\ln I_{etch}/I_{illu}$  is comparably high. When the breakdown stops, the illumination has to be strongly increased to keep the overall current constant.
2. The valence of mesopores is  $v = 2.0$  while macropores have  $v \approx 2.7$  [32]. The externally measurable valence is a mixture depending on the exact weighting of both processes. However, when the low valence process dies out, the total valence rises which in turn leads to a higher number of holes for the same etching current.

In conclusion, the pore morphology only depends indirectly on the absolute applied current density  $j$ . More important is the source of holes and the applied potential. The two growth modes can be summarized as follows:

- Macropores: Backside illumination (bsi) strongly favors this pore type. While still crystallography plays a role (cf. chapter 5) the  $\langle 100 \rangle$  - direction towards the illumination source is strongly favored. A certain amount of oxidation leads to smooth, rounded pores. Sharp kinks which would be starting points for side (meso-)pores are avoided.
- Mesopores: Growth depends strongly on the applied potential. The shape and orientation of the octahedrons is given by the directions of best (wall) and worst (tip) passivation. With low oxidative electrolytes octahedral shapes clearly evolve while strong oxidizing electrolytes lead to strongly rounded cavities. All  $\langle 100 \rangle$  tips show a rather equal probability (on a local scale) for breakdown and continuation of growth which explains the often found horizontal growth.

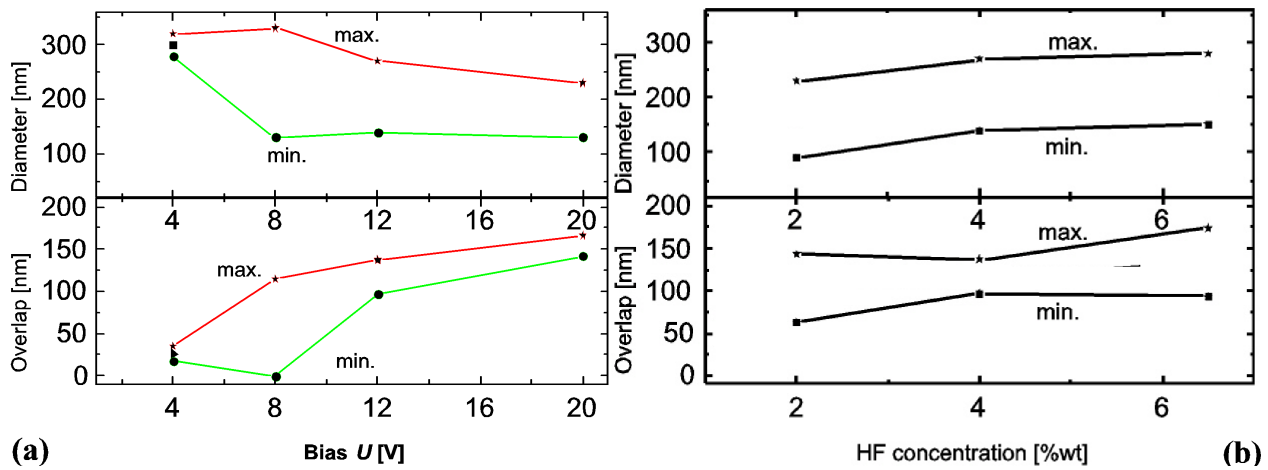


Figure 7.19: Evaluation of octahedron diameter and overlap versus applied bias (a) and HF concentration (b). The diameter decreases with increasing bias while the overlap rises. Both parameters increase when the HF concentration is increased.

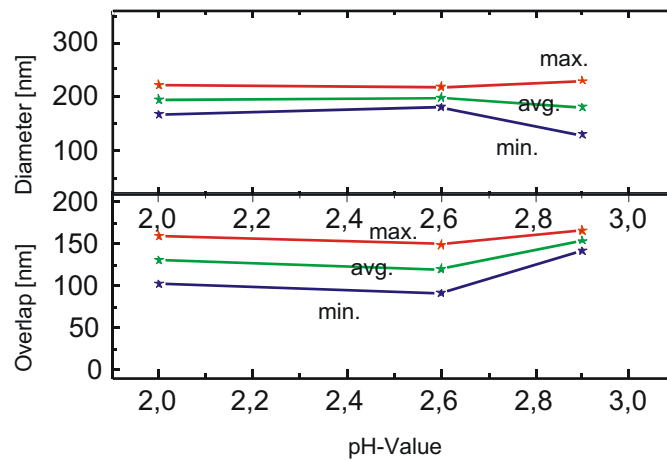


Figure 7.20: Evaluation of octahedrons' diameters and overlaps versus pH ( $c_{HF} = 4 \text{ wt}\%$ ,  $U = 20 \text{ V}$ ,  $j = 2 \text{ mA/cm}^2$ ): Neither the size nor the overlap of the octahedrons changes significantly during an acidification of the electrolyte.

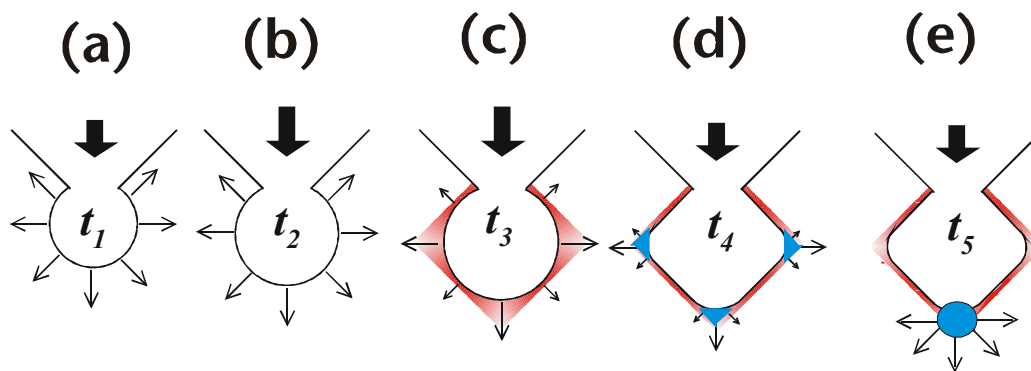


Figure 7.21: Growth sequence for octahedral chains. First, the new cavity grows isotropically because the local current density is very high and passivation cannot occur (a,b). With increasing size,  $j_{loc}$  drops and passivation (shading at cavity walls) gains influence (c,d), which transforms the sphere into an octahedron. The tips are the worst passivated  $\langle 100 \rangle$  - directions. During tip formation, the curvature there increases again (cf. also Fig. 7.23), which finally leads to the start of a new cavity (e).

### Model for the octahedral pore growth

Fig. 7.21 illustrates in more detail the underlying mechanism of the octahedral growth: When a new cavity has started the local current density  $j_{loc}$  is very high, so passivation cannot set in and the dissolution proceeds isotropically (a,b). With increasing cavity size the local current density decreases so far that passivation (red shading) can set in (c). Now, the best passivating (111) surfaces are not etched much further while the  $\langle 100 \rangle$  directions with the worst passivation of all crystallographic directions in silicon continue etching at a much larger speed (d). When most of the cavity walls are passivated, a new cavity starts at one of the tips, and the cycle repeats.

When regarded in the framework of the CBM, a high current density means that the current bursts are rapidly following each other (Fig. 7.22a). In the present experiments DMF was used as electrolyte which produces only negligible amounts of oxide and therefore oxide formation and dissolution is not included in the CBCs. When the local current density gets lower (because of a larger cavity) the CBCs have a longer duration (Fig. 7.22b) so passivation can set in between the direct dissolution parts of the CBCs.

Combining the experimental results for the overlap of adjacent octahedrons in Fig. 7.19, and taking into account that the electrical field strength is the decisive parameter to allow for the necessary avalanche breakthrough, the experimental results are consistent with the assumption that a new octahedra starts, as soon as a critical electrical field strength at a pore tip is reached. The field strength at a curved surface, where a certain voltage is applied to, increases with increasing curvature. In the case of the octahedrons this means that the field strength drops while the cavity grows isotropically because the surface curvature decreases (Fig. 7.23(a) time  $t_1$  to  $t_2$ ). When passivation sets in (Fig. 7.23(a) time  $t_3$ ) the curvature increases again in the area of the tip. Increasing the etching potential the necessary curvature to reach a certain effective field strength is smaller (Fig. 7.23b,c) and a new cavity can form earlier which increases the overlap of the octahedrons.

A pure isotropic reaction would only allow for  $o \geq d/2$  (i.e. the center of the new octahedron

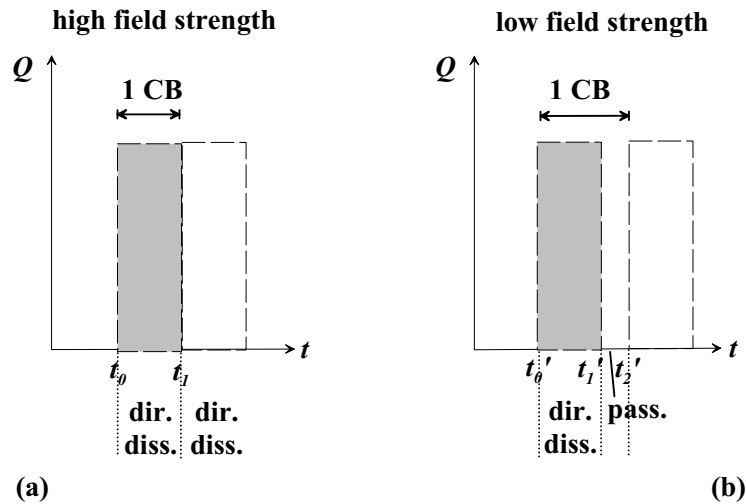


Figure 7.22: Current Burst Cycles (CBC) for high (a) and low field strengths (b). In case of a high field strength (a) a high number of holes is available and the CBC only consist of direct dissolution (oxide formation is neglected in this special case because it is largely suppressed in the used organic electrolytes). (b) With less field strength passivation can set in after the direct dissolution.

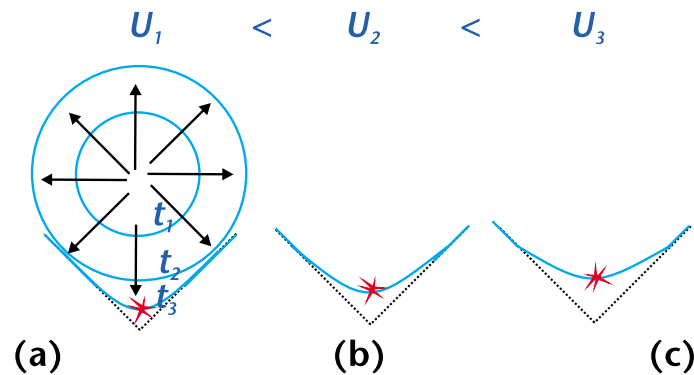


Figure 7.23: Model for the dependence of octahedral morphology on applied bias: The electrical field strength  $\vec{E}$  is the driving force to generate holes for the formation of octahedral cavities. Increasing the cavity diameter by isotropic dissolution (between time  $t_1$  and  $t_2$ ) reduces the curvature of the cavity and thus  $\vec{E}$ . When the preferential dissolution of the  $\langle 100 \rangle$  tips starts ( $t_3$ ), the curvature increases again. Assuming that a critical field strength is necessary to start a new cavity the curvature of the octahedral tips, a higher externally applied potential  $U$  leads to an earlier start of a new octahedron (b, c).



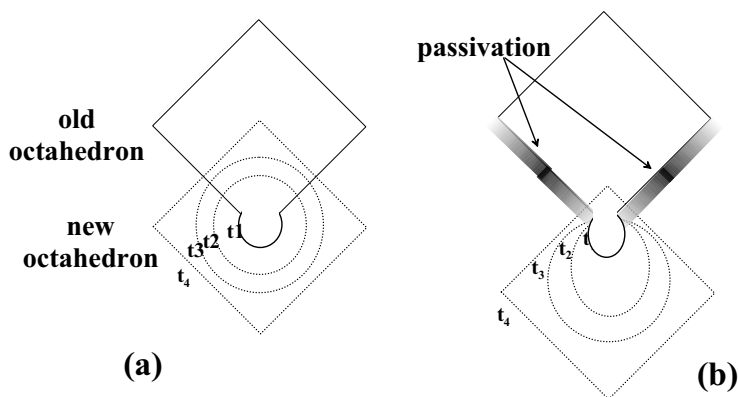


Figure 7.24: If the surface passivation in the old octahedron is weak (a) then it is possible to closely stack the octahedrons, which also necessitates that some portions of the walls are back etched. Under strong surface passivation (b) the walls of the old octahedron and their surface passivation “squeeze in” the oxidative growth so that the pitch between adjacent octahedrons gets larger than  $d/2$ .

is at the tip of the old octahedron) which is obviously not the case at low voltages (Fig. 7.19). One possible explanation (among several more) for this behavior is that a behavior like this would also call for a “back etching” of already formed out octahedral walls (Fig. 7.24), which are protected by H-passivation and the large space charge region in the silicon. Therefore especially at low potentials, where the H-passivation is a significant protection, the cavity growth could first be squeezed slightly and the center of the new octahedron would then be lower than the tip of the old one and smaller overlaps become possible (Fig. 7.24). See

The changes in diameter due to HF changes are in contradiction to other experimental observations (cf. section 7.1 and [45]) where mesopores shrink with the increase of  $c_{HF}$ . In the present experiments these results might be due to the large span of diameters measured for each concentration which would also allow to insert a falling trend line. In any case these data should be verified with a finer scaling for the concentration as well as maybe with a different tool like the transmission electron microscope (TEM) or a high-resolution SEM (HRSEM) to allow any further interpretation. Therefore the overlaps shall also not be discussed further in this case, because they are calculated using the diameter.

The change of the pH showed no clear influence on the diameter or the overlap (Fig. 7.20). A shift to more acidic pHs (from 2.9 to 2.0) should only have minor influence on the concentration of (undissociated) HF (responsible for the H-passivation of the surface (cf. Fig. 3.1 and 4.7) and the oxide dissolution).

## 7.3 Fast macropore growth

### 7.3.1 Introduction and experimental set-up

Macropores in n-type silicon can be grown with an extremely high structural quality when using aqueous HF in combination with backside illumination (cf. section 5.2.1). However, this is bought at the price of a slow growth speed ( $1 \mu\text{m}/\text{min}$ ). From an application point-of-view, an etching time of 14 hours and more to etch through a single wafer of  $525 \mu\text{m}$  (e.g. for the production of stable membranes) hinders effective mass production which will be certainly necessary as soon as more products based on macro PS arise. Furthermore, the domain of sub- $\mu\text{m}$  macropores grown with the conventional backside illumination (bsi) technique requires highly doped silicon with an extremely good diffusion length which is not easily obtained. With bsi only pore diameters down to 350 nm have been realized [161]; smaller pores do not seem possible with bsi. On the other hand, the growth rate of mesopores in n-type silicon (cf. sections 5.2.2 and 7.1) is strongly increased with HF concentration and current density allowing for growth velocities up to  $v = 100 \mu\text{m}/\text{min}$  [32]. The pore size can be tuned by e.g. the HF concentration as shown in section 7.1 although it is not clear where and if here a fundamental upper limit exists. The decisive drawback of mesopores is their mediocre morphology, i.e. the pores are often highly branched and serrated which makes e.g. coating processes for applications like fuel cells a much harder task than for the very regular macropores.

In InP two types of pores exist (cf. section 5.3): Crystallographically ("crysto") oriented pores which grow at low current densities and current-line ("curro") oriented pores with submicron sizes that grow at high speeds ( $\geq 10 \mu\text{m}/\text{min}$ ). The curro size can be varied between 50 nm and 2000 nm with an exceptionally good pore quality. The approach in the following section was to emulate the curro conditions in Si, i.e. to multiply the growth speed to economically reasonable values while keeping a structural quality like bsi macropores. An additional goal was to produce "nice" macropores in the previously unreachable size region below 350 nm. To achieve these goals the implications of the current burst model (CBM, cf. section 4.6.2) guided the optimization of the experiments: A first prerequisite to reach higher growth speeds is of course a higher current density  $j$ . From the analysis of the situation in InP in the spotlight of the CBM, it turns out that there are at least three other features which make the curro mode in InP unique:

- carrier generation by electrical breakdown
- less oxidation
- closest packing of the pores (leading to an effective passivation of the walls via depletion).

Implementing this for the Si-HF system, the resistivity of the Si should be low enough to make breakdown currents possible at acceptable voltages ( $U < 50 \text{ V}$ ). Organic electrolytes have a strongly reduced oxidation power, therefore being desirable candidates, while a drastically higher HF concentration  $c_{\text{HF}}$  should be chosen to allow for a faster dissolution of the oxide which is scaling almost linearly with the HF concentration. In conventional macropore growth this doesn't lead to good results because the stability of the pore walls decreases rapidly as soon as  $c_{\text{HF}}$  is increased. Thus, a high  $c_{\text{HF}}$  renders deep pores ( $t > 250 \mu\text{m}$ ) impossible with the bsi technique. Therefore, a dense nucleation and hence a close packing of the pores is essential for passivation.

The experiments were carried out using the etching setup with the peristaltic pump (cf. section 6.1.2) (pump rate always 100 r.p.m.). The samples were etched in potentiostatic mode ( $U = 20 - 50$  V) as well as in galvanostatic mode ( $j = 50 - 180$  mA/cm<sup>2</sup>). In some experiments one or several short high voltage pulses ( $U = 50$  V for  $t = 0.1 - 0.2$  min) were used to enhance the pore nucleation. The temperature was kept constant at  $T = 15, 20, \text{ or } 25$  °C. The etching time was in all experiments  $t = 60$  min except otherwise noted.

The electrolytes were either based on (deionized) water or organic electrolytes (N,N - dimethylformamide (DMF), Merck Inc., No. 103053, p.a. grade or acetonitrile (MeCN) Merck Inc., No. 100003, p.a. grade). In several experiments, tetrabutylammonium perchlorate (TBAP, Fluka Inc., No. 86893 (puriss.) or 86885 (purum)) was added as a conducting salt. The HF base solution was 48 wt% hydrofluoric acid (Merck KGaA, No. 100334, p.a. grade) in the case of aqueous electrolytes, while with the organic electrolytes 73 wt% HF (Fluka Inc., No. 47610 (techn.)) was used to avoid as much residual water from the HF base solution as possible. The electrolytes were immediately bubbled with nitrogen after mixing. Except otherwise noted the bubbling stayed on as long as the electrolyte was in use. The final HF concentrations were between  $c_{HF} = 12 - 20$  wt%. In all experiments with aqueous electrolytes 0.5 ml surfactant (WAKO Inc., Nr. NCW - 601A, cf. section 2.4.2 for detailed information about the used surfactants) was added to an electrolyte volume of 300 ml. In a series of experiments with MeCN the following commercially available surfactants from Clariant Inc. were compared to the results with the WAKO surfactant:

- anionic (Genapol LRO liquid)
- cationic (Dodigen 226)
- non-ionic (Genapol UD 088)

Commercially available n-Si (111) and (100) (MEMC,  $\rho = 10$  m $\Omega$ cm, resp. 0.7 - 1.0  $\Omega$ cm) were employed, using GaIn for an ohmic backside contact. The samples were analyzed after the etching by optical microscopy as well as by SEM (Philips XL30) in cross section and plain view.

## 7.3.2 Experimental results

### Aqueous electrolytes

In a first series, similar samples (n(111),  $\rho = 0.014$   $\Omega$ cm) like in section 7.1 were etched galvanostatically in  $c_{HF} = 5$  wt% aqueous HF. At  $j = 10$  mA/cm<sup>2</sup>, a voltage of 0.1 - 0.5 V was necessary which produced a crater with a depth of 11 - 16  $\mu$ m whose bottom was covered with a 5  $\mu$ m thick mesoporous layer (Fig. 7.25a). The diameter of individual pores could not be resolved. As indicated in section 5.2.2 the diameter shrinks with decreasing current density, so the results from section 7.1 ( $j = 30$  mA/cm<sup>2</sup>) suggest that the pore diameter in this case should be below 50 nm. Increasing the current density to  $j = 80$  mA/cm<sup>2</sup> required voltages between 2.6 and 2.7 V. The result was an electropolished crater which was not further analyzed. Using  $c_{HF} = 15$  wt% and  $j = 80$  mA/cm<sup>2</sup> a 130  $\mu$ m deep crater was formed (Fig. 7.25b) which was decorated with a 20 - 60  $\mu$ m thick mesoporous layer (Fig. 7.25c) for which again the individual pores could not be imaged. The necessary voltage was 1.4 V.

Similar experiments were conducted with medium doped wafers (n(111),  $\rho = 0.4 - 1.02$   $\Omega$ cm). With  $c_{HF} = 5$  wt% and  $j = 10$  mA/cm<sup>2</sup>, voltages between 15 and 45 V were necessary.



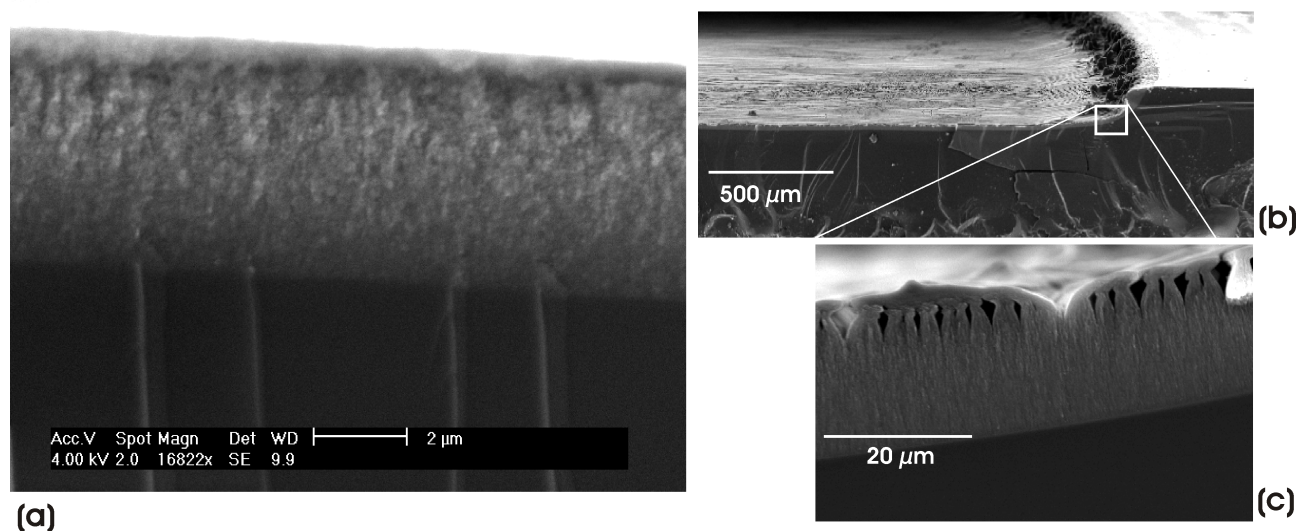


Figure 7.25: SEM cross sections of etched  $n^+$  wafers: (a)  $c_{HF} = 5 \text{ wt\%}$ ,  $j = 10 \text{ mA/cm}^2$ , a crater with a depth  $11 - 16 \mu\text{m}$  developed whose bottom is a  $5 \mu\text{m}$  thick mesoporous layer (which is shown in (a)); (b)  $c_{HF} = 15 \text{ wt\%}$ ,  $j = 80 \text{ mA/cm}^2$ , the sample mainly electropolished ( $t = 130 \mu\text{m}$ ) with a  $20 - 60 \mu\text{m}$  meso layer at bottom; (c) Magnification of (b) shows mesoporous layer near O-ring where probably mechanical stress caused large voids near top of the mesoporous layer. The pore size was not resolvable.

The cross sections (Fig. 7.26a,b) show a top layer of submicron sized pores with a depth of  $t = 20 \mu\text{m}$ . At several spots semispherical breakouts (“hanging hedgehogs”) formed below the top layer with depths of up to  $100 \mu\text{m}$ . Interestingly, the mesopore morphology of the top layer directly above such a “hedgehog” (Fig. 7.27a) consists of tiny, fir-tree shaped pores with a high porosity while at places where no breakout happened (Fig. 7.27b) the layer is perforated by needle-like pores with a lower porosity. The morphology of pores clearly changes from the mesoporous top layer to larger pores in the semispherical bulbs. A void of approx.  $10 \mu\text{m}$  thickness separates the “hedgehogs” from the substrate around it, where a third, even larger type of pores started to grow. Albeit the radiant look of some parts of these structures a close inspection shows that all pores probably run along  $\langle 100 \rangle$  directions.

At higher current densities ( $j = 80 \text{ mA/cm}^2$ ), similar voltages were necessary ( $U = 28 - 42 \text{ V}$ ). In this case, again a submicron pore layer ( $t = 75 - 85 \mu\text{m}$ ) was on top of some cavities with depth up to  $200 \mu\text{m}$  (Fig. 7.26(c,d)). Unlike the results at lower current densities the pores below the top layer were often completely destroyed, only leaving a semispherical cavity. With a higher HF concentration ( $c_{HF} = 15 \text{ wt\%}$ ,  $j = 80 \text{ mA/cm}^2$ ), the switch in morphologies disappeared (Fig. 7.26(e,f)). Pores with a diameter of  $d = 1.2 - 2.4 \mu\text{m}$  grew down to a depth of  $t = 180 - 250 \mu\text{m}$  at the bottom of a shallow crater of  $10 - 20 \mu\text{m}$ . Again, albeit the pores sometimes mimic a current line growth (cf. Fig. 7.26e), they still follow mainly the preferential crystallographic directions (Fig. 7.26(f)). The etching voltage stayed in a more narrow range ( $U = 24 - 26 \text{ V}$ ) than for the low HF concentration experiments.

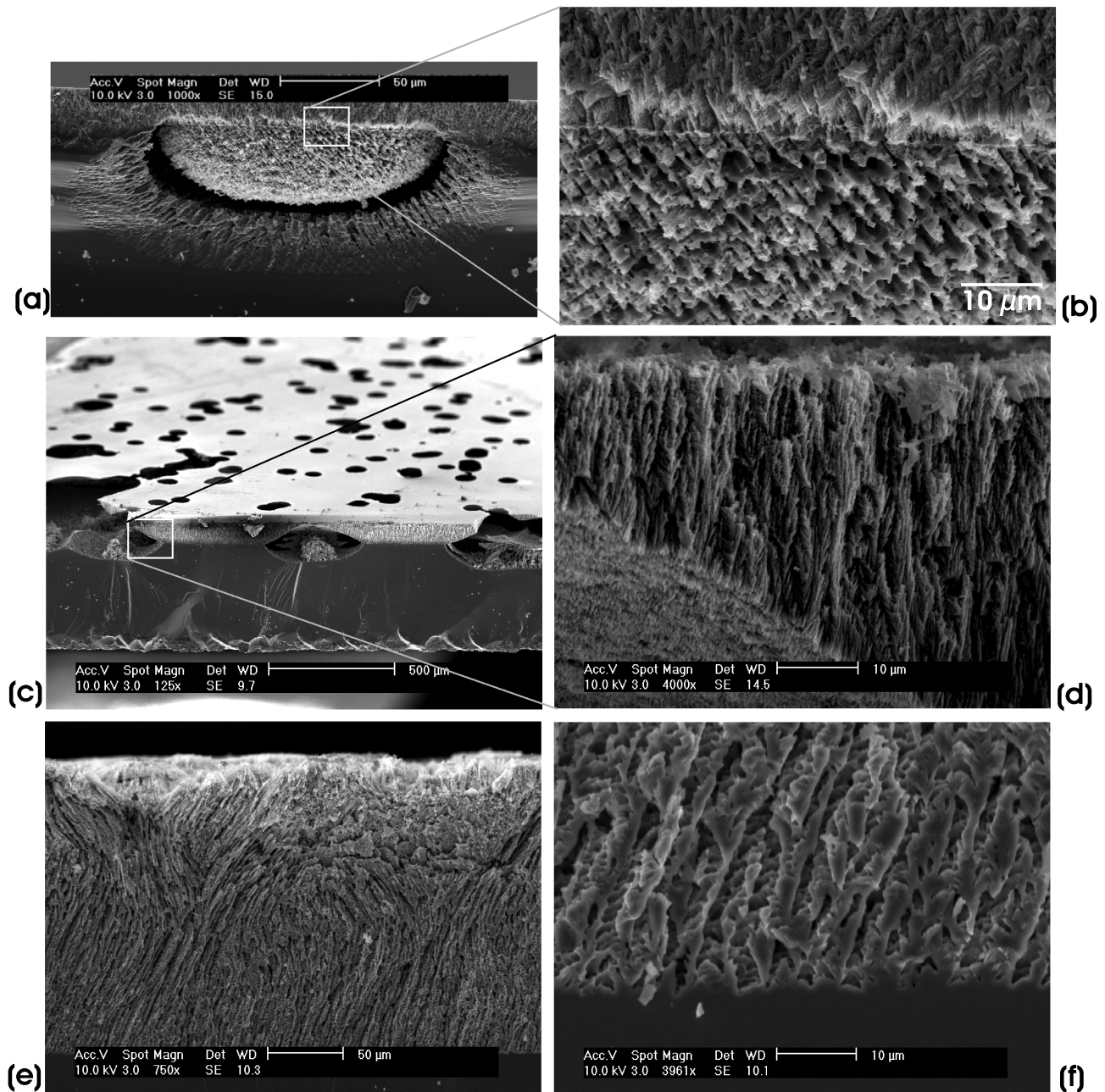


Figure 7.26: SEM cross sections of etched 0.7 Ωcm n-type wafers: (a)  $c_{HF} = 5 \text{ wt\%}$ ,  $j = 10 \text{ mA/cm}^2$ , a mesoporous layer covers some semispherical breakout spots with larger pores. (b) Magnification of (a). (c) At  $j = 80 \text{ mA/cm}^2$ ,  $c_{HF} = 5 \text{ wt\%}$ , the top layer is thicker, and the breakouts develop into completely empty cavities. (d) Magnification of (c). (e)  $c_{HF} = 15 \text{ wt\%}$ ,  $j = 80 \text{ mA/cm}^2$ : A single layer of micron sized pores results. (f) Magnification of (e).

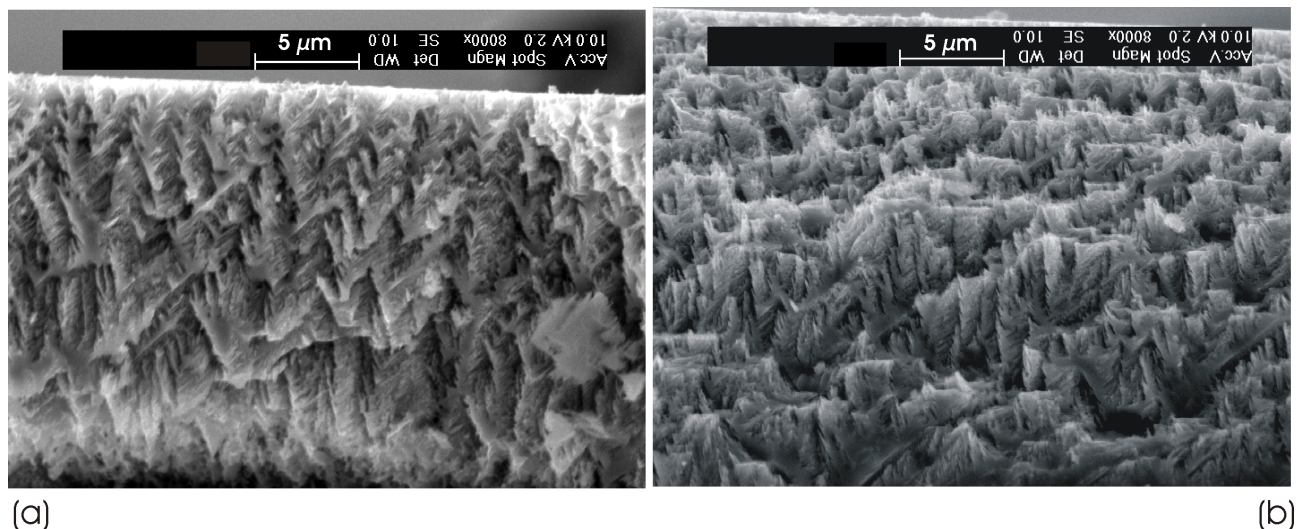


Figure 7.27: Morphology of the top mesopore layer from Fig. 7.26(a): (a) Directly above “hedgehog”. (b) Adjacent top layer parts where no “hedgehog” grew.

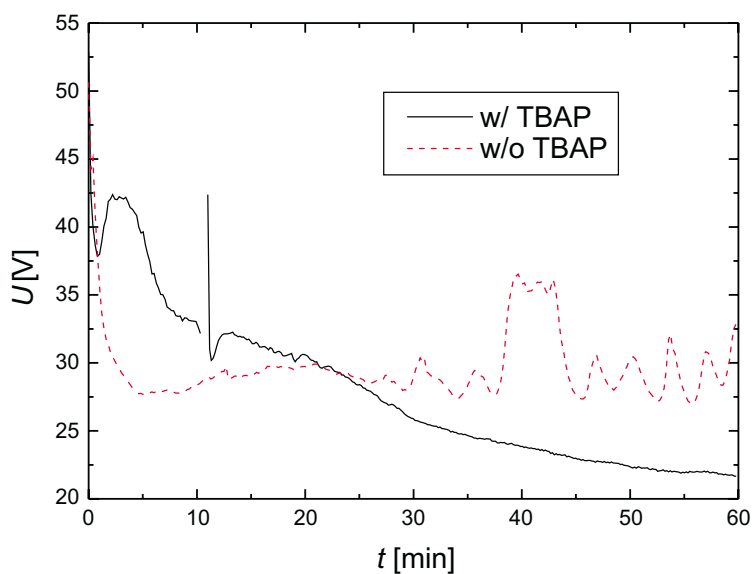


Figure 7.28: Voltage transients of n-Si (100) in 15 wt% HF/DMF (red/dashed line) and HF/DMF/TBAP (black/solid line). Without TBAP the voltage drops from initially high values around 50 V down to 30 V, where it stays for 30 minutes. In the last 30 min pronounced oscillations are visible in the transient. Upon the addition of TBAP the voltage always exhibits a short dip after the etching is switched on (at start and also after 11 min, where the etching was shortly stopped). Overall, the voltage continuously decreases from over 40 V to 22 V at the end of the etching.

## DMF based electrolytes

To suppress oxidation as far as possible the next series of experiments was conducted with DMF based HF using (100) as well as (111) wafer. Because the results on  $n^+$  wafers in aqueous solutions showed almost only electropolishing covered with some mesoporous remainders, all further experiments were only continued on medium doped wafers. Similarly, only experiments using the high HF concentration ( $c_{HF} = 15 \text{ wt}\%$ ) were conducted, because the inhomogeneous morphology at 5 wt% aq. seemed little promising.

Without a conducting salt, the etching potential dropped in the first five minutes from over 50 V to 28 V (Fig. 7.28). After that it stayed for most of the etching around  $30 \pm 3 \text{ V}$ , exhibiting pronounced oscillations with a period of 2 - 4 minutes. When adding TBAP the potential dropped only for one minute from over 50 V down to 38 V and then rose again to 42 V after approx. 4 min from the start. At 11 minutes the etching was shortly stopped due to technical reasons. After it was again switched on, again the voltage exhibited a short dip before it merged into the behavior before the switch-off. Neglecting the short shut down at 11 minutes, the voltage dropped continuously down to 22 V at the end of the etching. It was not possible to fit the curve with a simple function properly, e.g. exponential or power law.

Fig. 7.29 shows the morphology of (111) wafers etched in DMF without TBAP. Mostly the etched layer either fell off directly during the etching or during rinsing afterwards, which left a crater of approx.  $150 \mu\text{m}$  depth. At the bottom of this crater a puff pastry like structure (Fig. 7.29e) with a total thickness of approx. 35 microns remained for imaging. The voltage transient of the (111) sample exhibited similar oscillations like for the (100) sample (cf. Fig. 7.28), which suggests a direct link between the voltage oscillations and the layered morphology. Each of the layers (Fig. 7.29f) is 2 microns thick and consists of porous silicon with very small pores in the sub-100 nm regime which could not be individually resolved. The layers are separated by 700 to 1000 nm which are (almost) void. The surface (Fig. 7.29 (a-c)) exhibits far reaching tripod structures. They are composed of grooves with triangular cross section where the groove walls are decorated with pores of a much smaller dimension. Below these elevated structures (b,c), also planar ordering structures with three fold symmetry are visible (d) that extend over 100 microns. In all structures the same three crystallographic directions (or projections in the case of the planar structures) occur which are likely to be the  $\langle 100 \rangle$  directions.

When TBAP is added to the solution, most of the porous layer remained stable during rinsing. In cross section (Fig. 7.30(e-g)) pores with a diameter of 350 to 520 nm and a length of 200 to  $250 \mu\text{m}$  are visible, which grow perpendicular to the surface, i.e. along a  $\langle 111 \rangle$  direction which is normally a stop direction for etching in silicon. The images in Fig. 7.30 (a-d) show the surface with increasing depth: (a) The uppermost part of the surface exhibits a mountain like structure with tripods, which look similar to the case without the addition of TBAP (cf. Fig. 7.30(a-d)). (b-d) Below that complex three-dimensional network, the pores grow perpendicular and show several size and ordering stages: The pores show sizes between 1 and  $5 \mu\text{m}$  and no ordering (upper left corner of (b)). In the next layer the majority of pores is 3 -  $4 \mu\text{m}$  sized and a certain degree of arrangement becomes visible (middle part of (b)). Looking deeper, the pore size drops significantly to  $d \approx 320 \text{ nm}$  (c). Finally, the pores arrange in a (yet poly crystalline) self-ordered hexagonal lattice with an interpore distance (= pitch)  $p = 450 \pm 50 \text{ nm}$  and pore diameters  $d = 350 \pm 50 \text{ nm}$ . The walls between the pores are at many regions less than 100 nm thick which explains the fragility of the porous layer in cross section: If the pores (almost) touch each other, the remaining silicon structures are thin triangular wires in the center of the pore triangles which are connected to each other by thin films of silicon.



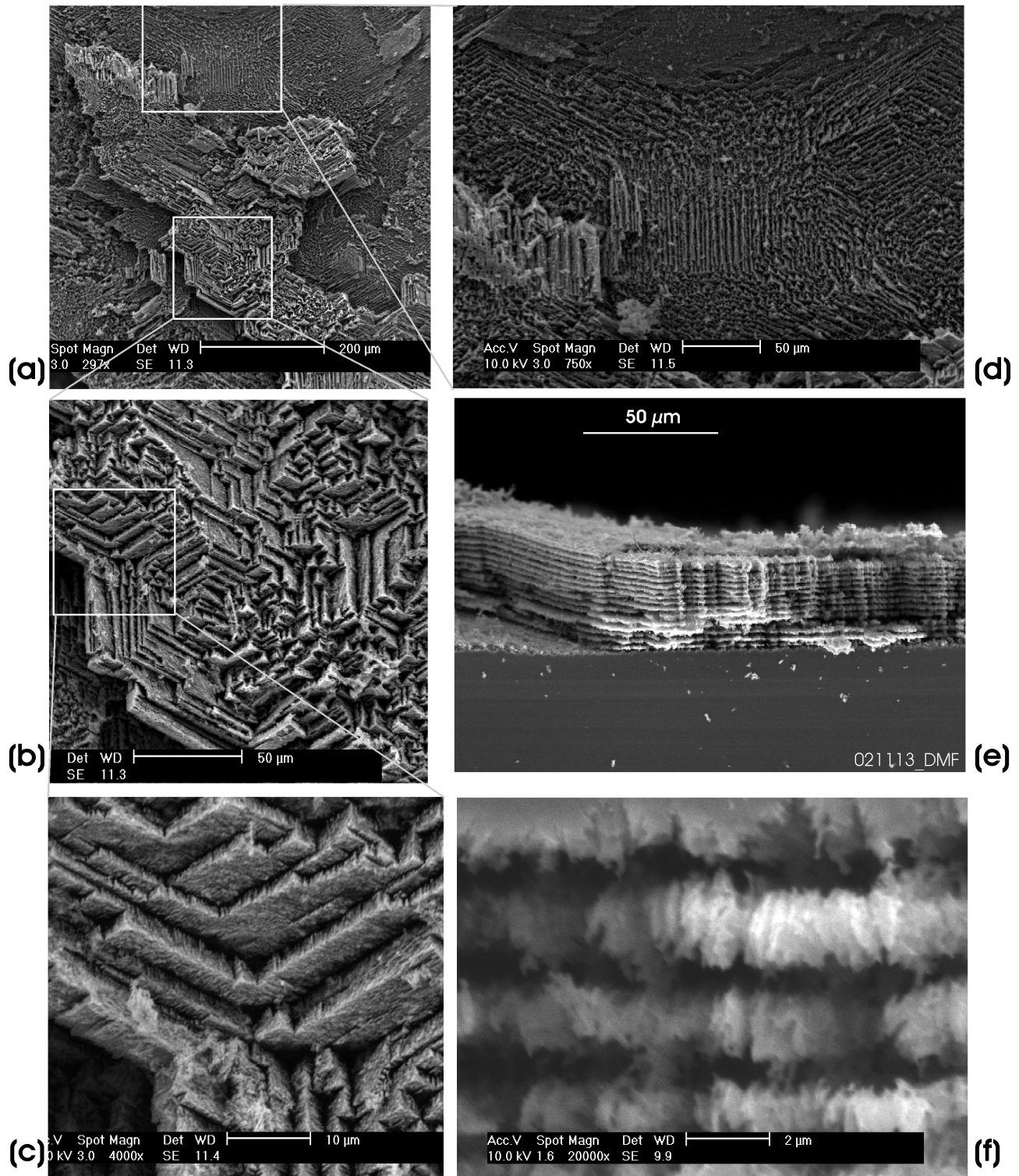


Figure 7.29: SEM images of n(111) wafers etched 15 wt% DMF: (a-d) surface in different magnification levels; (e-f) cross section.

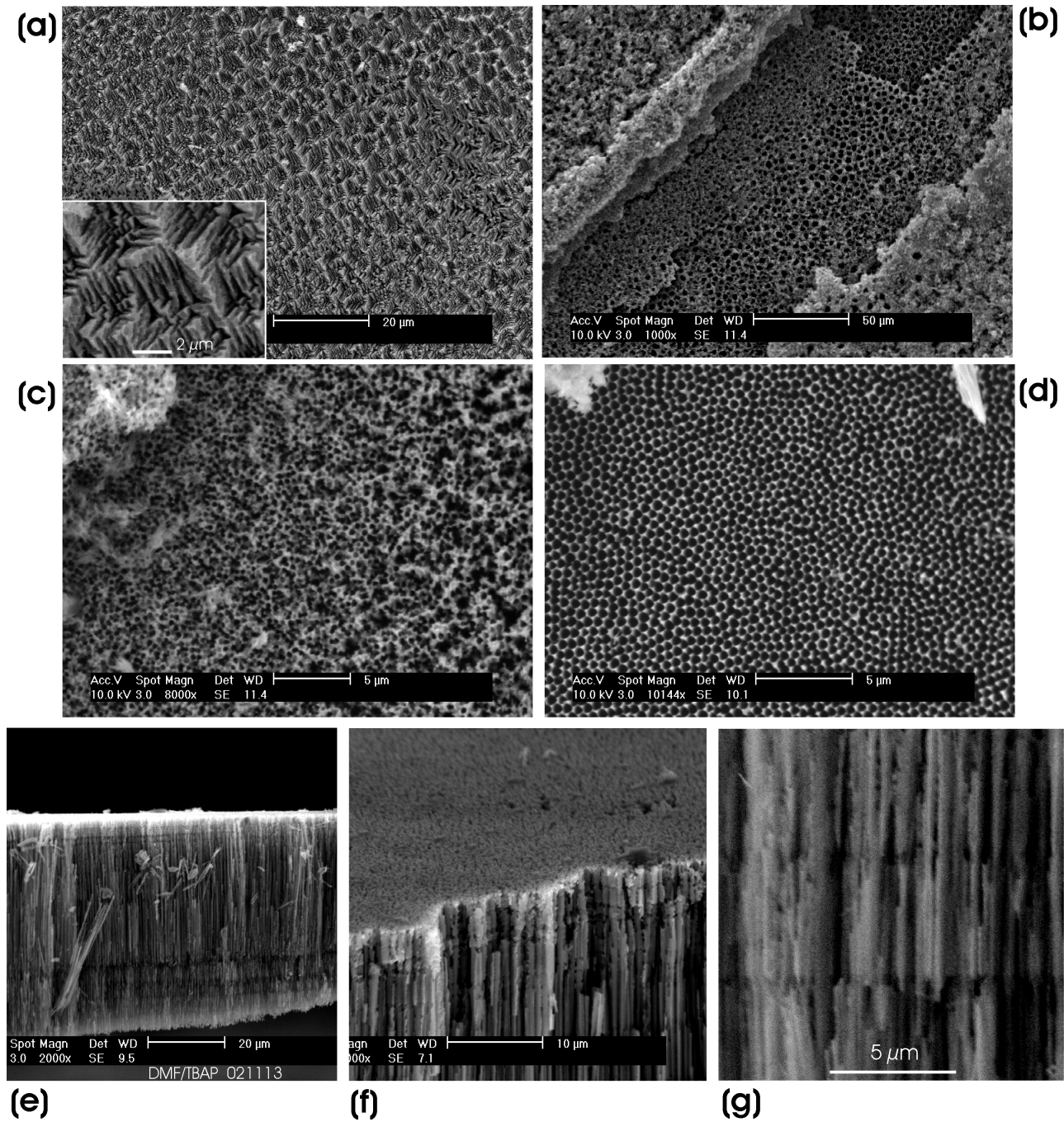


Figure 7.30: SEM images of n(111) wafers etched with 15 wt% DMF/TABP: (a-d) surface with increasing depth (Inset of (a): magnification of (a)); (e-g) Cross section, untilted (e), tilted (f), and at higher magnification (g).

When the thin connections break, the silicon wires fall out of the structure as it is shown in Fig. 7.30(e).

### MeCN based electrolytes - general observations

Before the results for etching in MeCN (where most of the experiments were done) are discussed in detail, several remarks on the behavior of the system shall be made to explain the extreme diversity of results.

One major challenge in the interpretation of this pore system is its strong history dependence: It has been shown in InP (section 5.3) that the diffusion of certain species becomes strongly limited in a crystal pore layer. When the limitation has reached a certain degree (depending on the actual experimental parameters like current density, acid concentration, substrate doping, etc.) the pore growth switches to curro mode, i.e. the pores grow perpendicular to the equipotential lines. Always such a limiting crystal layer has to build up before the curro mode can start, even if the etching is only switched off for some seconds [96]. This implies that the actually growing pore type is - for this type of pores - NOT only given by the current density  $j$  and other external parameters but also by the “history” of the spot on the sample. This concerns as well a dependence on time (e.g. “Has the etching been suspended?”) as well as in space: e.g. when the porous layers above already pose a strong diffusion limitation, the thickness of the crystal layer after a break will be thinner than starting from a fresh surface.

The same kind of considerations are true for the growth regime in silicon which has been investigated here. The experiments with MeCN show that the pores which grow at a certain depth depend extremely on the “history” above that spot. Several scenarios have been encountered during the experiments:

- A membrane (Fig. 7.31c) lifted off during the etching accompanied by a heavy drop in the potential (Fig. 7.37). The pores on the original surface are very small (Fig. 7.31c), but widen until they get very unstable, i.e. have very thin walls compared to the diameter. After the lift-off, small, stable pores renucleate on the bottom of the large pores (cf. Fig. 7.31d).
- Some parts of the sample show large voids (Fig. 7.34), which originate probably from highly porous sample regions that collapsed during the etching. This of course offers totally different diffusion conditions for the pores below.
- The pores go through different size regimes (Fig. 7.34 and 7.31). The exact reason for the switching point is often a) unclear and b) not visible in the electrical signal because it happened only on a part of the sample (see also the following paragraphs).
- After initial nucleation on a fresh surface the pores spread in the volume often via two different mechanisms (Fig. 7.32 and 7.33): a) Small crystal pores which branch along crystallographic directions into the depth. b) Bigger holes which rapidly fan out into numerous large pores below the hole. These two pore types compete to occupy all available surface. This competition depends to a large variety of factors (density of large holes, size of large holes, branching frequency of both types...)

Another effect which is uncommon to most other pore types is that practically the only passivation mechanism for the pore walls is a close packing of pores. Of course also for bsi pores a close packing of pores is necessary for best results but growth with similar morphology

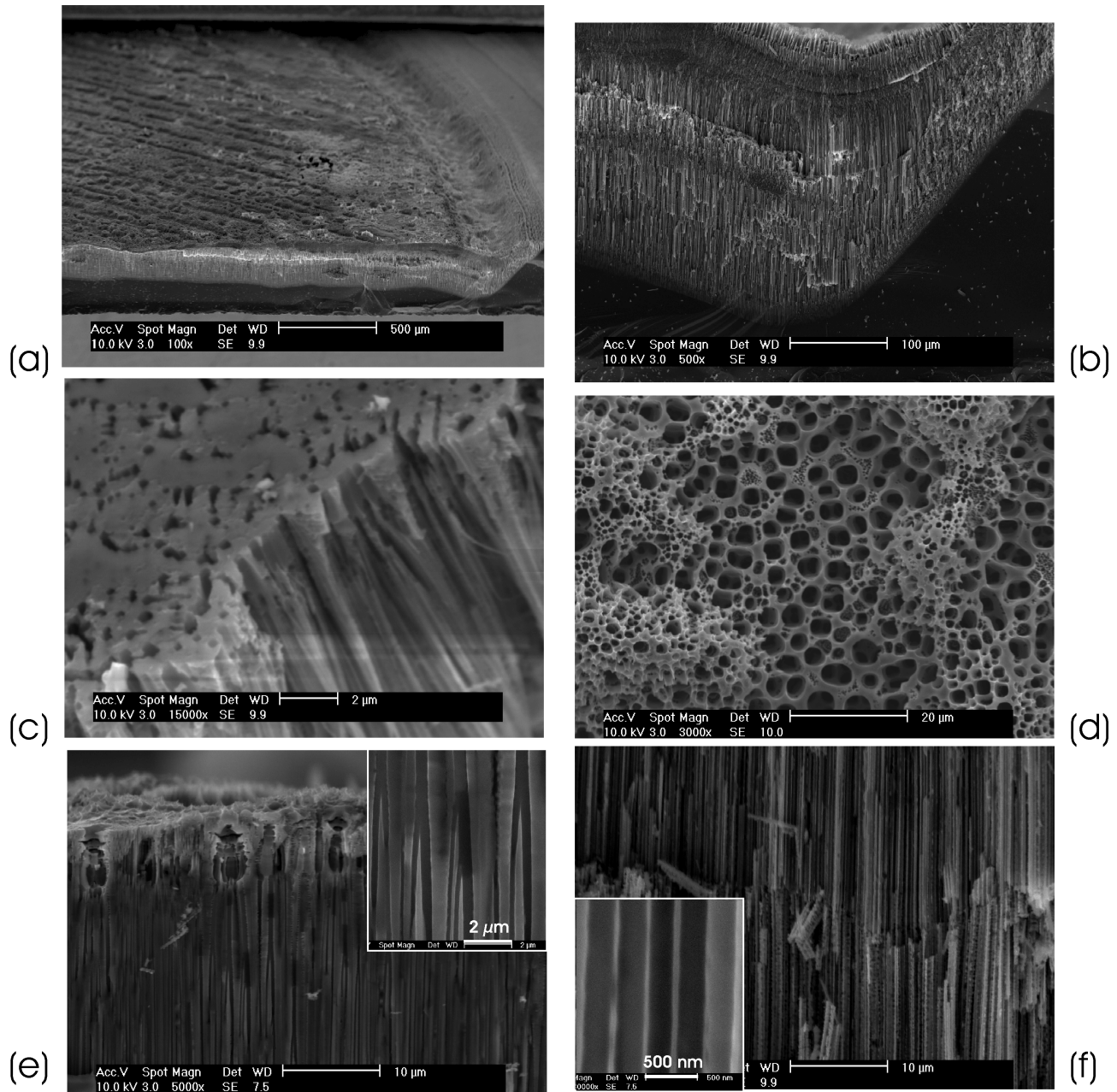


Figure 7.31: SEM gallery of n-Si (100) in 15 wt% MeCN/TBAP etched 60 min @ 25 °C: (a) Overview of tilted cross section and surface. Because a membrane has lifted off during etching the surface is rough. Near the o-ring a depression ( $\approx 50\mu\text{m}$  deep) is visible. (b) Magnification of cross section at o-ring. The pores go through several size regimes. (c) Cross section and surface of the membrane ( $d \approx 200 - 400 \text{ nm}$ ). (d) Surface of the sample (beneath the membrane), big pores ( $d \approx 3 - 4 \mu\text{m}$ ) combined with several different types of submicron pores. (e) Upper part of cross section towards the middle of the sample: After a chaotic surface with a variety of larger cavities, smaller pores ( $d = 140 - 410 \text{ nm}$ ) are developing (Inset: Magnification of pore splitting). (f) Deeper part of cross section shows smooth pores ( $d \approx 250 \text{ nm}$ , inset shows magnification) which can switch collectively to a growth mode with rougher walls (lower part of picture).



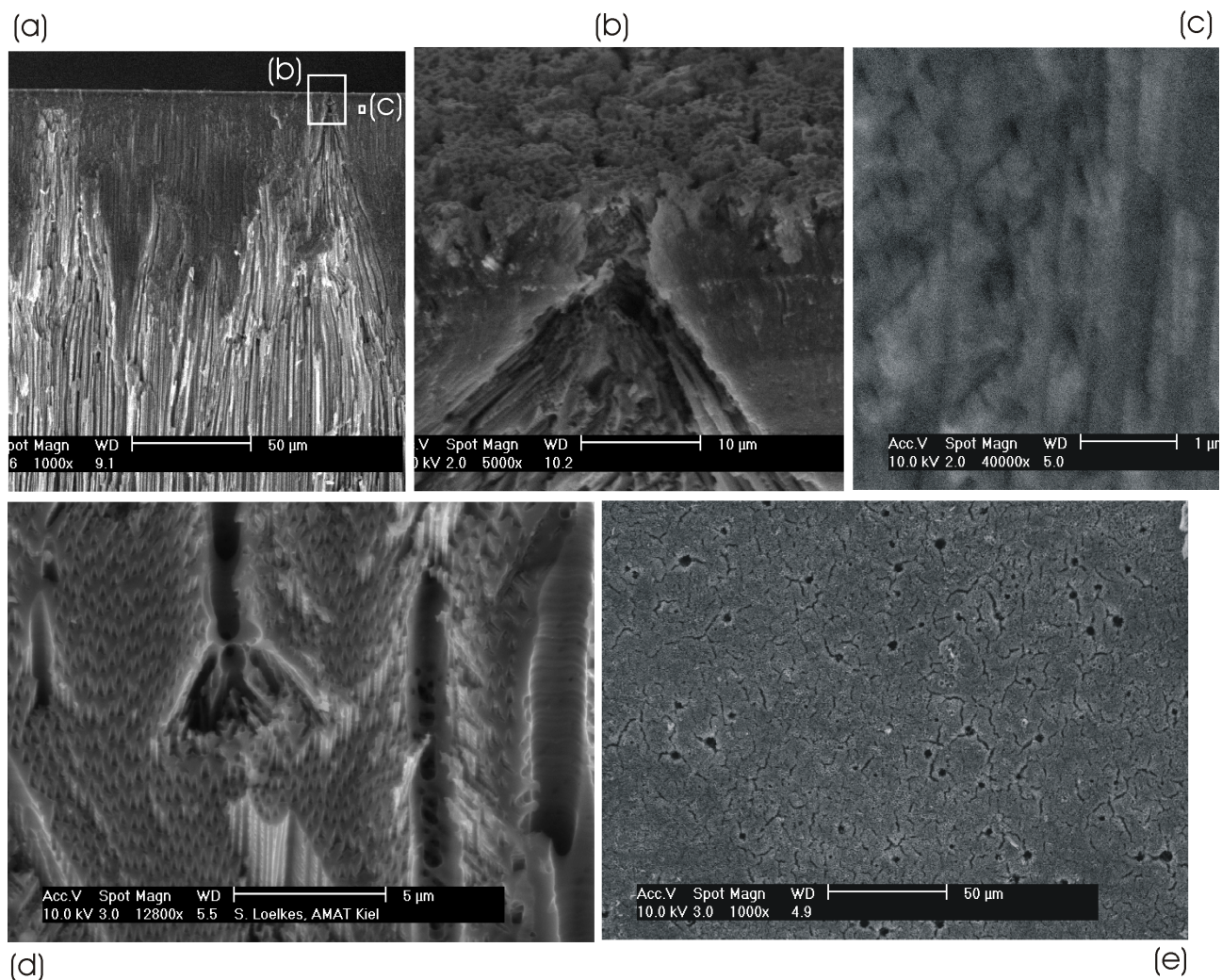


Figure 7.32: Pore types and spreading mechanisms (n-Si (111) in 15 wt% MeCN/TBAP etched 60 min @ 20°C,  $j = 80 \text{ mA/cm}^2$ , 0.1 min 50 V pulse at start): (a) Overview of cross section; at the top of the sample, several large funnels (b) ( $d \approx 5 \mu\text{m}$ ) quickly spread into a multitude of  $d \approx 1 - 2 \mu\text{m}$  pores. Between the funnels very small pores (c) ( $d \approx 30 - 90 \text{ nm}$ ) are found which are superseded completely after 90  $\mu\text{m}$  of etching. (d) Bevelled cross section of the upper part shows the coexistence of both pore types from (b) and (c). (e) Surface image.

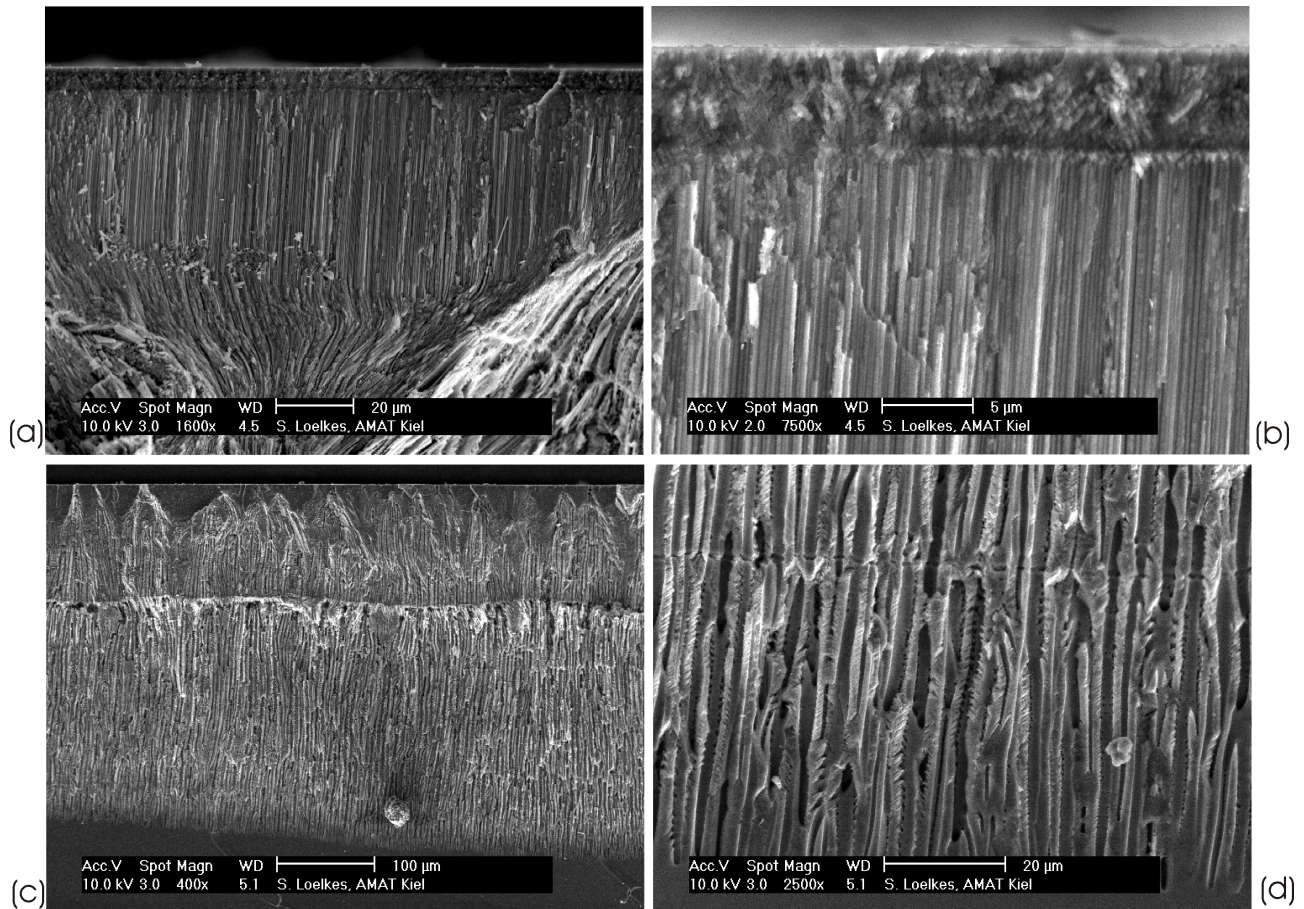


Figure 7.33: Different nucleation types (n-Si (111) in 15 wt% MeCN/TBAP (0.11 M) etched 60 min @ 20°C,  $j = 80 \text{ mA/cm}^2$ , 0.1 min 50 V pulse at start and after each 10 minutes): (a) Most of the surface is covered by 5  $\mu\text{m}$  thick layer of cristo pores, below which thin curro pores start. At the bottom corners, funnels with larger pores can be seen, which cut the way of the thin cristo pores. (b) Magnification of the cristo-curro transition. (c) Overview of sample cross section. (d) The pore tip region in a depth of 390  $\mu\text{m}$ .

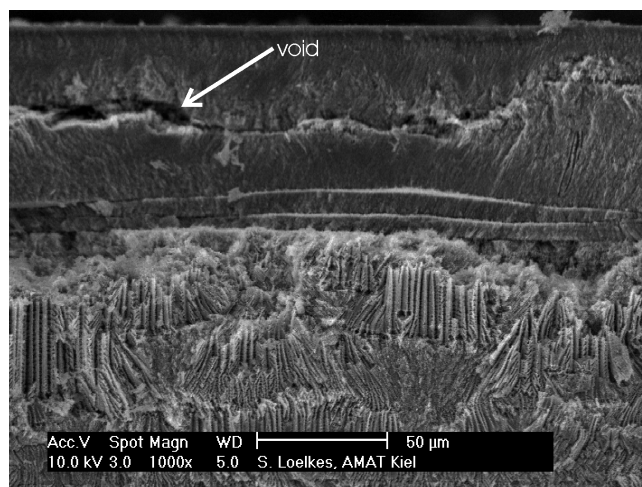


Figure 7.34: Pore variety within a single sample (n-Si (111) in 15 wt% MeCN/TBAP (0.05 M) etched 60 min @ 20°C,  $j = 80 \text{ mA/cm}^2$ , 0.1 min 50 V pulse at start): Although the electrolyte was fresh and  $\text{N}_2$  bubbled and the etching proceeded without current breakdowns (cf. text), the sample shows a whole zoo of different pore types.

still remains possible with a substantial distance between the pores [58]. In the present case however, the mandatory short distance between pores leads also to a larger interaction between pores. It is already known from InP [95] that in *curro* pore ensembles the interaction between the individual pores is strong, e.g. oscillating pores synchronize. On the other hand, this correlated growth induces also that a "misbehavior" of a single pore often lashes back on a larger ensemble. In the present experiments the following collective phenomena have been observed:

- Pores start to oscillate (Fig. 7.35(a,b)).
- Pores branch at the same time (Fig. 7.36).
- Pores change their direction synchronously (Fig. 7.35(c)).

Combined with the "history" effect explained above this often led to samples which are divided into a variety of different regions (cf. Fig. 7.34), albeit the etching cell itself has shown in other cases extremely homogeneous behavior, i.e. this is most probably a system inherent feature. The factors (externally as well as internally induced) which can lead to such a behavior are numerous and especially during the first experiments were not always clear, and many of the results suggest that some of these factors are not clear even after almost 150 experiments. To some extent, one can call this a chaotic system similar to the case of pool billiard. Although the whole physics behind each collision of two balls is known in theory, it has been shown to be unpredictable how the balls will exactly distribute after the opening break because tiny changes in the starting conditions lead to totally different end results. Translating this back to the "fast macropore" system this means that it can be possible to find a certain parameter window where the system behaves very regularly but - if it is a chaotic system - outside this window, behavior will be hardly classifiable.

Additionally the high currents AND voltages combined with badly conducting electrolytes, posed new challenges to the used potentiostat. Therefore in the first 40 experiments the voltage



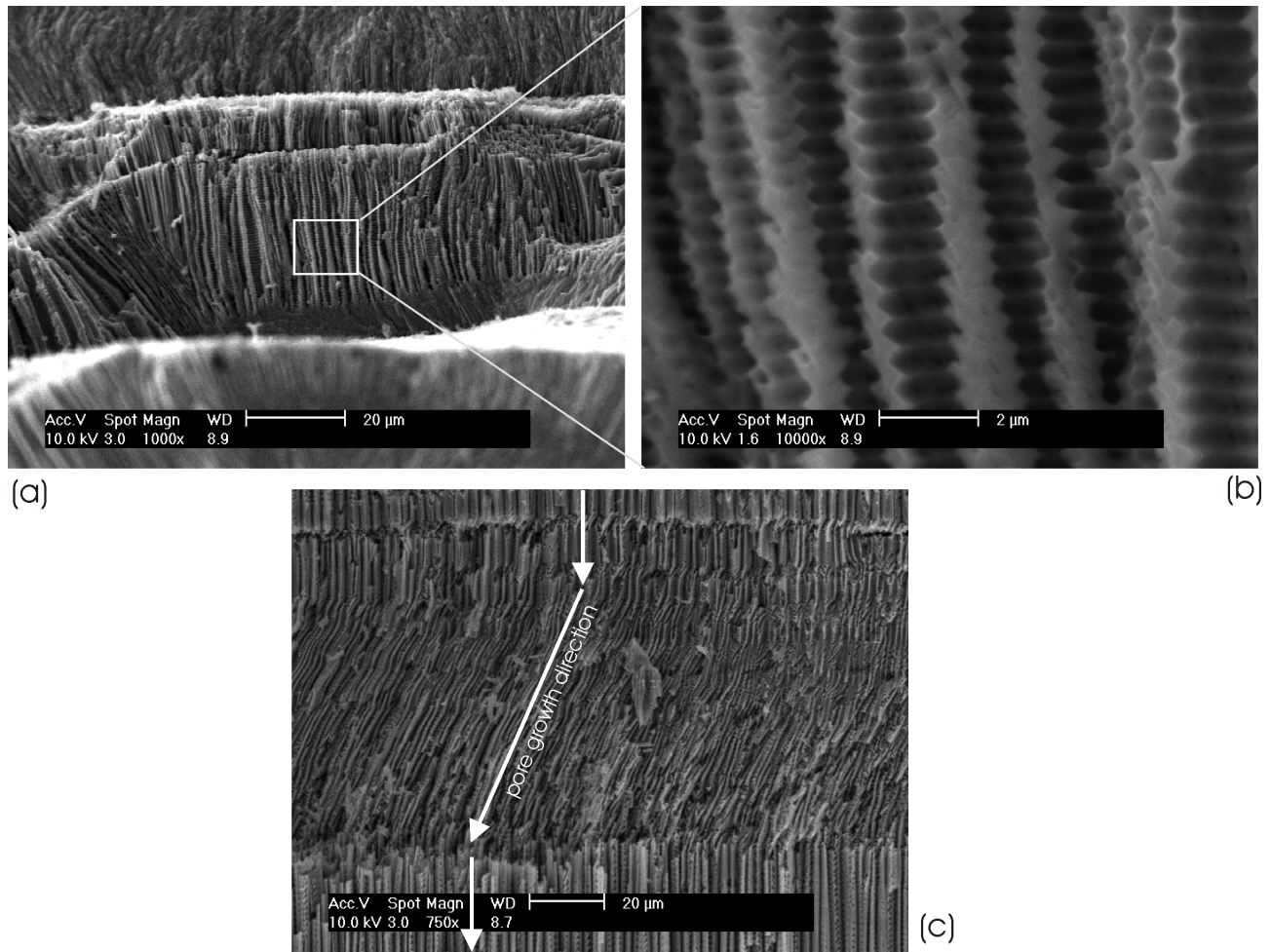


Figure 7.35: Collective phenomena during fast macropore growth (n-Si (111) in 15 wt% MeCN/TBAP etched 60 min @ 20°C,  $j = 80 \text{ mA/cm}^2$ , 0.1 min 50 V pulse after 10 min): (a) Pore diameters oscillate collectively. This occurs only isolated on a  $50 \times 100 \mu\text{m}^2$  part of the cross section. The oscillations periods are approx. 1 - 10 s. (b) Magnification of (a). (c) Across the whole sample, the pores collectively change their growth direction.

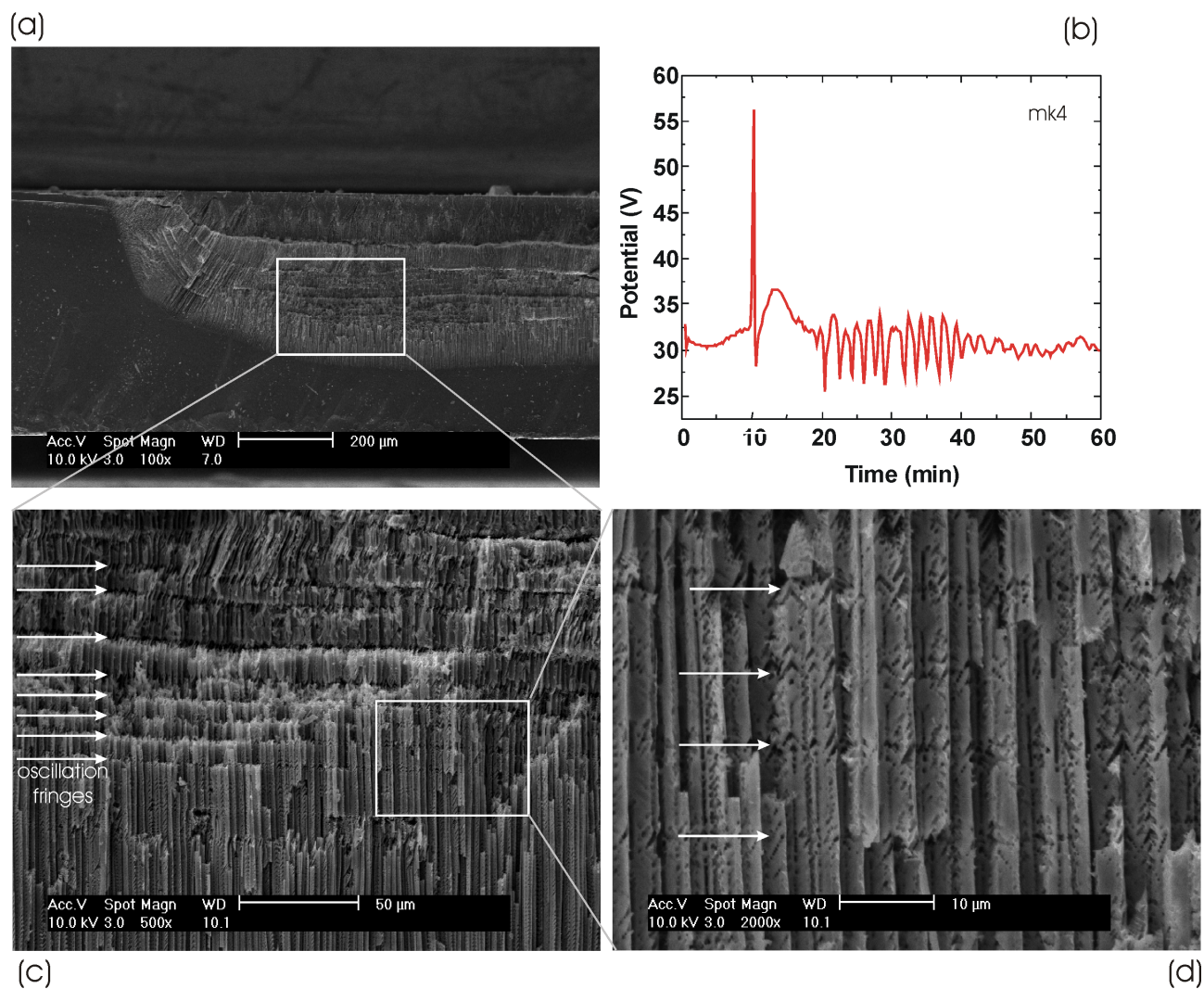


Figure 7.36: Periodic and collective branching of fast macropores (n-Si (111) in 15 wt% MeCN/TBAP etched 60 min @ 20°C,  $j = 80 \text{ mA/cm}^2$ , 0.25 min 50 V pulse after 10 min): (a) In the cross section oscillation fringes across the whole sample are visible. (b) The voltage shows several oscillations following the pulse after 10 min. (c,d) In the cross section magnifications the fringes turn out to be collective branching events.

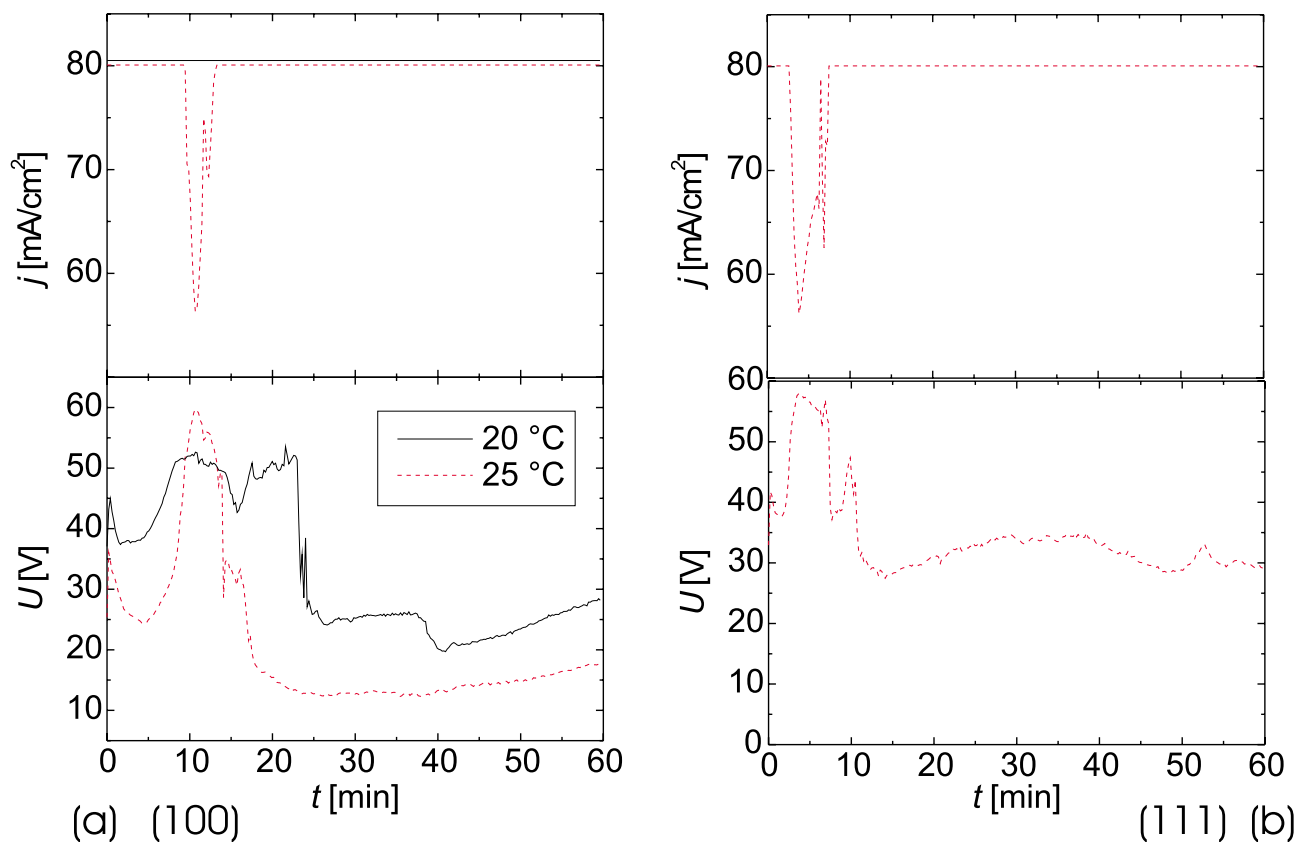


Figure 7.37: Current and voltage transients during fast macropore etching (n-Si in 15 wt% MeCN/TBAP etched 60 min,  $j = 80 \text{ mA/cm}^2$ ,  $T = 20^\circ\text{C}$  (solid lines) resp.  $T = 25^\circ\text{C}$  (dashed lines)): (a) (100) silicon. (b) (111) silicon.

was limited to approx. 50 V (between sense and reference) which led in some cases to a breakdown in current for a short time in galvanostatic experiments or in the voltage during potentiostatic series (cf. Fig. 7.37). All experiments where a prolonged breakdown occurred were discarded because measurements where neither the current density nor the voltage are well defined cannot be interpreted. For the majority of the experiments a newly constructed potentiostat was used which supports voltages up to  $U = 120 \text{ V}$  and currents up to  $I = 1 \text{ A}$ .

The voltage transients (Fig. 7.37) always showed a quick decrease in the first minutes. In many cases afterwards the voltage soon rose to a plateau of 50-60 V for a not well defined time. Then the voltage dropped significantly (often several ten volts) to a relatively stable voltage for the rest of the etching. As indicated in Fig. 7.37 a higher temperature leads typically to a lower voltage. In addition, (100) substrates required a much lower voltage for most periods than (111) substrates.

In summary, the correlation of morphological results to etching parameter variations is not as simple as in several other pore growth regimes (cf. the mesopores (section 7.1 or the bsi pores (section 5.2.1)). Also "simple" morphological data like the pore diameter defied a simple linking to e.g. current density. Fig. 7.44 shows e.g. that an electrolyte which has not been bubbled with nitrogen permanently leads to larger pores and a significantly different pore distribution and morphology. And, if the nucleation of pores was only a little bit different, this changed the whole further pore growth and "overruled" other intentional parameter changes. The SEM can

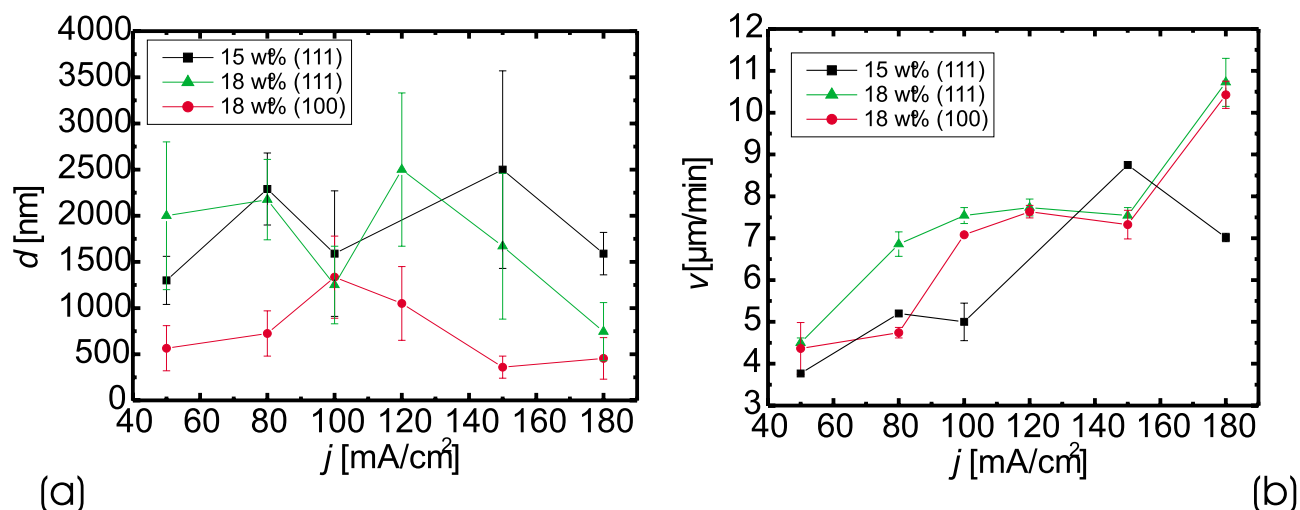


Figure 7.38: HF/MeCN/TBAP - system: Pore diameter  $d$  (a) and etching velocity  $v$  (b) versus current density  $j$  for galvanostatic conditions.

only give spotlights of a few ten to hundred square microns of a total cross section of several mm<sup>2</sup>. This together with the fact that sometimes the pore diameter changes several times during the growth makes a quantitative comparison hard (in the following section, the pore diameters was always measured in the tip region). Therefore, the following section shall only summarize those experiences which seem to be characteristic of this growth mode as well as those quantitative and qualitative correlations which showed to be resistant to the restrictions explained above.

### MeCN based electrolytes - parameter optimization

Systematic variation of the current density  $j$  (Fig. 7.38) with various HF concentrations and substrate orientations showed that only the etch velocity  $v$  clearly increases from values around 4  $\mu$ m/min (@  $j = 50$  mA/cm<sup>2</sup>,  $c_{HF} = 18$  wt%) up to over 10  $\mu$ m/min (@  $j = 180$  mA/cm<sup>2</sup>). Other HF concentrations showed essentially the same monotonic behavior. The diameter  $d$  of the pore tips didn't exhibit a close relationship to the impressed current density as the graphs for various conditions show.

For the HF concentration  $c_{HF}$  it is vice versa (Fig. 7.39): Here the diameter  $d$  decreases monotonically with increasing HF concentrations, e.g. from  $d = 3065 \pm 1125$  nm (@  $c_{HF} = 12$  wt%,  $j = 80$  mA/cm<sup>2</sup>, n(111)) down to  $d = 2175 \pm 435$  nm (@  $c_{HF} = 18$  wt%). The etch velocity  $v$  stayed constant with a variation of HF, e.g. between 7.0 and 8.1  $\mu$ m/min (for  $j = 120$  mA/cm<sup>2</sup>,  $c_{HF} = 12 - 20$  wt%, n(100)).

Most of the experiments were carried out galvanostatically. Although the pores were of quite diverse quality (cf. Fig. 7.34 and remarks on p. 107ff.) in nearly all cases macropores with diameters of several hundred nanometers resulted at the bottom of the sample. Potentiostatic conditions showed a different behavior: The experimental window where similar pores like in the galvanostatic case could be produced was quite small. At "low" voltages like  $U = 20$  V, only networks of thin breakthrough pores perforate the sample. At high voltages like e.g.  $U = 50$  V even the new potentiostat reached its limit of  $I = 1$  A. Fig. 7.40 ( $U = 35$  V,  $c_{HF} = 15$  wt%) depicts one of the experiments which were more in line with the galvanostatic experiments.



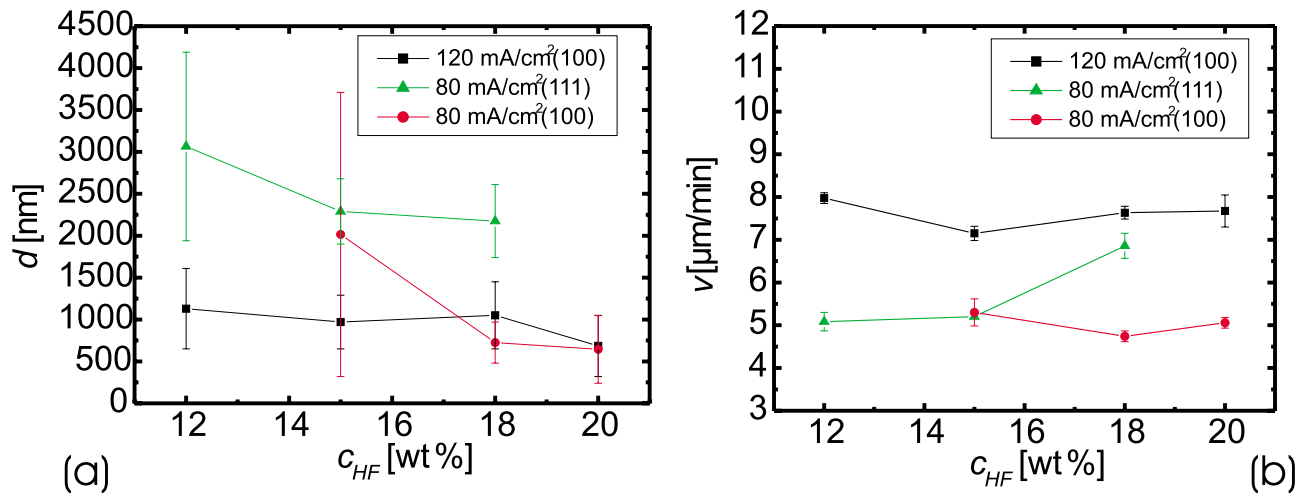


Figure 7.39: HF/MeCN/TBAP - system: Pore diameter  $d$  (a) and etching velocity  $v$  (b) versus HF concentration  $c_{HF}$  for galvanostatic conditions.

As can be seen from the overview cross section in (a) also in the potentiostatic experiments a spreading of larger pores occurs which supersedes the smaller, well ordered pores (b). However, this spreading occurs only after a pore depth of 50  $\mu\text{m}$ , while in galvanostatic experiments such a behavior always occurred right from the beginning. The small pores in between have a diameter of  $d = 40 - 75$  nm and appear well ordered as the bevelled cleavage in (c) shows.

Fig. 7.41 summarizes the impact of the voltage  $U$  during potentiostatic experiments on the diameter  $d$  and the etch velocity  $v$  of the pores: As previously explained the diameters stay very small up to 30 - 35 V and increase then steeply at 40 V. At 50 V the potentiostat always reached its limit. The etch velocity increases continuously, e.g. (@ 18 wt%, n(100)) from  $v = 2.4\mu\text{m}/\text{min}$  to  $v = 5.0\mu\text{m}/\text{min}$ .

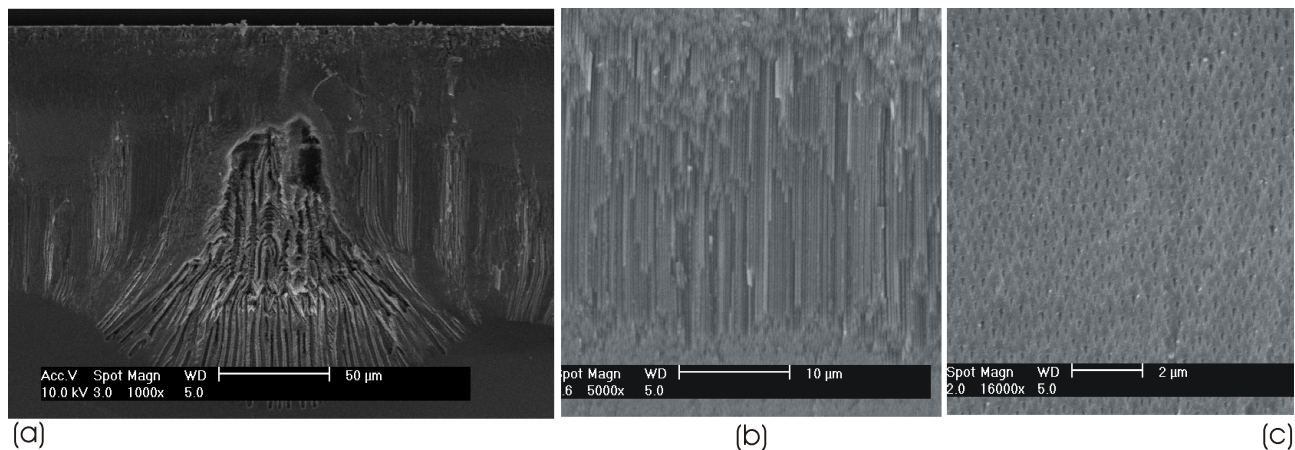


Figure 7.40: HF/MeCN/TBAP - system: Pore morphology for potentiostatic ( $U = 35$  V) conditions: (a) Large pores ( $d \approx 1.0 - 2.5\mu\text{m}$ ) "break out" in an etching depth of approx. 50  $\mu\text{m}$ . Around these spots very small pores grow (b). A spot with a bevelled cleavage (c) reveals that these pores have diameters between 40 - 75 nm and that they are highly ordered.



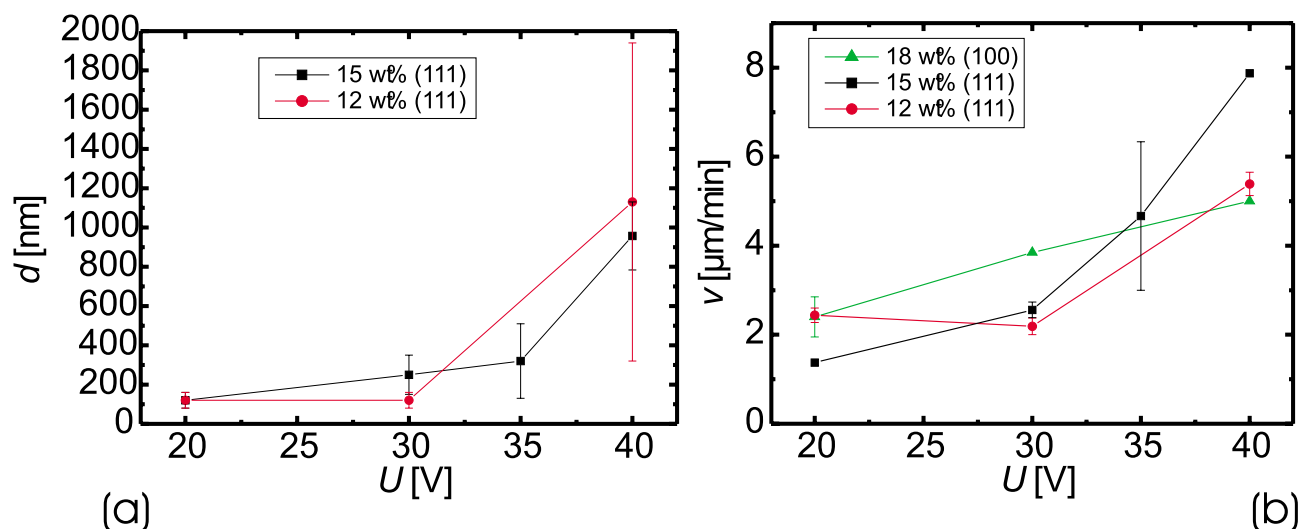


Figure 7.41: HF/MeCN/TBAP - system: Pore diameter  $d$  (a) and etching velocity  $v$  (b) versus applied bias  $U$  for potentiostatic conditions.

Also the influence of the conducting salt TBAP was investigated in one set of experiments. Without TBAP it was within the range of the (old) potentiostat nearly never possible to carry 80 mA/cm<sup>2</sup>. The resulting samples were always highly porous and most of the porous layer washed off during rinsing. Optical microscopy suggested a morphology like in the case of pure DMF (Fig. 7.29); this is the reason why this route was not further pursued. Albeit the number of experiments with other TBAP concentrations is too small to justify a final statistical evaluation, it showed that a reduction by 50 % doesn't seem to have a clear influence on the etching velocity, diameter, or morphology. However, it becomes clear that at even lower TBAP concentrations a transition range must exist because the results without TBAP exhibit a totally different behavior.

The temperature of the electrolyte was varied in a number of n-Si (100) experiments (Fig. 7.42). Similar to the variation of the current density (Fig. 7.38) the diameter seems to depend much stronger on other parameters than the temperature. The etch velocity clearly increases with rising temperature from  $r = 4.8 \pm 0.4 \mu\text{m}/\text{min}$  (@ 15 °C,  $j = 80 \text{ mA}/\text{cm}^2$ ) to  $r = 5.7 \pm 0.3 \mu\text{m}/\text{min}$  (@ 25 °C).

In III/V compounds it has been shown [95] that one or more short high voltage pulses at the beginning of the etching helps tremendously to homogenize the nucleation. Otherwise, often only some defective spots start to carry all current like in the case of GaP while the rest of the surface remains inert. To get a homogeneous porosity it is necessary to render the whole surface in an equal status by the mentioned pulse (sequence). Because of the sometimes heterogeneous results (cf. p. 107ff.) also in the present etching system the impact of pulsing was investigated. Pulses at the beginning as well as in the middle of the etching have been tested. However, especially in this series of experiments, it later became clear that the electrolyte was not in all cases flushed with nitrogen continuously. It is noted with each experiment, if this was the case. Of course, it was not intended to modify the N<sub>2</sub> bubbling status at the same time but this shows once more the variety of (sometimes initially unclear) parameters which have significant influence on the resulting morphology.

For the pulses after some etching time, it showed that in most cases the effect was not visible

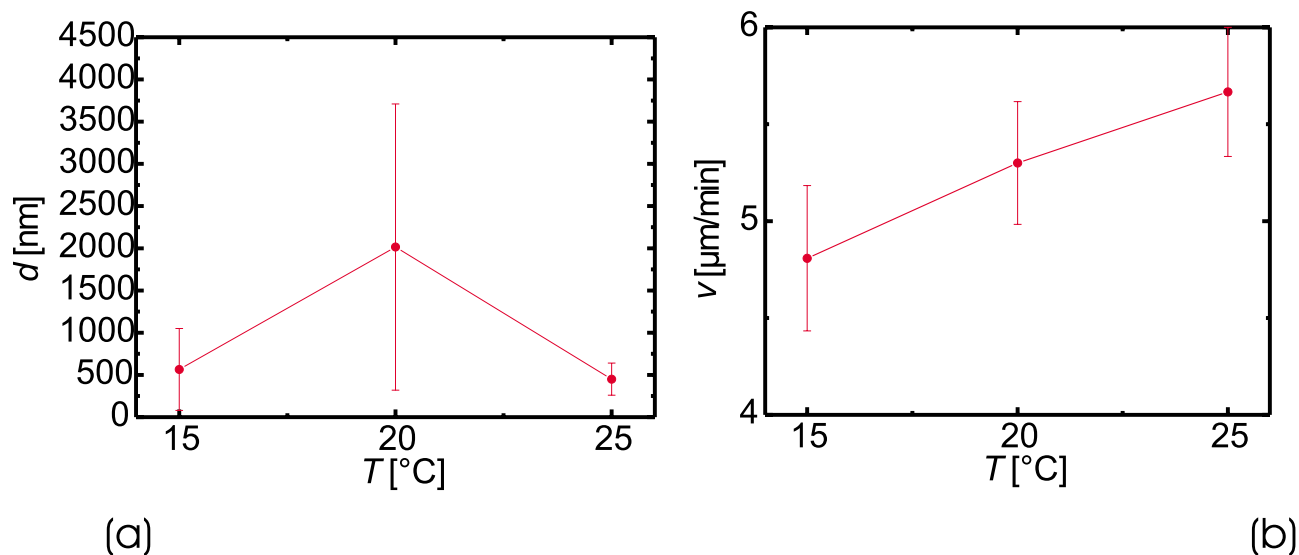


Figure 7.42: HF/MeCN/TBAP - system: Pore diameter  $d$  (a) and etching velocity  $v$  (b) versus electrolyte temperature  $T$  ( $j = 80 \text{ mA/cm}^2$ ,  $c_{\text{HF}} = 15 \text{ wt\%}$ , (100)).

in the pore morphology (e.g. as steps, changed porosity, branching, or diameter variation, cf. Fig. 7.33, where a pulse was given every 10 minutes). Only in some cases like in Fig. 7.36 an oscillatory behavior was triggered. When the samples were exposed to a short pulse at the start of the etching, more distinct features became visible: Fig. 7.43(a-c) shows the surface and cross section of a sample which was etched without prior voltage pulse ( $j = 80 \text{ mA/cm}^2$ ,  $c_{\text{HF}} = 15 \text{ wt\%}$ , n(111), correctly bubbled). At the surface even with larger magnifications, only scattered, tiny pits with diameters of some ten nm are visible. The cross section shows pores that have changed several times collectively their growth direction and that especially in the upper part the mechanical stability lacks because of a too high porosity. The pore tips have diameters between  $1.9$  and  $2.6 \mu\text{m}$  and show a triangular pore cross section, where the dark lines in the pore centers of picture (c) mark one corner of this triangle. The depth is approx.  $310 \mu\text{m}$ .

When a similar experiment is carried out with a short pulse at the beginning ((d-f): 0.05 min, (g-i): 0.1 min, both with probably insufficient  $\text{N}_2$  bubbling), the surface becomes covered with densely packed shallow pits with diameters of  $100 - 200 \text{ nm}$ . Between them micron sized funnels establish. The funnels become larger with prolonged pulsing time. In the cross section these funnels (cf. also Fig. 7.32 and 7.33) develop into larger pores which supersede smaller pores in between them. With 0.05 min pulsing time the spreading starts at a depth of approx.  $20 \mu\text{m}$ , while a pulse of 0.1 min leads to a spreading after  $7 \mu\text{m}$ . The pore depth was  $390 \pm 10 \mu\text{m}$  for the shortly pulsed sample versus  $t = 430 \pm 50 \mu\text{m}$  for the 0.1 min sample. The pore tips<sup>3</sup> show diameters from sub-100nm up to  $3000 \text{ nm}$  and the pore morphology is wavy and irregular compared to the non-pulsed (and sufficiently bubbled) sample.

The effect of bubbling became even more evident after comparing two other experiments with different  $\text{N}_2$  rinsing status: Fig. 7.44(a-c) shows a sample which was etched with a fresh electrolyte and a pre etching pulse of 0.1 min, while the sample in (d-f) was pulsed for 1.0 min at the beginning of the etching in an old, partially insufficiently bubbled electrolyte. For the

<sup>3</sup>Fig. 7.43(i) shows the pores near the o-ring, therefore the pores are curved.

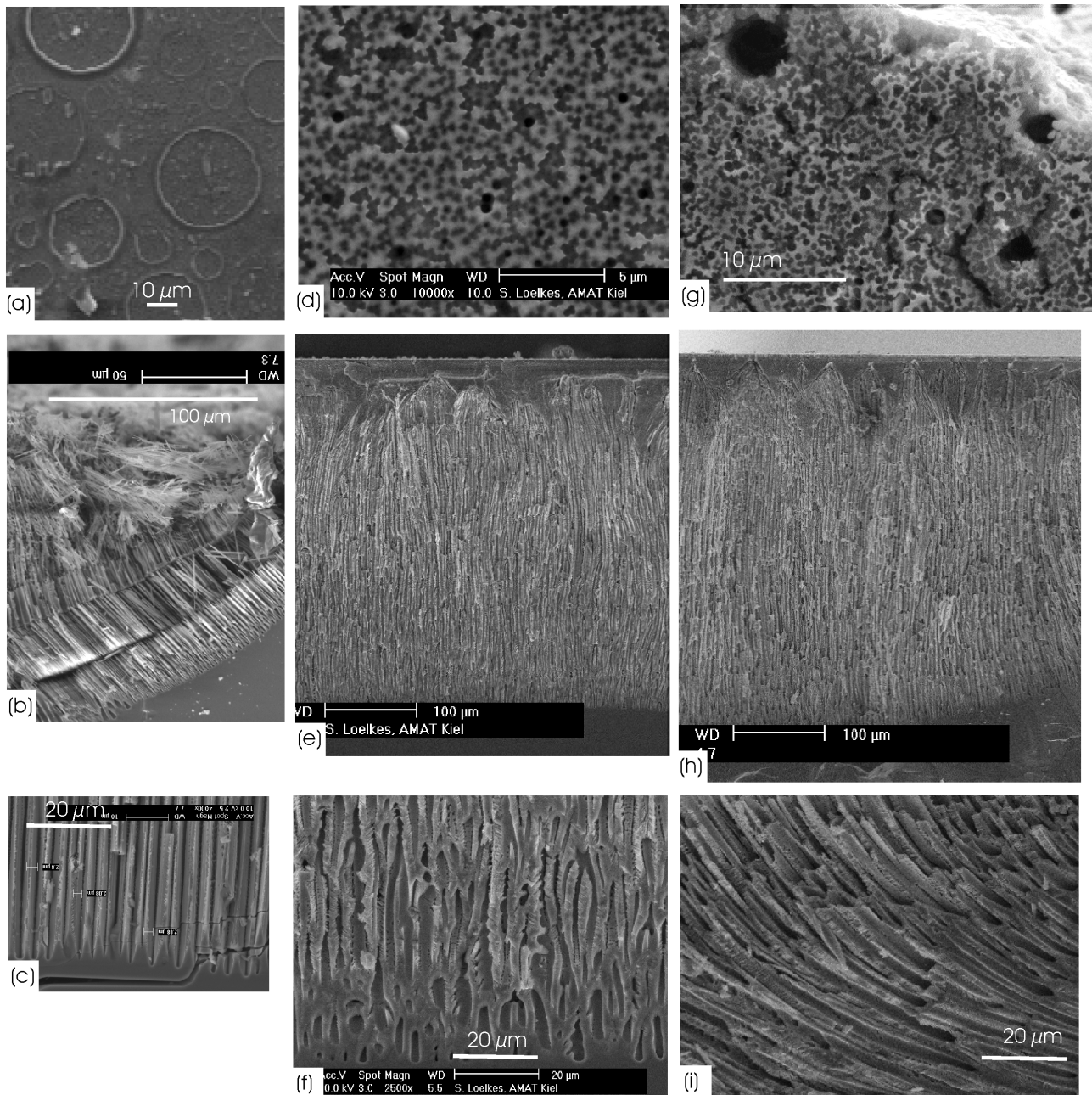


Figure 7.43: Influence of the length of a high voltage pulse at the beginning of the etching: (a-c) Without a pulse, (d-f) pulse length 0.05 min, (g-i) pulse length 0.1 min.

shortly pulsed samples, the surface shows only a few scattered 50 - 150 nm large pores (a). The other sample (d) shows similar small pits like the other pulsed samples from Fig. 7.43 but no funnels. The cross sections (b,e) exhibit totally different courses of etching: While the shortly pulsed/well bubbled sample undergoes several ruptures and direction changes of the pores, on the second sample large pores similar to those of Fig. 7.43(e,h) grow in a swinging fashion after an initial layer of very small pores. The magnification of the pore tip (c,f) shows clearly the differences: The pores from the fresh electrolyte have diameters of  $d = 1.4 - 3.8\mu\text{m}$  and show frequent side branches. The pores from the insufficiently bubbled electrolyte have diameters of up to  $5\mu\text{m}$  and have irregular walls, which show some branching but not in such a repetitive fashion like in the other experiment.

In many macropore etching experiments surfactants are added to the etching solution with tremendous effect on the pore quality (cf. section 5.2.1). It has also been shown that different surfactant types exhibit totally different effects on the morphology. Therefore the effect of surfactants was also tested for the present pore etching system (@  $j = 80\text{ mA/cm}^2$ ,  $c_{HF} = 15\text{ wt\%}$ ,  $0.11\text{ M TBAP}$ ).

Fig. 7.45 compares the voltage transients of the surfactant containing electrolytes with that of an electrolyte without surfactant. Already at first glance it becomes clear that a tiny amount of surfactant is enough to change the system completely. The anionic and the cationic surfactant resemble the pure electrolyte: They reach quickly (after 5 minutes) a first minimum between 35 and 40 V. After an intermediate peak between 50 and 60 V, the potential drops to an absolute minimum of 15 V after 15 - 20 min of etching. From there on, the potential increases gently up to 25 V at the end of the etching. The WAKO and other non-ionic surfactant also have some similarities: Here it takes approx. 30 minutes to reach a maximum voltage after an initial dip of the voltage down to 23 V. The last 30 minutes the voltages drop to 15 - 25 V. The non-ionic surfactant shows several drastic fluctuations in the voltage.

This surfactant experiments will be used to describe several general phenomena which occurred also under other conditions but in most cases not so pronounced. Except for the WAKO surfactant, in all cases a membrane lifted off during or after the etching. When looking at the surface below the membrane for the sample etched with the cationic surfactant, the uppermost part (Fig. 7.46a) is covered with large, unordered pores ( $d = 2 - 4\mu\text{m}$ ) as well as with submicron sized pores. Below this, crossing lines (width: 400 - 600 nm) of pores with clear crystallographic orientation along  $\langle 100 \rangle$  are visible (Fig. 7.46(b,c))<sup>4</sup>. The individual pores are square shaped with tips pointing in  $\langle 100 \rangle$  - direction. Similar patterns were found on other (100) sample surfaces, but never on (111). In cross section (Fig. 7.47) the two different pore size regimes are again found at the top of the porous layer (b). After the pore growth switches to the smaller pores the pore sizes stay almost constant between 330 and 500 nm (b,c). The pores end extremely spiky (c). Fig. 7.48 shows another example etched under similar conditions but without surfactant where this phenomena is also visible. Here the pores form round tips from where spikes of several microns length start. Please note that the round as well as the spike tip fronts are extremely homogeneous. Both of these samples show also vertical stripes during the etching which extend over the whole sample. When magnifying these lines it can be seen that here the pore growth switched from smooth to rubbly pore walls, similar to a switch from *crysto* to *curro* on (111B) InP [95].

With the non-ionic surfactant, the surface (Fig. 7.49a) showed in a certain depth small pores ( $d \approx 100\text{ nm}$ , Fig. 7.50a) which on some spots exhibit a six-fold coordination symmetry

<sup>4</sup>The sample edges have a  $\langle 110 \rangle$  direction (cleavage directions in Si!). The  $\langle 100 \rangle$  directions are then under  $45^\circ$  to the sample / image edges.



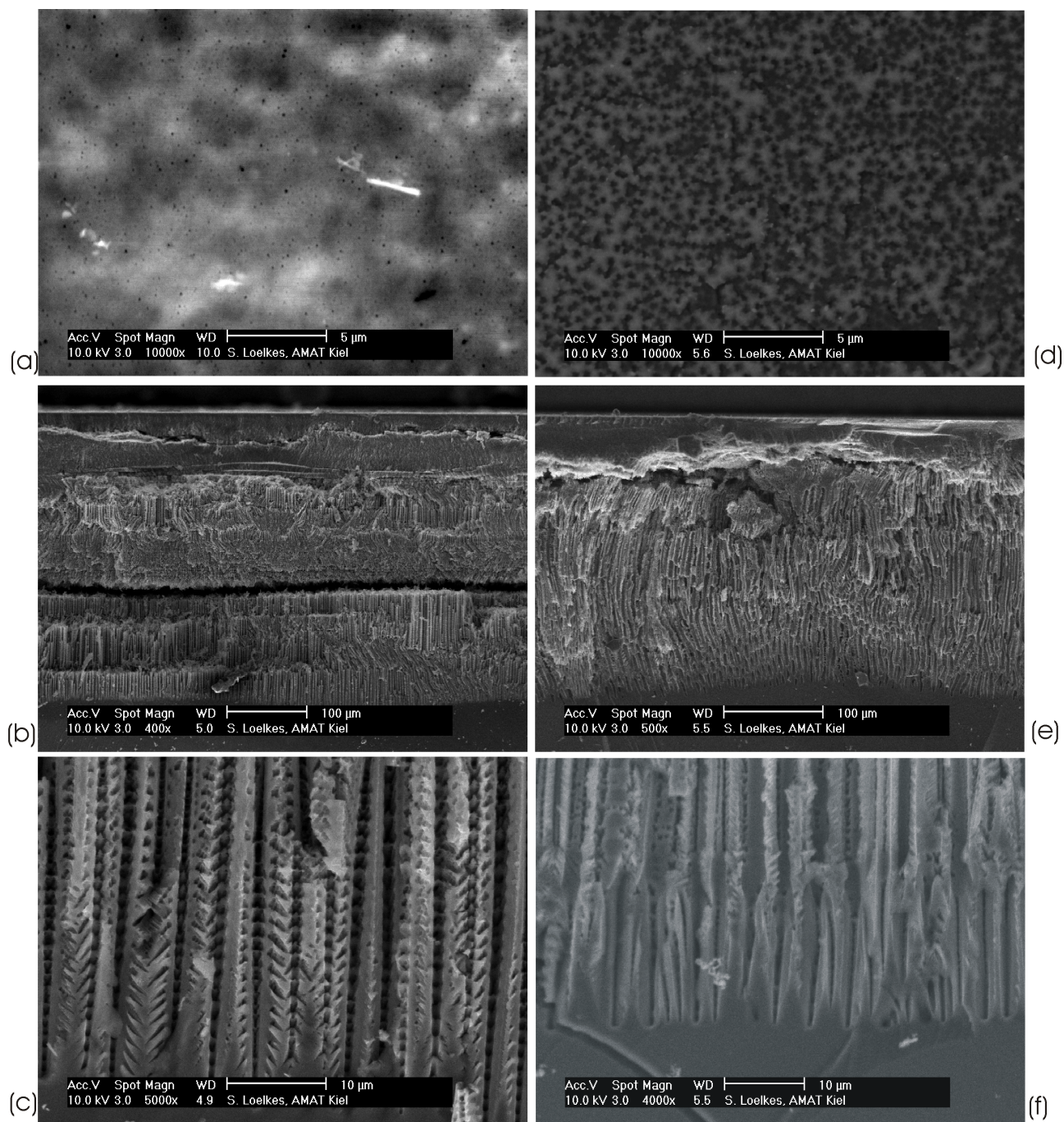


Figure 7.44: Influence of high voltage pulsing and  $\text{N}_2$  bubbling (n-Si (111) in 15 wt% MeCN/TBAP (0.05 M) etched 60 min @  $20^\circ\text{C}$ ,  $j = 80 \text{ mA/cm}^2$ : (a-c) New and well  $\text{N}_2$  rinsed electrolyte and high voltage pulse of 0.1 min: The diameters have diameters of  $d = 1.4 - 3.8 \mu\text{m}$  and show repetitive side branching. (d-f) Insufficiently bubbled electrolyte, 1.0 min pulse at beginning: The pores show diameters up to  $d = 5 \mu\text{m}$  but no branching.

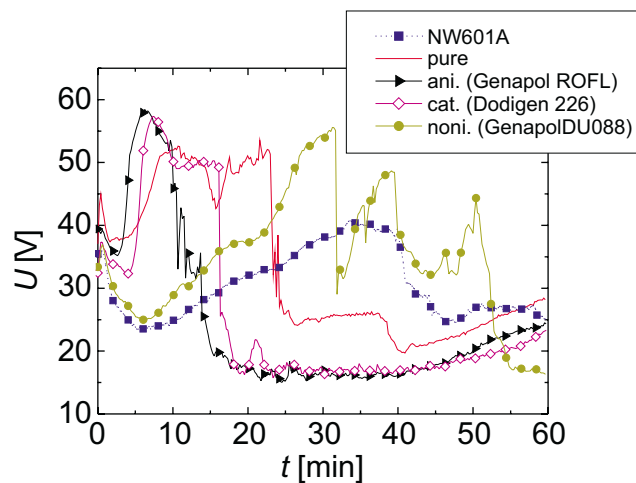


Figure 7.45: Voltage transients  $U(t)$  after the addition of different surfactant types.

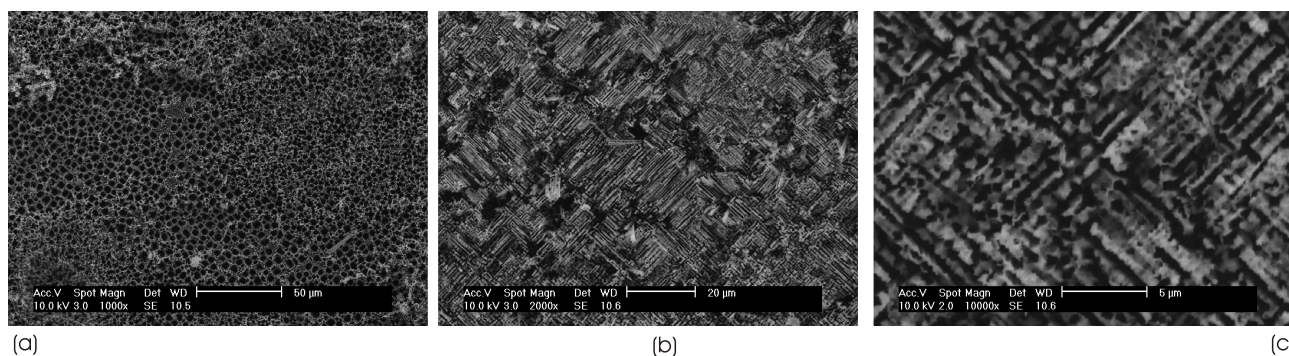


Figure 7.46: Typical surface structures on (100) wafers after fast macropore etching ( $c_{HF} = 15 \text{ wt\%} + 0.11 \text{ M TBAP} + \text{cationic surfactant}$ ,  $j = 80 \text{ mA/cm}^2$ ): (a) Directly underneath a splashed-off membrane mainly large pores ( $d = 2 - 4 \mu\text{m}$ ) are found. (b) Subjacent, criss-cross patterns of pores formed. The quadratic pores align along  $\langle 100 \rangle$  directions. (c) Magnification of (b).



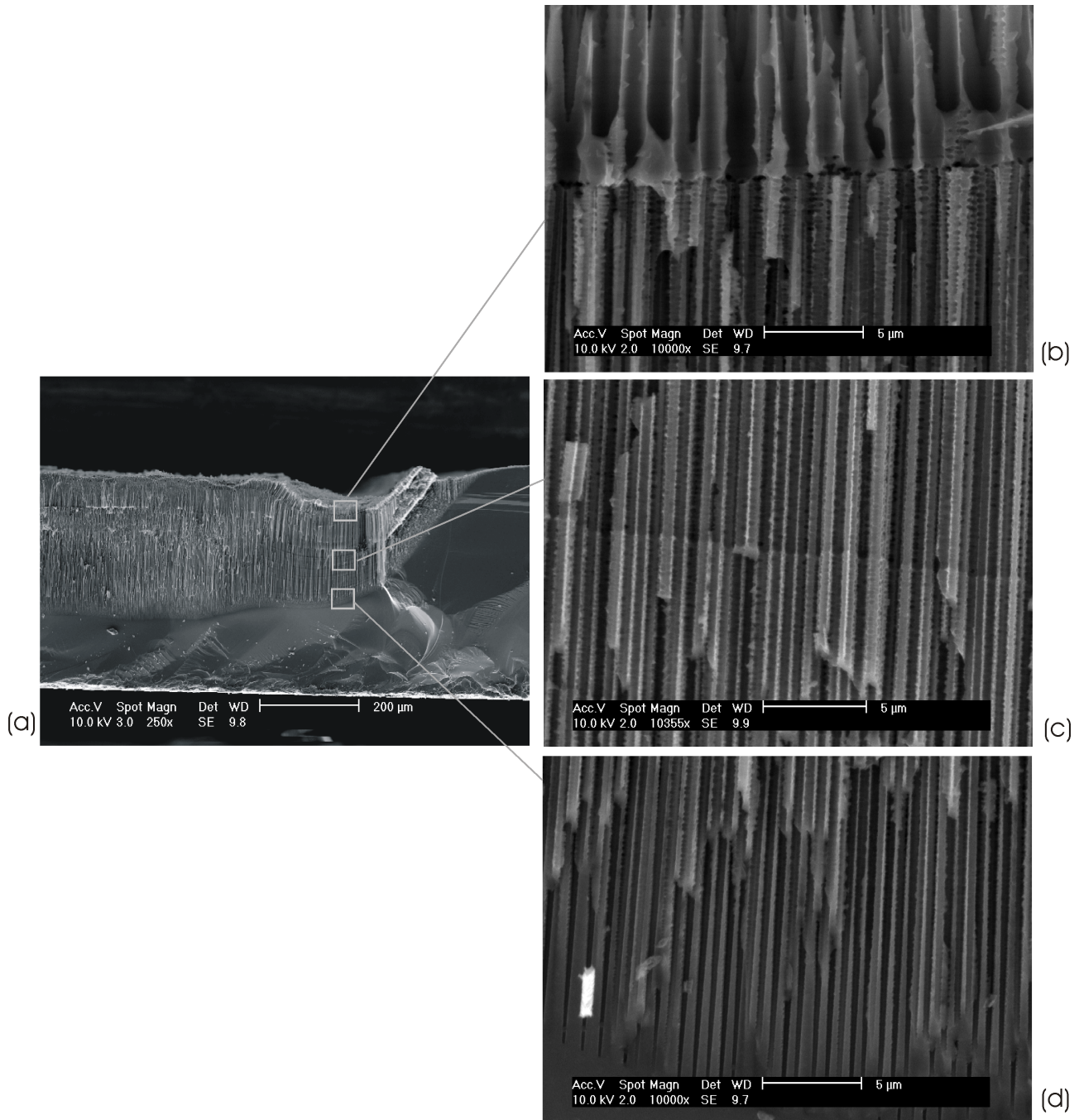


Figure 7.47: Typical cross section after galvanostatic etching ( $C_{HF} = 15 \text{ wt}\% + 0.11 \text{ M TBAP} + \text{ cationic surfactant}$ ,  $j = 80 \text{ mA/cm}^2$ , (100) Si): (a) Overview. (b) Interface between the larger to the smaller pores (cf. Fig. 7.46). (c) Magnification of sample-wide stripe. Often the growth changes at these lines from smooth to rough pores (cf. also Fig. 7.31f). (d) The pores end with extremely long and sharp tips.

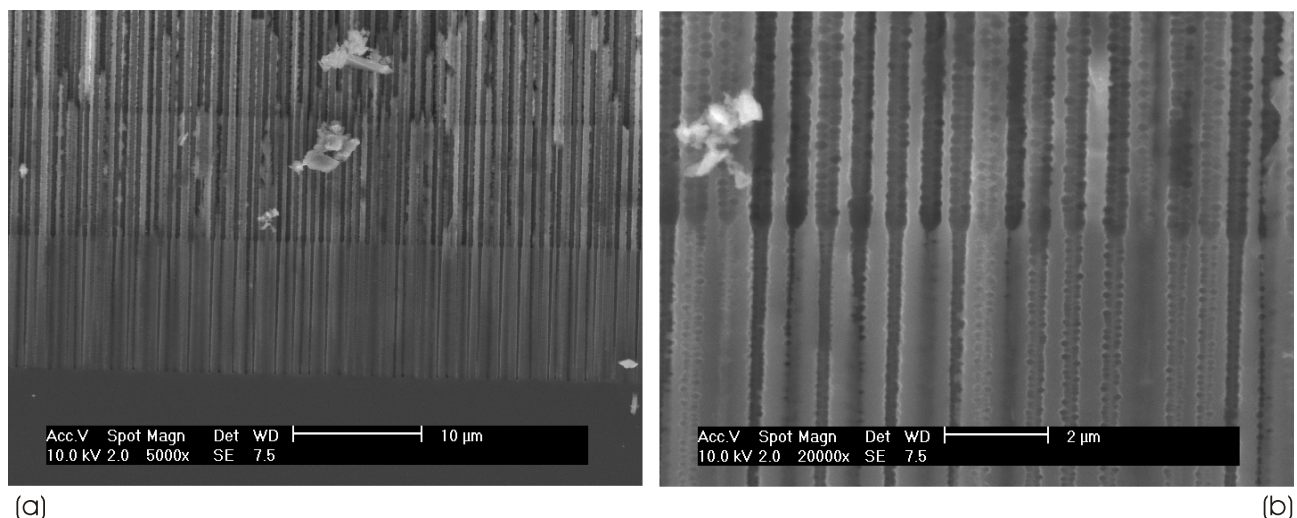


Figure 7.48: Example of peaked and homogeneously ending pore tips ( $c_{HF} = 15$  wt%, 0.11 M TBAP,  $j = 80$  mA/cm<sup>2</sup>, (100)): (a) The pores ends with a 10 micron long, peaked tip. (b) Magnification of (a): All pores end rounded at the same depth from where the sting-like tips start.

as well as a sometimes pronounced four-fold symmetry. The autocorrelation analysis of the pore positions (Fig. 7.49a, inset) shows for the first neighbors nearly no preferential direction<sup>5</sup>. However, the second nearest neighbors exhibit clearly a twelve-fold symmetry. In the analysis of the co-ordination number most of the pores have 4,5, or 6 neighbors (Fig. 7.50b).

In the cross section (Fig. 7.49b) the pore walls are much thicker and of worse quality than with the other surfactants. The pores have diameters  $d = 280 - 320$  nm, at other cross section pictures even pore diameters down to 100 nm are found. The pore depth is inhomogeneous and the etching reached at one spot the backside of the wafer.

In a further experiment, the same surfactant was added after 32 minutes of etching, while the system was analyzed every two seconds by FFT impedance spectroscopy.

After or during the etching a membrane peeled off, so probably the part which is seen in the optical microscopy cross section (Fig. 7.51a), shows only the last 20 minutes of the etching (after the last drastic voltage drop @20 minutes (cf. Fig. 7.51c)). In the upper part, the cross section is rather dark, which indicates a high porosity (similar to other experiments without surfactant, cf. e.g. Fig. 7.31f). The lower part of the cross section appears brighter because of a lower porosity. In the lowest part the unetched silicon can be seen (which shows of course the highest reflection). This indicates that the pores simply became smaller when the surfactant was added like in the other experiment with this surfactant (cf. Fig. 7.49) where the pores became much smaller and the walls were thicker than in comparable experiments without surfactant.

In the voltage transient (Fig. 7.51c) the addition of the surfactant is only visible as a small dip. However, all data fitted from the impedance measurements clearly document the addition of the surfactant (Fig. 7.51(d,e)). Fig. 7.51b) shows the equivalent circuit which has been used:

- The serial resistance  $R_s$  and the parallel resistance  $R_p$  decrease.

<sup>5</sup>With the “eyes of a father”, a four-fold symmetry can be alleged.



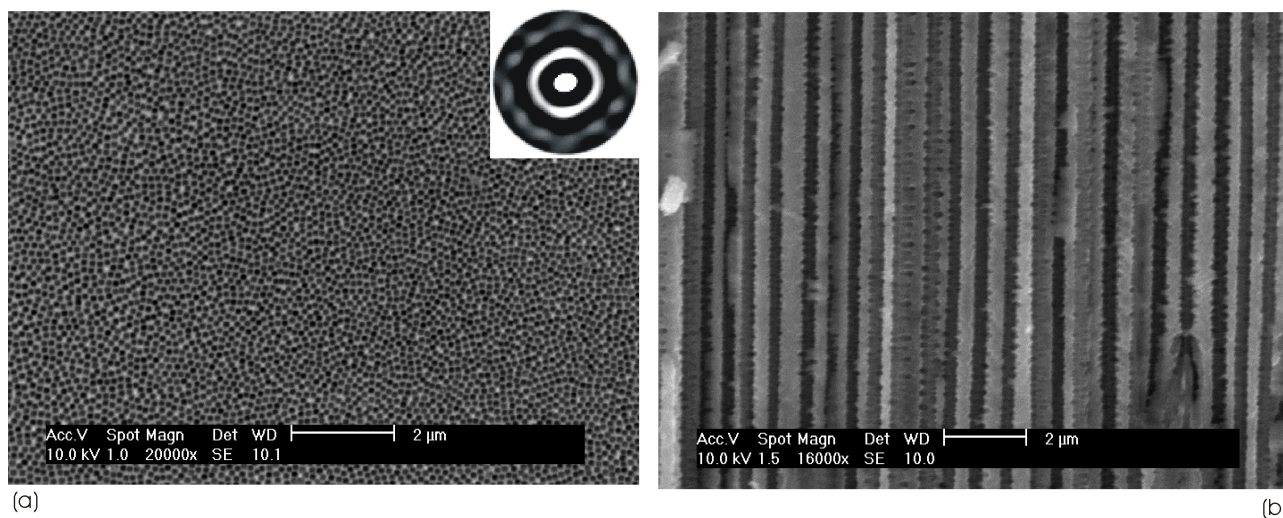


Figure 7.49: Geometrically frustrated structures on (100) substrates ( $c_{HF} = 15 \text{ wt}\% + 0.11 \text{ M TBAP} + \text{non-ionic surfactant}$ ,  $j = 80 \text{ mA/cm}^2$ , (100) Si): (a) The pore ensemble exhibits triangular as well as four-fold symmetry elements (Inset: The second nearest neighbors in the auto correlation function are ordered with a twelve-fold symmetry.). (b) Cross section.

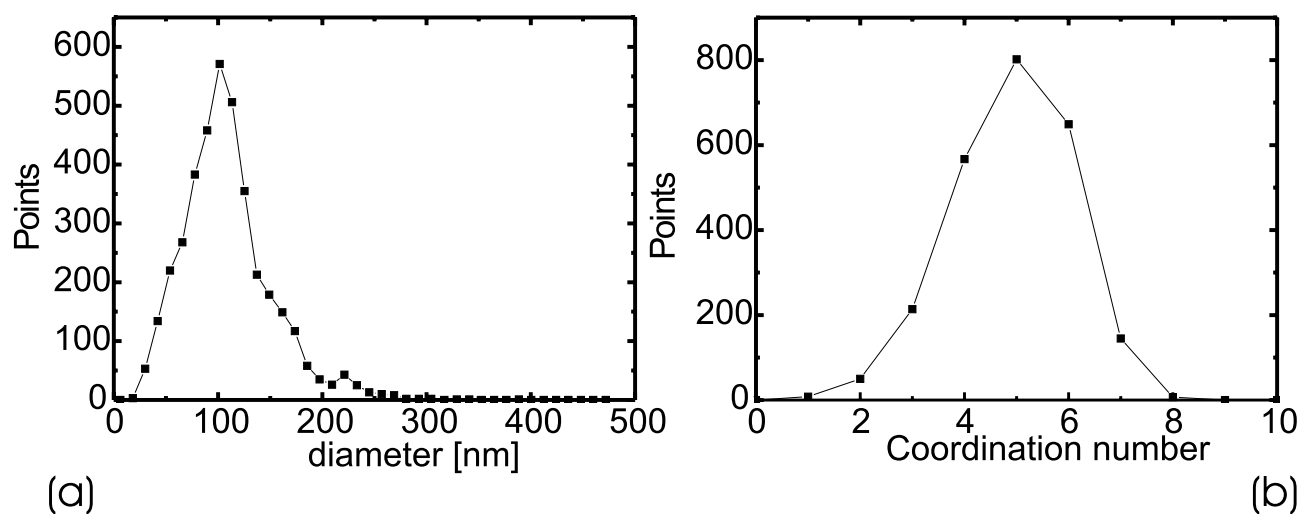


Figure 7.50: Evaluation of the geometrically frustrated structure (from Fig. 7.49: (a) Diameter and (b) coordination number of pores.

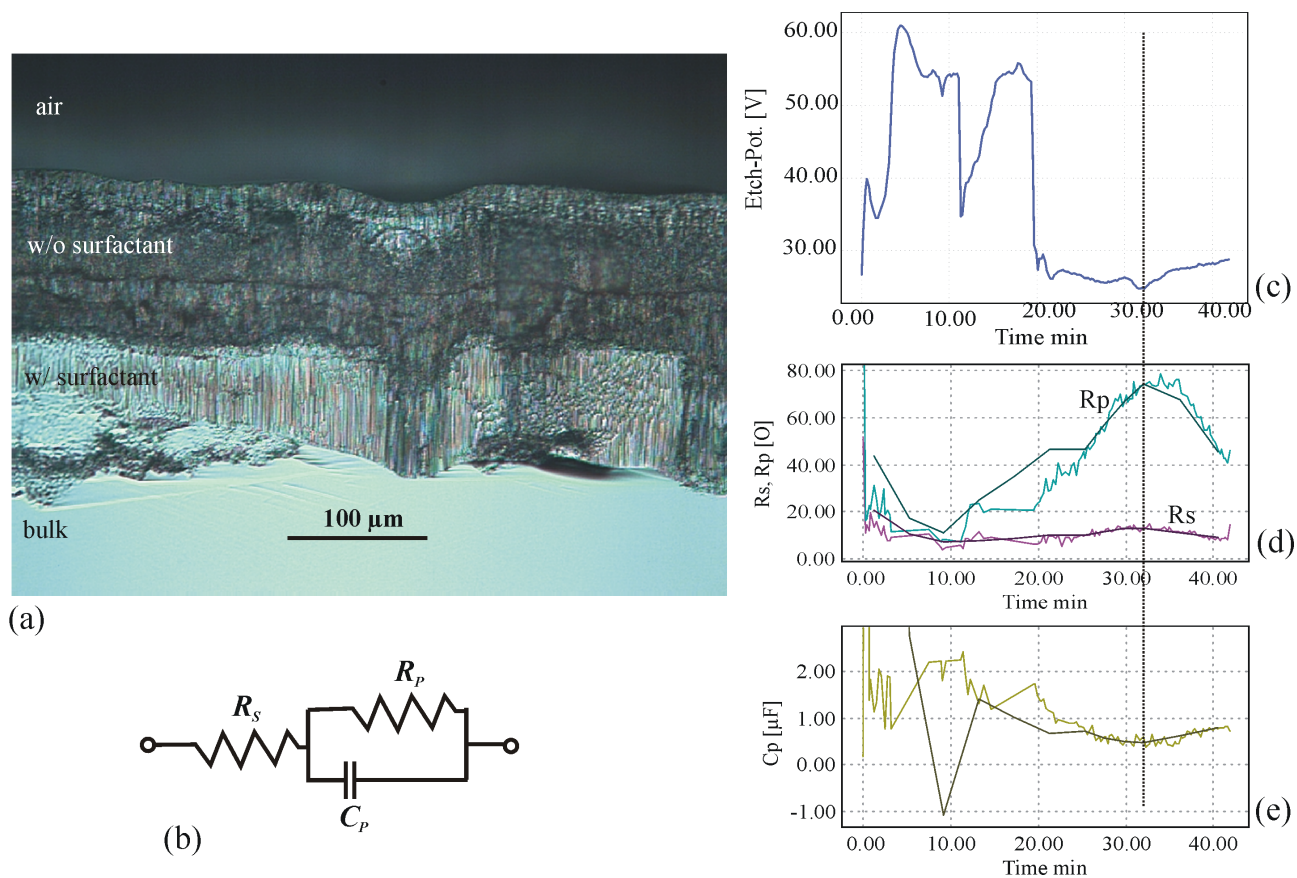


Figure 7.51: Impedance analysis of the impact of surfactant addition ( $c_{HF} = 15 \text{ wt}\% + 0.11 \text{ M TBAP} + \text{non-ionic surfactant}$  added after 32 minutes (marked with a dotted line in (c-f),  $j = 80 \text{ mA/cm}^2$ , (100) Si): (a) In the cross section the morphology changes clearly. (b) Equivalent circuit for the impedance analysis. (c) Voltage transient. (d,e) Values for the equivalent circuit elements derived from the impedance analysis.

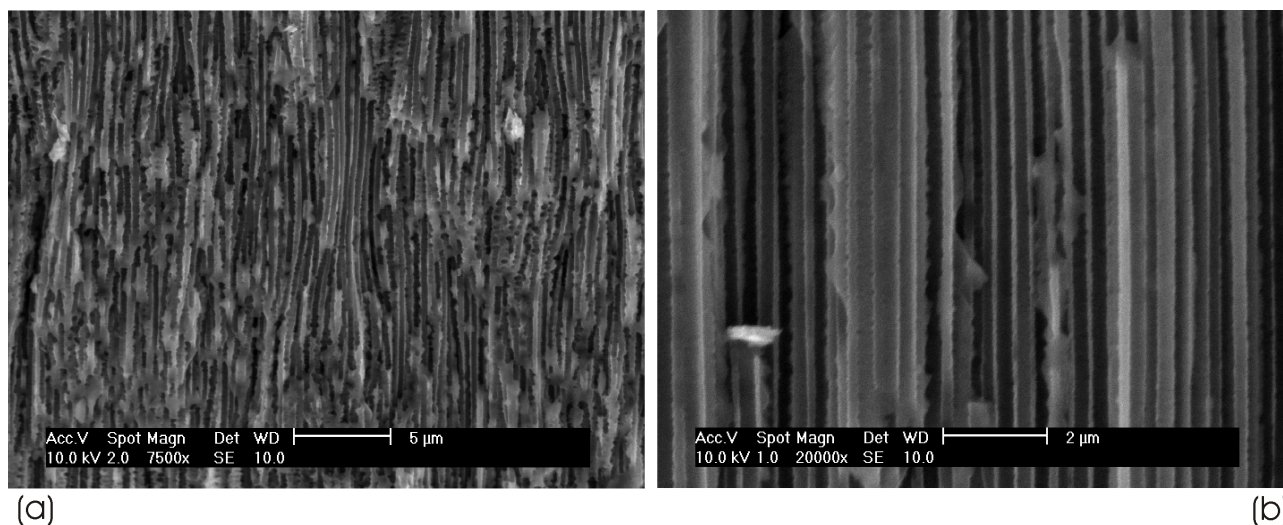


Figure 7.52: Cross section after etching with an anionic surfactant ( $c_{HF} = 15 \text{ wt}\% + 0.11 \text{ M TBAP} + \text{anionic surfactant}$ ,  $j = 80 \text{ mA/cm}^2$ , (100) Si): (a) Especially in the upper part of the sample the pores dynamically rearrange which leads to swinging pore shapes. (b) In the lower part of the sample mainly very close spaced pores with smooth walls are found.

- The parallel capacity  $C_p$  increases.

The anionic surfactant exhibited similar pores ( $d = 150 - 500 \text{ nm}$ ) like without surfactant. The pore walls are very smooth (Fig. 7.52b) in most cases and very thin (wall thickness  $\leq 100 \text{ nm}$ ). In some parts of the sample it becomes clearly visible that the pores don't follow a crystallographically predetermined direction, but that they grow along the directions of current flow (Fig. 7.52(a)). The pore depth reached  $300 - 360 \mu\text{m}$ .

The experiment with the WAKO surfactant was the only one, where no membrane fell off from the sample. The optical microscope's resolution was too coarse to reveal any pores on the pale blue surface. For the SEM images a part of the upper surface was gently ripped off (cf. Fig. 7.53a). While again on the top surface only scattered submicron pores were found the underlying porous layer exhibits closely spaced pores with diameters between  $220$  and  $330 \text{ nm}$ . The tilted surface image in Fig. 7.53(b) reveals that the resulting structure is highly porous with walls in the sub- $100 \text{ nm}$  region. The cross section (a,c,d) shows that the surface is perfectly flat and only from a few spots the pores start to grow. When the pores have reached a close-packed structure they grow vertically with extremely smooth walls (f). The pore growth is vertically sectioned every approx.  $50 \text{ microns}$  which is not directly expressed in the voltage transient (Fig. 7.45). Probably, the pores have collectively widened at the sectioning lines which led to a "terrace" look (c). In some parts of the sample the pore walls became too thin (e) and only the nanowires (e, inset) between the pore triangles remained. The pores in the other sections of the sample were the smoothest ones found in all experiments (f).

From the large amount of probed conditions, Fig. 7.54 shows the fastest pores which have been grown with an acceptable quality. The HF concentration in this case was  $c_{HF} = 20 \text{ wt}\%$  and the current density  $j$  was  $150 \text{ mA/cm}^2$ . The sample orientation was (100). The etching rate reached  $10.1 \mu\text{m}/\text{min}$  (etching time:  $40 \text{ min}$ ). The pore growth starts with a layer of very small pores down to a depth of  $15 - 50 \mu\text{m}$  before the system switches to the pore type which is seen near the tips (Fig. 7.54). The pores have diameters of approx.  $1.0 \pm 0.25 \mu\text{m}$

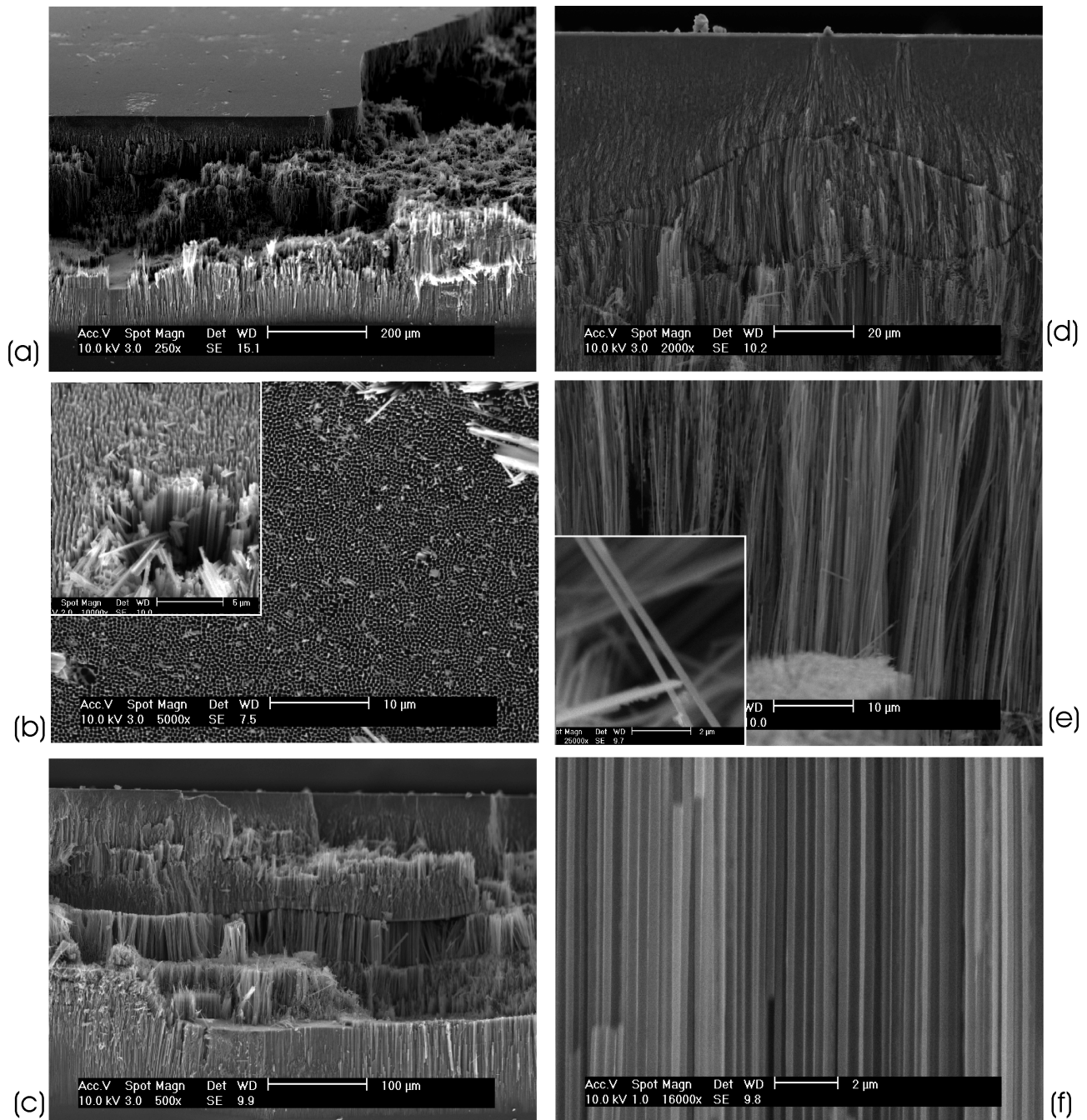


Figure 7.53: Sample with an intact surface ( $c_{HF} = 15 \text{ wt}\% + 0.11 \text{ M TBAP} + \text{WAKO surfactant}$ ,  $j = 80 \text{ mA/cm}^2$ , (100) Si): (a) Overview of tilted cross section (a part of the uppermost surface was removed intentionally for the SEM examination). (b) Surface where uppermost layer was removed (Inset: Magnification of collapsed spot on the surface (tilted)). (c) Cross section with terrace-like sectioning of pore growth. (d) Magnification of uppermost spreading of pores. (e) Area where only nano wire fields remained (pore walls etched off) (Inset: Zoom on nano wire). (f) Area with extremely smooth macropores.



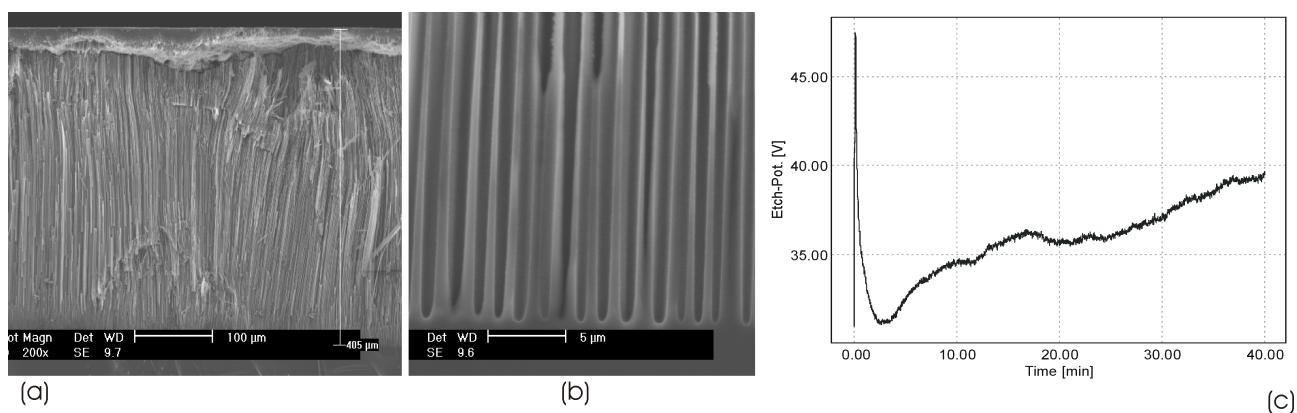


Figure 7.54: The fastest growing, high quality pores achieved in the present work ( $c_{HF} = 20 \text{ wt}\% + 0.11 \text{ M TBAP}$ ,  $j = 150 \text{ mA/cm}^2$ , (100) Si): (a) Overview of cross section. (b) Magnification of pore tips. (c) Voltage transient.

(measured at the top of Fig. 7.54b as well as in other heights). The voltage transient (Fig. 7.54c) shows a minimum of  $U = 31 \text{ V}$  after 3 minutes and rises continuously to reach  $39 \text{ V}$  when the etching was stopped after 40 minutes. Several samples with a similar pore quality showed also a similar transient in the voltage, i.e. a dip after the first minutes and then a monotonically rising voltage.

Fig. 7.55 shows a summary of all experimental conditions where fast growing macropores with an acceptable quality (smooth walls, low or no branching tendency) were found. To get high quality pores of the presented kind the following conclusions can be drawn:

- (100) substrates are superior to (111) substrates to suppress branching.
- The HF concentration should be high<sup>6</sup>. E.g. at  $c_{HF} = 20 \text{ wt}\%$  almost all galvanostatic experiments resulted in good pores.
- The current density has to be chosen according to the  $c_{HF}$ , but tendentially a higher current density gives better pores.
- While potentiostatic experiments can sometimes yield good results, in most cases several different pore types appear simultaneously or the growth mode doesn't switch to the curro mode. Galvanostatic conditions should therefore be preferred.
- Pulsing at the beginning of the experiment does not enhance the etching. The exact impact of the pulsing on the etching would still have to be clarified (because the present experiments on pulsing were additionally influenced by insufficient electrolyte bubbling).
- Already without surfactant the pore quality can be very good (cf. Fig. 7.54). A surfactant should therefore only be added after a careful consideration of the type of surfactant, because the role of the surfactant is obviously not simply limited to reducing the surface tension of the electrolyte in contact with the substrate.

<sup>6</sup>Please note that for  $15 \text{ wt}\%$ , the majority of parameter variations has been made, therefore this concentration is overrepresented in the table

orien- tation	HF	TBAP	Tensides	T	GS/PS	t	j_min	j_max	U_min	U_max	d_min	d_max	t_pores	t_pores	etchrate	etchrate
	[wt%]															
100	12	0,1		20	GS	60		50			500	700	260	260	4,3	4,3
100	12	0,1		20	PS	40				20	160	1610	95	122	2,4	3,1
100	12	0,1		20	PS	40				30	160	1210	110	116	2,8	2,9
100	15	0,1		20	GS	60		50			750	2000	200	200	3,3	3,3
100	15	0,11		20	GS	60	80	80	32	41	100	5000	360	360	6,0	6,0
100	15	0,05		20	GS	60					260	3330	300	315	5,0	5,3
100	15	0,11		25	GS	60	55	80	13	60	260	640	320	360	5,3	6,0
100	15	0,11		20	GS	60	80	80	20	53	100	330	250	300	4,2	5,0
100	15	0,11	anionic	20	GS	60	56	80	18	58	150	500	300	360	5,0	6,0
100	15	0,11	cationic	20	GS	60	62	80	18	57	330	500	180	320	3,0	5,3
100	15	0,11	NW601	20	GS	60	80	80	24	40	220	330	300	340	5,0	5,7
100	15	0,1		20	GS	60		80			320	3710	299	337	5,0	5,6
100	15	0,1		20	GS	60	80	100			250		350	350	5,8	5,8
100	15	0,1		20	GS	60		100					325	325	5,4	5,4
100	15	0,1		20	GS	60		120			650	1290	471	486	7,9	8,1
111	15	0,11		20	PS	60				35	40	2500	109	166	1,8	2,8
100	18	0,1		20	GS	60		50			320	810	225	299	3,8	5,0
100	18	0,1		20	GS	60		80			480	970	277	292	4,6	4,9
100	20	0,1		20	GS	60		80			240	1048	296	311	4,9	5,2
100	20	0,1		20	GS	60		100			500	875	446	446	7,4	7,4
100	20	0,1		20	GS	40		120			320	1050	292	322	7,3	8,1
100	20	0,1		20	GS	40		150			780	1250	405	405	10,1	10,1
100	20	0,1		20	PS	10				40	239	392	188	188	18,8	18,8
111	20	0,1		20	GS	60		50			866	1730	340	340	5,7	5,7
111	20	0,1		20	GS	60		100			3000		425	425	7,1	7,1
111	20	0,1		20	GS	40		120			1470	1900	299	299	7,5	7,5
111	20	0,1		20	GS	40		150			1040	1730	334	334	8,4	8,4

Figure 7.55: Overview of conditions which led to a high pore quality in the HF/MeCN/TBAP system.

### 7.3.3 Discussion

#### Oxide influence

As Fig. 7.39 shows, an increase in HF concentration does not speed up the growth of this pore type. Standard mesopores (cf. section 7.1) however, obtained in aqueous electrolytes show a distinct acceleration of growth rate with HF concentration. In the respective section, this was explained by the oxide dissolution rate which is rate determining for many pore systems [5]. Here clearly, oxide dissolution is not limiting. But the classic dependance of the diameter on the HF concentration (cf. section 7.1 for mesopores, [51] for macropores) is still weakly valid: As already sketched in section 7.1 the pore size is coupled to the size of correlated oxide domains [5]. This, in turn, is inversely coupled to the HF concentration [82], which explains the decreasing diameters for larger HF concentrations. Also the comparison of the results in H<sub>2</sub>O and organic electrolytes, suggests that low oxidative capabilities are essential to reach this growth mode.

The diameter shows no clear correlation to the current density, while the growth rate speeds up drastically. The acceleration is similar to the case of conventional mesopores (cf. section 5.2.2), but clearly unlike bsi macropores, which simply get larger upon an increase of current density (cf. section 5.2.1) but do not grow faster. Lehmann [32] explains this by postulating that the current density which is carried at the pore tip is always  $j_{PSL}$ . The system will always try to regulate the pore diameter accordingly, i.e. the pores will become larger when a higher current is forced through the individual pore as well as smaller, if the current per pore is reduced. Föll et al. [5] derive from the high valence of approx. 2.7, that conventional bsi macropores grow with a significant amount of oxidation. Therefore the time between two current bursts is essentially given by the oxide dissolution time. A request for a higher current density can only be fulfilled by a larger active area because the oxide dissolution rate could only be changed by a change in chemistry, i.e. by a change of the HF concentration.

With this behavior, the presented pores clearly deviate from most other pore systems. Classically, most pores grow in an oxide dominated mode (cf. bsi macropores). In case of p-type electrodes, the supply with holes is relatively high, so macropore growth essentially only becomes possible when oxide growth is hindered [51]. The passivation kinetics is also very dominant in the majority of pore systems (grown in crystalline semiconductors) because most pores exhibit crystallographical preferences. Because electrochemical dissolution via an oxide has always shown to be isotropic<sup>7</sup>, only a differing passivation kinetics can explain this behavior (cf. section 5.4). An extreme reduction of passivation and oxidation capabilities like e.g. the use of pure MeCN [48,51] almost always leads a bad pore quality.

One of the few pore systems which behaves similar to this fast pore growth is the cristo-curro pore system in InP (cf. [95]):

- Switch between small crystallographically oriented pores to current line oriented pores (cf. Fig. 7.33)
- Interaction between neighboring pores (cf. Fig. 7.35), e.g. oscillations, which can even synchronize to externally detectable current or voltage oscillations (cf. Fig. 7.36).
- High oxide dissolution rate (InP oxide even dissolves in water [95]).

---

<sup>7</sup>Strictly speaking also oxide growth can show preferential directions [28], but when the oxide dissolution time is several order of magnitude larger (and, as the oxide itself has no crystalline structure, isotropic) the overall silicon removal process via an oxide again becomes isotropic.

Langa [95] assumes a dominance of the oxidative component during the growth of InP curro pores compared to cristo pores. This refers to the much larger size of the curro pores, their smoothness, and their lack of any crystallographical preference. The drastic increase in growth speed is however contradictory to a dominance of oxidation. Even with a bad oxide quality, the growth speed should at best be as fast as direct dissolution.

To summarize: For fast macropore etching

- the pore size is still determined by the oxide domain size.
- it is doubtful that the growth speed is limited by the oxide dissolution rate.

### Passivation influence

In InP as well as in the present pore system in Si, it is inherently clear that surface passivation selectivity is responsible for the crystallographically oriented pores<sup>8</sup>, while it cannot be decisive for current line pores. Yet another only vaguely explained phenomena in InP is the point that always a cristo layer precedes a curro layer, even when curro pore growth is only stopped for a short time [96]. Föll et al. [96] attribute to the cristo layer a not further specified function as a “diffusion limitation for reaction products or educts”. While other species might still be of some importance, all presented results for the fast pore etching system can be understood, if assuming that the cristo layer is essentially a diffusion blocker for the surface passivating species. The diffusion limitation only exists at high current densities, because the reservoir of passivating species gets only depleted if the re-supply by diffusion is slower than the consumption at the pore tip due to a high etching speed. So starting from zero current (i.e. inside as well as outside the pores a high enough concentration of passivating species exists) always cristo pores will grow at the beginning of an etching experiment. This also explains why it is always necessary to grow a cristo layer after a stop in curro etching.

Another hint for the dominant role of surface passivation for this pore type is the strong influence of non-ionic surfactants: In the present system the addition of the WAKO surfactant leads to a homogenization of the nucleation sites and obviously the branching below the nucleation sites does not lead to crystallographically oriented side pores, but the pores seem to “spray” out of the nucleation spots (Fig. 7.53). Unlike the funnels which occurred in other cases (e.g. Fig. 7.32), here the spreading pores are extremely small, which makes a decisive influence of any oxidative component unlikely. Therefore it is justified to reduce the effect of this surfactant to its impact on passivation. It shall also be noted that even an extensive literature research didn’t bring up any influence of all the used surfactants on oxide growth or dissolution. Furthermore, the WAKO surfactant has been shown (cf. section 5.2.3) to influence the direct dissolution in silicon. With alkaline anisotropic etching solutions (which are exclusively based on a complexation of silicon with no indirect oxidative dissolution) the etch rate as well as the selectivity between different surface orientations decreases. Without an oxidizing component, such a behavior is only possible by enhancing and assimilating the passivation for all surface orientations.

The other non-ionic surfactant does exactly the opposite, i.e. it seems to slow down passivation kinetics, thereby enabling a faster etching, because surfaces are passivated worse. This then leads to a smaller active surface to carry the same current, so the pores become smaller.

Summarizing, this merges to the following picture for the fast growing macropores:

---

<sup>8</sup>Nomen est omen.



- During crysto pore growth the passivation species' reservoir depletes.
- When curro pore growth starts, the passivation kinetics for the different directions have essentially become slow and equal.
- The reduced passivation kinetics allows for a faster pore growth.

### Growth model

Fig. 7.56 summarizes the growth model for the fast growing macropores in Si (based on the model of Langa [95]):

(a) After the initial nucleation crysto pores grow with a high degree of direct dissolution. The direction of the pores is given by selectivity of the surface passivation.

(b) At high current densities, the supply via diffusion with passivating species cannot keep up with the extreme growth speed beyond a certain pore depth. The selectivity for passivation gets lost and the pore growth switches to current line pores, i.e. perpendicular to the equipotential surfaces.

(c) When the density of pores is yet low, the pores will grow only on average perpendicular to the surface and will not be perfectly straight, because the other pores are too far away and only pose weak boundaries. Also the pore size will not change significantly, unless the pores get close together.

(d) By successive branching the crysto pore density increases drastically. At a certain depth no further branching is possible. If this depth matches to the depth where the diffusion limitation gets essential, a high density of (ordered) curro pores can be expected. If choosing experimental conditions where the diffusion limitation starts before a sufficiently high density of crysto pores is reached, the curro pores will grow less ordered and therefore probably less stable.

Figs. 7.47, 7.48 show that often the pores do not exhibit rounded pore tips like known from bsi macropores, but spiky tips. In some cases also a round pore tip was seen from which a 10 micron spike extended. This behavior suggests that the oxidative part of the tip reaction cannot be dominating. Otherwise never such a sharp pore tip would result. All of this becomes understandable when a forerunner/trailer concept is endeavored (Fig. 7.57):

As already explained section 4.6.2 the CBM describes a current burst as a sequence of direct dissolution, oxidation, oxide dissolution, and passivation. The fast growth rates can be explained by the strong dominance of the direct dissolution, which is further enhanced by the reduced surface passivation due to the diffusion limitation. Normally (in standard macropores) after direct dissolution the CB spot is oxidized and the next CB starts only after a "very long" oxide dissolution time. This is what happens at the flanks of the tips. There, mainly oxidation gently rounds the pores until the pore reaches its full diameter when the SCR protection of the walls is fully active (signed by an increasingly bluish coloring in Fig. 7.57). The rounded, q-tip-like pore tip somehow marks the depth at which the pore has reached its full diameter. The length of the spiky tip classifies the imbalance between the tip reaction speed and the more oxidatively governed flank reaction speed. When looking from the top, this looks like a mainly directly dissolving like tip surrounded by an oxide dominated ring.

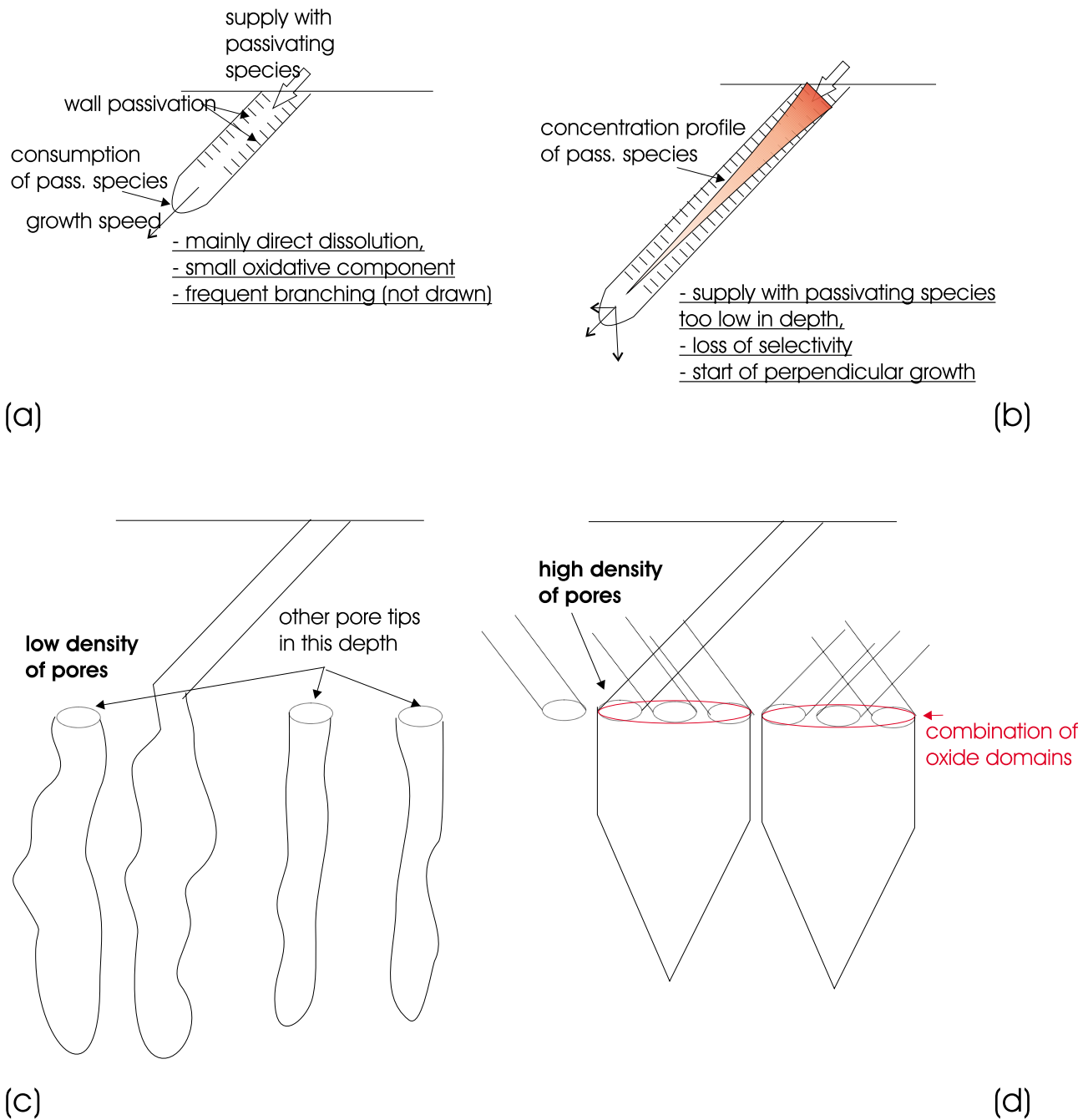


Figure 7.56: Growth sequence for fast growing macropores: (a) Start of crystal growth (b) Shortly before total depletion of passivating species and loss of selectivity. (c,d) After the switch to the curro mode (= loss of selectivity in passivation): (c) A low pore density leads to wavy pores which grow individually downwards. (d) A high density of pores enables the union of the oxide domains from several pores to form a new, larger pore.

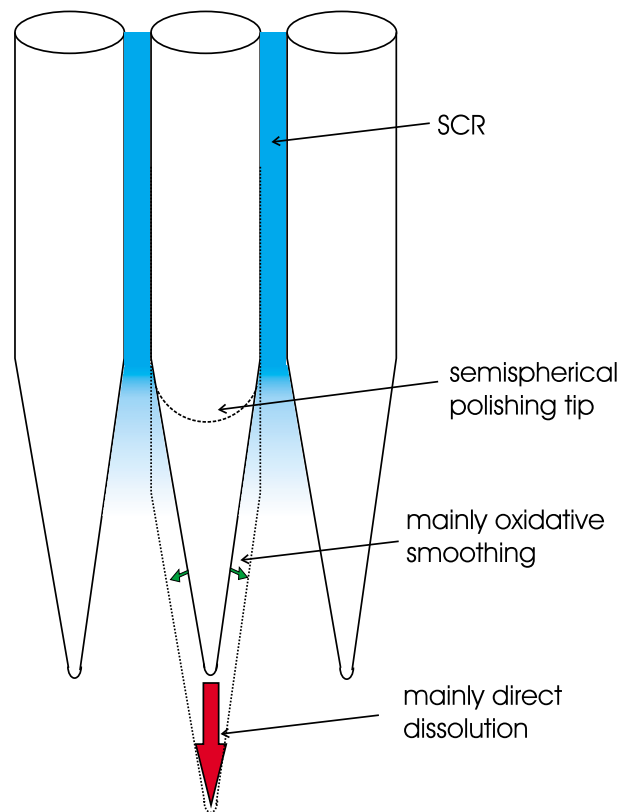


Figure 7.57: Forerunner/trailer concept for fast macropore growth: While the main part of dissolution happens at the sharp tip, an oxidative smoothing follows.

### Voltage transients versus morphology

When comparing the  $U(t)$  curves of the experiments, the following features are often seen (cf. e.g. Figs. 7.37, 7.45):

1. a rapid drop in the first few minutes,
2. a rise to a high voltage plateau around 50 - 60 V,
3. one or more drastic drops in the voltage,
4. a slowly rising voltage over several ten minutes until the end of the etching.

When comparing this to the morphology, it turns out that always when item 2) and 3) were present in the voltage transient, a membrane peeled off and the pores switch from initially very small pores to extremely big pores. In one or more discrete steps the voltage dropped, probably always synchronous with a discrete and distinct decrease in pore size. Finally, a stable pore size was reached which grew over several hundred microns with the slightly increasing potential. When no membrane lifted off and the pores grew with a single size after a nucleation layer (Fig. 7.54c) item 2) and 3) were not present.

The initial drop in the voltage can be linked to the nucleation. It is known from macropore growth [5] that the nucleation, i.e. the opening of the surface passivation requires a higher potential. When the nucleation is finished the voltage increases again due to diffusion limits inside the pores [32]. The same happens here: At the beginning, very small pores with low to medium density nucleate. Depending on the etching conditions this can pose a severe diffusion limitation which causes the rapid increase in the potential. To counteract, the active area is increased as well as the valence, which results in large pores with extremely thin walls. Only due to the SCR in the walls, this structure can be stable at all. Above some critical voltage like 50 - 60 V (cf. e.g. Fig. 7.37) other, currently not further clarifiable, mechanisms set in, which limit the voltage increase. This meta-stable structure grows for a certain time into the depth before it becomes unstable due to e.g. mechanical stress.

When the structure collapses and the diffusion limitation breaks down either by lift-off of a membrane or by heavy cross-linking between the pores, the voltage drops and a re-nucleation of smaller pores occurs. While this new pore ensemble grows into the depth it again poses a diffusion limitation and the voltage rises. But because the density and size of the pores is not as small as with the initial pores, the increase is smaller. Sometimes this re-nucleation process happens several times during the etching (cf. the non-ionic surfactant in Fig. 7.45). In the case of high HF concentrations and optimal growth conditions (cf. Fig. 7.54), the nucleation is so homogeneous that over the whole etching time such a re-scaling of pores does not occur.

When comparing the voltage transients for (100) and (111) samples (Fig. 7.37) the latter ones always require a (much) higher voltage. This is due to the still easier passivation on the (111) surfaces. A pore growth perpendicular to the surface along the field lines necessitates therefore a higher voltage. As seen in Fig. 7.43(b) often not all pores follow the  $\langle 111 \rangle$  direction. This mixing of growth conditions on one and the same sample also suppresses the clear slow increase in the stable growth phase as seen on (100) samples.

### Solvent versus morphology

Based on the model sketched in the last section the morphologies of pore etching in the different electrolytes shall be analyzed. First, the dual morphology in aqueous electrolytes at low HF

concentrations shall be discussed where semispherical breakout spots are covered by a mesoporous layer. Obviously, the mesopores which form at the beginning of the etching exhibit a different morphology at certain spots of the sample (cf. Fig. 7.27). Such a non-uniform nucleation behavior is not unique but frequently occurs in other semiconductor pore systems like GaP, InP or GaAs [95]. Unlike e.g. GaP, where the pore nucleation is very inhomogeneous [162] and seems to start only at dislocation sites, silicon has an extremely high crystal quality, so the homogeneity of mesopore nucleation is better. Still, some surface defects due to sample preparation surely exist.

In III/V semiconductors, Langa [95] has shown that the local current density is the decisive parameter, which governs the morphology under comparable growth conditions. Therefore it is assumed in the present case that the different mesopore morphology above the “defective” sites is caused by a slightly higher (local) current density than at the rest of the sample. In Fig. 7.27 it can also be seen that the mesopores (a) below the “defective” spots are larger and the overall porosity seems higher than at “non-defective” spots, which also supports the idea of an initially higher local current density (cf. section 5.2.2).

Whether a self-amplification of such inhomogeneities or an assimilation with the rest of the sample occurs, depends on the individual pore system. In the present case, clearly a self-amplification happens (Fig. 7.58). As explained in the growth model section on p.133ff. the fast macropore growth mode is based on a depletion of passivating species due to high current densities. A larger current then means a stronger diffusion limitation. Less passivation facilitates again dissolution, which increases the current. Thus, a positive feedback can happen locally, when the current is inhomogeneously distributed.

Fig. 7.58 sketches the growth sequence with such a positive feedback: At the starting time  $t = t_0$  the current density at a nucleation defect is slightly higher ( $j = j_{1,2}$ ) than on the surrounding surface ( $j = j_0$ ). This imbalance aggravates with depth due to a faster depletion with passivating species in the defective region. The current density in the defective regions will rise, which leads in a galvanostatic experiment to a decrease of the applied voltage. This decrease slows down the mesopore growth, which is directly coupled to the applied voltage. The result will be an increase of the imbalance in current density with depth ( $t_0 \rightarrow t_1$ ). When the passivation depletion in the defective regions has reached a critical status ( $t = t_2$ ) the growth switches locally to the curro growth mode. The effectiveness of this special growth mode causes practically all current of the sample to run through these spots, and the rest of the sample stops growing (or grows with drastically reduced speed).

Because the new, larger pore type just starts at certain spots the curro spots can and will expand semispherically into the free volume (Fig. 7.58  $t = t_{3,4,5}$ ). Such a spreading of pores is already known from InP [95] where substrates have been lithographically prepatterned with stripe windows. There the pores expanded semicylindrically into the free volume however these were true current line pores without any crystallographic orientation. Here crystallography still dictates the pore directions in the “hedgehogs”. As it is also seen in Fig. 7.26(a) the pores in the “hedgehog” become smaller and more numerous to the outer part of the structure. This is entailed by the fact that the active etching area increases while the structure grows. Because the current of the individual “hedgehog” will stay more or less constant when only the “hedgehogs” are active, the current density through the outer boundary of the structure will decrease continuously. The pores then become smaller until only a fine network remains with a high porosity. Not in all cases a void shell with a corona of pores like in Fig. 7.26(a) was observed, but very often. Probably, when the pores get very fine the mechanical stability lacks and an outer rim of the “hedgehog” collapses and forms the void. The diffusion conditions

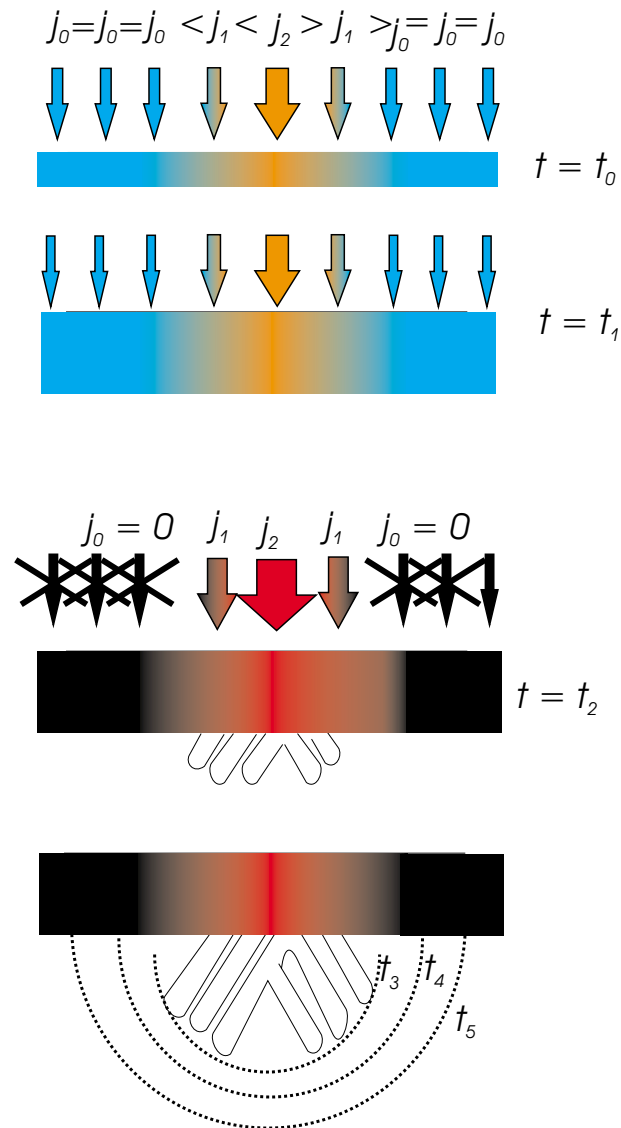


Figure 7.58: Growth model for low HF concentrations in water: Due to a different nucleation, certain areas draw a higher current than others and run quicker into a depletion of passivating species. There the growth earlier switches to the curro mode which leads to an abrupt stop of the growth in other parts. The active spots then expand semispherically into the free volume.

change abruptly and new pores have to nucleate. Again, they start very large and quickly become smaller when the pore growth proceeds semispherically.

When the current density is higher (Fig. 7.26c,d) the nucleation shifts towards a larger number of “defective” spots and the mesopore layer becomes thicker. Now, the shift from the meso- to the macropores happens earlier after nucleation (due to the higher current densities). Because of the high current density, the mesopore growth efficiency is similar to that of the curro pores, i.e. the mesopores do not stop fully when the curros set in, but continue to grow. The curros expand within the mesopore layer which could describe the formation of the funnel structures. When the curro pores get ahead, the surrounding mesopores are effectively cut off the current flow and then stop growing. The higher current density also causes a higher porosity in the funnels which then often collapse completely, only leaving some debris at the bottom.

At 15 wt% the “hedgehog” pores nucleate nearly homogeneously. Because now these pores are everywhere, the pores do not expand semispherically anymore, simply because there is no free volume. This also explains why the pore sizes don’t change as drastically as in the case of etching in the low HF solution. A mesopore layer on top is not visible anymore, however this follows the trend already seen when going from Fig. 7.26(a) to (c) that under more violent conditions the mesopore layer above the macropores becomes thinner and eventually fully collapse to leave only a funnel after the etching. The rough surface at 15 wt% indicates that there was initially a mesopore layer but that it was washed away after the development of the mesopores.

In summary, the results in aqueous electrolytes resemble to a certain degree the cristo-curro transition in InP. The second pore type:

- doesn’t grow from surface directly, which suggests that they first need a certain kind of diffusion limitation;
- grows more effectively than the mesopores (i.e. with less voltage to reach the same current), otherwise the system would not switch into this growth mode;
- consists of drastically larger pores.

Why is such a growth not possible on highly doped samples? For macropore growth a high selectivity between pore tip and walls is necessary. On medium to low doped samples the breakdown voltage necessary for hole generation is drastically higher than on highly doped samples. The pore walls of macropores are in most cases protected by surface passivation and/or a space charge region depletion. On highly doped samples the space region is much thinner which would result in nm-sized walls which wouldn’t be stable. Also passivation can only set in if a significant difference in the hole supply exists and some surface elements remain current less for a while so that they can get passivated. On highly doped samples these difference are simply too small, which explains that the samples in the present work mainly electropolished.

With pure DMF the oxidation power of the electrolyte, its passivation abilities, and its conductivity are strongly reduced compared to aqueous solutions. The complex surface patterns (cf. Fig. 7.29) suggest that this doesn’t hinder the nucleation of mesopores which also exhibit a branching pattern like it would be expected from InP. The mesopores have smaller sizes than with aqueous electrolytes. Here the much lower oxidation power of DMF should be the reason, i.e. the oxidative part during the mesopore growth is largely suppressed. Similar to aqueous electrolytes, after a certain thickness a switch in growth mode occurs, but a stable

currentline growth mode is not possible here. Instead, larger cavities are formed. Similar to the hedgehogs in certain aqueous solutions, after the cavity formation a re-nucleation of pores follows. The inability to switch into the current mode becomes understandable when considering the drastically lower conductivity without TBAP. Therefore when the orientation selectivity is lost, the high ohmic losses prevents deep pores and a more or less isotropic dissolution quickly leads to a large cavity. That this process sequence happens repetitively aliments the image of a dynamic depletion of a certain species due to the block by the cristo layer.

The addition of TBAP yields similar surface structures, however below the tripods the growth changes into a true currentline mode. A growth along the otherwise unfavorable  $\langle 111 \rangle$  direction is a phenomena which has not been observed in Si before. What has changed by the addition of the conducting salt? Mainly the conductivity of the electrolyte, but the mesopores also become larger (cf. the individual “hairy” pores constituting the tripod in Fig. 7.29c with the pores forming the tripods in Fig. 7.30a, inset). This points according to the CBM to a larger oxidation portion in the reaction, i.e. the nominal oxidation power of the electrolyte is increased. The surface structures look very similar to (100) InP where pore growth proceeds first along the  $\langle 111B \rangle$  directions (crysto pores) and switches then to a close packed curro pores which grow perpendicular to the equipotential lines, i.e. normally perpendicular to the surface. Also a similarity to the results in aqueous electrolytes are seen in the switch from cristo to curro pores, however the pores are smaller with DMF/TBAP. Again the concept of oxidation power can be invoked, which attributes water a higher oxidation power than organic electrolytes (with some rare exceptions like formamide [51]). Also the passivation is expected to be worse in organic electrolytes, which is reflected in the true current line growth of the curro pores compared to aqueous electrolytes.

### Nucleation behavior

The MeCN/TBAP results show that it is not always mandatory to have a cristo layer on top of the curro pores, but also a direct nucleation at the top is possible. This manifests in a funnel of pores (cf. Fig. 7.53). The pores branch quickly, but not along crystallographic directions like cristo pores. Please note that this is unique to silicon, while in InP only a branching with clearly defined angles inside the cristo layer is found. Even under inhomogeneous nucleation conditions like the InP waveguides shown by Langa [95], the cross section of the sample only exhibits non-branched currentline pores.

During the presented experiments it showed that

1. high voltage pulses at the beginning support funnel formation, i.e. oxide formation is supported. This is consistent with Lehmann’s observation that the mesopore valence increases with current density [45].
2. insufficient bubbling leads to larger pores. It is known that the oxidation power of organic electrolytes increases by the absorption of ambient oxygen and water [5] which again intensifies oxidation.

The funnels nucleate directly at the top, which indicates that the passivation selectivity must be already initially much lower than in InP; otherwise a growth in  $\langle 111 \rangle$  direction would not be possible. The size of these structures should be defined over the correlated oxide domains, i.e. more oxidation (due to pulsing or insufficient bubbling) promotes funnel formation. However, oxidation cannot be dominant because then the funnel pores would be much slower than the rest of the pores which is obviously not the case.



The nucleation of the funnels is thus a manifestation of macropores in a sea of mesopores. This is again some kind of “domain” formation [163]. Which pore type nucleates on a surface is a (difficult) question of the etching conditions. As in the case of the aqueous electrolytes the funnel pores probably benefit from the positive feedback loop already sketched above: Because the funnels can draw a larger current density (because there is no cristo layer above) the passivation depletion is more severe there. This leads to a faster growth of the funnel pores which after some time will fan out into the free volume, which leads finally to a “crowding out” of the other curro pore type. In some cases like the potentiostatic experiments from Fig. 7.40 the funnels probably nucleated only scarcely. With a dense nucleation of funnels an arbitrary cross section always slices a significant number of funnels, so many of them are visible (in cross section) directly from the top. For a scarce nucleation of funnels, the funnel nucleation points often have a significant distance to the cleavage edge. In cross section the sliced funnels then look like they “break” out of the cleavage plane in a depth of e.g. 100 microns. A second reason for a “late” breakout can be that the speed advantage of the funnel pores depends on the etching conditions. In the experiments with different pulsing times (Fig. 7.43) a longer pulsing time led to an earlier spreading of the funnels.

It also showed that the funnel pores often don’t have the extreme degree of ordering compared to current line pores that started below a cristo layer. Furthermore they often show tiny side branches, rough pore walls, and not a straight perpendicularity, but wavy pores which seem to mosey between their neighbors. The problem is here that the pore ensemble doesn’t start simultaneously like after the abrupt change from cristo to curro pores, but sequently new pores are splitted off, which does not necessitate such a close packing. As sketched in Fig. 7.56 only an ultimate proximity of neighboring pores enforces a straight growth downwards because other limitations like surface passivation are not present in this system.

For the formation of nice pores two possible conclusions can be drawn (also taking in mind the parameter table from Fig. 7.55):

- Avoid the nucleation of funnels, i.e. suppress inhomogeneous nucleation
- or
- enforce a real close packing of the funnel pores by choosing a high current density which urges them to branch more often.

### Close packaging patterns

Not too surprising, the close packing of the curro pores shows a different pattern depending on the substrate orientation. On (111) a standard hexagonal close packing occurs (Fig. 7.30), however on (100) the pores exhibit triangular ordering patterns as well as quadratic ones (Fig. 7.49). The coordination number analysis shows also a peak around 5 nearest neighbors. While a clear pattern for the next nearest neighbor is not seen in the auto-correlation which analyzes the self-similarity of the pore pattern in real space, the second nearest neighbor exhibits a quite uncommon 12-fold symmetry.

When the (111) surface pattern in different depth levels (cf. Fig. 7.30) are assembled to a schematic picture (Fig. 7.59) the pore growth proceeds as follows: First, a layer of cristo pores grows, which are all oriented along  $\langle 100 \rangle$  directions. These directions form a tripod on a (111) surface similar to the edges of a cube standing on its corner. Like that the tripod patterns from Fig. 7.30(a), which only occurred on (111) substrates, become understandable. With increasing depth the density of cristo pores will increase due to branching until a shift to

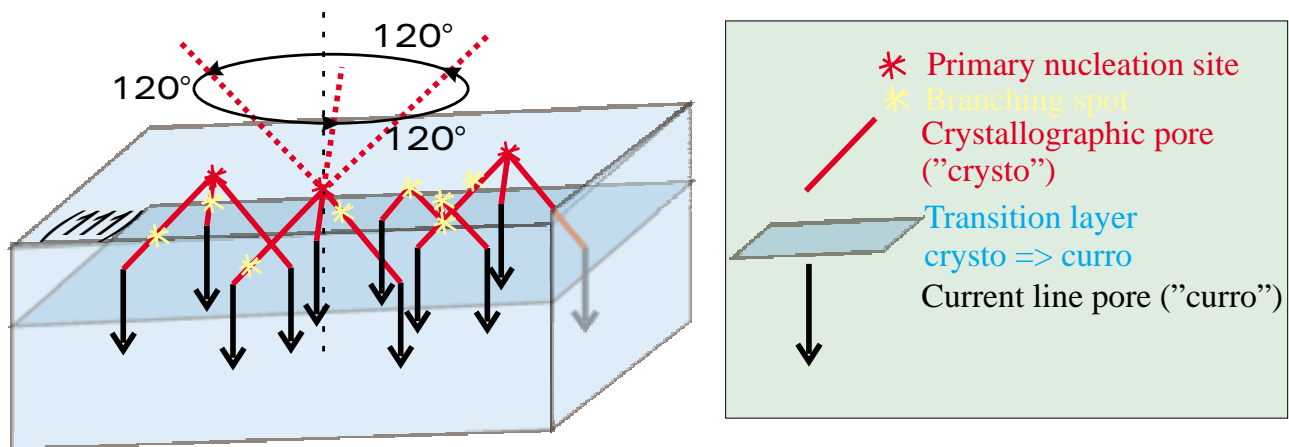


Figure 7.59: Pore pattern formation on (111) wafers: The crysto pores grow as tripods along the  $\langle 100 \rangle$  directions. This symmetry matches the triangular symmetry induced by close packing after the switch to the curro mode.

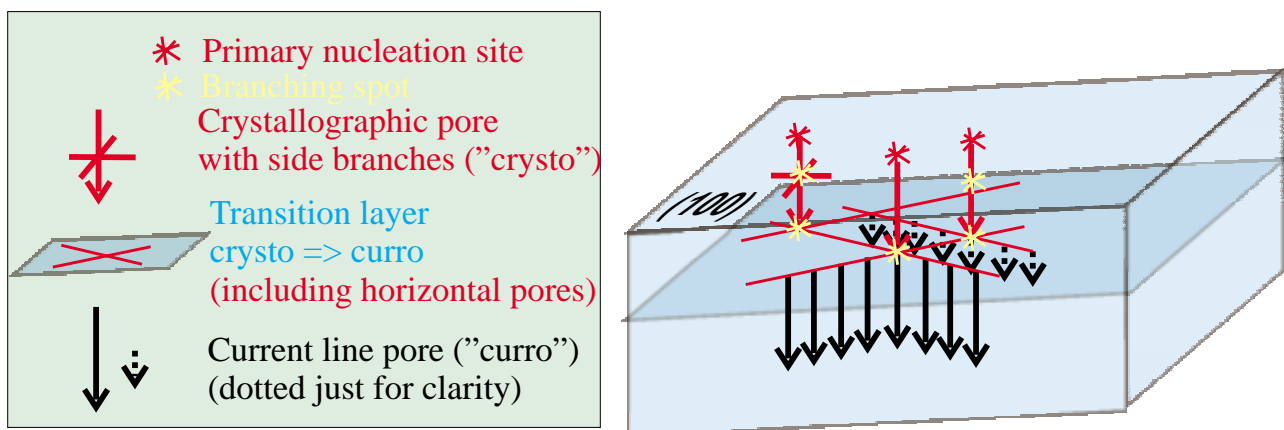


Figure 7.60: Pore pattern formation on (100) wafers: The crysto pores grow perpendicular to the surface and branch with a four-fold symmetry along the  $\langle 100 \rangle$  directions. This symmetry collides with the triangular symmetry induced by close packing after the switch to the curro mode. The resulting pore crystal then exhibits a geometrically frustrated pattern.

the current line oriented growth in a close-packed lattice to maximize the active area becomes favorable. The three-fold branching symmetry matches here the three-fold symmetry inherent to close-packed, round structures.

A totally different nucleation pattern arises in the case of (100) wafers (Fig. 7.60): The preferential growth directions for mesopores are now perpendicular to the surface and parallel to the surface. The initial nucleation does not show ordering (cf. Fig. 7.46), but below branching will occur and lead to an increased mesopore density with increasing depth. Horizontal cleavages will always yield flat structures (cf. Fig. 7.46) which exhibit criss-cross patterns along the laterally lying  $\langle 100 \rangle$  directions. The geometrically frustrated structure in the curro layer from Fig. 7.49 could therefore result from a competition of the four-fold branching symmetry in the crysto layer and the three-fold symmetry of close packed pores. While the situation is tangled for the nearest neighbors, in the second nearest neighbors the least common multiple of the two symmetries, which is twelve, prevails.

Geometrical frustration is a phenomenon sometimes encountered in condensed matter physics in which the geometrical properties of the atomic lattice forbid the existence of a unique ground state, resulting in a nonzero residual entropy [164]. In magnetic materials geometric frustration results e.g. when the spins shall be distributed on a triangular lattice for an anti-ferromagnetic material. Already after placing the first two spins on a triangle, it is not possible to satisfactorily (i.e. with a minimum in energy) place the third spin, because it will be obviously parallel to one of its two triangular neighbors. The most common example of a geometrically frustrated material on an atomic scale is however ordinary water ice (so-called ice-I), where the oxygen atoms reside in a well-ordered lattice, but where the hydrogen atoms are very unordered. This leads to the residual entropy of around 3.40 J/K/mol. Also on larger scales geometric frustration effects have caused interesting new effects, e.g. the blue phase of chiral nematic liquid crystals stems from frustration effects. While the geometrically frustrated pore structure is certainly too large to cause new magnetic effects, e.g. a frustrated ordering of pores in a 2D photonic crystal could be a possible field of application, though this still has to be measured. Up to now, this is the only known self-organized pore type which exhibits such a frustrated behavior.

### Role of surfactants

Prior to an analysis of the results, already from the known properties of the semiconductor electrolyte junction (cf. section 2.3) the response of the contact to an applied anodic potential can be classified (Fig. 7.61):

(a) When the surface is fully passivated, i.e. no unsaturated bonds (which act as surface states) are present, the applied potential drops mainly in the semiconductor. The potential which drops in the electrolyte and which can therefore drive an electrochemical reaction is low like the resulting current. When additional charges are brought to the interface (e.g. as ionic surfactants) the semiconductor adjusts its space charge region (SCR) to change the number of mirror charges. For n-type silicon an additional anion on the electrolyte side is answered by an extension of the SCR, which is identical to increasing the reverse potential, i.e. the contact is even driven into the blocking regime. This, on the other hand, minimizes the flowing current and hence the dissolution of silicon at this spot. Similar a cation will diminish the SCR and thus act like a lower reverse potential and promote dissolution.

(b) When the surface passivation is bad, many surface states exist and pin the Fermi level. The space charge region (compared to a fully passivated surface) has only a negligible extension

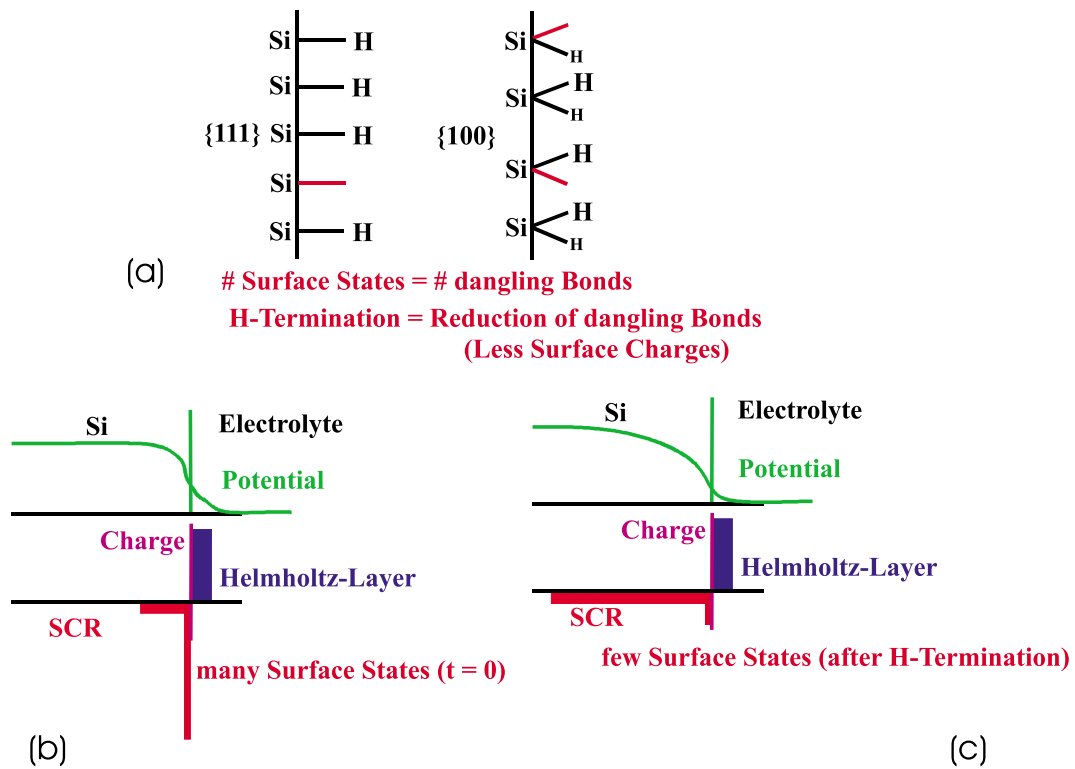


Figure 7.61: Influence of surface states on the charge and potential distribution along the semiconductor-electrolyte contact: (a) Illustration of the surface termination in silicon. (b,c) Potential distribution with (b) many surface states (= bad passivation) resp. (c) few surface states (= good passivation) (after [92]).

or fully vanishes for a sufficiently high number of surface states. The number of charges per area at the surface can reach up to the density of surface atoms. An applied potential drops much less in the semiconductor due to the high charge density at the interface. This increases the potential drop in the electrolyte for driving the electrochemical reaction. Such sites are essentially unprotected and are etched very quickly. Under such conditions, still the effect of additional charges is occurring as sketched in (a), but the passivation of defective surface sites will have a tremendous effect on the resulting potential distribution which can easily overcome the effect sketched in (a).

The interface capacity which can be measured during e.g. impedance spectroscopy consists in fact of a serial connection of capacities (SCR, surface states, Helmholtz layer and (here not applicable) oxide layers). The total capacity is calculated via  $C_{total}^{-1} = C_1^{-1} + C_2^{-1} + \dots$ . When the capacities are largely different, which they are here because of totally different length scales and charge densities, the total capacity is essentially given by the smallest capacity in the line. The Helmholtz layer has a high charge density ( $\rho \approx 10^{19}e/cm^3$ ) and hence a very small extension ( $d \approx 1 - 10nm$ ), so the resulting capacity is huge compared to the SCR capacity ( $\rho \approx 10^{16}e/cm^3, d \approx 1 - 2\mu m$ ). If surface states exist their capacity depends on their areal density. However if only 1% of all surface atoms are not passivated in a semiconductor with a doping of  $10^{16} cm^{-3}$  then already the capacity of the surface states exceeds the SCR capacity [28]. As sketched above, the SCR, which is normally built up under reverse bias collapses when surface states are present beyond a homeopathic dose. Therefore a surface with locally bad passivation has to be seen as a parallel connection of SCR dominated capacities  $C_{SCR}$  and other areas with a significantly larger capacity  $C_2$ , where the SCR collapsed. As the total capacity of a parallel connection of capacities is simply the sum of the individual capacities, the worse passivation of some surface parts leads to a larger externally measured capacitance  $C_P$  (in case (b) compared to (a)).

Ionic surfactants carry always a charge and are thus always acting in the way sketched in (a). Additionally, surfactants can influence the surface reactions by facilitating or by worsening the transport of reaction products and educts. It is therefore likely that surfactants can have a heavy impact on the surface passivation reaction, positive or negative. Of course surfactants are complex molecules and can change the surface reactivity via several other effects (e.g. formation of micelles) which are not covered by the model sketched above.

Like already mentioned in the section 5.2.3, surfactants in electrochemical etching have been mainly seen as a measure to reduce surface tension. However, the works of Ogata et al. [132], Chao et al. [112], and Schweizer et al. [133] (cf. section 5.2.3) have shown that the surfactant molecules definitely change the interface potential distribution. While the results of the last two groups are essentially explained by the argument of additional charges on the surfactants, the results of Ogata cannot. Here the cationic surfactant leads to the worst result on a p-type semiconductor, i.e. the band bending is decreased<sup>9</sup> and the chemical dissolution (which is working via a complexation of the Si atoms like the direct dissolution in electrochemical etching of silicon) of the microporous structure is promoted. While the charges introduced by the cationic surfactant of course still act as sketched above, this positive effect on the passivation is most probably overcompensated by a higher content of surface defects when using the chosen surfactant. This would also explain why also non-ionic surfactants can have a significant impact on the pore morphologies.

In the present work, the ionic surfactants only showed small effects for the morphology

---

<sup>9</sup>Please note that even on p-type in the low voltage regime the contact still operates in depletion. A “forward” characteristic with accumulation is only seen using organic electrolytes which avoid oxidation (cf. section 3.2).

and the  $U(t)$  curve compared to etchings without surfactant. This suggests that in this pore system the additional charges brought into the interface region by the surfactant are not the dominating effect of the surfactant. The remaining off-sets in the voltage transients compared to an electrolyte without surfactant, can be easily explained by a slightly different nucleation and/or pore size as explained on p. 136.

The non-ionic surfactant showed the most pronounced reaction. For NCW 601-A it is known from literature (cf. section 5.2.3) that it reduces the selectivity and the etch rate during anisotropic chemical etchings. Also in pure chemical etchings based on a direct complexation of the silicon the orientation dependance is given by the degree of passivation on the respective surfaces. A reduced selectivity means nothing else but an equalization of the passivation kinetics for all directions. If the passivation is enhanced on all surfaces this leads to an overall reduced etch rate. In the present work, the pores become extremely smooth. This could be explained by the reduction of the passivation selectivity, which levels out any differences and inhibits hillock formation on the walls. Already for the “spraying” out pores directly underneath the sample surface the loss of strict crystallographic orientation can be observed. Furthermore, it is observed that pores are packed closer with tendentially thinner walls, i.e. the active area increases when NCW 601-A is added to the solution. Because the total currents applied to the samples are the same ( $I = 80 \text{ mA/cm}^2$ ), an increase in active area means a decrease of the local current density. A lower current density in the CBM can be caused by a longer interval between current burst nucleations. The probability for the nucleation of a new CB at the same spot decreases monotonically with the degree of surface passivation. The enhanced passivation caused by NCW 601-A thus leads on average to a slower growth and closer packed pores as observed.

The pores on the top surface of the NCW 601-A sample (Fig. 7.53) are extremely small which is contrary to a pore system with a high degree of oxidation [5]. In many pore systems, additional oxidation in the reaction is the reason for a loss of crystallographic orientation of pore growth, because oxidation has always been shown to be isotropic (cf. section 4). However, a surfactant normally doesn't introduce additional oxidation [132] as also seen in the present experiments. Therefore oxidation can be ruled out as a reason for the broader pores which do not grow along the classical directions.

Genapol UD-088 just behaves the other way round: Here the pores have smaller diameters and the walls are thicker and rougher than without surfactant. In the framework of the model given above this can be explained by a worsening of the passivation. Then the average time for a CB gets shorter and a higher current density can be transport through a certain area. In a galvanostatic experiment this results in a reduction of the active area, i.e. by a shrinking of the pores. The rough walls and tiny side pores are an additional sign of a bad surface passivation. The impedance measurements show a decreasing parallel resistance upon the addition of the surfactant, i.e. the chemical reactions at the interface get easier. This is again a hint for the worse protection of the interface which promotes reactions at this interface. The slight reduction in serial resistance is not directly clear. The capacity increases, which can be explained under the assumption of higher density of defects caused by worse passivation kinetics.

### 7.3.4 Conclusions

Starting from the promising results in InP, a new pore growth regime in silicon was found with the following features:

- The pores grow with the same high speed as mesopores. With this technique the etch

time for deep macropores could be reduced to economically sensible values of 30 - 90 minutes.

- Their structural quality is comparable to bsi macropores.
- The pore size for macropores of high structural quality could be extended down to  $\approx 100$  nm diameter.
- The pores tend to self-organize hexagonally close-packed, or as “frustrated” structures previously not discovered in pore crystals.

During the experiments and their analysis, it was possible to:

- clarify the role of surfactants,
- formulate a consistent growth model for this pore type, and
- optimize the growth conditions for the fast-growing macropores.

These pores in silicon are closely related to the curro pores in InP. Here especially the strong interaction between pores is similar: Pores oscillate collectively, up to externally visible voltage oscillations. Such behavior is (almost) new to silicon, and has only been rarely observed [51]. The high density of pores in the new system also introduces self-organization to silicon pores which was previously only known in this extend from InP. Another similarity is the collective switch of all pores from a pore type with strict crystallographic orientation (“crystos”) to a much larger pore type which orients exclusively along the electrical field lines (“curros”).

However, also striking differences to InP exist. While a cristo layer is a must in InP for curro pore growth, it is possible in silicon to directly nucleate curros at the surface. Also the behavior seen in aqueous electrolytes where a switch from mesopores to still crystallographically oriented curro-like pores occurs, is (yet) unique to silicon. Last, but not least, the difference in preferential pore growth direction in silicon ( $\langle 100 \rangle$  resp.  $\langle 113 \rangle$ ) compared to InP ( $\langle 111B \rangle$ ), gives the unique possibility in silicon to generate a geometrically frustrated pore crystal.

In silicon, this pore system is still its infant state. For any (industrial) application it is certainly necessary

- to further investigate the huge parameter field to find an experimental window where reproducibility and stability of this growth mode can be guaranteed;
- to optimize the nucleation conditions to have only cristo pores or directly nucleated curro “funnels”. As long as they co-exist the competition between these two nucleation modes will make a clear understanding of the system difficult;
- to investigate this pore type on pre-structured samples. It is known from InP that the growth of curros at lithographically predefined spots is by far more complicated than the growth of ordered bsi macropores in silicon.





# Chapter 8

## Porous oxides - Experimental results

### 8.1 Introduction and experimental set-up

Almost always when water is present in solution (even in sub-% traces), an oxide forms during the anodization on the silicon surface (cf. section 4.2). Choosing optimal conditions (low current density, low water content) it is possible to produce anodic oxides which can rival the quality of thermal oxides, but normally the anodic oxides are of a worse quality [28]. A dissolution of silicon oxide is in most cases only possible by fluoride containing solutions, therefore anodization in a fluoride-free media leads to an ever increasing oxide layer. Up to 11 nm, Lehmann [68] measured the oxide to be dense, afterwards it becomes porous. This behavior can recur periodically and can lead to externally measurable oscillations in the current or the voltage [61, 68].

If fluoride containing electrolytes are employed the formation process is always accompanied by oxide dissolution. Although this increases the complexity, it is unavoidable to study this system to fully understand the behavior of the Si-HF contact and e.g. the porosification of silicon (cf. chapters 3 and 5). The standard anodic oxidation experiments in aqueous HF addresses voltages below 10 V (cf. section 4.5), only some authors have investigated the regime up to 100 V [20, 69, 71] where always porous oxides result (cf. section 4.3).

Already from the fundamental point of view the investigation of the formation mechanisms of porous silica is interesting to get a deeper understanding of the Si-HF contact. But also from an application point-of-view low-k dielectrics in microelectronics will have to rely soon on porous oxides [14]. So-called controlled pore glasses (CPG) are heavily used in chromatography and other biochemical applications [165]. Besides that the discovery of highly ordered structures in alumina [17] has nourished the hope that similar structures could be feasible by electrochemistry in other oxides, namely silica.

A problem during the study of porous silica in fluoride media is the extremely fast dissolution rate especially after the experiment. This necessitated always a very fast removal of the specimen from the solution for any ex-situ analysis. Furthermore, several porous systems rely heavily on local differences in the pH value, e.g. during the pitting corrosion of metals the pH inside a pit (expanding later on into a pore) is markedly lower than in the bulk solution [166]. Also the dissolution rate of silica decreases strongly with increasing pH (cf. section 4.4), hence for the present work weakly buffered slightly alkaline ammonium solutions were chosen.

Preliminary work [167] has shown that under conditions similar to those in the present work the cyclic voltammogram exhibits a significant hysteresis. Layers from potentiostatic experiments were analyzed mainly by optical spectroscopy. Fittings of the optical data revealed

layer thicknesses between 100 and 500 nm where most of the layer was porous with a thin ( $\approx 10$  nm) layer of dense (i.e. non-porous) oxide between the substrate and the porous silica.

All experiments of the present work were carried out with the RDE (rotation rate  $\nu = 1500 \text{ min}^{-1}$ , unless otherwise noted) set-up described in section 6.1.3, where also the sample preparation is noted. The samples were all cut from commercially available p-type (100) wafers ( $\rho = 1 - 15 \Omega\text{cm}$  resp.  $\rho = 2 - 10 \Omega\text{cm}$ ) with an ohmic backside contact and tape-coated from the front side to define a circular electrode area of  $A = 0.15 \text{ cm}^2$ , resp.  $A = 0.04 \text{ cm}^2$  (for high current density experiments).

The electrolytes were mixed using millipore ultra-pure water,  $\text{NH}_4\text{F}$  salt and  $\text{NH}_3$  (25 wt%, p.a. grade, Merck Inc.), with fluoride concentrations of 0.1 - 0.75 M. The buffer ratio was chosen 25:1, e.g. 0.25 M  $\text{NH}_4\text{F}$  : 0.01 M  $\text{NH}_3$ , unless otherwise noted. Thus the ammonia buffer already operates on the extreme left of Fig. 2.11 ( $\text{pH} \approx 8-9$ ), which was chosen intentionally to enable a local switching of the solution to much more acidic values.

Two types of experiments were mainly performed:

1. cyclic voltammograms from  $U = 0$  to 30 V and back with a slow sweep rate of  $r = 10 - 50 \text{ mV/s}$ .
2. fast potentiodynamic sweeps from  $U = 0$  V to approx. 25 V ( $r = 500 \text{ mV/s}$ ) and then back to a desired potential, e.g.  $U = 15$  V, where the sample was anodized potentiostatically for 10 minutes.

The first type of experiments was designed to explore the electrochemical behavior of the system, especially the earlier mentioned hysteresis. The samples which resulted had in most cases a dull surface, because they had gone through all different regimes of the  $IV$  curve and were therefore not further analyzed by microscopy. The second type of experiments were ideal to trigger the hysteresis of the system and “enter” the upper branch of the  $IV$  curve to grow homogeneous thin films during a potentiostatic anodization. These films were analyzed by optical and electron microscopy using a Philips XL-30 respectively XL-40 SEM. As  $\text{SiO}_2$  is highly insulating, the samples were always coated with 9-10 nm Au or Au/Pd prior to the imaging unless otherwise noted.

## 8.2 Experimental results

At first, the system was investigated by cyclic voltammetry (Fig. 8.1). The electrolyte was in this case 0.25 M  $\text{NH}_4\text{F}$ . In all cases the voltammogram exhibits a strong hysteresis, i.e. on the positive scan the current stayed below  $10 \text{ mA/cm}^2$  (below 10 V even in the sub-mA range). At approx.  $U = 19$  V to  $U = 21$  V the current density rises by two orders of magnitude. The absolute value reached during that steep increase depended strongly on the rotation rate  $\nu$  of the electrode (e.g.  $j = 140 \text{ mA/cm}^2$  @  $\nu = 1500 \text{ min}^{-1}$ ), while the sweep rate only altered the steepness of the flanks of the curves. Between  $\approx 21$  V and  $\approx 24$  V the current increased modestly with a slope  $a$  of 3-5  $\text{mA}/(\text{cm}^2\text{V})$ . At  $U = 24$  V the characteristic bends to rise again linearly, but with a higher slope  $b \approx 25 \text{ mA}/(\text{cm}^2\text{V})$ . Only  $a$  exhibited a monotonic increase with increasing  $\nu$ , while  $b$  didn't show a clear correlation to  $\nu$ .

The negative scan matched the positive scan until  $U \approx 21$  V (where the positive scan came up with the steep rise). Here the negative scan continued with slope  $a$  down to 10 V. The scan then quickly falls off to the same level as the positive scan at  $U \approx 7$  V.

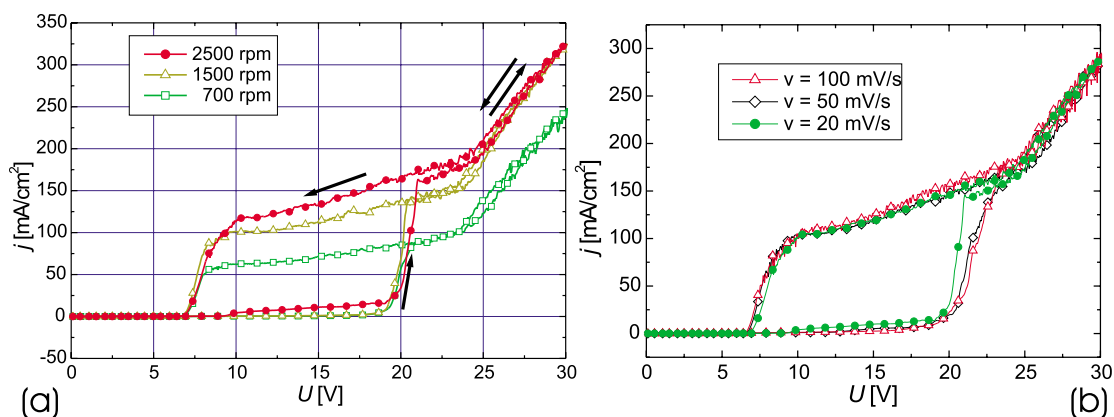


Figure 8.1: (a)  $IV$  - curves (scan rate  $r = 20$  mV/s) for different rotation speeds of the rotating disk electrode (RDE) ( $0.25$  M  $\text{NH}_4\text{F}$ ): 700 rpm (green/open squares), 1500 rpm (brown/open triangles), and 2500 rpm (red/filled circles). (b) The scan velocity's influence on the  $IV$  - curve is minimal ( $0.25$  M  $\text{NH}_4$ ).

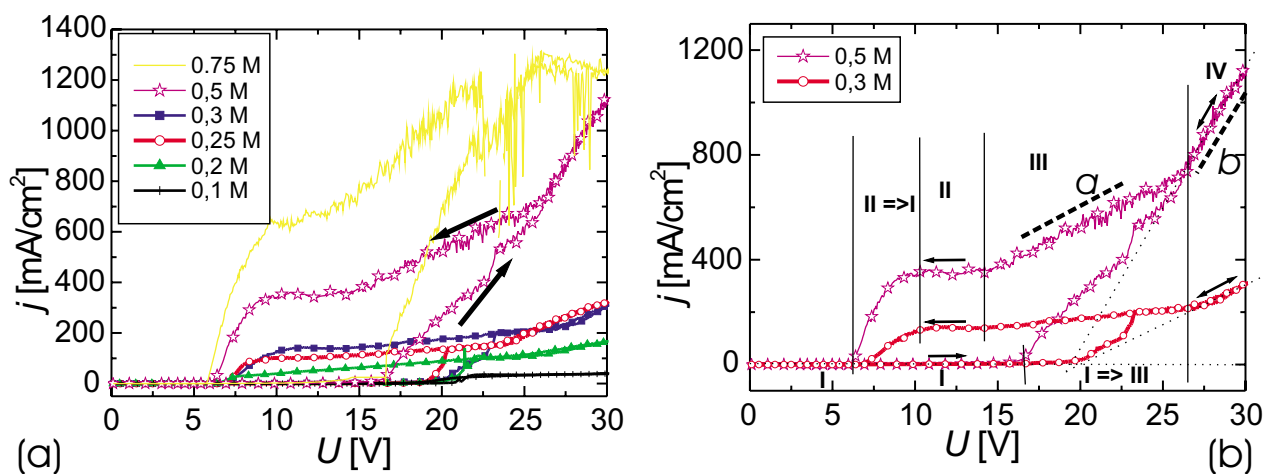


Figure 8.2:  $IV$  - curves for different  $\text{F}^-$  - concentrations: (a) Overview. (b) The  $IV$  - curves can be separated in the following sections: (I) Starting from  $U = 0$  V the current stays very low as expected from alkaline fluoride media. (I  $\Rightarrow$  III) At  $U = 17 - 20$  V the current strongly increases. (III) The current rises linearly (slope  $a$ ) with  $U$ . (IV)  $j$  increases again linearly but with a larger slope  $b$ . The backward direction starts to deviate from the forward scan in region (III) where  $j$  falls off linearly until  $U = 14$  V. (II) From 14 to 10 V the current density stays constant (except for low fluoride concentration  $c_F \leq 0.2$  M). (II  $\Rightarrow$  I) The backward scan rapidly falls off between 10 and 7 V volts. (I  $\Rightarrow$  III) The forward and backward direction only show sub-mA current densities.

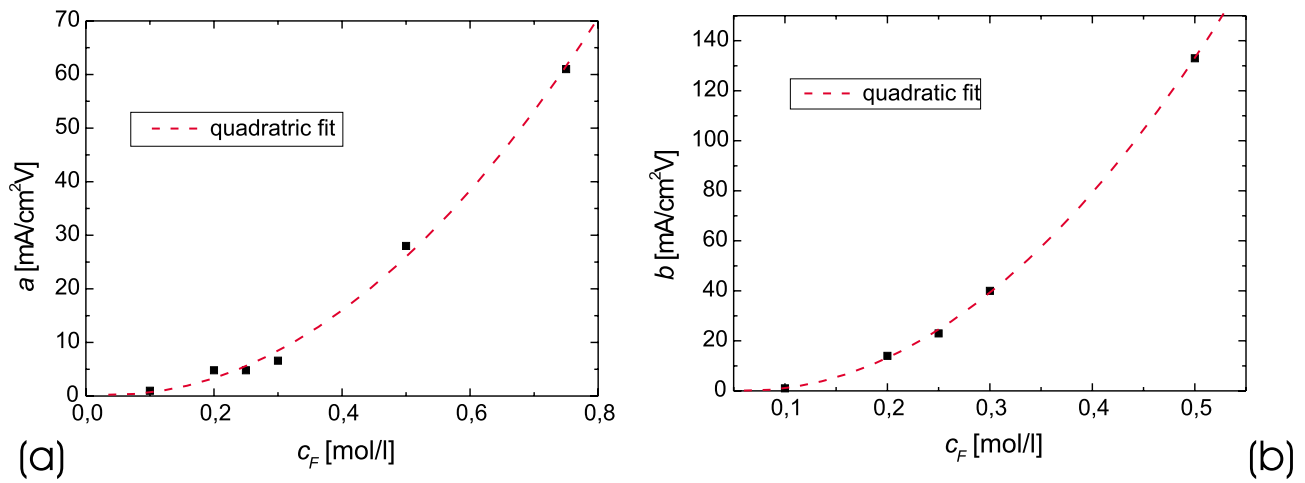


Figure 8.3: Analysis of the slopes  $a$  (a) and  $b$  (b) of the  $IV$  curves from Fig. 8.2.

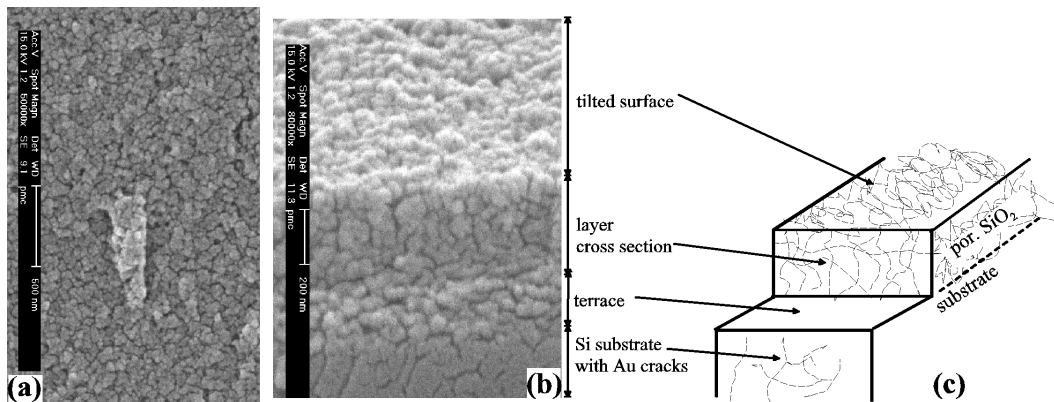


Figure 8.4: Morphology of porous SiO<sub>2</sub> grown at  $U = 10$  V ( $c_F = 0.3$  M): (a) SEM plain view. (b) SEM tilted cross section. (c) Schematic drawing of the cross section.

The cyclic  $IV$  curves (Fig. 8.2a) show that the fluoride concentration  $c_F$  has a strong impact on the hysteresis: While with  $c_F = 0.1$  M a hysteresis between the scan directions is almost absent,  $c_F = 0.75$  M leads to a huge hysteresis where the current density exceeds  $j = 1200$  mA/cm<sup>2</sup>. In the latter case, the potentiostat operated at its limit and heavy gas evolution in the regime beyond 20 V led to breakdowns in the current. Generally in all experiments an increasing gas evolution (probably oxygen [20]) was observed when surpassing approx. 20 V which also led to an increase in the current signal noise. The voltammogram can be divided in several regions (Fig. 8.2b), which only become fully visible with the higher concentrations (described in the order of appearance on the cyclic voltammogram):

- I: The current density stays very low from  $U = 0$  to approx. 17 - 20 V.
- I  $\Rightarrow$  III: Transition region where the current rises very strongly. For very slow sweeping speeds the increase can be almost vertical.
- III: Slow linear rise of the current density with slope  $a$  between  $U \approx 14$  V and  $U \approx 26$  V.
- IV: Strong linear increase of  $j$  with slope  $b$  for  $U > 26$  V.
- II: Plateau in the current density on the negative scan.
- II  $\Rightarrow$  I (between 10 and 7 V): Merging of the negative scan into the positive scan. Afterwards similar low currents like on the positive scan (between 7 and 0 V).

Both slopes  $a$  and  $b$  show a quadratic dependance on  $c_F$  (Fig. 8.3).

Fig. 8.4 shows the SEM plain view and cross section of a thin film silica sample grown at  $U = \text{const.} = 10$  V ( $c_F = 0.3$  M). The sample shows clear interference colors which change upon tilting as known from other thin films [168]. The color under a given angle is almost equal over the whole etching area, which points towards a good homogeneity of the thickness because the interference colors already change with some ten nm difference in the film thickness. The fine structure on the surface (Fig. 8.4a) shows a granular structure with cracks of approx. 10 nm. The individual grains have a size of 10 - 50 nm. In the cross section (Fig. 8.4b) in the lower part of the image the silicon substrate also shows some crack-like structures, which clearly originate from the Au sputtering prior to the SEM imaging. In the middle of the image the porous SiO<sub>2</sub> layer is visible with a thickness  $t \approx 500 \pm 50$  nm. During the SEM preparation, the porous layer did not cleave like the substrate, therefore the substrate forms out a small terrace (cf. Fig. 8.4c) and the porous layer resides a little bit further in the back. While in the porous layer the same cracks as on the substrate occur, the surface as well as the cross section are heavily corrugated and seem to be composed of spherical structures with dimensions of  $50 \pm 10$  nm.

For  $U = 15$  V, more experimental conditions were probed (Figs. 8.5, 8.6) than at 10 V. At  $c_F = 0.2$  M (Fig. 8.5(a,b)) the sample's appeared dull and grey. A closer inspection with the SEM revealed that the layer thickness was approx. 3  $\mu\text{m}$  with large cracks (crack width  $\approx 1\mu\text{m}$ ) at the top. Again a granular micro structure is clearly visible in the cross section. At  $c_F = 0.3$  M the sample showed interference colors, which are in good accordance with the SEM cross sections (Fig. 8.5(c,d)) which are similar to the experiments at 10 V. The thickness  $t = 440 \pm 50$  nm is comparable to that of the lower voltage.

At  $c_F = 0.5$  M ( $U = 15$  V), the sample reflects in a pale yellow color with less brilliance than with  $c_F = 0.3$  M. In the SEM images (Fig. 8.6(a,b)) still a thin film ( $t \approx 170 \pm 90$  nm) is visible, but it is decorated with a network of wall structures. The walls have a width of 200

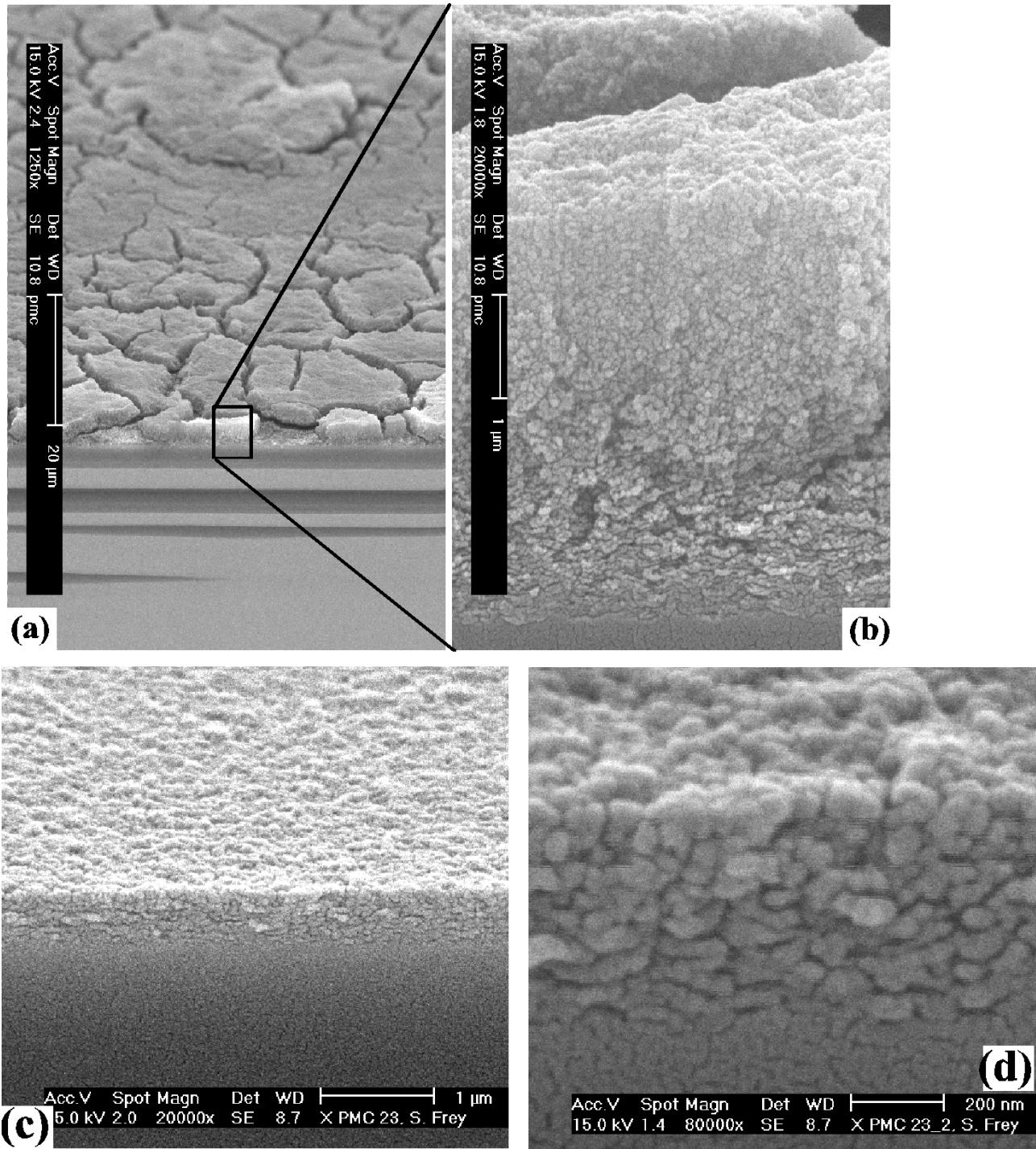


Figure 8.5: Morphology of porous SiO<sub>2</sub> grown at  $U = 15$  V (tilted SEM cross sections): (a,b)  $c_F = 0.2$  M: The layer is several micron thick and large cracks have formed. (a,b)  $c_F = 0.3$  M: The layer is flat ( $t = 440 \pm 50$  nm) and without cracks.



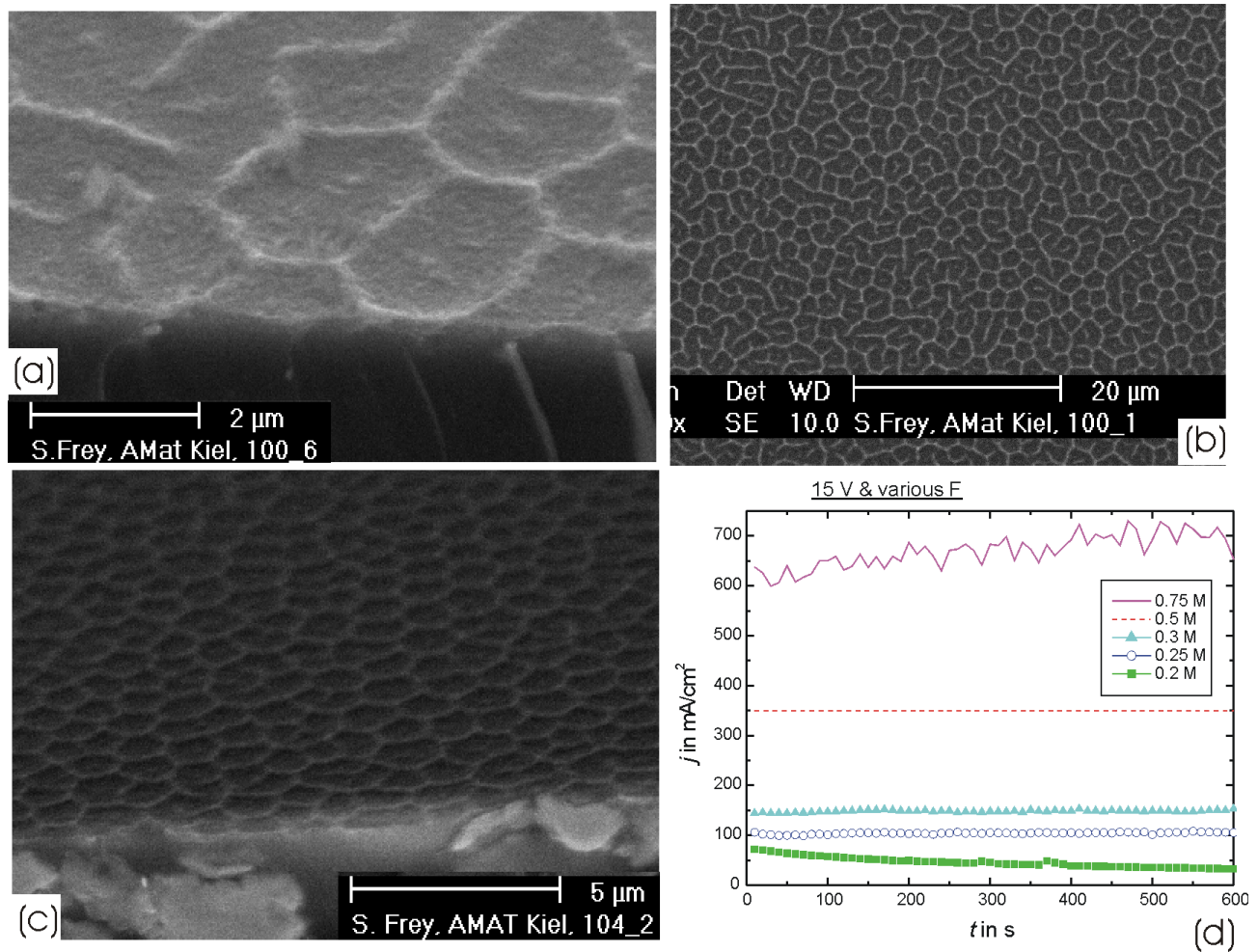


Figure 8.6: (a-c) Morphology of porous  $\text{SiO}_2$  grown at  $U = 15$  V: (a,b)  $c_F = 0.5$  M: A partially connected wall network forms on a thin flat layer ((a): tilted SEM cross section, (b): plain view). (c) With  $c_F = 0.75$  M the surface is segmented by polygon structures (tilted cross section). (d) Current density transients at  $U = 15$  V for various fluoride concentrations (for  $c_F = 0.5$  M the data file was destroyed and only the  $j$  value at the start of the etching can be given.).

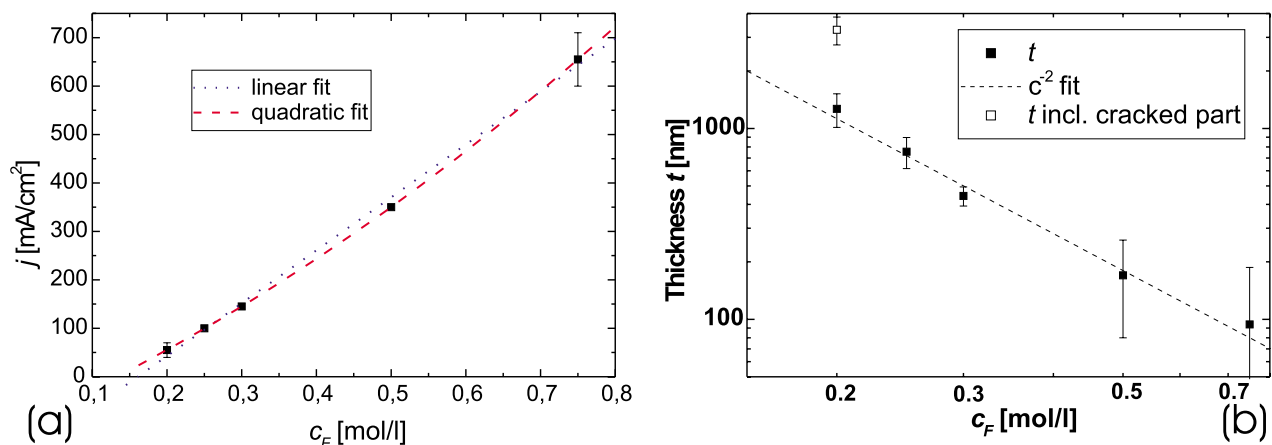


Figure 8.7: Correlation of current density  $j$  (a) resp. layer thickness  $t$  (b) and fluoride concentration  $c_F$ .

- 300 nm but only a low height of  $\approx 100$  nm. The network exhibits characteristic dimensions of 1 - 2  $\mu\text{m}$  (e.g. between parallel walls or the diameter of closed polygons). While some closed structures appear, still most of the structures are open. With  $c_F = 0.75$  M ( $U = 15$  V, Fig. 8.6c) the network mainly consists of closed polygon structures with sizes between 800 and 1500 nm. Again the walls are very flat and the underlying flat porous  $\text{SiO}_2$  layer is very thin (estimation:  $t = 0 - 180$  nm).

The current densities in the potentiostatic experiments (Fig. 8.6d) scale with the fluoride concentration (Fig. 8.7a) as already seen from the cyclic voltammograms (Fig. 8.2). Again, a quadratic fit describes best the dependance between concentration and current density, however also a linear fit is possible. None of the acceptable fits do pass through the origin. The current density transient for 0.2 M is slowly decaying (best fitted with an exponential decay) from 70 to 40  $\text{mA}/\text{cm}^2$ , while it stays constant over the whole anodization time for 0.25 M ( $j = 100$   $\text{mA}/\text{cm}^2$ ) and 0.3 M ( $j = 145$   $\text{mA}/\text{cm}^2$ ). At  $c_F = 0.5$  M the data file was corrupt and therefore only the current density noted at the beginning of the potentiostatic anodization phase can be given ( $j = 350$   $\text{mA}/\text{cm}^2$ ). With the highest concentration  $c_F = 0.75$  M the current density signal is very noisy and slowly rises from 600 to 710  $\text{mA}/\text{cm}^2$ .

The thickness of the thin film (excluding the wall structure height) shows a clear  $c_F^{-2}$  dependance. For the cracked structures at  $c_F = 0.2$  M the non-cracked part was used for the fitting. The cracks are so large that they effectively short-circuit the surrounding cracked material concerning the support with electrolyte and the current flow. For any consideration concerning the steady state oxide thickness only the non-cracked part of the oxide is thus meaningful.

At 20 V, the current density (Fig. 8.8) depended quadratically on the fluoride concentration  $c_F$ . During the anodization the current density slowly rose with exception of the 0.2 M measurements which exhibited an initial strong dip and then stayed constant. With increasing fluoride concentration also the noise level increased.

Morphologically, under all conditions a corrugated surface with micron-sized depressions resulted at  $U = 20$  V (Figs. 8.9, 8.11). At  $c_F = 0.2$  M, the structures have diameters  $d \approx 940 - 2810$  nm (Fig. 8.9a), i.e. the size variation is still significant. Also, there is no ordering visible on the surface. The cross section (Fig. 8.9b) shows that also these larger structures are again composed of the granular media as the thin films at 15 V. At  $c_F = 0.3$  M (Fig. 8.9(c-e)),



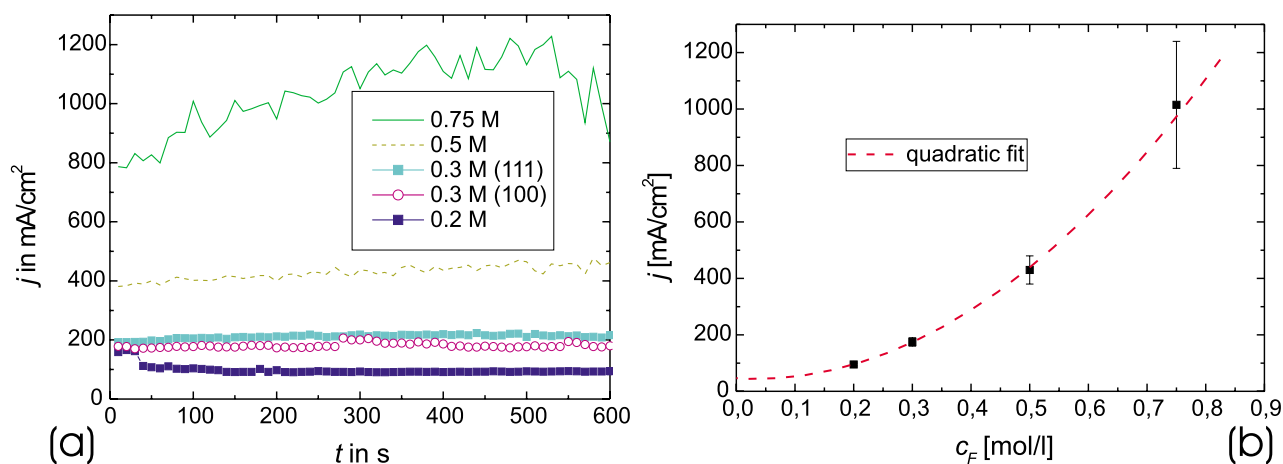


Figure 8.8: (a) Current density transients at  $U = 20$  V for various fluoride concentrations. (b) Correlation of current density  $j$  and fluoride concentration  $c_F$ .

the structures become much more ordered and the size distribution is narrower. An auto-correlation and a FFT analysis of the surface pattern showed that the distances and sizes are narrowly defined, but there are no global preferential ordering directions. The structures become smaller ( $d \approx 500 - 1800$  nm) with lower walls.

A closer inspection of the cross section (Fig. 8.10) of such samples shows that effectively the structures are not depressions in the film on a planar substrate, but the substrate underneath has become corrugated. The granular film then covers the substrate like a frosting. Please note that this substrate “deformation” is seen on all macro structured samples, even if here only typical zoom image (Fig. 8.10) is shown.

At  $c_F = 0.5$  M (Fig. 8.11(a-e)) the structures become flatter and smaller ( $d \approx 860 - 1070$  nm). Going to  $c_F = 0.75$  M, only faint remainders of the macrostructure are visible ( $d \approx 750 - 1000$  nm). Much more pronounced is the formation of funnels with a diameter of 1.9 to 3.8  $\mu\text{m}$ . Fig. 8.12 correlates the size  $d$  of the macro structures with the fluoride concentration  $c_F$ . Besides a general monotonic decrease of size, no exact fitting function can be given, because the data points are too few and the size variation especially at low  $c_F$  is too large.

In an additional series, the response to a change in the buffer strength was investigated. Therefore the amount of  $\text{NH}_3$  was changed for constant  $c_F = 0.3$  M. For each  $\text{NH}_3$  content (0.006 M (buffer ratio 50:1), 0.012M (25:1), 0.03 M (10:1), 0.3 M (1:1), 7.5 M (1:25)) a cyclic voltammogram (Fig. 8.13) was recorded and an anodization at 15 and 20 V was conducted. The hysteresis in the voltammogram showed to be most pronounced for the most acidic solution (50:1) (similar to 25:1, cf. Fig. 8.2). While the shape is still similar at the 10:1 buffer ratio, the current negative scan decreases stronger between 20 and 10 V. Like the other curves, the voltammograms for the buffer ratios 1:1 and 1:25 exhibit a drastic current increase on the positive scan at some point between 15 and 25 V. After that, however, the current decreases exponentially and the curve shape depends strongly on the scan velocity. The morphology analysis showed that only the 50:1 and 25:1 solution produce similar structures (i.e. a approx. 500 nm thick film at 15 V and micron-sized macro “bowls” at 20 V). The 10:1 sample etched inhomogeneously, and showed at 15 V a rough porous film. At 20 V, the same rough film resulted decorated with some scattered macro structures which tend to align probably along

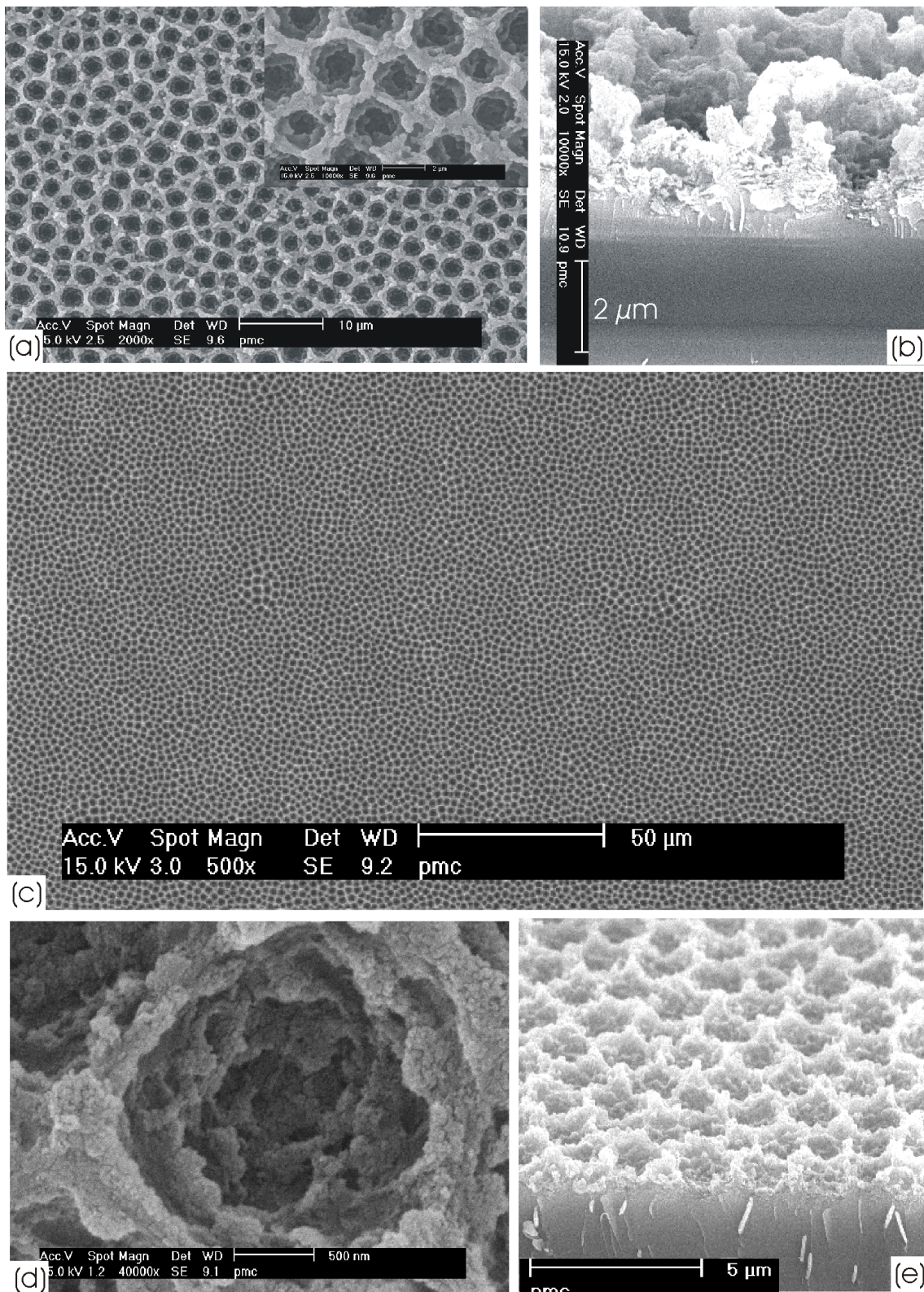


Figure 8.9: Morphology of porous SiO<sub>2</sub> grown at  $U = 20$  V: (a,b)  $c_F = 0.2$  M: The surface is covered with closely packed macro structures with a depth of 1660 - 2070 nm and diameters of 940 - 2810 nm ((a): plain view, (b): tilted cross section). (c-e)  $c_F = 0.3$  M: (c) Overview of the surface. (d) Zoom into one of the macro structures. (e) Tilted cross section.

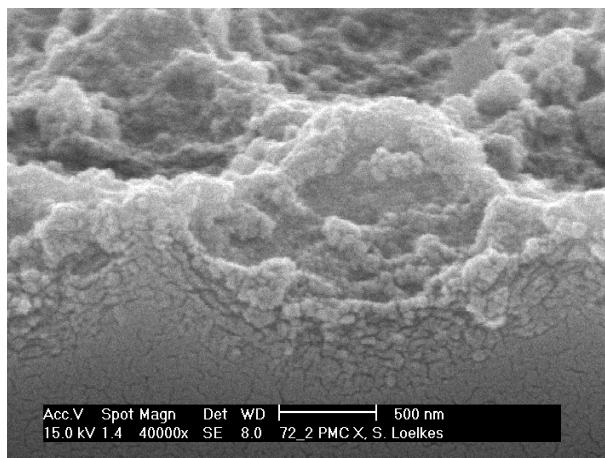


Figure 8.10: Magnification of the macro structure cross section ( $c_F = 0.3$  M,  $U = 20$  V, buffer 50:1).

cracks in the film. From the SEM pictures of the 1:1 and 1:25 solution samples, some surface film can be conjectured but a detailed analysis was beyond the resolution limit of the SEM.

To investigate the influence of the silicon substrate on the morphology, differently doped and oriented wafers were prepared with an ohmic backside contact (all p-Si: (111)  $0.7 - 1.3 \Omega\text{cm}$ , (111)  $\rho = 3 - 6 \Omega\text{cm}$ , (111)  $\rho = 100 - 200 \Omega\text{cm}$ ). Additionally, p<sup>+</sup>-Si wafers ((100)  $\rho = 5 - 25 \Omega\text{cm}$ ) were investigated, which did not need a special backside contact because of their high doping.

For the lowest doped wafer it was not possible to pass a significant current through the electrode which was probably due to the high resistivity of the wafer and/or the backside contact. All other samples were investigated by cyclic voltammetry and potentiostatic anodization in a  $c_F = 0.3$  M solution. The voltammograms stayed essentially as shown in Fig. 8.2. Also the morphology after the potentiostatic anodization did not show significant differences. Unlike pores in silicon (cf. e.g. section 7.3), the macro structure dimensions and especially their ordering behavior was not impacted by the choice of substrate orientation.

During the anodization of silicon in fluoride containing electrolytes, the system undergoes several oscillation regimes (cf. section 4.5). The oscillation frequency measured is proportional to  $j/U$ , a relationship which has proven to be correct even at higher voltages (Fig. 4.9). To identify resonant frequencies for the present etching system, an AC voltage (peak-to-peak amplitude: 100 mV) with variable frequency was impressed on the potentiostatic anodization voltage with a frequency generator (Hewlett-Packard Inc.). The current response was analyzed by a standard lab oscilloscope by tracking the shape of the  $IV$  - Lissajous curves. The frequency was manually increased from the mHz regime to 100 Hz. When the Lissajous ellipse collapses to a simple 45° line, the phase angle between current and voltage is zero which should be the central frequency of a (first order) resonance. By that technique the first resonant frequency was detected at 8-9 Hz which is a factor of 3 higher than expected from Fig. 4.9. The results were verified by varying the frequency and regarding the AC answer in the current signal. Also there, the same oscillation frequency was detected, while no resonance appeared in the frequency range around 3 Hz. To check the impact on the morphology, several sample were anodized with larger amplitudes and different AC current shapes. It showed that it was not even necessary to impress a resonant signal permanently, but that also a 100 ms pulse, where the anodization voltage was



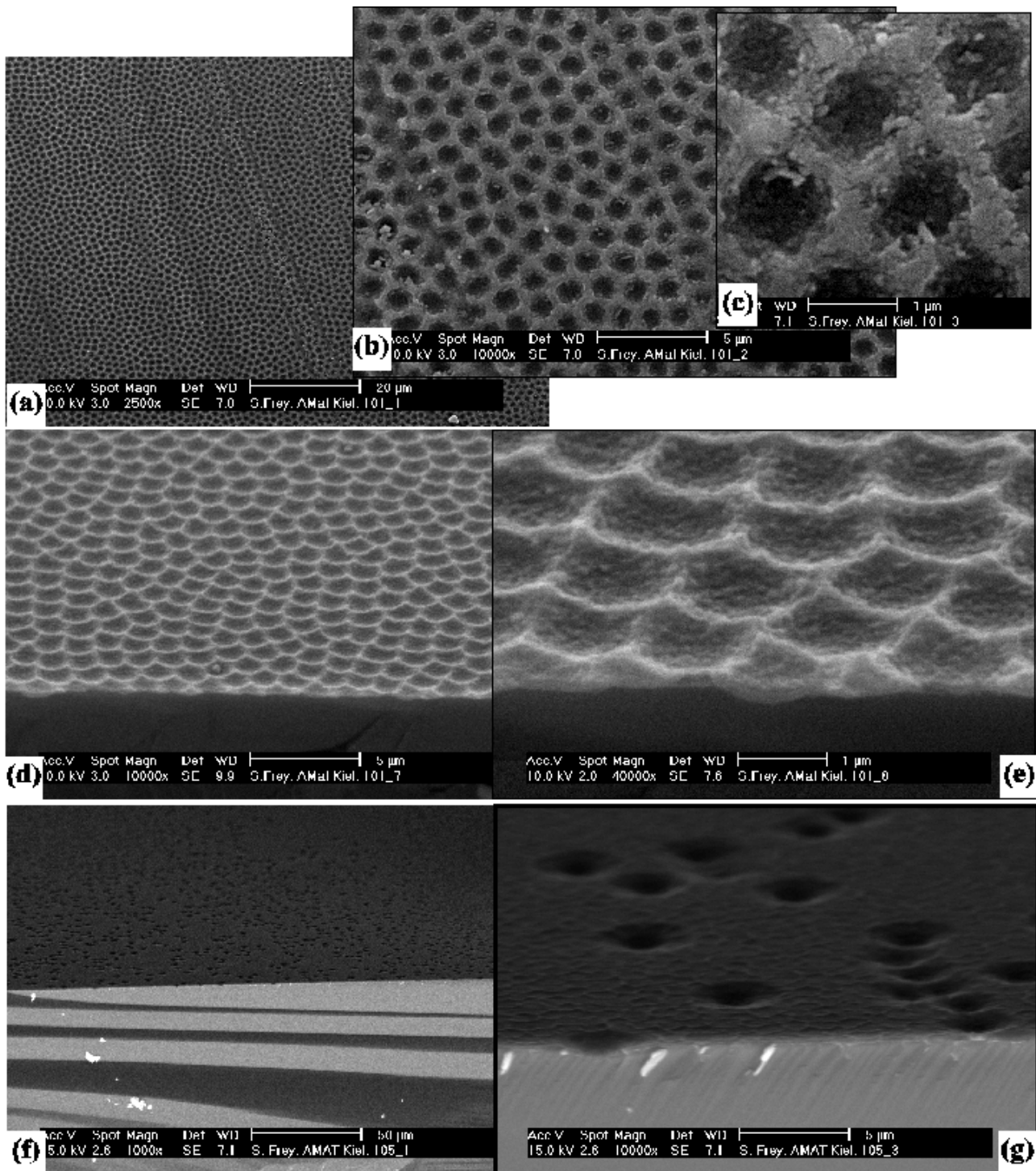


Figure 8.11: Morphology of porous  $\text{SiO}_2$  grown at  $U = 20$  V: (a-e)  $c_F = 0.5$  M: The structures become flatter and smaller ((a-c): plain views, (d,e): tilted cross sections). (f,g)  $c_F = 0.75$  M, tilted cross sections: While the lattice of the macro structures known from the lower concentrations is only faintly visible, new funnel-like structures appear numerous on the surface.

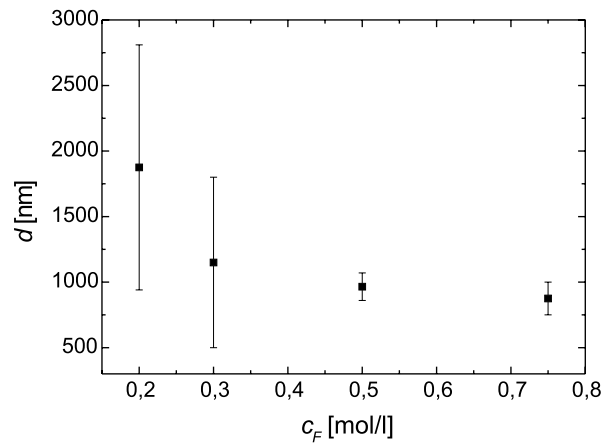


Figure 8.12: Diameter  $d$  of the macro structures versus fluoride concentration  $c_F$ .

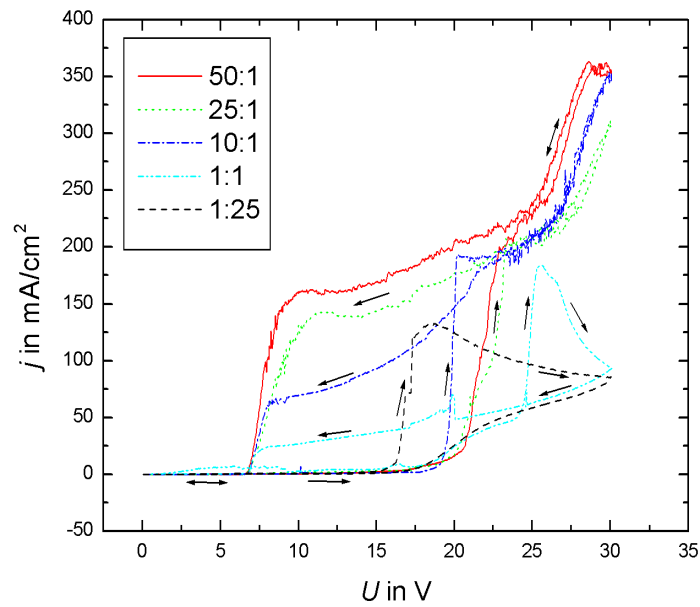


Figure 8.13:  $IV$  curves for different buffer strengths and pHs: All curves exhibit the strong rise around 20 V. For the 1:1 and the 1:25 buffers, the current afterwards decays exponentially, while the other buffers exhibit the characteristic hysteresis.

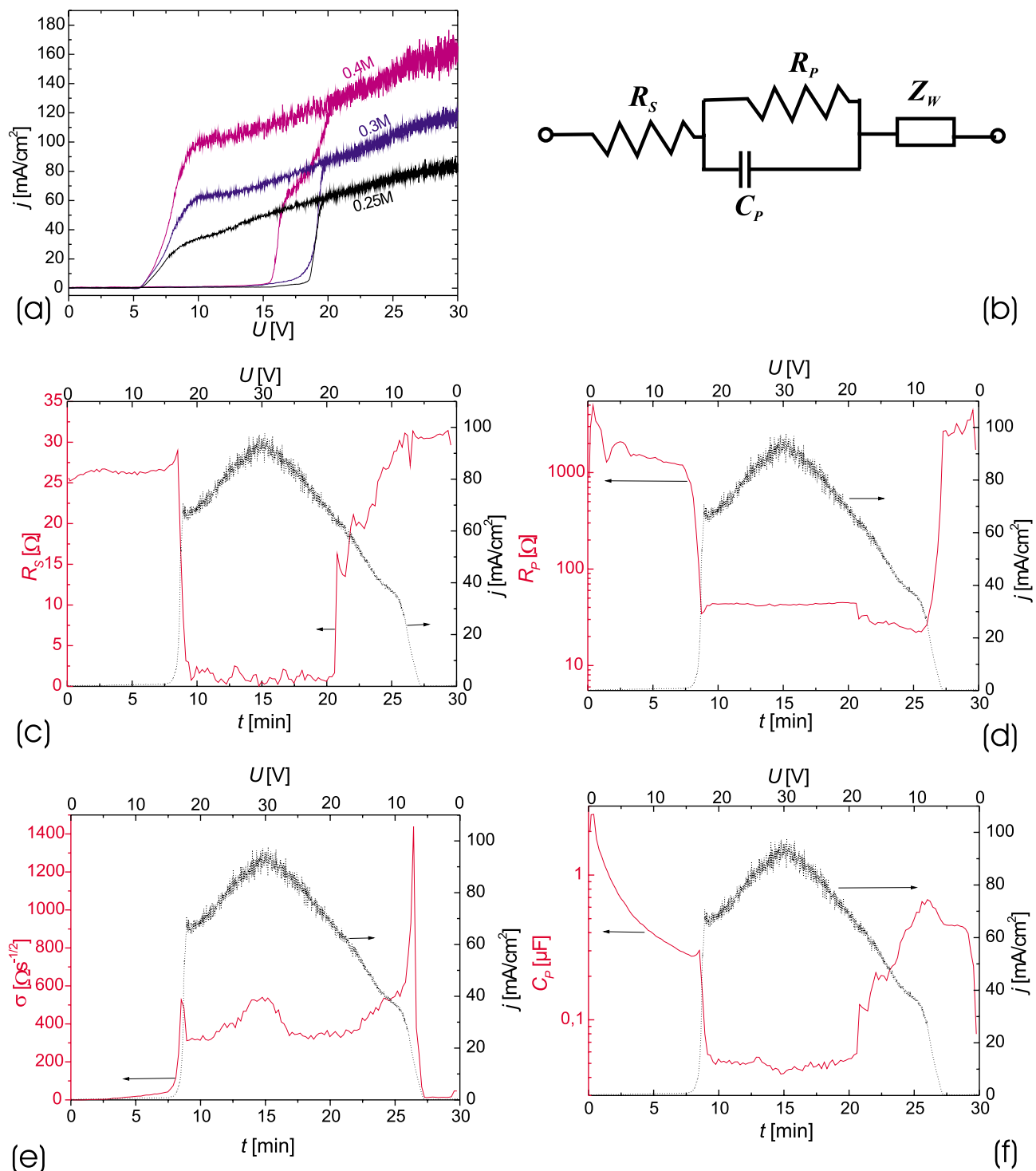


Figure 8.14: (a) Voltammograms for different  $c_F$  concentrations on the peristaltic pump set-up. (b) Equivalent circuit used for the impedance analysis. (c-f) Results from the impedance measurements during cyclic voltammetry ( $c_F = 0.25$  M; the current density  $j$  is plotted for comparison.): (c) Serial resistance  $R_S$ . (d) Parallel resistance  $R_P$ . (e) Warburg impedance  $\sigma$ . (f) Parallel capacitance  $C_P$ .

reduced shortly from 15 to 10 V, was enough to trigger a (damped) oscillatory behavior in the system. Analogous to Ozanam et al. [83], who showed that sustained oscillations can be obtained by adding a matching resistance in series with the electrochemical cell, also in the present system a variable resistor was added to check whether sustained oscillations can be triggered. With  $R = 587 \Omega$ , the system could be set in an undamped oscillating state for minutes by a short introductory pulse. However, the SEM analysis did not yield significant differences to the samples shown in Figs. 8.5(c-d) and 8.9(c-e), therefore this route was not further pursued.

To analyze the impedance response of the system, the cyclic voltammograms were repeated on the peristaltic pump system (cf. p. 65). Although this system cannot supply the extremely good diffusion conditions of the RDE, still it was possible to reproduce the hysteresis (Fig. 8.14a). The current density was lower at identical fluoride concentrations which can be explained by a worse diffusion. Also the slopes and currents loose their clear quadratic dependencies on  $c_F$ . Furthermore the characteristics do not exhibit the second linear regime with the slope  $b$ . Fig. 8.14(c-f) shows the individual components of the equivalent circuit (Fig. 8.14b) extracted from the impedance analysis ( $c_F = 0.25 \text{ M}$ ):

- $R_S$ : The serial resistance drops from  $25 \Omega$  to  $0.5 - 2 \Omega$  at the moment where the current begins to rise (region I  $\Rightarrow$  III from Fig. 8.2). Then it stays low until, on the negative scan, it begins to rise at approx. 19 V again. It finally reaches values around its starting value when arriving at 8 V. For the rest of the measurement, it stays between 27 and  $30 \Omega$ .
- $R_P$ : The parallel resistance drops 1.5 orders of magnitude from  $\approx 1000 \Omega$  to  $20 - 40 \Omega$  while the current is on the upper branch of the voltammogram.
- $\sigma$ : The Warburg impedance strongly rises during the high current phase. In nearly all measurements, when the current ran through the steep flanks at approx.  $U = 16 \text{ V}$  and  $U = 9 \text{ V}$ ,  $Z_W$  always displayed extreme spikes. As the fits in this jump region often show significant deviations from the measurement curves, these spike could also be measurement artifacts.
- $C_P$ : The capacitance drops strongly on the lower branch of the voltammogram from over  $2 \mu\text{F}$  to  $0.3 \mu\text{F}$  at  $U = 16 \text{ V}$ . During the strong increase of the current the capacitance instantaneously drops to  $C_P \approx 0.05 \mu\text{F}$ , where it stays until the negative scan reaches 19 V. Then  $C_P$  rises up to  $0.65 \mu\text{F}$  @ 9 V and drops then again.

Additionally, potentiostatic film growth experiments at 15 and 20 V were performed to verify a comparability of the two set-ups. SEM analysis showed that the layer thickness at 15 V ( $t \approx 640 \text{ nm}$ ) was very similar to that of the same concentrations on the RDE set-up (Fig. 8.7). At 20 V macro structures with  $d \approx 1500 \text{ nm}$  were grown, which are also similar to the results on the RDE set-up using  $0.25 \text{ M NH}_4\text{F}$  (Fig. 8.12).

When tracking the impedance data during the potentiostatic anodization at  $U = 15 \text{ V}$  resp.  $U = 20 \text{ V}$ , all 4 equivalent circuit elements stayed essentially constant during the anodization time. Unlike the RDE measurements, here the 15 V measurements showed more noise than at  $U = 20 \text{ V}$ . The absolute values of  $R_S$ ,  $R_P$ ,  $\sigma$ , and  $C_P$  deviated only slightly for the two voltages and followed exactly the trends given from the cyclic voltammograms (cf. Fig. 8.14).

The rest of the presented experimental results stems again from the RDE set-up. As already discussed within the results on  $U = 10 \text{ V}$  (Fig. 8.4), the gold sputtering during the SEM

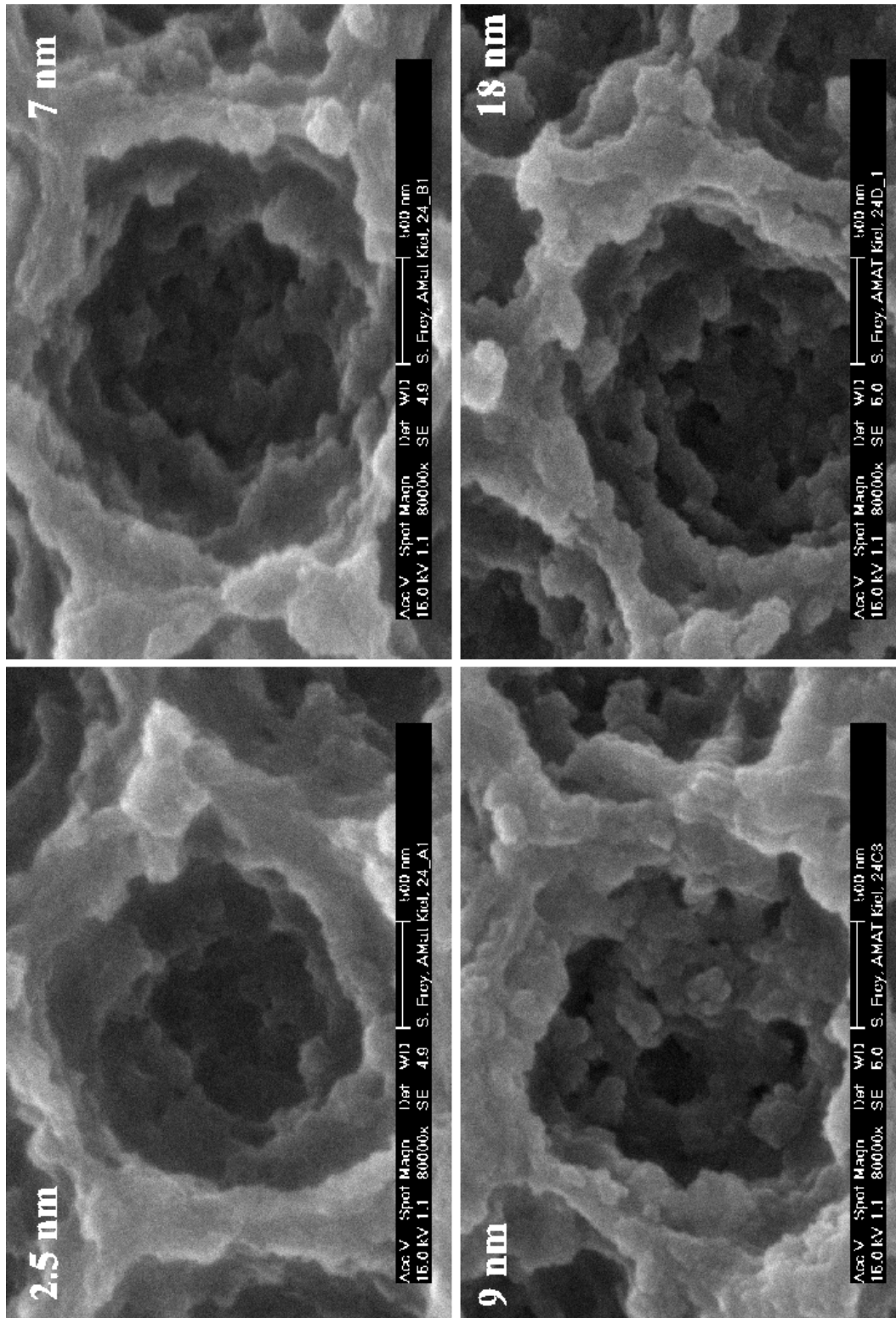


Figure 8.15: Magnification of a macrostructure (obtained with  $c_F = 0.3$  M and  $U = 20$  V) with different Au/Pd sputtering thicknesses  $t_{Au}$  prior to the SEM imaging: (a)  $t_{Au} = 2.5$  nm. (b)  $t_{Au} = 7$  nm. (c)  $t_{Au} = 9$  nm. (d)  $t_{Au} = 18$  nm.



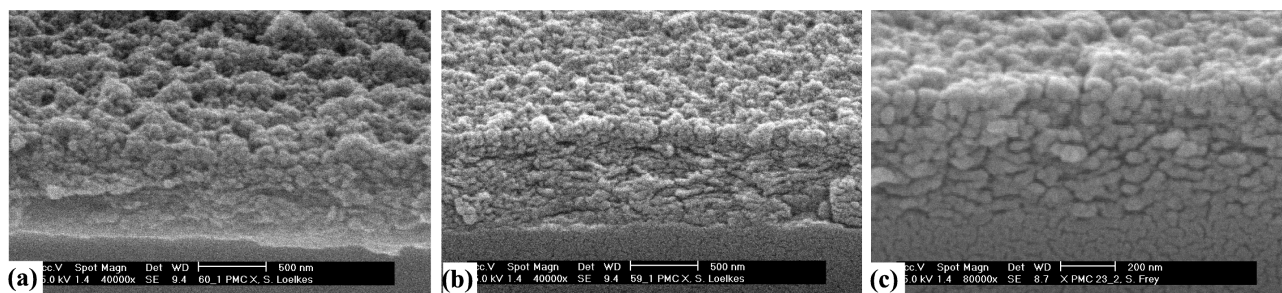


Figure 8.16: Influence of rotation speed on layer morphology at  $U = 15$  V (all tilted cross sectional views): **(a)** 100 rpm, **(b)** 500 rpm, **(c)** 1500 rpm. With decreasing rotation speed the layers get thicker and rougher. At 100 rpm 50 - 120 nm large holes form on the surface.

preparation can lead to artifacts on the SEM images. On the other hand, without sputtering it had been previously impossible to image the cross section of the porous layers [77] probably due to the insulating character of  $\text{SiO}_2$ . To evaluate the influence of the Au sputtering further, a sample was successively sputtered with different Au/Pd amounts (Fig. 8.15). 2.5 nm Au/Pd layer thickness, already most of the structural features can be seen, but some blurring remains. At 7 nm layer thickness a similar result is yielded. At 9 nm thickness, much more fine structures (granules with diameter of 50 - 100 nm) become visible. A doubling of the thickness to  $t_{\text{Au}} = 18$  nm does not improve the resolution further.

In a further series, the influence of the RDE rotation speed on the morphology was investigated. At  $U = 15$  V (Fig. 8.16). With decreasing rotation speed the layers become thicker and rougher. Additionally, larger voids form (cf. black dots on Fig.8.16(a)). At  $\nu = 1500 \text{ min}^{-1}$  the layer thickness is 550 - 610 nm and the layer is flat. The thickness increases to 770 - 960 nm at  $\nu = 500 \text{ min}^{-1}$ , where also first voids with sizes of 25-50 nm become visible on the surface. At  $\nu = 100 \text{ min}^{-1}$ , the surface is very rough and the voids become more frequent with average sizes of 50 - 120 nm. The layer thickness is  $t = 810 - 960$  nm.

At 20 V (Fig. 8.17), the decrease in rotation led to deeper macro structures (cf. Fig. 8.9(c-e) for a comparison with  $\nu = 1500 \text{ min}^{-1}$ ):

- $100 \text{ min}^{-1}$ : The macro structures are approx.  $4 \mu\text{m}$  deep. The sizes vary from 1.3 to  $3.9 \mu\text{m}$ . The self-ordering gets lost.
- $500 \text{ min}^{-1}$ : The depth of the structures ( $0.6 - 0.9 \mu\text{m}$ ) is slightly larger than at  $\nu = 1500 \text{ min}^{-1}$ . The sizes are also slightly more spread ( $d = 1.3 - 1.9 \mu\text{m}$ ) compared to  $\nu = 1500 \text{ min}^{-1}$  ( $d = 1.3 - 1.6 \mu\text{m}$ ). The self-ordering becomes slightly weaker.

To track down the transition between the two morphology types, the regime between  $U = 15$  V and  $U = 20$  V (again at  $\nu = 1500 \text{ min}^{-1}$  and  $c_F = 0.3$  M, same conditions as Fig. 8.5(c-d) resp. Fig. 8.9(c-e)) was inspected more closely. Samples were grown at  $U = 15.7$  V (Fig. 8.18),  $U = 16.3$  V (Fig. 8.19), and  $U = 17.5$  V (Fig. 8.20) and afterwards analyzed in the SEM.

At 15.7 V, on the middle of the sample (Fig. 8.18a), small, isolated wall structures with a length of  $1 - 2 \mu\text{m}$  appear. Towards the outer boundaries of the etched area these structures become more numerous (Fig. 8.18b) and interconnect partially. In the cross section (Fig. 8.18(c-d)) the layer thickness in the middle of the sample is 340 nm which decreases towards the etch boundary to 150 nm decorated with wall structures of 190 nm height. It seems that the

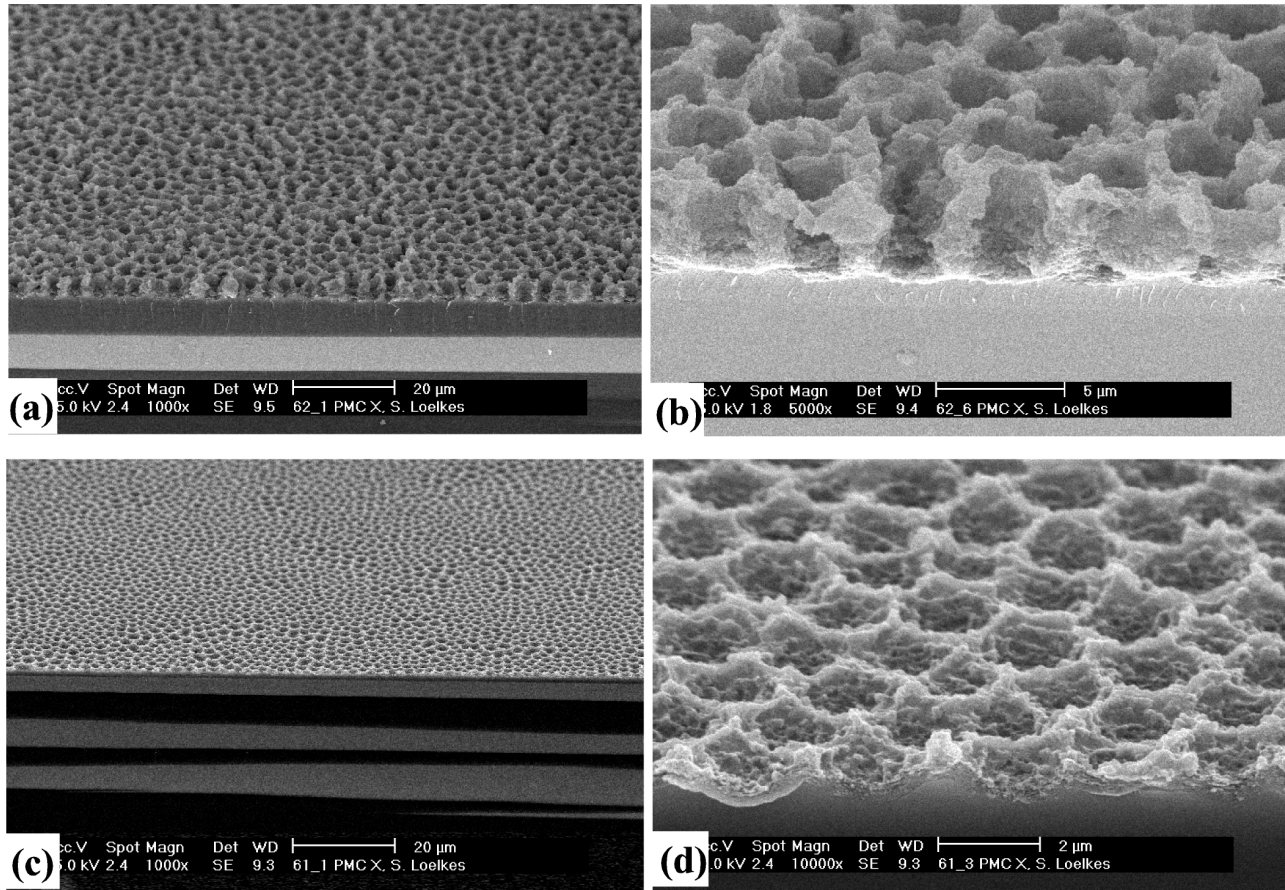


Figure 8.17: Influence of rotation speed on layer morphology at  $U = 20$  V (all tilted cross sectional views): (a), (b) 100 rpm, (c), (d) 500 rpm (1500 rpm can be seen in Fig. 8.9).

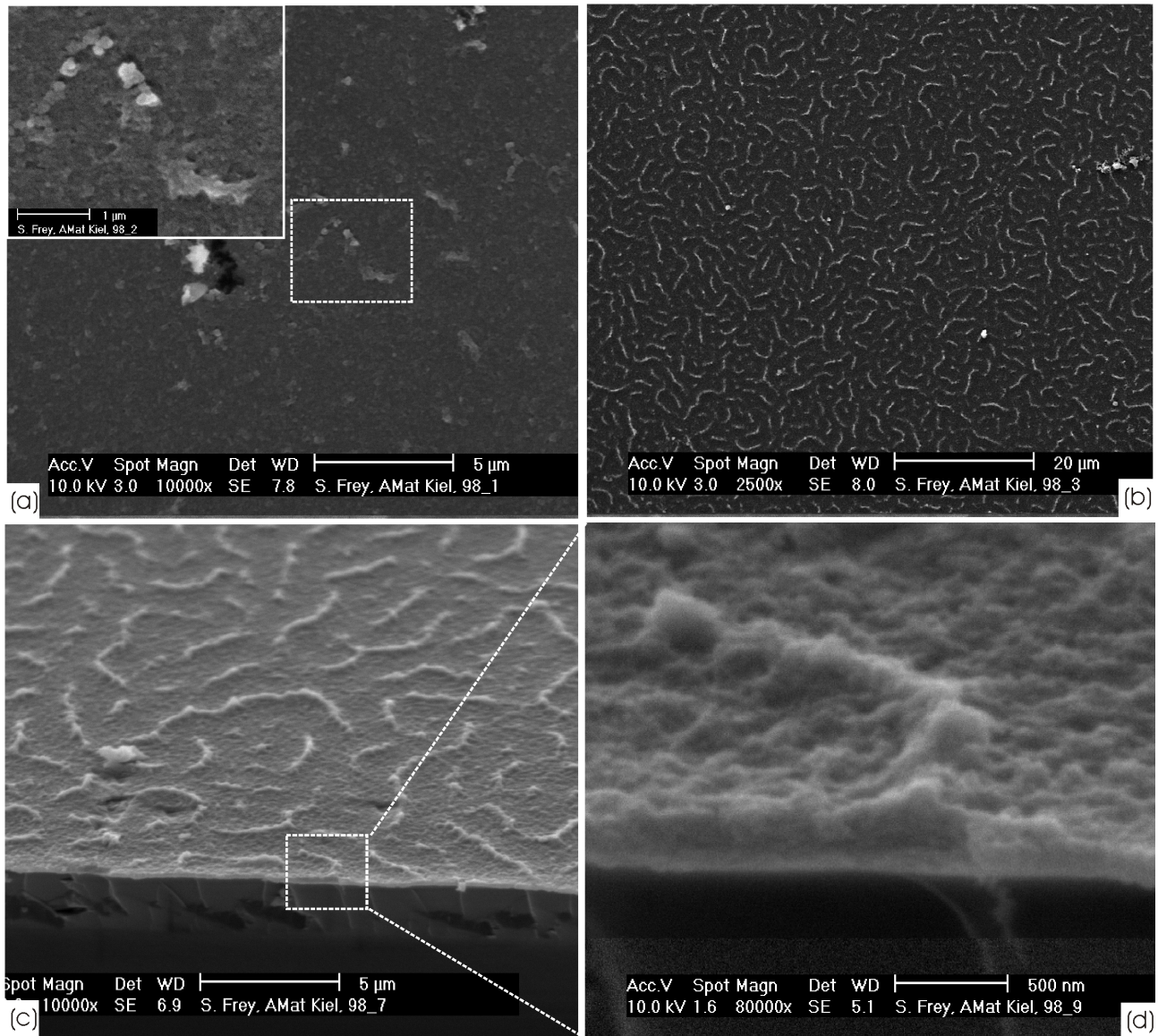


Figure 8.18: Layer morphology at  $U = 15.7$  V: (a) Surface in the middle of the sample (Inset: Magnification of dashed rectangle.). (b) Surface near tape. (c) Cross section near tape. (d) Magnification of one of the wall structures from (c).



areas between the walls have decreased their layer thickness while the walls are the remainders of the “old” layer (like the one see at the middle of the sample).

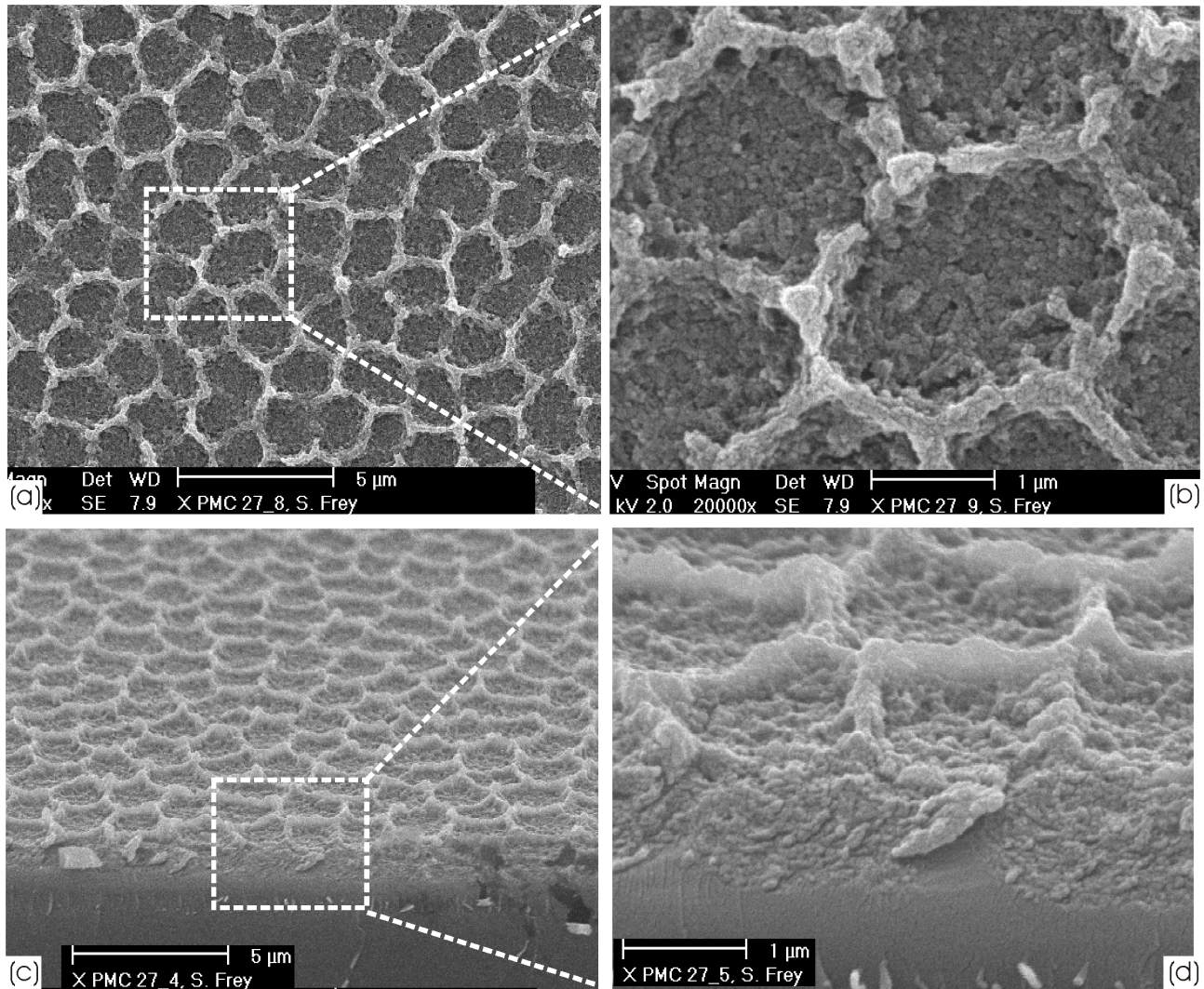


Figure 8.19: Layer morphology at  $U = 16.3$  V: (a) Surface image: The wall structures have now become interconnected and segment the surface in micron sized, but still almost flat compartments. (b) Magnification of (a). (c) Tilted cross section. (d) Magnification of (c).

With increasing potential, i.e. at  $U = 16.3$  V (Fig. 8.19), the walls further connect to segment the surface in compartments with diameters between  $0.6$  and  $2.6$  μm (Fig. 8.19(a-b)). A thin film layer below the walls was not anymore resolvable with the SEM, however as seen in the cross section the whole surface is covered with granules and becomes slightly corrugated at the bottom of the compartments (Fig. 8.19d). But essentially the substrate still looks flat, decorated with a network of walls (Fig. 8.19c). The walls have an approximate height of  $190 - 370$  nm.

At  $U = 17.5$  V (Fig. 8.20) the macro structures get even deeper and become more rounded. The size distribution also becomes narrower ( $d = 1.0 - 1.5$  μm). Compared to samples etched at  $20$  V (Fig. 8.9(c-e)) the structures are less deep and less ordered. A magnification of the inside the macro structures (Fig. 8.20c) reveals granular constituents with sizes between  $30$

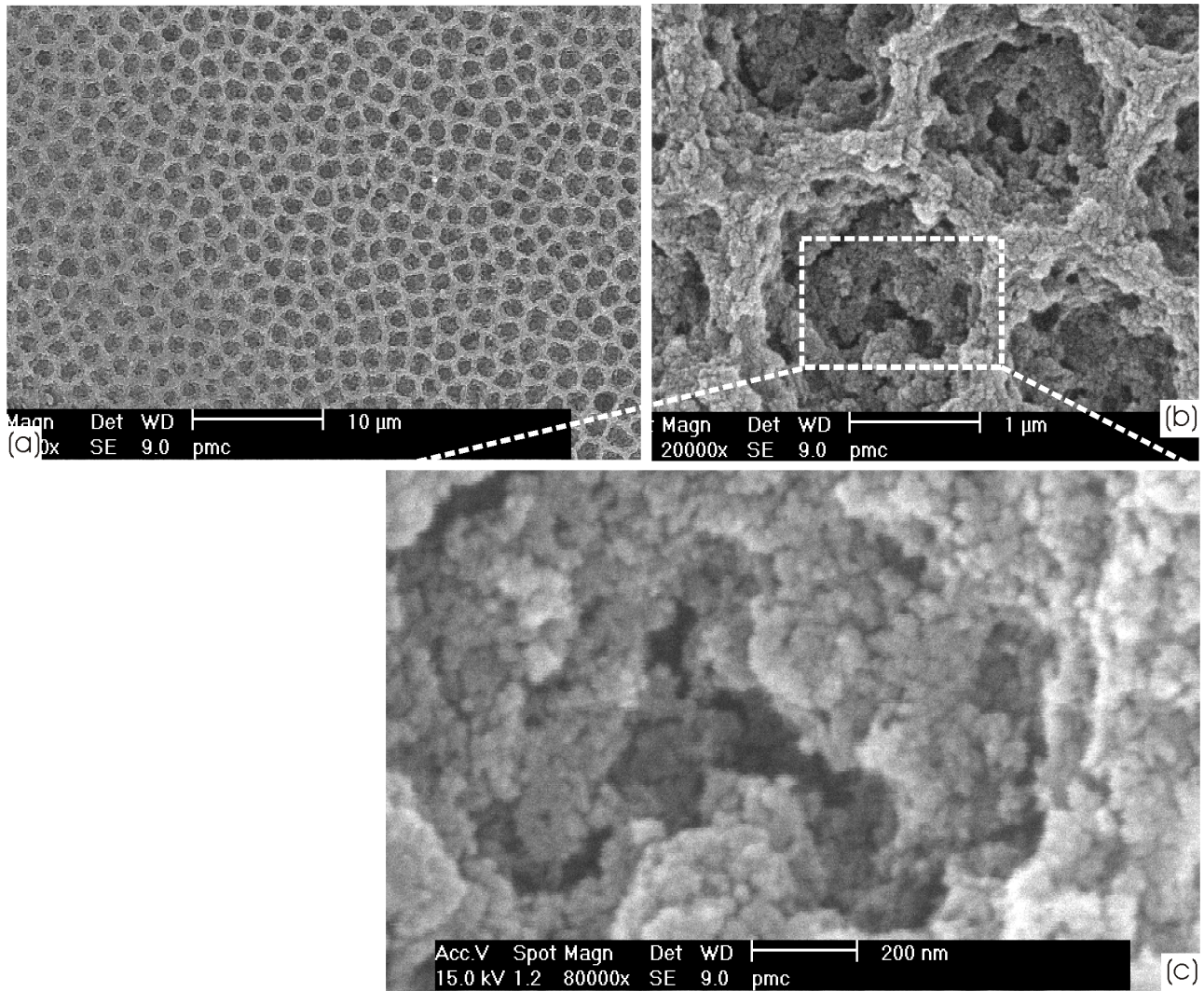


Figure 8.20: Layer morphology at  $U = 17.5$  V: (a) The surface is covered by fully closed macrostructures. (b,c) Magnifications.



and 40 nm. Although even smaller elements can be seen this already critically approaches the sputtering thickness of Au/Pd prior to the SEM imaging.

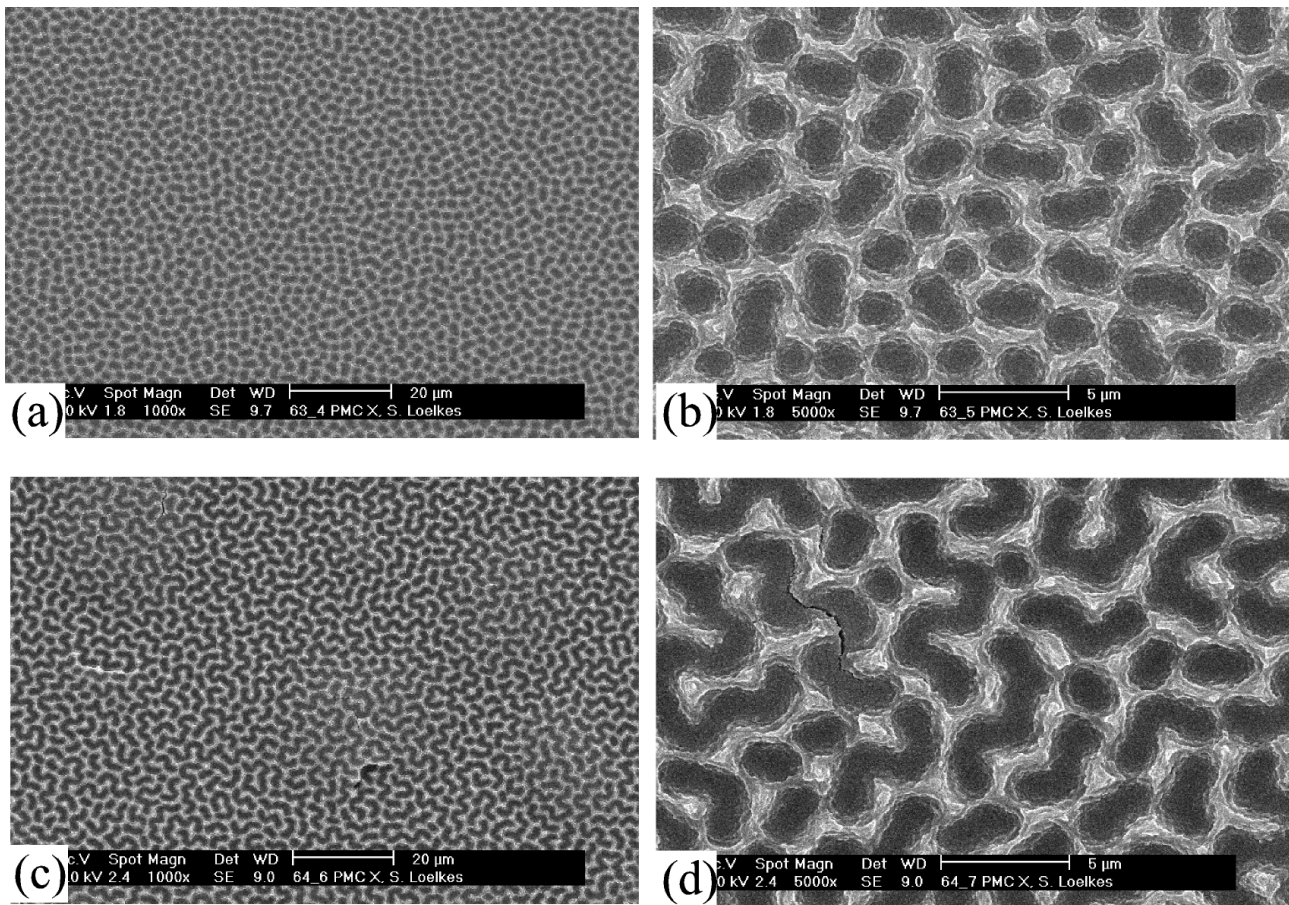


Figure 8.21: Anodization at higher voltages: (a),(b):  $U = 25$  V. (c),(d):  $U = 30$  V. The macro structures start to coalesce. At  $U = 25$  V, at many sites two macro structures merge. At 30 V, a labyrinthine pattern has formed consisting of interconnected depressions.

When applying higher voltages than  $U = 20$  V, the macro structures reunite: At  $U = 25$  V (Fig. 8.21(a-b)), very often two macro “bowls” merge resulting in elongated structures. The structures are less decorated with granules. A labyrinth-like structure is yielded at  $U = 30$  V (Fig. 8.21(c-d)). There, several previously isolated structures, form multiply bent lines. However, this interconnection only leads to line-like structures, never to structures with larger dimensions in all directions. Albeit the structure strongly mocks preferential directions, a closer analysis did not yield any global preferential directions.

Finally, it was tested whether the macro structures would follow a lithographic pre-patterning. Therefore p-Si (100) ( $\rho = 30 - 70 \Omega\text{cm}$ ) wafers with a hexagonal KOH pre-patterning (Fig. 8.22(b(inset)), cf. e.g. [32] for further informations on this technique) with a pitch  $p = 2 \mu\text{m}$  was anodized at 20 V for 10 minutes. When using a fluoride concentration of  $c_F = 0.2$  M the hexagonal pattern is still recognizable in the macro structure ordering (Fig. 8.22(a)), but contains many defect due to some larger structures. At  $c_F = 0.36$  M (Fig. 8.22(b,d)) the surface pattern remains stable without defects for a total etching depth of over 100 micron (Fig. 8.22(e)). The cross section documents that the structures themselves are again “only” surface

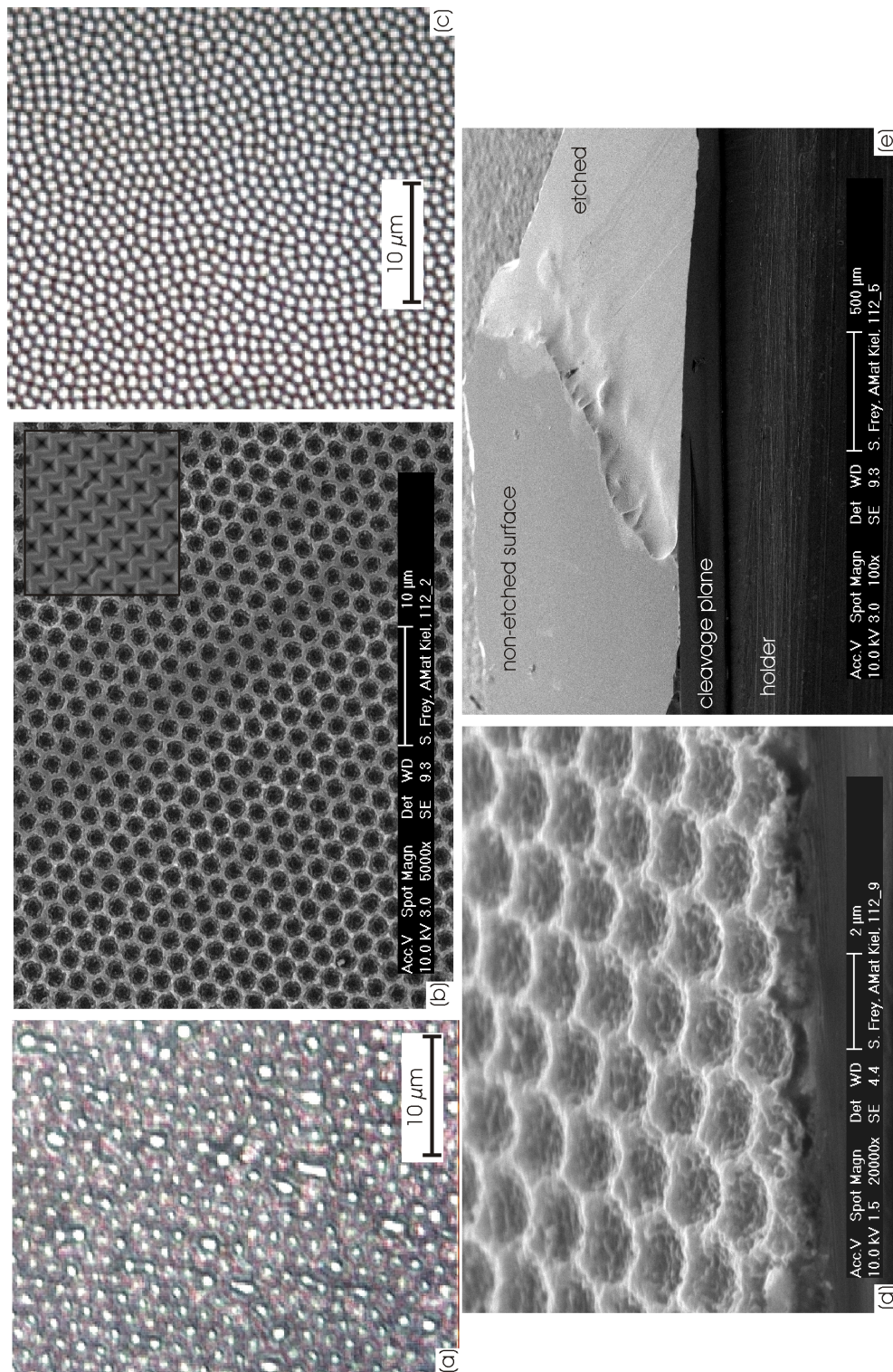


Figure 8.22: Response to a pre-structuring ( $p = 2.0 \mu\text{m}$ ) for different fluoride concentrations: (a) (optical microscopy plain view) At  $c_F = 0.2 \text{ M}$  the hexagonal lattice is still visible, but contains defects. (b) (SEM plain view) At  $c_F = 0.36 \text{ M}$ , a defect free transfer of the pattern is yielded (Inset: pre-structuring). (c) At  $c_F = 0.5 \text{ M}$ , the pre-patterning gets lost during anodization. (d) Tilted SEM cross section of (c). (e) Overview cross section of (c) which demonstrates that the etching depth is over 100 microns.

corrugations and not deeper, elongated pores. When choosing a higher fluoride concentration  $c_F = 0.5$  M (Fig. 8.22(c)) the initial structuring gets completely lost and results in a random arrangement of the macro “bowls”. These have a pitch  $p \approx 1.3 \mu\text{m}$  and diameters  $d \approx 1 \mu\text{m}$  and are thus similar to those in Fig. 8.11(a-e).

## 8.3 Discussion

### 8.3.1 Granular morphology

In all cases for the flat films a granular morphology with grain sizes between 30 and 100 nm turned up (cf. e.g. Figs. 8.4, 8.5). In case of the macro structures (cf. e.g. Fig. 8.10) an approx. 500 nm thick layer of granules covers the surface corrugation.

In the literature, several authors have concluded from measurements [81,90] and modelling [82,89] that the growth of the anodic oxide proceeds discontinuously in individual pulses or bursts. The thickness grown in such an individual bursts is strongly potential dependant and given by Ozanam et al. [90] to be approx. 5 nm @ 3 V and 8 nm @ 5 V (for  $c_F = 0.05$  M and pH = 3). While Ozanam et al. [90] only indicate that the current comes in pulses without further specifying a microscopic mechanisms for that pulsing, the Current Burst Model (CBM) by Carstensen et al. [169] holds local conducting channels in the oxide responsible for those pulses or bursts. These bursts can agglomerate in domains (i.e. all bursts in one single domain grow in a correlated manner) with sizes which can be significantly larger than the thickness of the oxide layer (Ozanam et al. [90] determined an upper limit of 50 - 500 nm for these domains). Nast et al. [170] scanned the oxide surface with AFM during the oscillations at 6 V ( $c_F = 0.1$  M and pH = 4) and found an island growth of the oxide. The diameters of the islands were between 15 and 50 nm, while the oxide thickness was approx.  $7.5 \pm 1.5$  nm. Hence, as a rule of thumb, a burst thickness of  $1.0 \pm 0.5$  nm/V can be assumed. In the present experiments the voltage was between 10 and 30 V, i.e. also the individual current bursts should have a size between 10 and 30 nm. For all images the samples were coated with  $\approx 10$  nm Au/Pd, so the thickness is probably over-estimated in the SEM pictures. Please note that under standard anodic oxidation conditions individual current bursts can be hardly resolved due to two major reasons:

- The voltage is normally much lower (typically 3 - 8 V) therefore also the structural sizes are in the sub-10 nm range and thus with SEM not resolvable anymore.
- The standard solutions have pH = 3-4, where any oxide, especially with nm thickness, is quickly dissolved.

The structural sizes of a few ten nanometers are in accordance with other publications in this field (cf. section 4.3) taking into account the higher formation voltage. Also the observation of globular structures has been reported in some cases [71,171].

Fig. 8.23 schematically shows how the oxide could grow at the Si-SiO<sub>2</sub> and become porous with a thin dense layer below. Although simplified, Fig. 8.23 essentially shows the assumed underlying mechanism: At a thin spot of the oxide the field strength due an applied voltage will be highest. Thus the probability that a new CB starts there is highest. The new CB grows until it reaches a certain stop thickness (a→b), where the field strength has dropped below a second critical value. Due to the volume expansion when silicon is converted into silica, the surrounding oxide is pushed to the side and upwards. After a certain time, again a CB will



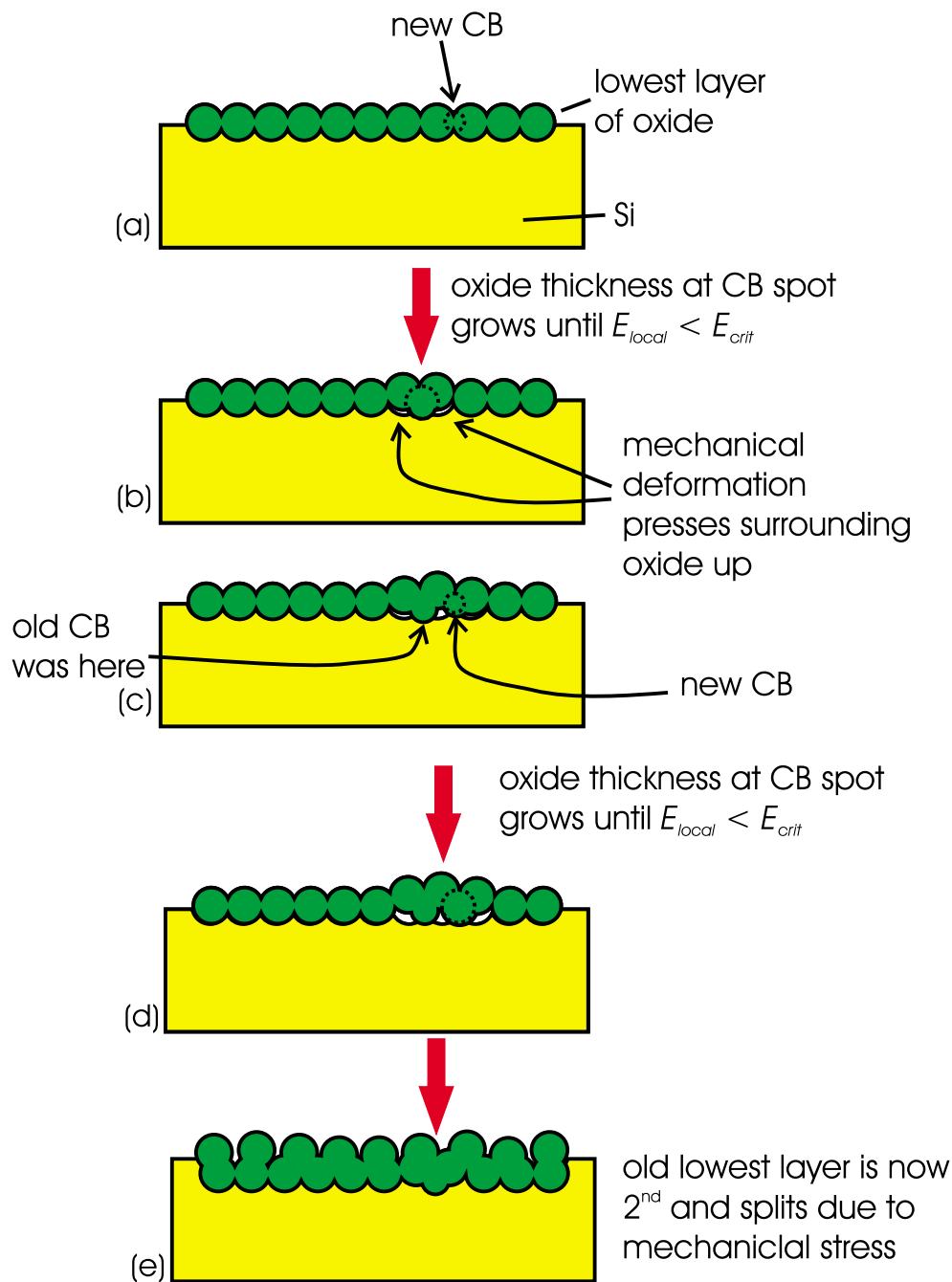


Figure 8.23: Growth of the anodic oxide at the Si-Oxide interface: (a) At a thin spot, a new CB starts. (b) The CB is finished. The new oxide bump has caused the surrounding oxide to lift slightly. (c) After a certain time, a second CB starts in the vicinity. (d) The second CB stops. The deformation of the layer continues. (e) The old lowest layer has become the second layer and splits at the weakest spots due to mechanical stress.

start in the neighborhood (c→d) and further increase the deformation of the layer. In a similar fashion bit by bit a new oxide layer grows below the old one and pushes the latter one upwards. The lowest layer of the oxide will remain unbroken all the time, but the stress causes the upper layers to break at the weakest spots (e). What remains are the isolated oxide bumps grown during single CBs. This simple picture can only explain how the granular structure might be formed, but does not try to explain the larger macro structures.

Due to the isolating nature of SiO<sub>2</sub>, Au- or Au/Pd - sputtering (with approx. 10 nm nominal layer thickness) of the samples was mandatory for SEM inspection the cross section and the detailed surface structure of the samples. Under standard conditions for sputtering Au or Au/Pd for SEM purposes (i.e. to suppress charging) the metal first forms isolated islands on the surface [172,173] up to some nm (1-4 nm) sputter thickness. Then the islands partially coalesce and a network of cracks between these structures remains (nominal thickness up ≈ 8-10 nm). For 10 nm and thicker layers the cracks close and a thin continuous metal film results. The individual islands (or grains) can have larger dimensions than the film thickness, generally however the ratio between width and height of the individual grains does not exceed 3:1. Most authors therefore only reported decoration artifacts for magnifications of 100,000 times and above. In rare cases, however, also grain sizes up to 50 nm diameter [172] are reported.

From that point of view, pictures like 8.4(a) have to be seen critically because this could be an image of the crack network which forms between isolated Au/Pd clusters. In 8.4(b) at the bottom the substrate with pure Au related cracks is visible. In Fig. 8.5(b) which was only taken at 20k magnification, still the Au structures are visible at the bottom, but very faintly. The globular structures above are clearly recognizable ( $d \approx 30$  nm). Similarly, in Fig. 8.5(c,d) clearly a surface and cross section corrugation occurs.

The analysis with gradually increased sputtering thickness (Fig. 8.15) shows that a minimum of 9 nm Au/Pd is necessary to form a conductive cover layer, otherwise the high-resolution images do not attain the full sharpness (Fig. 8.15(a,b)). This is similar to the standard literature values for Au films on planar substrates. At 9 nm (c) and 18 nm (d) also small structures of approx. 50 nm diameter become visible. It remains unclear whether these are induced by a decoration artifact of large Au grains (cf. e.g. [172] for 30 nm grains at 10 nm sputter thickness) or whether these structures are in fact parts of the porous SiO<sub>2</sub> layer. Although strong indications from the results on porous silica from other groups (see above) and the discretized growth mechanism of anodic oxide are given that the growth proceeds via these ball-like structures, this point should be verified by other techniques. This means as well other sputtering materials, e.g. carbon, as also other imaging techniques like AFM or TEM.

### 8.3.2 Reactions, etch rates and the influence of the buffer

The oxide forming current  $I_{ox}$  and the oxide etch rate  $\alpha$  are always linked by Eq. (4.13), i.e.  $\frac{ds}{dt} = \beta j_{ox} - \alpha$ . If a certain oxide thickness  $s$  establishes this is sign of a steady state, i.e.  $\frac{ds}{dt} = 0$ , which is also valid for a porous oxide.

In the present system, things get however more complicated due to several reasons:

- Significant parts of the current are non-(Si)-oxidizing currents  $j_{nox}$ , e.g. are used for the oxidation of O<sup>2-</sup>. Then Eq. (4.13) can only be solved fully if  $j_{ox} = j_{total} - j_{nox}$  is known.
- All major reactions in the system (see below) produce or consume protons. The system is only weakly buffered, i.e. the pH can switch rapidly when more protons are generated resp. OH<sup>-</sup> are consumed than the buffer strength (cf. section 2.4.1) can withstand. Thus

the etch rate  $\alpha$ , which depends strongly on the local pH (cf. section 4.4), will also be heavily influenced.

- The results of Bailes et al. [171], Lharch et al. [71], and Grésillon [167] show that between the porous oxide and the silicon substrate a dense, i.e. fully insulating, oxide layer of up to 10 nm thickness exists.

The major reactions in this system are:

1. Silica formation (cf. section 4.2):  $\text{Si} + 2 \text{H}_2\text{O} + 4 \text{h}^+ \rightarrow \text{SiO}_2 + 4 \text{H}^+$ .
2. Silica dissolution by  $\text{HF}_2^-$  (cf. section 4.4):  $\text{SiO}_2 + 3 \text{HF}_2^- \rightarrow \text{SiF}_6^{2-} + \text{OH}^- + \text{H}_2\text{O}$
3. Silica dissolution by HF (cf. section 4.4):  $\text{SiO}_2 + 6 \text{HF} \rightarrow \text{SiF}_6^{2-} + 2 \text{H}^+ + 2 \text{H}_2\text{O}$
4. Water electrolysis:  $2 \text{H}_2\text{O} + 4\text{h}^+ \rightarrow \text{O}_2 \uparrow + 4 \text{H}^+$

When the influence of the individual species on the silica etch rate is determined,  $\text{HF}_2^-$  is approx. 4 times more effective than HF, but the concentration of  $\text{HF}_2^-$  is generally less than that of HF. Overall however, the dissolution will mainly be caused by reaction (2), therefore the pH is increased by the dissolution. On the other hand reactions (1) and (4) diminish the pH.

When the voltage is increased, it takes up to approx. 18 V, until the current begins to rise drastically. Below 18 V, the system most probably behaves as already described by other authors for the voltage regime up to 8 V (cf. section 4.2): The oxide is dense and its steady state thickness will rise with rising potential [174]. The steady state is again characterized by Eq. 4.13, i.e. the high pH causes a low dissolution rate  $\alpha$  and this causes a very low current density  $j_{ox}$  (cf. also Fig. 4.7 for the scaling of the characteristic currents with pH). The oxide thickness just before the point, where the positive voltammogram scan starts to rise at 18 V can be determined from the impedance measurements (Fig. 8.14): With  $\varepsilon_{\text{SiO}_2} = 3.9$  (thermal oxide, values for anodic oxides can deviate slightly), the capacity of  $C_P = 282 \text{ nF}$  (@ 15 V), yields an oxide thickness of  $t_{ox} = 12.3 \text{ nm}$ . Furthermore it is seen in Fig. 8.2 that the point at which the positive scans “explodes” shifts with increasing fluoride concentrations towards lower potentials.

As well Bailes et al. [171] as also Lharch et al. [20,71] observed a porosification of the oxide with the strong increase in  $j$  at approx. 6 V (both measured at pH = 3,  $c_F = 0.05 \text{ M}$  resp.  $0.1 \text{ M}$ ). The oxide thickness up to this point is approx. 3-5 nm. As already discussed in section 4.3, Lehmann [68] measured the stress at the silicon electrode surface during current oscillations. At least for non-fluoride media, he was able to show that the oxide layer, as soon as its thickness surpasses 11 nm, becomes entirely porous.

The point of the strong current rise in the positive voltammogram scan in alkaline electrolytes at approx. 18 V is therefore most probably associated with the porosification of the oxide layer. The critical potentials and oxide layer thicknesses, at which breakdown occurs, depend strongly on the pH and the fluoride concentration of the electrolyte as results from this work compared to other works show [20,171]. As the etch rate increases with lower pH (down to pH = 3) as well as with the increase of  $c_F$ , at least as a guideline, the etch rate of a certain electrolyte can be seen as the decisive parameter for that breakdown.

The current on the upper branch is several orders of magnitude higher than on the lower branch. Because the (porous) oxide layer thickness approaches a constant value for a certain

current density<sup>1</sup>, a new steady state must have established. For such high current densities however, the etch rate  $\alpha$  has to rise also by the same orders of magnitude according to Eq. (4.13). When comparing the obtained  $IV$  curve with the curve for acidic HF (Fig. 4.5), it is seen that the upper branch of the  $IV$  curve at alkaline pH (Fig. 8.2), is matching quite closely with the voltammogram for acidic pH. For high buffer strength and pH (Fig. 8.13), it is seen that the current “explosion” also happens, but is quickly quenched with an exponential current decrease after the peak. Therefore one can conclude that the upper branch of the voltammogram designates a local acidification at the electrode. This only works when the buffer strength is low enough so that the buffer can be set out of function locally. The etch rate increases approximately one order of magnitude per pH value (cf. Fig. 4.7), i.e. a (local) shift of the pH from approx. 8 to 3 means a factor of  $10^5$  in the etch rate. Although certainly a porous oxide etches faster than its dense counterpart because the quality and etching area is different, these effects become minor in comparison to a pH shift.

To allow for a lower pH, it is necessary to set the buffer at least locally out of function by additional protons. While the oxide production itself causes an acidification of the medium, this is counteracted by the dissolution reaction which causes an alkalization. The second acidifying process is the splitting of water (reaction (4)); normally this process rarely occurs at a silicon electrode which oxidizes because it requires an electrochemical potential of  $U = +1.0$  V (versus SCE), while the redox couple for the silicon oxidation is already at  $U = +0.9$  V [28]. Thus under standard conditions always an oxide is grown which quickly reduces the voltage available for electrochemical reactions due to its insulating character. However when the oxide is porosified, suddenly the full voltage, which dropped before in the dense oxide, now is available at the interface. This certainly drives the potential beyond the necessary 1.0 V vs. SCE and protons are produced in larger quantities which then helps to remain a low pH against the buffer.

The currents on the upper branch (at least with the RDE) vary quadratically with the fluoride concentration (for  $U = 15$  V the relationship is not as clear as for  $U = 20$  V). Hassan et al. [175] investigated the anodic currents at the RDE at various fluoride concentrations and pHs. At least up to pH = 4 and not too high fluoride concentrations, always a linear dependance of the diffusional currents on  $c_F$  was observed and a quadratic dependance for the kinetic currents (cf. p. 69 for the theory on RDE systems). As the experimental conditions are very similar in the present experiments (at least on the upper “acidic” branch), it is concluded that actually the currents are kinetically limited at 20 V and above. This also coincides with the fact that the slope  $b$  does not depend clearly on the rotation rate  $\nu$ . For the slope  $a$  a dependance on the rotation rate is seen, and the correlation for the absolute current values could be quadratic but also linear. The situation is more complicated and indicates a mixed control of diffusion and kinetics.

The linear behavior of  $j(U)$  on the upper branch is a sign that the current through the system is limited by a process which exhibits an ohmic character. As both slopes  $a$  and  $b$  depend quadratically on the fluoride concentration, also this process with ohmic behavior does, i.e. its “resistivity” should scale with  $c_F^{-2}$ . Furthermore, the porous layer thickness (Fig. 8.7) at 15 V depends also quadratically on the reciprocal of  $c_F$ . In a rough approximation, the ohmic resistivity through a porous media will depend linearly on the thickness of the media, following the formula  $R = \rho \frac{l}{A}$  ( $\rho$ : specific resistivity;  $l/A$ : “length”/cross sectional area of the resistive element), which could explain the simultaneous scaling of the layer thickness  $t$  and the slope  $a$

---

<sup>1</sup>Grésillon [167] has shown that the layer thickness is independent of the etching time, at least for  $t_{etch} \geq 3$  min.

at  $U = 15$  V.

### 8.3.3 Impedance analysis

The impedance measurements (Fig. 8.14) show an extreme drop in the capacity from approx. 300 nF down to 50 nF when entering the high current regime. The parallel resistance  $R_P$  drops from over 1000  $\Omega$  down to 45  $\Omega$ . The rapid increase is - as previously stated - associated with a porosification of the oxide. The massive decrease in the parallel resistance could be already explained by a few current carrying spots (e.g. cracks in the oxide or thin parts of a dense oxide), because the resistance of parallel surface elements will mainly display the lowest resistance. But the total capacity of parallel surface elements is always the sum of their individual capacities, therefore to get a sixth of the original capacity would require a dense oxide thickness of approx. 70 nm. Such a high (dense) thickness of an anodic oxide has however not been observed in silicon before and neither is it in accordance with the SEM observations.

When the capacity of the porous layer is modelled, it has to be taken into account that the pores are filled with aqueous electrolyte, which has a dielectric constant of  $\varepsilon_{H_2O} \approx 80$  at such low frequencies. The matrix (i.e. the pore walls) are  $\text{SiO}_2$  ( $\varepsilon_{\text{SiO}_2} \approx 3.9$ ). The porosity necessary for a certain  $\varepsilon_{por.Ox}$  can then be determined via the Bruggemann approximation or another of the EMA approximations given in section 6.2.2. To achieve a capacity of  $C_P = 50$  nF with a material thickness of 500 nm requires a dielectric constant  $\varepsilon_{por.Ox} \approx 28$  (ions in the solution are neglected). The porosity according to the Bruggemann EMA is then 51 %. Already this simple approximation makes clear that the porous layer is not field-free. This is somewhat surprising because normally the field in an electrolyte is quickly screened within a few  $\text{\AA}$  in the Helmholtz layer. Here however, the density of ions in the porous oxide is diluted so far that the field is only screened outside the porous oxide.

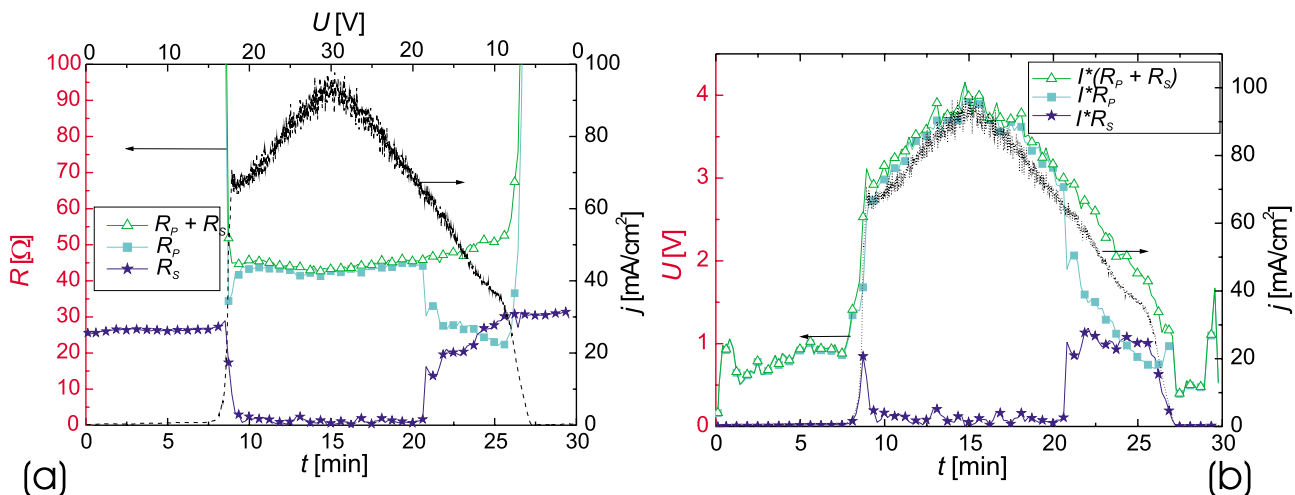


Figure 8.24: Impedance analysis (same data as Fig. 8.14, during cyclic voltammogram (0 - 30 V), sweep speed: 33 mV/s): (a) Serial resistance  $R_S$  and parallel resistance  $R_P$  and their sum during versus time. (b) Voltage drops at  $R_P$  resp.  $R_S$ . At 21 min. a process with  $U = 1.0$  V shifts from the parallel resistance to the serial resistance.

Fig. 8.24(a) shows the serial resistance, the parallel resistance and their sum as measured during the impedance experiments with  $c_F = 0.25$  M. When the current rises drastically at

17 V during the positive scan, the parallel resistance reduces to 45  $\Omega$  and the serial resistance drops to values around 1  $\Omega$ . At 19 V on the reverse scan,  $R_P$  drops suddenly by 15  $\Omega$  and  $R_S$  rises by the same value. The sum of the two resistances stays nearly constant during the whole high current phase. When the current is multiplied with the individual resistances, the voltage losses at each resistor become visible (Fig. 8.24b): At voltages up to 17 V during the positive scan, nearly all voltage drops at the parallel resistance. The values are a little below 1.0 V, so this should be the voltage which is necessary to drive the silicon oxidation which requires 0.9 V. When the current increases at 17 V, for a short time the voltage dropped at the serial resistance rises up to 0.8 V. Then the voltage is again mainly consumed at the parallel resistance until 19 V are reached on the negative scan. There the voltage dropped at the serial resistance rises to approx. 1 V and stays more or less constant until the current drops and the whole voltage is again consumed at the parallel resistance. As previously mentioned, water electrolysis requires exactly 1.0 V. As all electrochemically driven processes, it would show an exponential characteristic in the large signal if it would be the rate limiting process in the system. Here it is in series with several ohmically behaving processes, thus the electrolysis will behave like a Zener diode in series with a resistor, i.e. it consumes its 1 V, but not more.

As stated in the experimental section, also on the peristaltic pump set-up, where the impedance measurements were performed, potentiostatic thin film experiments at 15 and 20 V were executed. These showed the same morphologies as on the RDE set-up, i.e. 500 nm thick flat layers at 15 V and decorated macro structures at 20 V (sizes between 1 and 2  $\mu\text{m}$ ). If now the morphologies are correlated with the impedance data, the flat layers are associated with hydrolysis outside the porous layer (i.e. the 1 V process is included in  $R_S$ ) while during the growth of the macro structures the hydrolysis happens parallel to the capacitance, i.e. within the porous decoration of the macro structures. Still, also in the macro structure case, the hydrolysis has to happen at the outer edge of the porous layer, otherwise the capacity could not be so low.

This may explain as well the short peak at 19 V on the positive scan: it probably originates from the hydrolysis, which happens directly after the oxide layer has become porous and the porous oxide hasn't built up fully yet. As soon as the porous layer reaches a certain thickness the process slips into the layer and becomes part of the parallel resistance in the small signal analysis.

Other concentrations (0.3 and 0.4 M) also exhibit this shifting behavior, the sum of both resistances is almost constant, but the fractions shift. However, only the lowest concentration (i.e. 0.25 M) shows this clear step, where the 1.0 V process shifts out of the porous oxide. This might be due to the same reason as already seen on the RDE: With increasing concentration the macro structures already start to form at lower voltages. Probably on the peristaltic pump set-up, already at 0.3 M only the macro structure conditions are present in the whole high current phase, therefore the shift is not seen. Unfortunately, only with the lowest concentration morphology images have been made (for the peristaltic pump set-up).

Above 18-19 V the capacity as well as the resistances stay nearly constant (cf. Fig. 8.14). Moving to lower voltages on the negative scan, the parallel resistance drops linearly from 32 to 22  $\Omega$  (after the aforementioned process has shifted to  $R_S$ ). For  $U$  in the range of 8 V the parallel resistance rises again to values above 1 k $\Omega$ . The capacitance doubles from 60 to 120 nF when the electrolysis shifts outwards and rises monotonically from 120 nF to 650 nF. It was not possible to fit the increase by a simple function. When 650 nF is reached the current breaks down. Such a capacity is equivalent to a dense SiO<sub>2</sub> layer thickness of approx. 5.3 nm. Because the current decreases by several orders of magnitude and the parallel resistance rises

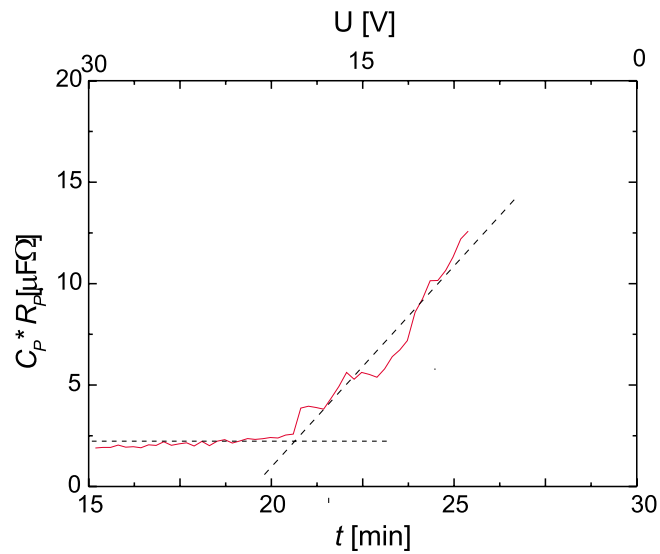


Figure 8.25: The product  $R_P * C_P$  from the impedance analysis shows a constant value in the regime of the macro structures ( $U \approx 20 - 30$  V) while it decreases linearly with potential in the flat layer regime ( $U \approx 10 - 20$  V; the time x-axis was kept to make the graph comparable with the other impedance graphs).

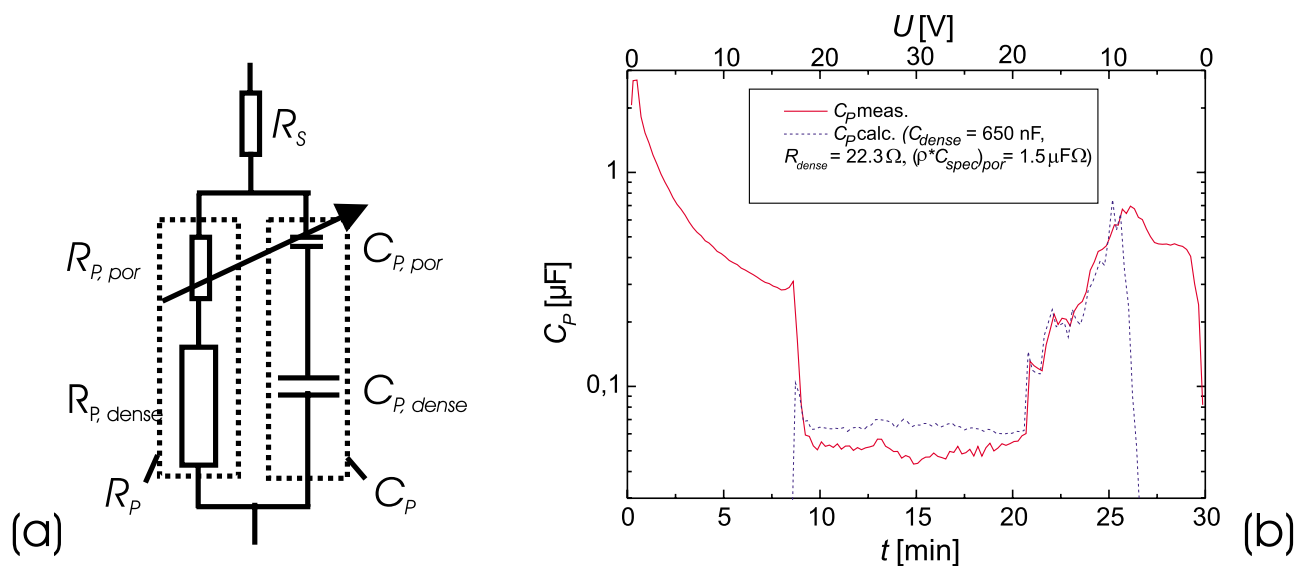


Figure 8.26: (a) Equivalent circuit used for the theoretical calculation of  $C_P$  using the measured  $R_P$ . (b) Comparison of the measured  $C_P$  with the calculated  $C_P$ .

by two orders of magnitude, it can be assumed that at this point the porosification of the oxide stops permanently. The further reverse scan (i.e. roughly for  $U < 8\text{V}$ ) is again the classical regime where the dissolution of the dense oxide is in equilibrium with the production of new (dense) oxide according to Eq. (4.13).

The product of  $R_P$  and  $C_P$  (Fig. 8.25a) shows a linear increase between 19 and 9 V, which is puzzling at first sight. The linear decrease in a “normal” resistance  $R = \rho l/A$  often points towards linear decrease of the length  $l$  of the resistor. Similarly the “normal” parallel plate capacity increases with  $1/l$  according to  $C = \varepsilon_0 \varepsilon_r A/l$ . Thus if an element represents a capacity in parallel with a resistor a re-scaling of length (as well as area) leads to a constant  $C_P * R_P$  product. In electrochemical systems, in most cases at least one of elements of this product does not obey the classical geometrical scaling laws. In the present system however a variation of the thickness of the porous oxide layer could be the reason for the characteristic of  $R_P$  and  $C_P$ . Therefore the system was modelled according to Fig. 8.26(a): The measured capacitance  $C_P$  was splitted in a part belonging to the porous oxide  $C_{P,por.} = C_{spec.,por.} A/l_{por}$  ( $C_{spec.,por.}$ : specific capacitance,  $l$ : thickness of the porous oxide layer into which the electrical field extends) and a part belonging to the dense oxide  $C_{P,dense} = \text{const.}$ . In series, the total capacitance is given by the reciprocal of the individual capacities:

$$C_P = \left( \frac{1}{C_{P,dense}} + \frac{l_{por}}{A * C_{spec.,por.}} \right)^{-1} \quad (8.1)$$

Under normal circumstances the capacitance of the dense oxide layer is much higher (some hundred nF) than that of the porous oxide (some ten nF). In series, the capacitance is to a large degree determined by the smallest capacity, therefore in good approximation an additional length scaling of the dense oxide capacity can be neglected.

The total parallel resistance  $R_P$  was calculated on the basis of a constant resistance  $R_{P,dense}$  of the dense oxide and a thickness dependant resistance of the porous oxide  $R_{P,por.} = \rho_{por} * l/A$  ( $\rho_{por}$ : specific resistance of the porous oxide):

$$R_P = R_{P,dense} + \rho_{por} * l_{por}/A \quad (8.2)$$

As sketched above, it is expected that at the breakdown of the hysteresis at 8 V the voltage drops entirely in the dense oxide. The parallel resistance associated with the dense oxide in the high current regime is likely to be defined by some leakage spots, which probably become more numerous at higher voltages. Therefore the parallel resistance of  $22.3 \Omega$  shortly before the hysteresis breakdown has to be seen as an upper limit of the ohmic resistance of the dense oxide in this regime. Also here, an additional length scaling of the dense oxide resistance along the classical  $R = \rho * l/A$  formula has been neglected.

From Eq. (8.2) the thickness of the porous oxide layer is calculated and entered into Eq. (8.1). Fig. 8.26(b) shows that with some optimization in the fitting parameters a very good matching of the modelled capacitance with the actually measured ones is achieved. In the regime between 20 and 30 V the calculated curve does not match the measurement, because the additional off-set caused by the electrolysis process has not been included in the modelling.

Neither in the present work nor in the preliminary works [167], a clear dependance of the layer thickness on potential was observed. Instead it was even seen that any subsequent scans after a first “virgin” voltammogram did not or only partially exhibit the hysteresis, which could be caused by remaining porous oxide from a previous scan. When the oxide thickness is too large after a change in the conditions, the extremely slow dissolution rate causes that even,



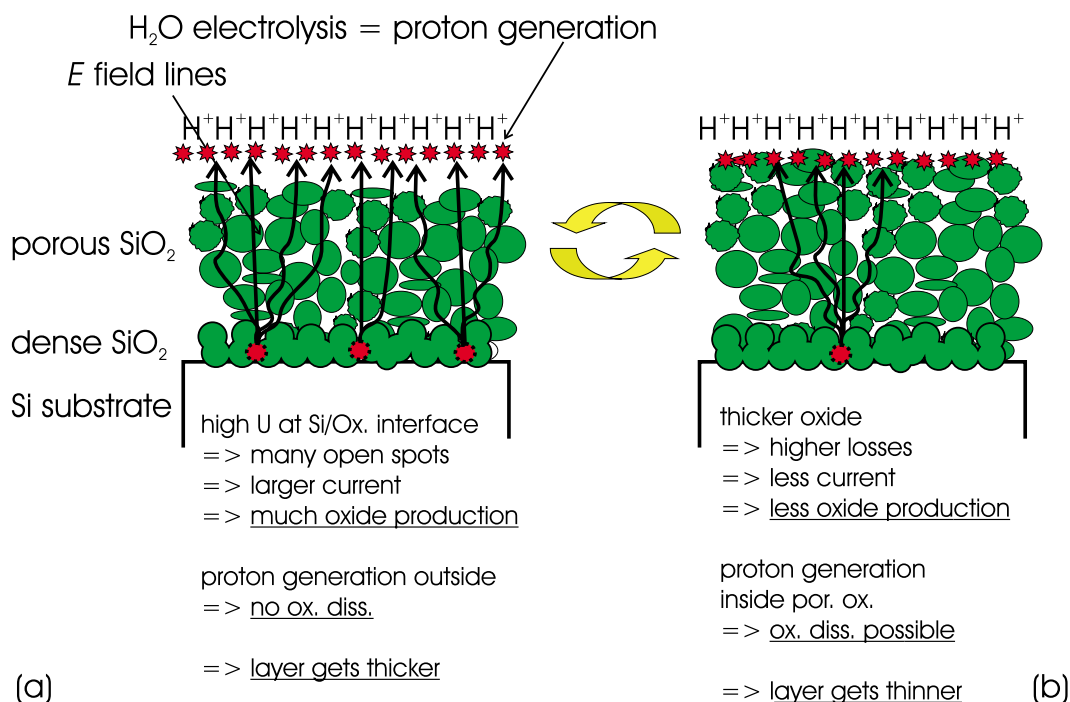


Figure 8.27: Schematic drawing: In the flat layer regime the proton generation interface shifts back and forth with respect to the porous silica / electrolyte interface: (a) The proton generation interface is outside the capacity. A dissolution is not possible and the oxide layer grows. (b) When the oxide layer gets thicker, more losses occur inside the oxide and the proton generation interface moves closer to the substrate. Less oxide is formed during that phase and the uppermost part of the oxide (where no field is present) can be dissolved.

when the field retracts, the porous layer thickness still remains nearly constant and changes only slowly. Therefore in the SEM images no distinct thickness difference is measured albeit the impedance analysis yielded that the relevant thickness is much smaller. When the field has fully retracted into the dense oxide, the point has come where the hysteresis breaks down.

The transfer of the results between the two set-ups is limited because the large signals definitely do not match (cf. Figs. 8.2 and 8.14a). Especially the second linear regime with slope  $b$  is not observed on the peristaltic pump set-up. The RDE offers extremely good diffusion conditions, especially at fast rotation rates like  $1500 \text{ min}^{-1}$ . The peristaltic pump set-up has some (compared to the RDE) severe diffusion limitations which are impressed at least on the large signal. On the other hand, the small signals at frequencies higher than 100 Hz normally cut out diffusion effects, therefore at least qualitatively, the results from the small signal analysis should be portable. Also the morphologies seem to be unaffected by the diffusion limitations because the layer thickness resp. the macro structure sizes are nearly identical on both set-ups for  $c_F = 0.25 \text{ M}$ .

### 8.3.4 Flat and corrugated morphology

The results for the flat, non-corrugated oxide layer can be summarized and interpreted as follows: As discussed in section 8.3.3 for the flat layers the proton generation process lies outside the capacity. These generated protons are driven away from the oxide layer by the

electrical field. As long as the field leaks out of the porous layer, it is therefore very hard for the protons to enter the porous oxide and aid the dissolution process. Hence dissolution is suppressed in field-filled areas and only oxide growth occurs (Fig. 8.27a). Also the number of open channels in the lowest oxide layer will scale with the field strength in this area. The oxide thickness thus becomes larger. At a certain point, situation (b) from Fig. 8.27 is reached, i.e. the Helmholtz layer and with it the proton production will reach into the oxide layer. Now a dissolution of the layer becomes possible. When the oxide layer has reached this thickness, also the oxide production current is somewhat less because less voltage is available at the inner interface due to the higher ohmic losses. This altogether causes a decrease in the oxide thickness. At a certain point the layer thickness is so small again that the electrolysis “jumps” out of the layer and the cycle repeats.

The experiments with the macro structures can be summarized by the following results:

- The structure sizes and pitches depend mainly on the fluoride concentration  $c_F$ .
- The rotation rate  $\nu$  strongly influences the depth of the structures.
- When an external pitch is impressed by lithography, it has to match the system-inherent pitch very exactly. If the external and the internal pitch match, the structural ordering is extremely stable.
- The doping or orientation of the silicon substrate is only of minor influence.
- The structures occur when the electrolysis process shifts from the parallel to the serial resistance.

The negligible influence of the substrate indicates that again the chemistry of the system contains the decisive mechanism. The dependance on the rotation rate suggests a diffusion phenomena, because only diffusion related processes are changed when the rotation rate is changed. The shift of the electrolysis process indicates that actually proton generation is the rate determining process. Other diffusion processes, e.g. through the  $\delta$  - layer in front of the RDE surface, operate on different length scales ( $\delta \approx 20\mu\text{m}$ ) and can be excluded as a responsible process for the 1-2 micron structures.

As discussed before the protons play an extraordinary role because they enhance the dissolution rate of silica drastically. When the proton generation process shifts into the layer the “back and forth” motion of the proton source is not anymore necessary for the dissolution of the porous layer. This enhances the oxide dissolution rate and thus the layer thickness readjusts to that new situation according to the continuity equation Eq. 4.13. The oxide thickness diminishes from 340 to 150 nm when this effect sets in (cf. Figs. 8.18ff.). When the layer is flat (Fig. 8.28a) this causes the spots, where this occurs, to be etched faster. The structures probably arrange in a manner that the spots which produce more protons supply their surrounding regions. The pattern which results is then an image of the diffusion and etching conditions (cf. Fig. 8.28(a-c) for the dependance on potential). With an increased fluoride concentration a proton is faster consumed because of a higher etching rate. The area which can be supplied by a proton source becomes smaller and hence the structure sizes become smaller. The experiments with the lithography show that this process is very strongly self-stabilizing: If the pitch is too large the pre-structure is completely overwritten because the protons cannot reach all necessary spots to span the large structures and new walls are quickly rising and stabilized. At

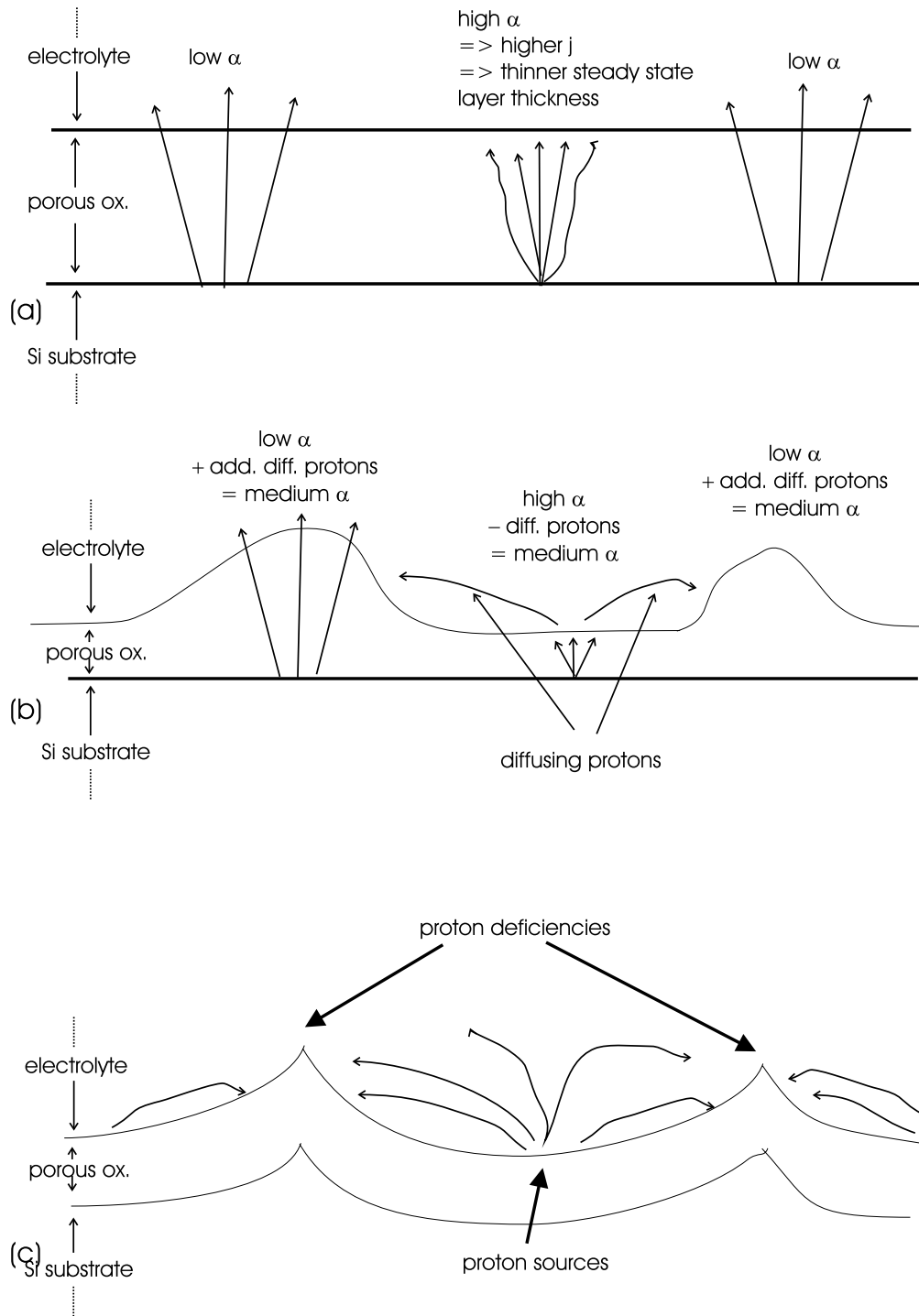


Figure 8.28: Model for the transition from flat layers to macro structures: (a) At the beginning of the transition, spots where the proton generation interface has already shifted to  $R_P$ , have a higher dissolution rate  $\alpha$ . (b) Thus the layer thickness decreases at these spots. Due to the diffusion of protons into the other regions the dissolution rates are equalized. (c) At higher voltages, a “bowl”-like shape develops (cf. Fig. 8.10), where the valleys act as proton sources and the peaks represent proton deficient regions. The shape adjusts according to diffusion laws so that the dissolution rates become equal.

the correct pitch, the positions of the valleys and peaks have an extreme stability. Therefore a too small pitch will still be obeyed, only some structures coalesce, reflecting the underlying “natural” structure size.

At higher voltages more protons are produced, which reduces the thickness of the porous decorating. Little by little each of the proton deficiencies becomes also a proton source. However, the exact mechanism leading to the structures at 25 and 30 V still has to be elucidated.

## 8.4 Conclusions

Further investigations in the regime of porous anodic silica formation have been performed continuing the work of Lharch et al. [20, 71] and Grésillon [167].

The variety of all the different stages of the system during cyclic voltammetry are sketched in Fig. 8.29: Up to approx. 15 - 20 V the anodic oxide remains dense. The thickness increases with increasing potential and nearly all potential drops across the dense oxide. At approx. 20 V the thickness exceeds a critical value. For 0.25 M the impedance measurements give a thickness of approx. 12 nm for this event. From literature it is known that the critical thickness before porosification is lower when the pH is lower. Similarly the present experiments show that a higher  $c_F$  leads to an earlier porosification.

When the critical thickness is exceeded probably the whole dense oxide becomes porous. The voltage is not anymore “consumed” in the (ex-) dense oxide and the potential necessary to start water electrolysis is reached in the electrolyte. This, as well as the oxide formation reaction itself produce protons resp. consume  $\text{OH}^-$ . The weak buffer is quickly exhausted in the vicinity of the electrode and the pH drops rapidly.

The porous oxide thickness grows until the electrical field strength in the oxide has again dropped below a certain limit and the oxide dissolution rate can cope again with the oxide growth rate. A new steady state between porous oxide thickness and oxide dissolution rate establishes. The electrolysis process is in parallel to the measured capacity. Probably the Helmholtz capacity in this region becomes so small that it becomes comparable to the porous oxide capacity. Under such conditions the fitted parallel capacity includes the Helmholtz capacity.

When the applied potential is reduced, the electrolysis process shifts to the serial resistance and the layer becomes flat. Lowering of the potential (between 19 and 10 V) moves the line, up to which the electrical field reaches into the porous oxide, towards the porous/dense oxide layer interface. When the interface arrives there and the entire voltage drops again across the dense oxide, the field strength soon drops below the critical value for a stable dense oxide. When this happens the electrolysis stops and the pH rises to alkaline values. The current adjusts to the drastically reduced etch rate caused by the high pH. The porous layer remains as debris on top due to the high pH.

It was possible to further clarify the following aspects of this extremely versatile system:

- Two different morphologies could be identified by cross section and plain view SEM images. Thin films of some hundred nm thickness, probably composed of granular  $\text{SiO}_2$  media, form between 10 and 16 V. The film thickness is directly correlated to the fluoride concentration via  $c_F^{-2}$ .
- Beyond 16 V the surface becomes corrugated with micron-sized, self-organized depressions. These “macro bowls” coalesce above 20 V in yet not understood patterns. Prob-

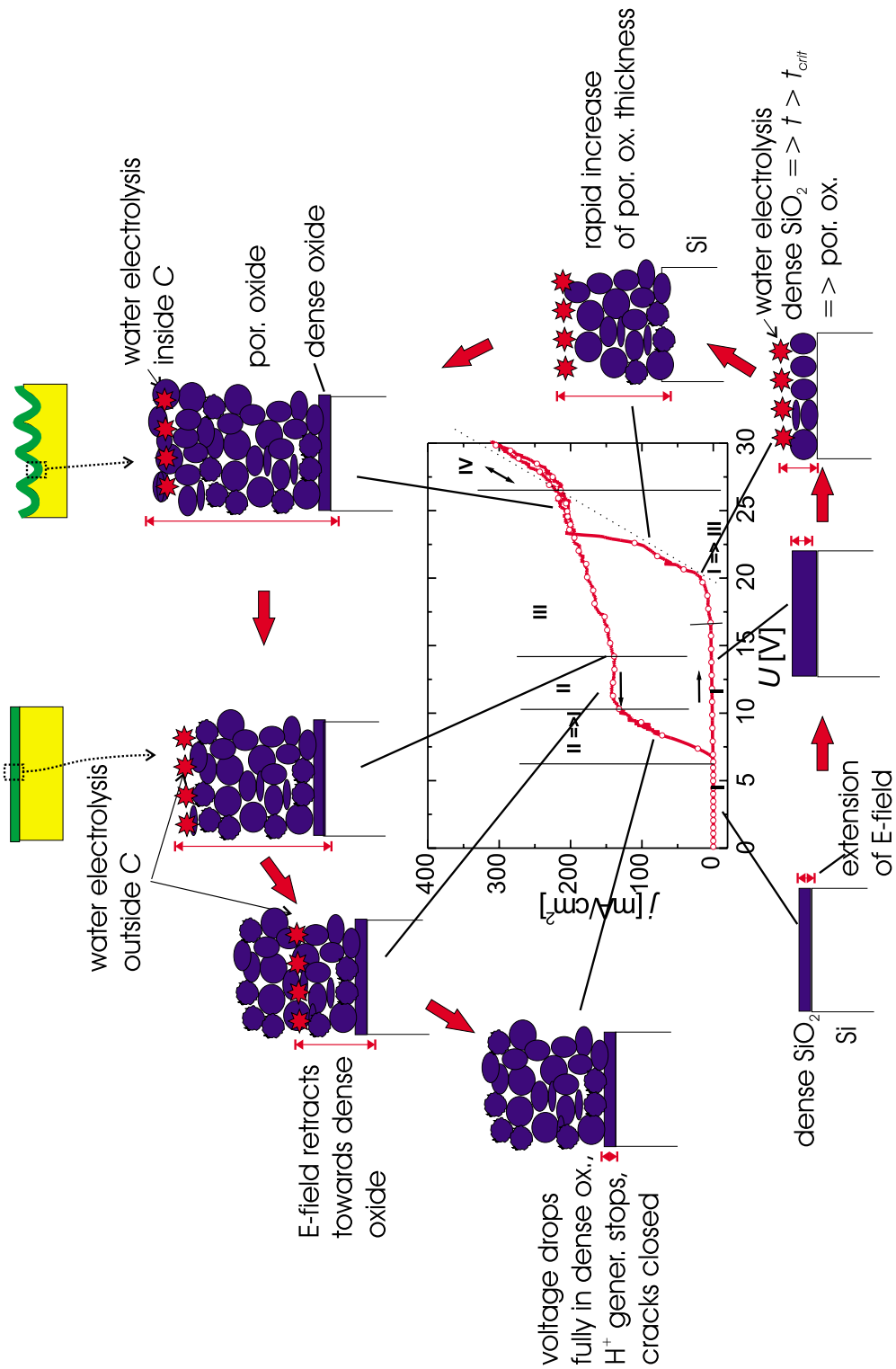


Figure 8.29: Model for the individual stages of porous silica formation during the cyclic voltammetry.

bly the diffusion properties of protons define the structural properties of the macro structures. Thus it was possible to grow ordered structures by the use of photolithographic pre-patterning and matching chemical conditions.

- The system is mainly chemically defined (by  $c_F$ , rotation rate, buffer etc.), while the impact of the semiconductor substrate (beyond the basic property to be p-type silicon) is negligible.
- The movement of the proton generation location (i.e. the screening layer) could be identified as the decisive parameter which most probably leads to the morphology dependency on the voltage.
- An intensive impedance analysis was carried out and aided crucially to the understanding of the underlying processes. Especially it could be demonstrated that the porous oxide is not field-free how it would normally be expected in electrolytic systems.
- A model for most stages of the system could be developed.

# Chapter 9

## Summary and outlook

### 9.1 Results and outlook on porous silicon

Porous silicon has been investigated for 50 years since Uhlir discovered a (micro)porous covering during electropolishing of silicon [176]. Albeit this early discovery, it took over 40 years until macropores in silicon were found [46] and still a vast portion of the parameter space for porous silicon formation is unexplored. The first part of this work is based on investigations concerning mesopores and small, fast growing macropores with high structural quality. Up to now, mainly macropores grown on n-type with backside illumination reach the structural quality and reproducibility necessary for an industrial production process. Under standard growth conditions these pores have diameters of a few micron. Smaller pores require special substrate materials, with which pore sizes down to 350 nm were realized, however this seems to be near some fundamental limits which occur at 200 nm [98]. The slow growth speed of approx  $1 \mu\text{m}/\text{min}$  is a severe hindrance for an economical fabrication of macropore based devices in larger amounts and at lower prices. Mesopores on the other hand don't suffer from this and can be grown at variable speeds up to  $25 \mu\text{m}/\text{min}$ . This speed increase is however accompanied by a hardly controllable morphology. The pores frequently branch and often have the shape of dendrites, but they are useful for those application where e.g. only a certain porosity of a layer is needed without high demands to the exact pore geometry.

During this PhD work, mesopore growth was investigated in an industry project on thin porous films on silicon in the pore size range of 3 - 30 nm. Therefore the influence of the electrolyte composition on the pore diameter, porosity, and growth rate was checked. While HF showed the expected behavior (faster and smaller pores), the ethanol content led surprisingly to slower and enlarged pores. By comparison with literature on the dissolution behavior of thermal oxides in ethanol-containing solutions, it was possible to identify ethanol as a hindrance for oxide dissolution. A major practical aspect of the project was the development of a fast and destruction-free technique to analyze the grown layers. The characteristic "footprint" measured with optical reflectance spectroscopy proved to be suitable to check the transfer of the etching recipes from the small laboratory etching set-up to a large area etching system for 4" - 8" substrates. Also the lateral homogeneity of the mesopore etching was verified with this technique.

In a previous work [51], it was shown that mesopores can enter a self-organized, pulsed growth mode under special conditions: There the pores grow as chains of connected octahedrons, which become best visible, when organic electrolytes with low water content are used. During the present thesis the parameter dependance of the size and stacking density of these

structures was investigated. While the HF concentration and the pH did not affect significantly the structural dimensions, the octahedrons became bigger and closer stacked when the formation voltage was increased. It was possible to develop a model based on critical field strengths to explain this closer stacking.

Besides silicon, several other semiconductor pore systems become more and more investigated [95]. While still the high price of the substrate material and the limited range of available specifications pose a certain limitation, pores in germanium and III/V compounds have enriched the “pore zoo” drastically. Namely InP exhibits macropores (so-called “curro” pores, because they grow along the current lines) which grow at the speed of silicon mesopores but with the quality of silicon macropores. Based on the results in InP, it was possible during this work to identify a new growth regime for macropores in silicon. Thus macropores in silicon could be grown with speeds of up to 10  $\mu\text{m}/\text{min}$  while the pore quality can keep up with the best macropores known so far. Furthermore, the diameter of those pores could be reduced down to 100 nm, while the maximum achievable pore depth is yet only limited by the wafer thickness.

This novel pore system behaves in many aspects like its counterparts in InP:

- The pores show strong interaction features like collective oscillations in diameter as well as in the externally measured electrical signals.
- They tend to self-organize in close-packed structures. While the pores can form a hexagonally close packed pore crystal like in InP, also a new form of pore self-organization in a so-called geometrically frustrated structure was found. The type of ordering is determined by the substrate orientation.
- The nucleation often proceeds via crystallographically oriented mesopores. However, unlike InP, in silicon it was possible to nucleate the fast macropores also directly on the surface.

Suitable parameters for this pore type could be identified by an intensive parameter scan. The role of surfactants during pore etching was analyzed by impedance spectroscopy and led to an extension of the existing model. While prior investigators mainly concerned the charge carried by the surfactant, the new results suggest a modification of the surface passivation kinetics by the surfactant.

The growth model for these pores was re-fined and defines key-requirements for achieving this mode:

- Oxidation has to be suppressed by the use of organic electrolytes with low oxidation power and high HF concentrations.
- When oxidation is kept low, the interface passivation becomes the rate determining process. As soon as the supply with passivating species fails to kept up with the pore growth, the pores switch into the fast growth mode.
- The pores have to be nucleated densely, because the only remaining stabilization mechanism is the close packing of the pores. Thus the space charge regions of adjacent pores overlap and the pore walls become depleted of carriers.

This pore type still has a high development potential; the investigations presented here are just the beginning. A promising guideline for future investigations is a better understanding and an optimization of the nucleation behavior. The nucleation is “the nuts and bolts” of this



special pore type because it decides upon the density of pores in a certain depth. Furthermore, the uppermost layer of pores acts as a strong diffusion blocker, whose effectiveness determines the switching point into the fast growth mode.

Yet only unstructured samples were investigated. For many practical applications, a targeted positioning of the pores is often requested. While the conventional silicon macropores show a very good response to pre structuring, pores in III/V semiconductors have difficulties with following orders nucleation etch pits. This concerns the direct nucleation at the surface, but also the growth and branching behavior below. Thus growth at defined spots will require surely some more work.

## 9.2 Results and outlook on porous anodic oxides

The second large block during this PhD thesis was the investigation of porous anodic oxides. Anodic oxide films on silicon are investigated since the 1930s [32]. Generally, low voltages in HF containing electrolytes lead to porous silicon formation. Already there, anodic oxidation often has a decisive influence on the pore shape and growth behavior. At higher voltages, exclusively an anodic oxide forms on the surface. Simultaneously to its formation, this oxide is dissolved by the fluoride containing electrolyte. The surface underneath the oxide layer can be smoothed in this “electropolishing” regime. The silicon oxide (or “silica”) is much more stable than most other semiconductor oxides, which causes diverse phenomena at the silicon electrode to be mainly dependent on the dissolution rate of the oxide. At voltages between 3 and 8 volts the system exhibits pronounced oscillations in the oxide thickness and the electrical signals.

Porous oxides require formation voltages of more than (roughly) 10 V. Other porous oxides, e.g. highly ordered alumina or silica based on other fabrication techniques, e.g. spin-on glasses for the microelectronics had significant success in the recent years. However, on the anodic formation of porous silica, only a few papers have been published. In this work, the anodization in weakly buffered alkaline fluoride media was investigated. The background for this choice of electrolyte was two-fold:

- The dissolution of silica has a complex pH dependency; in alkaline media it is strongly suppressed. Thus it was expected that thicker layers could be formed.
- Furthermore, during the “pitting corrosion” a locally lower pH leads to the formation of pores. Therefore a weakly buffered system was chosen to enable similar phenomena in the Si/HF system.

The investigations were performed with a rotating disk electrode (RDE) as well as with a peristaltically pumped system. The analysis yielded the following results:

- The cyclic voltammogram exhibits a giant hysteresis of several orders of magnitude for the current during the positive versus that during the negative scan. The alkaline milieu shifts the critical voltage at which the porosification starts to significantly higher values around 20 V. After the porosification, most probably the electrode becomes locally acidic. Several elements of the voltammogram exhibit a quadratic dependance on the fluoride concentration  $c_F$  which suggests mainly a kinetic limitation of the current.
- Potentiostatic growth at 10 - 15 V for several minutes results in thin films of probably granular  $\text{SiO}_2$  structures. The layer thickness is proportional to  $c_F^{-2}$ .

- At 20 V, potentiostatic experiments lead to corrugations of the surface on a micrometer scale, which are covered by a thin film of granular oxide. The structural sizes are narrowly distributed and a high degree of self-organization occurs for most probed conditions. The dimensions and the ordering are not controlled by the orientation or doping level of the silicon substrate but exclusively to the chosen chemistry. With photo lithography a perfect ordering is achieved, but only if the chemistry of the system is tuned accordingly.
- At higher voltages the macro structures coalesce and can form labyrinth-like patterns.
- Impedance measurements during the anodization give strong indications that the electrical field at the electrode extends throughout the porous film and that at the outer interface of the porous oxide, water electrolysis produces additional protons. The shift of this process into the porous oxide was identified to accompany (or even cause) the switch between the two morphology types.

For the different stages of the oxide growth, formation models have been elaborated. The granular structure of the flat films as well as the decoration of the macro structures should be caused by the discontinuous “burst” growth of anodic silica. The macro structures are probably defined by the diffusion conditions for protons. So, it is assumed that the valleys of the structure are producing more protons than they consume, while the peaks are proton sinks. Flat layers of porous silica have been investigated earlier by other authors. Sometimes similar macro structures occurred, but never in this clear form with such a high degree of ordering.

For the future, it is definitely necessary to make further investigations, with other parameters before this system will be fully understood. Also additional *in-situ* techniques, e.g. electroluminescence measurements [20] or further impedance measurements, should help. The microstructure of the flat layers should be investigated with other techniques like TEM or AFM which are more suitable for sub-100 nm structures than SEM. While for the flat layers the formation mechanism is more or less evident due to the discontinuous growth of anodic silica in general, the underlying mechanism for the macro structure formation is yet only based on several indications, but far from being proven. Especially the merging of the structures at higher voltages remains unclear and calls for further investigation. Also a comparison to other anodically grown porous oxide systems, namely alumina and titania, could be valuable to elucidate a way how to achieve similar pores in silica.

# Bibliography

- [1] J.D. Plummer, M.D. Deal, and P.B. Griffin. *Silicon VLSI Technology*. Prentice Hall, Upper Saddle River, 2000.
- [2] H. Föll. *Electronic materials*. Hyperskript, Universität Kiel, 2004.
- [3] Advanced Micro Devices (AMD). AMD, IBM Announce Semiconductor Manufacturing Technology Breakthrough (Press Release). [http://www.amd.com/us-en/Corporate/VirtualPressRoom/0,,51\\_104\\_543\\_91999,00.html](http://www.amd.com/us-en/Corporate/VirtualPressRoom/0,,51_104_543_91999,00.html), 13.12.2004:1, 2004.
- [4] G. Moore. From the archives: Gordon moore. *PCMag.com*, <http://www.pcmag.com/article2/0,1895,1172800,00.asp>, page 1, 1997.
- [5] H. Föll, M. Christophersen, J. Carstensen, and G. Hasse. Formation and application of porous Si. *Mat. Sci. Eng. R*, **39**(4):93, 2002.
- [6] S. Weinberg. Scientist: Four golden rules. *Nature*, 426:389, 2003.
- [7] M. Thönissen. *Spektroskopische Charakterisierung von Schichten und Schichtsystemen aus porösem Silicium im Hinblick auf optische und optoelektronische Anwendungen*. Dissertation, Forschungszentrum Jülich, 1999.
- [8] L. Ohlsen. Porous silicon electrode all-liquid fuel cells. *Phys. Stat. Sol. (a)*, 2005.
- [9] D.T. Mitchell, S.B. Lee, L. Trofin, N. Li, T.K. Nevanen, H. Söderlund, and C.M. Martin. Smart Nanotubes for Bioseparations and Biocatalysis. *J. Am. Chem. Soc.*, 124:11864, 2002.
- [10] O.A. Saleh and L.L. Sohn. An Artificial Nanopore for Molecular Sensing. *Nano Lett.*, **3**(1):37, 2003.
- [11] H. Cao, J.O. Tegenfeldt, R.H. Austin, and S.Y. Chou. Gradient nanostructures for interfacing microfluidics and nanofluidics. *Appl. Phys. Lett.*, 81:3058, 2002.
- [12] K.E. Geckeler and H. Eckstein (Eds.). *Bioanalytische und biochemische Labormethoden*. Vieweg, Braunschweig, 1998.
- [13] V. Lehmann. Porous silicon matrix for chemical synthesis and chromatography. *Phys. Stat. Sol.*, **202**:1365, 2005.
- [14] European Semiconductor Industry Association, Japan Electronics, Information Technology Industries Association, Korea Semiconductor Industry Association, Taiwan Semiconductor Industry Association, and Semiconductor Industry Association. International Technology Roadmap for Semiconductors. *ITRS*, 1:1, 2003.

- [15] Y. Lu, R. Ganguli, C.A. Drewien, M.T. Anderson, C.J. Brinker, W. Gong, Y. Guo, H. Soyez, B. Dunn, M.H. Huang, and J.I. Zink. Continuous formation of supported cubic and hexagonal mesoporous films by sol-gel dip-coating. *Nature*, 389:364, 1997.
- [16] H. Miyata, T. Suzuki, A. Fukuoka, T. Sawada, M. Watanabe, T. Noma, K. Takada, T. Mukaide, and K. Kuroda. Silica films with a single-crystalline mesoporous structure. *Nature Materials*, 3:651, 2004.
- [17] H. Masuda and F. Fukuda. Ordered metal nanohole arrays by a two-step replication of honeycombstructures of anodic alumina. *Science*, 268:1466, 1995.
- [18] O. Jessensky, F. Müller, and U. Gösele. Self-organized formation of hexagonal pore structures in anodic alumina. *J. Electrochem. Soc.*, 145:3735, 1998.
- [19] H.-J. Lewerenz and M. Aggour. On the origin of photocurrent oscillations at Si electrodes. *J. Electroanal. Chem.*, 351:159, 1993.
- [20] M. Lharch, M. Aggour, J.-N. Chazalviel, and F. Ozanam. Anodic dissolution and electroluminescence of p-si at high potentials in fluoride media. *J. Electrochem. Soc.*, 149, 2002.
- [21] R.E. Hummel. *Electronic properties of materials*. Springer, Berlin, 1992.
- [22] S.M. Sze. *Physics of semiconductor devices*. Wiley & Sons, New York, 1981.
- [23] A.J. Bard and L.R. Faulkner. *Electrochemical methods*. JohnWiley & Sons, New York, 1980.
- [24] W. Schottky. Halbleitertheorie der Sperrschicht. *Naturwissenschaften*, 26:843, 1938.
- [25] H.A. Bethe. Theory of the Boundary Layer of Crystal Rectifiers. *MIT Radiat. Lab. Rep.*, 43, 1942.
- [26] C.R. Crowell and S.M. Sze. Current Transport in Metal-Semiconductor Barriers. *Solid State Electron*, 9:1035, 1966.
- [27] S.R. Morrison. *Electrochemistry at semiconductor and oxidized metal electrodes*. Plenum Press, New York, 1980.
- [28] X.G. Zhang. *Electrochemistry of silicon and its oxide*. Kluwer Academic - Plenum Publishers, New York, 2001.
- [29] H. Föll. Properties of silicon-electrolyte junctions and their application to silicon characterization. *Appl. Phys. A*, 53:8, 1991.
- [30] K. Winnacker and L. Küchler. *Chemische Technologie*. Carl Hanser, München, 1986.
- [31] G.W. Trucks, K. Raghavachari, G.S. Higashi, and Y.J. Chabal. . *Phys. Rev. Lett.*, 65(4):504, 1990.
- [32] V. Lehmann. *Electrochemistry of silicon*. Wiley-VCH, Weinheim, 2002.

- [33] D.R. Turner. Electropolishing silicon in hydrofluoric acid solutions. *J. Electrochem. Soc.*, **105**:402, 1958.
- [34] B.R. Weinberger, G.G. Peterson, T.C. Eschrich, and H.A. Krasinski. Surface chemistry of hf passivated silicon: X-ray photoelectron and ion scattering spectroscopy results. *J. Appl. Phys.*, 60:3232, 1986.
- [35] H. Gerischer and M. Lübke. On the etching of silicon by oxidants in ammonium fluoride solutions. *J. Electrochem. Soc.*, **135**:2782, 1988.
- [36] J.-N. Chazalviel and F. Ozanam. In situ infrared characterization of the silicon surface in hydrofluoric acid. *J. Appl. Phys.*, 81(11):7684, 1998.
- [37] J.-N. Chazalviel and F. Ozanam. . *J. Electroanal. Chem.*, **269**:251, 1989.
- [38] V. Lehmann and S. Rönnebeck. The physics of macropore formation in low doped p-type silicon. *J. Electrochem. Soc.*, **146**:2968, 1999.
- [39] X.G. Zhang, S.D. Collins, and R.L. Smith. Porous Silicon Formation and Electropolishing of Silicon by Anodic Polarization in HF Solution. *J. Electrochem. Soc.*, 136:1561, 1989.
- [40] A. Benor. *In situ measurements during the growth of porous structures on p-type Si*. Master thesis, CAU Kiel, 2003.
- [41] A. Belaidi, M. Safi, F. Ozanam, J.N. Chazalviel, and O. Goroher. Surface chemistry during porous-silicon formation in dilute fluoride electrolytes. *J. Electrochem. Soc.*, **146**:2659, 1999.
- [42] G. Hasse, M. Christophersen, J. Carstensen, and H. Föll. New insights into si electrochemistry and pore growth by transient measurements and impedance spectroscopy. *phys. stat. sol. (a)*, **182**(1):23, 2000.
- [43] J.-N. Chazalviel, C. da Fonseca, and F. Ozanam. In situ infrared study of the oscillating anodic dissolution of silicon in fluoride electrolytes. *J. Electrochem. Soc.*, **145**:964, 1998.
- [44] M. Köhler. *Ätzverfahren für die Mikrotechnik*. Wiley-VCH, Weinheim, 1998.
- [45] V. Lehmann, S. Stengl, and A. Luigart. On the morphology and the electrochemical formation mechanism of mesoporous silicon. *Mat. Sci. Eng. B*, **69-70**:11, 2000.
- [46] V. Lehmann and H. Föll. Formation mechanism and properties of electrochemically etched trenches in n-type silicon. *J. Electrochem. Soc.*, **137**:653, 1990.
- [47] J.-N. Chazalviel. *The silicon/electrolyte interface* in: J.C. Vial and J. Derrien (eds.), *Porous silicon science and technology*. Springer, 1994.
- [48] E.K. Propst and P.A. Kohl. The electrochemical oxidation of silicon and formation of porous silicon in acetonitrile. *J. Electrochem. Soc.*, **141**:1006, 1994.
- [49] G. Mende, H. Flentner, and M. Deutscher. Otimization of anodic silicon oxide films for low temperature passivation of silicon surfaces. *J. Electrochem. Soc.*, 140:188, 1993.

- [50] J.H. Song and M.G. Sailor. Dimethylsulfoxide as a mild oxidizing agent for porous silicon and its effect on photoluminescence. *Inorg. Chem.*, **37**:3355, 1998.
- [51] M. Christophersen. *Untersuchungen zur Makroporenbildung in Silizium und deren technologischen Nutzung*. Doktorarbeit, Universität Kiel, 2002.
- [52] E.A. Ponomarev and C. Lévy-Clément. *Electrochemical and Solid-State Letters*, **1**(1):42, 1998.
- [53] A.G. Revesz. The defect structure of grown silicon dioxide films. *IEEE Trans. Electron. Devices*, 12:97, 1965.
- [54] R. Janssen. *Strukturelle und elektronische Eigenschaften amorpher Silizium-Suboxide*. Phd-thesis, TU Munich, 2000.
- [55] B.E. Deal and A.S. Grove. General relationship for the thermal oxidation of silicon. *J. Appl. Phys.*, **36**:3770, 1965.
- [56] F. Gaspard, A. Halimaoui, and G. Sarrabayrouse. Electrical properties of thin anodic silicon dioxide layers grown in pure water. *Rev. Phys. Appl.*, **22**:65, 1987.
- [57] H.-J. Lewerenz. Anodic oxides on silicon. *Electrochem. Acta*, **37**:847, 1992.
- [58] S. Ottow. *Elektrochemische Untersuchungen am Silizium/Flußsäure-Elektrolytkontakt und Anwendung von nano- und makroporösen Siliziumschichten*. Doktorarbeit, Universität Kiel, 1996.
- [59] M. Matsumura and S.R. Morrison. Anodic properties of n-Si and n-Ge electrodes in HF solution under illumination and in the dark. *J. Electroanal. Chem.*, **147**:157, 1983.
- [60] J.-N. Chazalviel. Ionic processes through the interfacial oxide in the anodic dissolution of silicon. *Electrochem. Acta*, **37**:865, 1992.
- [61] V.P. Parkhutik. Kinetics, composition and mechanism of anodic oxide growth on silicon in water-containing electrolytes. *Electrochimica Acta*, 36(10):1611, 1991.
- [62] F. Keller, M.S. Hunter, and D.L. Robinson. Structural features of oxide coatings on aluminium. *J. Electrochem. Soc.*, **100**:411.
- [63] R. Beranek, H. Hildebrand, and P. Schmuki. Self-organized porous titanium oxide prepared in  $\text{H}_2\text{SO}_4/\text{HF}$  electrolytes. *Electrochem. Sol. State Lett.*, **6**, 2003.
- [64] J. Choi, R.B. Wehrspohn, J. Lee, and U. Gösele. Anodization of nanoimprinted titanium: a comparison with formation of porous alumina. *Electrochim. Acta*, 49:2645, 2004.
- [65] P. de Rouffignac, Z. Li, and R.G. Gordon. Sealing porous low-k dielectrics with silica. *Electrochem. Sol.-State Lett.*, **7**(12), 2004.
- [66] M.J. Madou, S.R. Morrison, and V.P. Bondarenko. Introduction of impurities in anodically grown silica. *J. Electrochem. Soc.*, 135:229, 1988.
- [67] M. Aggour, M. Giersig, and H.-J. Lewerenz. Interface condition of n-Si (111) during photocurrent oscillations in  $\text{NH}_4\text{F}$  solutions. *J. Electroanal. Chem.*, **383**:67, 1995.

- [68] V. Lehmann. On the origin of electrochemical oscillations at silicon electrodes. *J. Electrochem. Soc.*, **143**:1313, 1996.
- [69] V.P. Parkhutik, E. Matveeva, R. Perez, J. Alamo, and D. Beltrán. *Mat. Sci. Eng. B*, **69-70**:553, 2000.
- [70] V.P. Parkhutik, Y. Chu, H. Huo, Z. Nagy, and P.A. Montano. X-Ray reflectivity study of formation of multilayer porous anodic oxides of silicon. *J. Por. Mat.*, 7:27, 2000.
- [71] M. Lharch, J.-N. Chazalviel, F. Ozanam, M. Aggour, and R.B. Wehrspohn. In situ investigation of porous anodic films of silica. *phys. stat. sol. (a)*, **197**:39, 2003.
- [72] J.-N. Chazalviel, M. Etman, and F. Ozanam. *J. Electroanal. Chem.*, 297:533, 1991.
- [73] J.S. Judge. *J. Electrochem. Soc.*, **118**:1772, 1971.
- [74] F. Yahyaoui, T. Dittrich, M. Aggour, J.-N. Chazalviel, F. Ozanam, and J. Rappich. Etch rates of silicon oxides in dilute fluoride solutions. *J. Electrochem. Soc.*, 150, 2003.
- [75] B. Garrido, J. Montserrat, and J. R. Morante. The Role of Chemical Species in the Passivation of  $\mu\text{m}$  Silicon Surfaces by HF in Water-Ethanol Solutions. *J. Electrochem. Soc.*, 143:4059, 1996.
- [76] H. Kikuyama, M. Waki, M. Miyashita, T. Yabune, N. Miki, J. Takano, and T. Ohmi. *J. Electrochem. Soc.*, 141:366, 1994.
- [77] J.-N. Chazalviel. *private communication*, 2005.
- [78] P. Gray and S.K. Scott. *Chemical oscillations and instabilities*. Clarendon Press, 1994.
- [79] A.T. Fechner. *Schweigg. J. Phys. Chem.*, 53:141, 1828.
- [80] M. Faraday. Experimental Researches in Electricity. *Phil. Trans. Roy. Soc., Ser. A*, 124:77, 1834.
- [81] F. Ozanam, J.-N. Chazalviel, A. Radi, and M. Etman. Current oscillations in the anodic dissolution of silicon in fluoride electrolytes. *Ber. Bunsenges. Phys. Chem.*, **95**:98, 1991.
- [82] R. Prange. *Elektrochemische Charakterisierung und Modellierung langsamer Strom- und Spannungszillationen am Silizium-Flußsäure-System*. Dissertation, Universität Kiel, 1998.
- [83] J.-N. Chazalviel, F. Ozanam, M. Etman, F. Paolucci, L.M. Peter, and J. Stumper. The p-Si/fluoride interface in the anodic region: Damped and/or sustained oscillations. *J. Electroanal. Chem.*, **327**:343, 1992.
- [84] H. Gerischer and M. Lübke. Electrolytic growth and dissolution of oxide layers on silicon in aqueous solutions of fluorides. *Ber. Bunsenges. Phys. Chem.*, **92**:573, 1988.
- [85] R.L. Smith and S.D. Collins. Porous silicon formation mechanisms. *J. Appl. Phys.*, **71**.
- [86] M.J. Eddowes. Anodic dissolution of p and n-type silicon. Kinetic study of the chemical mechanism. *J. Electroanal. Chem.*, 280:297, 1990.

- [87] J. Grzanna, H. Jungblut, and H.J. Lewerenz. A model for electrochemical oscillations at the si-electrolyte contact, part i. theoretical development. *J. Electroanal. Chem.*, **486**:181, 2000.
- [88] J. Grzanna, H. Jungblut, and H.J. Lewerenz. A model for electrochemical oscillations at the si-electrolyte contact, part ii. simulations and experimental results. *J. Electroanal. Chem.*, **486**:190, 2000.
- [89] J.-N. Chazalviel and F. Ozanam. A theory for resonant response of an electrochemical system: self-oscillating domains, hidden oscillation and synchronization impedance. *J. Electrochem. Soc.*, 139:2501, 1992.
- [90] F. Ozanam, N. Blanchard, and J.-N. Chazalviel. Microscopic, self-oscillating domains at the silicon surface during its anodic dissolution in a fluoride electrolyte. *Electrochem. Acta*, **38**:1627, 1993.
- [91] J. Carstensen, R. Prange, G.S. Popkirov, and H. Föll. A model for current oscillations in the Si-HF system based on a quantitative analysis of current transients. *Appl. Phys. A*, **67**:459, 1998.
- [92] J. Carstensen, M. Christophersen, and H. Föll. Pore formation mechanisms for the si-hf system. *Mat. Sci. Eng. B*, **69-70**:23, 2000.
- [93] E. Foca H. Föll and J. Carstensen. CBM review. page to be published, 2005.
- [94] E. Foca. *Simulation of Si electrode oscillations by rewriting and debugging a Monte Carlo program*. Master thesis, University of Kiel, 2003.
- [95] S. Langa. *Electrochemical pore etching in III-V compounds*. Doktorarbeit, Universität Kiel, 2004.
- [96] H. Föll, S. Langa, J. Carstensen, M. Christophersen, and I.M. Tiginyanu. Review: Pores in iii-v semiconductors. *Adv. Mat.*, **25**:183, 2003.
- [97] E. Propst and P.A. Kohl. The Photoelectrochemical Oxidation of n-Si in Anhydrous HF-Acetonitrile. *J. Electrochem. Soc.*, **140**(5), 1993.
- [98] V. Lehmann and U. Grüning. The limits of macropore array fabrication. *Thin Solid Films*, **297**:13, 1997.
- [99] S. Matthias and F. Müller. Asymmetric pores in a silicon membrane acting as massively parallel brownian ratchets. *Nature*, 424:53, 2003.
- [100] P. Kleimann, J. Linross, and S. Petersson. Formation of wide and deep pores in silicon by electrochemical etching. *Mater. Sci. Eng. B*, **69-70**:29, 2000.
- [101] S. Rönnebeck. *Anwendung makroporösen Siliziums in der Röntgentechnik*. Dissertation, Universität Kiel, 2001.
- [102] V. Lehmann. The physics of macropore formation in low doped n-type silicon. *J. Electrochem. Soc.*, **140**:2836, 1993.



- [103] S. Rönnebeck, J. Carstensen, S. Ottow, and H. Föll. Crystal orientation dependence of macropore growth in n-type silicon. *Electrochem. Solid-State Lett.*, **2**:126, 1999.
- [104] H. Föll, J. Carstensen, M. Christophersen, and G. Hasse. A new view of silicon electrochemistry. *phys. stat. sol. (a)*, **182**(1):7, 2000.
- [105] M.M. Rieger and P.A. Kohl. Mechanism of (111) silicon etching in HF-acetonitrile. *J. Electrochem. Soc.*, **142**:1490, 1995.
- [106] E.A. Ponomarev and C. Lévy-Clément. Macropore formation on p-type silicon. *J. Por. Mat.*, **7**:51, 2000.
- [107] S. Lust and C. Lévy-Clément. Macropore formation on medium doped p-type silicon. *phys. stat. sol. (a)*, **182**:17, 2000.
- [108] R.B. Wehrspohn, J.-N. Chazalviel, and F. Ozanam. Macropore formation in highly resistive p-type crystalline silicon. *J. Electrochem. Soc.*, **145**:2958, 1998.
- [109] M. Christophersen, J. Carstensen, and H. Föll. Crystal orientation dependence of macropore formation in p-type Si using organic electrolytes. *phys. stat. sol. (a)*, **182**:103, 2000.
- [110] J.-N. Chazalviel, R. Wehrspohn, and F. Ozanam. Electrochemical preparation of porous semiconductors: from phenomenology to understanding. *Mat. Sci. Eng. B*, **69-70**:1, 2000.
- [111] S. Lust and C. Lévy-Clément. Chemical limitations of macropore formation on medium doped p-type silicon. *J. Electrochem. Soc.*, **149**, 2002.
- [112] K.J. Chao, S.C. Kao, C.M. Yang, M.S. Hseu, and T.G. Tsai. Formation of high aspect ratio macropore array on p-type silicon. *Electrochemical and Solid-State Letters*, **3**:489, 2000.
- [113] U. Grüning, V. Lehmann, and C.M. Engelhardt. Two-dimensional infrared photonic bandgap structure based on porous silicon. *Appl. Phys. Lett.*, **66**:3254, 1995.
- [114] A. Birner, R. Wehrspohn, F. Müller, U. Gösele, and K. Busch. Silicon-based photonic crystals. *Adv. Mat.*, **13**:377, 2001.
- [115] V. Lehmann, R. Stengl, H. Reisinger, R. Detemple, and W. Theiss. Optical shortpass filters based on macroporous silicon. *Appl. Phys. Lett.*, **78**:589, 2001.
- [116] I. Avrutsky and V. Kochergin. Optical filtering by leaky guided modes in macroporous silicon. *Appl. Phys. Lett.*, **82**:3590, 2003.
- [117] X. Badel. *Electrochemically etched pore arrays in silicon for x-ray imaging detectors*. Phd thesis, KTH Stockholm, Sweden, 2005.
- [118] T. Laurell, J. Drott, L. Rosengren, and K. Lindström. Enhanced enzyme activity in silicon integrated enzyme reactors utilising porous silicon as coupling matrix. *Sensors and Actuators B*, **31**:161, 1996.
- [119] H. Ohji, S. Izuo, P.J. French, and K. Tsutsumi. Macroporous-based micromachining on full wafers. *Sensors and Actuators A*, **92**:384, 2001.

- [120] M.J.J. Theunissen. Etch channel formation during anodic dissolution of n-type silicon in aqueous hydrofluoric acid. *J. Electrochem. Soc.*, **119**:351, 1972.
- [121] H. Herino, G. Bomchil, K. Barla, C. Bertrand, and J.L. Ginoux. Porosity and pore size distributions of porous silicon layers. *J. Electrochem. Soc.*, **143**:1994, 1987.
- [122] A. Halimaoui. *Porous silicon: material processing*. In J.-C. Vial and J. Derrien, editors, *Porous Silicon and Technology*. Springer, 1994.
- [123] S. Frohnhoff. *Spektroskopische Untersuchungen zur Bildung und Degradation poröser Silicium-Schichten*. Dissertation, Forschungszentrum Jülich, 1993.
- [124] G. Bomchil, R. Herino, K. Barla, and J.C. Pfister. Pore size distribution in porous silicon studied by adsorption isotherms. *J. Electrochem. Soc.*, **130**:1611, 1983.
- [125] P.C. Searson, J.M. Macaulay, and S.M. Prokes. The formation, morphology, and optical properties of porous silicon structures. *J. Electrochem. Soc.*, **139**:3373, 1992.
- [126] C. Jäger, B. Finkenberger, W. Jäger, M. Christophersen, J. Carstensen, and H. Föll. Transmission electron microscopy investigations of the formation processes of macropores in n-si(001)/(111) and p-si(001)/(111). *Mat. Sci. Eng. B*, **69-70**:199, 2000.
- [127] T. Osaka, K. Ogasawara, and S. Nakahara. Classification of the pore structure of n-type silicon and its microstructure. *J. Electrochem. Soc.*, **144**:3226, 1997.
- [128] F. Cunin, T.A. Schmedake, J.R. Link, Y.Y. Li, J. Koh, S.N. Bhatia, and M.J. Sailor. . *Nat.Mat.*, **1**:39, 2002.
- [129] C. Mazzoleni and L. Pavesi. *Appl. Phys. Lett.*, **67**:1983, 1995.
- [130] M.G. Berger, M. Thönissen, W. Thei's, and H. Münder. Microoptical devices based on porous silicon. In *Optoelectronic properties of semiconductors and superlattices*, London. Gordon and Breach science publisher.
- [131] T. Yonehara. *BESOI with porous silicon: ELTRAN* in: L.T. Canham, *Properties of porous silicon*. IEE-Books, London, 1997.
- [132] T. Tsuboi, T. Sakka, and Y.H. Ogata. Polarization behavior during porous silicon formation: effect of surfactant. *Electrochimica Acta*, **46**:1013, 2001.
- [133] S. Schweizer, R.B. Wehrspohn, and J. Schilling. Improved electrochemical etching of macroporous silicon - the role of surfactants. *203rd meeting of the Electrochem. Soc., Paris*.
- [134] S. Schweizer (Univ. of Paderborn/Germany). . *personal communication*.
- [135] M. Christophersen, S. Langa, J. Carstensen, I.M. Tiginyanu, and H. Föll. A comparison of pores in silicon and pores in iii-v compound materials. *phys. stat. sol. (a)*, **197**(1/2), 2003.
- [136] P.M. Sarro, D. Brida, W.v.d. Vlist, and S. Brida. Effect of surfactant on surface quality of silicon microstructures etched in saturated tmahw solutions. *Sensors and Actuators*, **85**:340, 2000.

- [137] J. Jeon, S. Raghavan, and R.P. Sperline. Behavior of Polyethylene Oxide Based Nonionic Surfactants in Silicon Processing Using Alkaline Solutions. *J. Electrochem. Soc.*, **142**:621, 1995.
- [138] T. Takizawa, S. Array, and M. Nakahara. Fabrication of vertical and Uniform-Size porous InP structures by electrochemical anodization. *Jpn. J. Appl. Phys.*, 33(5).
- [139] S. Langa, I.M. Tiginyanu, J. Carstensen, M. Christophersen, and H. Föll. Formation of porous layers with different morphologies during anodic etching of n-inp. *J. Electrochem. Soc. Lett.*, **3**(11):14, 2000.
- [140] P. Schmuki, L. Santinacci, T. Dienizian, and D.J. Lockwood. Electrochemistry and pore formation - pore formation on n-inp. *phys. stat. sol. a*, 182:51, 2000.
- [141] H. Löwe, P. Keppel, D. Zach, and C. Schmidt. *Halbleiterätzverfahren*. Akademie-Verlag, Berlin.
- [142] S. Langa, I.M. Tiginyanu, J. Carstensen, M. Christophersen, and H. Föll. Self-organized growth of single crystals of nanopores. *Appl. Phys. Lett.*, **82**(2):278, 2003.
- [143] J.R. MacDonald. *Impedance spectroscopy*. John Wiley & Sons, 1987.
- [144] G. Hasse. *Untersuchungen der kinetischen Prozesse an Silizium-Elektroden mit Stromtransienten- und Impedanzmessungen*. Dissertation, Universität Kiel, 2005.
- [145] www.wikipedia.de. Wasserstoffelektrode. <http://de.wikipedia.org/wiki/Wasserstoffelektrode>.
- [146] ET&TE Etch and Technology GmbH. . <http://www.et-te.com>.
- [147] J. Carstensen. private communication. *Christian-Albrechts-University of Kiel*, 2005.
- [148] U. Tietze and C. Schenk. *Halbleiterschaltungstechnik*. Springer, Berlin, 1999.
- [149] C. Gerthsen and H. Vogl. *Physik*. Springer, Berlin, 1995.
- [150] P.J. Goodhew and F.J. Humphreys. *Electron microscopy and analysis*. Taylor & Francis, London, 1988.
- [151] D. Mende and G. Simon. *Physik - Gleichungen und Tabellen*. VEB Fachbuchverlag, Leipzig, 1988.
- [152] D.A.G. Bruggemann. Berechnung verschiedener physikalischer Konstanten von heterogenen Substanzen. *Ann. Phys.*, **24**:636, 1935.
- [153] H. Looyenga. *Physica*, **31**:401, 1965.
- [154] J.C.M. Garnett. Colours in metal glasses and in metallic films. *Philos. Trans. Roy. Soc. London*, 203:385, 1904.
- [155] W. Theiß, S. Henkel, and M. Arntzen. Connecting microscopic and macroscopic properties of porous media: choosing appropriate effective medium concepts. *Thin Sol. Films*, **255**:177, 1995.

- [156] D. Bergmann. *Phys. Rep. C*, **43**:377, 1978.
- [157] S. Ottow, G. Popkirov, and H. Föll. *J. Electroanal. Chem.*, **455**:29, 1998.
- [158] <http://www.mtheiss.com>.
- [159] S. Langa, J. Carstensen, I.M. Tiginyanu, M. Christophersen, and H. Föll. Formation of tetrahedron-like pores during anodic etching of (100)-oriented n-GaAs. *Electrochem. and Solid State Lett.*, **5**:14, 2002.
- [160] E. Spiecker, M. Rudel, W. Jäger, M. Leisner, and H. Föll. Morphology, interface polarity, and branching of electrochemically etched pores in inp. *Phys. Stat. Sol.(a)*, page to be published, 2005.
- [161] J. Schilling. *Herstellung und optische Eigenschaften von 2D-und 3D-photonischen Kristallen aus macroporoeseem Silizium*. Dissertation, Martin-Luther-Universitaet Halle-Wittenberg, 2002.
- [162] B.H. Erne, D. Vanmaekelbergh, and J.J. Kelly. Morphology and strongly enhanced photoresponse of GaP electrodes made porous by anodic etching. *J. Electrochem. Soc.*, **143**:305, 1996.
- [163] S. Langa, J. Carstensen, M. Christophersen, K. Steen, S. Frey, I.M. Tiginyanu, and H. Föll. Uniform and nonuniform nucleation of pores during the anodization of si, ge, and iii-v semiconductors. *J. Electrochem. Soc.*, **152**, 2005.
- [164] [www.wikipedia.org. Geometrical frustration. http://en.wikipedia.org/wiki/Geometrical/\\_frustration](http://en.wikipedia.org/wiki/Geometrical_frustration).
- [165] R. Schnabel and P. Langer. Controlled-pore glass as a stationary phase in chromatography. *J. Chromatogr. A*, **544**:137, 1991.
- [166] A.J. Sedriks. *Corrosion of Stainless Steels*. John Wiley, New York, 1996.
- [167] B. Grésillon. *Caractérisation d'une couche de silice poreuse obtenue par voie électrochimique*. Stage de licence, CNRS/Ecole Polytechnique, Palaiseau, France, 2003.
- [168] E. Hecht. *Optics*. Addison Wesley Longman, Reading, 1998.
- [169] J. Carstensen, R. Prange, and H. Föll. A model for current-voltage oscillations at the silicon electrode and comparison with experimental results. *J. Electrochem. Soc.*, **146**:1134, 1999.
- [170] O. Nast, S. Rauscher, H. Jungblut, and H.-J. Lewerenz. Micromorphology changes of silicon oxide on si(111) during current oscillations: a comparative in situ afm and ftir study. *J. Electroanal. Chem.*, **442**:169, 1998.
- [171] M. Bailes, S. Böhm, L.M. Peter, D.J. Riley, and R. Greef. An electrochemical and ellipsometric study of oxide growth on silicon during anodic etching in fluoride solutions. *Electrochim. Acta*, **43**:1757, 1998.
- [172] B.H. Kemmenoe and G.R. Bullock. Structure analysis of sputter-coated and ion-beam sputter-coated films: a comparative study. *J. Microsc.*, **132**:153, 1983.

- [173] J. Goldstein, D. Newbury, D. Joy, C. Lyman, P. Echlin, E. Lifshin, L. Sawyer, and J. Michael. *Scanning Electron Microscopy and X-Ray Microanalysis*. Kluwer / Plenum, New York, 2003.
- [174] C. da Fonseca, F. Ozanam, and J.-N. Chazalviel. In situ infrared characterisation of the interfacial oxide during the anodic dissolution of a silicon electrode in fluoride electrolytes. *Surf. Sci.*, **365**:1, 1996.
- [175] H.H. Hassan, J.L. Sculfort, M. Etman, F. Ozanam, and J.-N. Chazalviel. Kinetic and diffusional limitations to the anodic dissolution of p-si in fluoride media. *J. Electroanal. Chem.*, **380**:55, 1995.
- [176] A. Uhler. Electrolytic shaping of germanium and silicon. *Bell System Tech. J.*, **35**:333, 1956.

# Partial publications

## Scientific books

1. K. Busch, S. Lölkes, R.B. Wehrspohn, and H. Föll (Eds.), *Photonic Crystals - Advances in Design, Fabrication, and Characterization*, Wiley-VCH, Weinheim (2004).

## Scientific Journals and Proceedings

1. S. Lölkes, M. Christophersen, S. Langa, J. Carstensen, and H. Föll, *Selforganized formation of crystallographically oriented octahedral cavities during electrochemical pore etching*, Mat. Sci. Eng. B, 101, 159, (2003).
2. H. Föll, S. Langa, J. Carstensen, S. Lölkes, M. Christophersen, I.M. Tiginyanu, *Engineering Porous III-Vs*, III-Vs Rev., 16, 42, (2003).
3. S. Langa, S. Frey, J. Carstensen, H. Föll, I.M. Tiginyanu, M. Hermann, and G. Böttger, *Waveguide Structures Based on Porous Indium Phosphide*, Electrochem. Sol. State Lett., 8, C30, (2005).
4. E. Foca, H. Föll, F. Daschner, V.V. Sergentu, J. Carstensen, S. Frey, R. Knöchel, and I.M. Tiginyanu, *Efficient focusing with a concave lens based on a photonic crystal with an unusual effective index of refraction*, Phys. Stat. Sol. (a), 202, R35, (2005).
5. S. Langa, J. Carstensen, M. Christophersen, K. Steen, S. Frey, I.M. Tiginyanu, and H. Föll, *Uniform and Nonuniform Nucleation of Pores during the Anodization of Si, Ge and III-V Semiconductors*, J. Electrochem. Soc., 152, C525, (2005).
6. S. Frey, B. Grésillon, F. Ozanam, J.-N. Chazalviel, J. Carstensen, H. Föll, and R.B. Wehrspohn, *Self-Organized Macrostructures in Anodically Formed Mesoporous Silica*, Electrochem. Sol. State Lett., 8, B25, (2005).
7. S. Frey, M. Kemell, J. Carstensen, S. Langa, H. Föll, *Fast pore etching*, Phys. Stat. Sol. (a), 202, 1369, (2005).
8. J. Carstensen, M. Christophersen, S. Lölkes, E. Ossei-Wusu, J. Bahr, S. Langa, G. Popkirov, H. Föll, *Large area etching for porous semiconductors*, Phys. Stat. Sol. (c), 2, 3339, (2005).
9. S. Langa, S. Lölkes, J. Carstensen, M. Hermann, G. Böttger, I. M. Tiginyanu, H. Föll, *Engineering the morphology of porous InP for waveguide applications*, Phys. Stat. Sol. (c), 2, 3253, (2005).

10. H. Föll, J. Carstensen, and S. Frey, *Porous and Nanoporous Semiconductors and Emerging Applications*, in: *Nanoporous and Nanostructured Materials for Catalysis, Sensor, and Gas Separation Applications*, edited by S.W. Lu, H. Hahn, J. Weissmuller, and J.L. Gole (Mater. Res. Soc. Symp. Proc. 876E, Warrendale, PA, 2005), R12.1.
11. H.-S. Kitzerow, G. Mertens, H. Matthias, H. Marsmann, R.B. Wehrspohn, S. Matthias, U. Gösele, S. Frey, and H. Föll, *Director fields of nematic liquid crystals in tunable photonic crystals*, Proc. SPIE Int. Soc. Opt. Eng., 5926, 592605, (2005).

### **Book contributions**

1. R.B. Wehrspohn, J. Schilling, J. Choi, Y. Luo, S. Matthias, S.L. Schweizer, F. Müller, U. Gösele, S. Lölkes, S. Langa, J. Carstensen, and H. Föll, *Electrochemically-prepared 2D and 3D photonic crystals*, in: K. Busch, S. Lölkes, R.B. Wehrspohn, and H. Föll (Eds.), *Photonic Crystals - Advances in Design, Fabrication, and Characterization*, Wiley-VCH, Weinheim (2004).

### **Patents and patent applications**

1. S. Langa, S. Lölkes, J. Carstensen, and H. Föll, *Verfahren zur Herstellung von integrierten Wellenleitern*, Publication-Nr.: DE 103 41 030 A1, Date of application 03.09.2003
2. S. Lölkes, H. Föll, J. Carstensen, and S. Langa, *Verfahren zur Herstellung von schnellwachsenden Poren in n-Typ Silizium*, Patent-Nr.: DE 10 2004 011 394 B3, Date of application 05.03.2004

### **Conference Oral Contributions and invited talks**

1. S. Lölkes, *Photonic Crystals*, Institutsseminar Fraunhofer-Institut für Siliziumtechnologie (ISIT), 16 May 2002, Itzehoe, Germany.
2. S. Lölkes, S. Langa, J. Carstensen, and H. Föll, *Self-assembled photonic crystals in Si and III-V compounds by electrochemical pore etching*, DPG-Frühjahrstagung, 24-28 March 2003, Hannover, Germany.
3. S. Frey, M. Kemell, J. Carstensen, S. Langa, H. Föll, *Fast pore etching*, Int. Conference of Porous Semiconductors - Science and Technology, 14-19 March 2004, Cullera, Spain.

### **Conference Posters**

1. S. Lölkes, M. Christophersen, S. Langa, J. Carstensen, and H. Föll, *Selforganized formation of crystallographically oriented octahedral cavities during electrochemical pore etching*, E-MRS Spring Meeting, 18-21 June 2002, Strasbourg, France.
2. S. Lölkes, S. Langa, M. Christophersen, J. Carstensen, and H. Föll, *2D & 3D Photonic Crystal structures by electrochemical Pore etching in Si and III-V compounds*, 3rd International Heraeus Summerschool, E-MRS Spring Meeting, 15-25 July 2002, Wittenberg, Germany.
3. S. Lölkes, S. Langa, M. Christophersen, G. Hasse, G. Popkirov, J. Carstensen, and H. Föll, *Elektrochemische Herstellung poröser Halbleiter - Nanostrukturen*, Materialwissenschaften in Hamburg, 14 October 2002, Hamburg, Germany.

4. S. Lölkes, S. Langa, J. Carstensen, and H. Föll, *Investigation of current oriented pore growth in silicon*, 203rd Spring meeting of the Electrochemical Society, 27 April - 2 May 2003, Paris, France.
5. S. Lölkes, S. Langa, J. Carstensen, and H. Föll, *Formation of mesopores with larger diameters*, 203rd Spring meeting of the Electrochemical Society, 27 April - 2 May 2003, Paris, France.
6. S. Langa, J. Carstensen, S. Lölkes, I. M. Tiginyanu, H. Föll, *Particularities of Anodically Etched Pores in (100) Substrates*, 203rd Spring meeting of the Electrochemical Society, 27 April - 2 May 2003, Paris, France.
7. J. Carstensen, K. Steen, M. Christophersen, J. Bahr, G. Popkirov, S. Langa, S. Lölkes, H. Föll, *Large area etching of porous semiconductors*, 203rd Spring meeting of the Electrochemical Society, 27 April - 2 May 2003, Paris, France.
8. S. Lölkes, S. Langa, J. Carstensen, and H. Föll, *Crystal orientation dependence of pores in InP for photonic crystal applications*, DPG-Frühjahrstagung, 08-12 March 2004, Regensburg, Germany.
9. J. Carstensen, M. Christophersen, S. Lölkes, E. Ossei-Wusu, J. Bahr, S. Langa, G. Popkirov, H. Föll, *Large area etching for porous semiconductors*, Int. Conference of Porous Semiconductors - Science and Technology, 14-19 March 2004, Cullera, Spain.
10. E. Foca, S. Frey, F. Daschner, V.V. Sergentu, J. Carstensen, R. Knöchel, I.M. Tiginyanu, and H. Föll, *Focusing microwaves with a concave lens based on a 2D photonic crystal*, DPG-Frühjahrstagung, 04-09 March 2005, Berlin, Germany.



# Curriculum vitae

Name: Stefan Thierry Frey, geb. Lölkes  
Place of residence: Dorfstraße 22, 24250 Warnau, Germany  
Born: 20. September 1974 in Bonn  
Marital status: married, 3 children  
Citizenship: German / French  
Parents: Nicole Schwaabe and Günter Lölkes

## Schooling

1981 - 1985 Elementary school, Neubiberg, Germany  
1989 - 1990 DSNY, White Plains, USA  
1985 - 1994 Gymnasium Neubiberg, Germany  
July 1994 Abitur

## Community service

1994 - 1995 Community service at the Johanniter-Unfall-Hilfe, Ottobrunn, Germany

## University Education

1995 - 1997 Study of Physics at the Ludwig-Maximilians-Universität, Munich, Germany  
1997 - 2000 Study of Physics at the Technischen Universität München  
since 2001 Scientific collaborator at the Technical Faculty of the Christian-Albrechts-Universität zu Kiel, Germany (Chair of Prof. Dr. Föll)  
May - July 2004 Visiting scientist at the CNRS / Ecole Polytechnique, Palaiseau, France (Group of Prof. Dr. Chazalviel)

# Acknowledgements

(I do that here in mixed language, because saying thanks can be a complex thing...)

An erster Stelle möchte ich Herrn Prof.Dr. Helmut Föll herzlichst für die Aufnahme in seinen Lehrstuhl und die vertrauensvolle Zusammenarbeit während der letzten 4 Jahre danken. Einige entscheidende Gedanken dieser Arbeit stammen von ihm und er war stets Diskussionen zu verschiedensten Themen aufgeschlossen. Auch bei "weltlichen" Themen wie der DFG - Schwerpunktsbetreuung oder der Herausgabe des PhC - Fachbuches hat er mich vorbehaltlos unterstützt. Last, but not least, möchte ich mich auch für seine (menschliche und finanzielle) Förderung meines Gastaufenthaltes an der Ecole Polytechnique bedanken.

Dr. Jürgen Carstensen möchte ich für die tagtägliche Betreuung der Arbeiten danken. Er war stets zur Stelle, wenn der Messaufbau oder die Software nicht wollten. V.a. aber hat er mit mir die verschiedenen Modellvorstellungen wieder und wieder diskutiert und entwickelt. Auch für seine unbeirrbar freundliche Art möchte ich mich bedanken(, die ich stellenweise arg strapaziert habe).

Je voudrais aussi exprimer ma gratitude à Prof. Jean-Noël Chazalviel et Dr. François Ozanam qui ont s'occupé intensivement de moi dans mes trois mois comme boursier de Marie-Curie (et aussi pour rendre possible cette aide!) dans leur labo. Merci pour me laisser participer de votre connaissance immense de l'électrochimie de silicium et pour m'enseigner français :)

Natürlich möchte ich mich auch bei unserer gesamten Arbeitsgruppe bedanken, in der es sehr viel Spass gemacht hat, zu arbeiten, schon allein wegen des entspannten Klimas: Jörg Bahr, der als Laboringenieur hier exzellente Arbeit leistet. Außerdem für Gespräche in Saunas und beim Kaffee und Mittagessen. Eigentlich ziemlich oft. Über Kinder, Häuser, Autos, Frauen, Eltern, Steuern, Politik. Über eben ziemlich vieles... Katrin Brandenburg, die als Sekretärin unsere Gruppe vor dem Versinken ins kreative Chaos tagtäglich bewahrt. Prof. Dr. George Popkirov, der mit seinen Potentiostaten und diversen anderen Geräten unsere Arbeit hier elektronikhardwaremäßig ermöglicht. Ausserdem danke für viele unterhaltsame Geschichten aus dem bulgarischen Alltag und kreative Ansichten zu nahezu allen lebensrelevanten Themen. Viele interessante Diskussionen zu Leben und Politik in Deutschland und Moldawien mit meinem Mitdoktoranden Eugen Foca. Einem anderen Mitdoktoranden, der leider (geographisch) von uns gegangen ist: Stefan Matthijssen. Eisen-Matthijssen! Du hast das richtige gemacht! Es wird klappen! Außerdem haben mein Leben hier in den letzten vier Jahren bereichert (das meine ich ernst!): Dr. Sergiu Langa, Gunther Hasse, Dr. Oliver Riemenschneider, Dr. Chen Fang, Emmanuel Ossei-Wusu, Dr. Marc Christophersen, Dr. Mohammad Hejjo Al Rifai, Kay Steen.

Besonders bedanken möchte ich auch bei meinen diversen Diplomanden und Praktikanten: Sinje Keipert, Zhen Yang, Malte Leisner und Patrick Schauer. Similarly my thanks go out to our international guest scientists, which worked with me: Suzanne Snyder from NEAHPower Inc., Seattle, USA and Dr. Marianna Kemell from Helsinki University, Finland.

Bei den restlichen Mitgliedern der Fakultät möchte ich mich ebenfalls bedanken, die mir während der letzten Jahre mit Rat und Tat zur Seite standen.

Mit Prof.Dr. Ralf Wehrspohn hat es vier Jahre lang Spass gemacht, das SPP sowie diverse andere Projekte zu schmeissen. Außerdem danke für die nette Verabschiedung aus dem SPP und das Abschiedsgeschenk! Bei ihm und Prof.Dr. Kurt Busch möchte ich mich bedanken für die reibungslose Zusammenarbeit bei der Editierung des PhC-Buches. An das gesamte DFG-Schwerpunktprogramm 1113 "Photonische Kristalle" sowie die anderen deutschen PhC Projekte geht mein Dank für Ihre Beiträge und ihre Akzeptanz meiner Person als Editor. Ebenso ergeht mein Dank dafür, dass mich sowohl die Projektleiter im SPP als auch Dr. Wehrberger von der DFG, stets als Gesprächspartner "auf Augenhöhe" behandelt haben (auch ohne Dr. . .). Auch bedanken möchte ich mich bei den anderen SPP-Doktoranden, mit denen ich mich darum gekümmert habe, dass es wirtschaftlich wieder aufwärts geht für die Marburger, Berliner, Hannoveraner und Regensburger Kneipen! Ebenfalls sehr lustig in Erinnerung: Die Katakomben von Bad Honnef und Biberbettwäsche.

In meinem Bemühen, Poren an lithographisch vorstrukturierte Plätze zu binden, haben mich folgende Institutionen und Personen unterstützt, wofür ich mich nochmals herzlich bedanken möchte: Prof.Dr. Ralf Wehrspohn (Uni Paderborn bzw. MPI Halle), Martin Herrmann (Walter-Schottky-Institut der TU München), Prof.Dr. Veyhl und Herr Seydlitz (FH Heide), Dr. Lindlein (Uni Erlangen) und Josef Kouba (Bessy, Berlin). Glaubt mir, der Tag des Kieloviten wird kommen, ebenso der des hexagonalen InP!

Meiner Mutter Nicole und Ihrem Mann Peter möchte ich herzlich für Ihre seelische und finanzielle Unterstützung all die Jahre danken. Ebenso danke an meinen Vater Günter (der wohl irgendwie das Physikkorn in mir gesät haben muss. . .) und seine Frau Annette. Meine Schwiegereltern Jutta und Rainer haben unzählige Tage während unserer Ferien auf unsere Kinder aufgepasst, ausserdem haben wir fast immer dort gewohnt, wenn wir in München waren. Jutta ist zudem für mehrere Wochen hierher gekommen, um Claudia zu helfen, während ich in Paris kleinen Oxidkügelchen nachgejagt habe. Vielen Dank!

Mein Dank geht auch an die Freunde, die sich über die Jahre hinweg stets mehr oder weniger ungläubig ungehört haben, was ich da so forsche: Klaus, Markus, Stefan, Matthi, Thomas, Philipp, Daniel, Tobi, Claudia, Biene und Ferdi. My special thanks goes out to the italian heavy-smoker Corrado! Thank you, you saved my (mental) life in Paris!

Am allermeisten danke ich jedoch meiner Frau Claudia: Sie hat in den letzten Jahren Ihre eigene Karriere für meine Promotion zurückgestellt und sich sehr viel (in den letzten Wochen praktisch ausschliesslich) um unsere Kinder gekümmert. Vielen, vielen Dank! Ich liebe Dich! Ebenso möchte ich meinen drei kleinen Mäusen - Alicia, Leandra und Gwendolin - sagen, dass ich sie liebe!